Author/s:
Jamieson, Emily Jane

Title:
Understanding Colloidal Adhesion in Polymer Surfactant Emulsions

Date:
2020

Persistent Link:
https://hdl.handle.net/11343/240284

Understanding Colloidal Adhesion in Polymer Surfactant Emulsions

Emily Jane Jamieson

ORCID Identifier – 0000-0001-6524-1508

Submitted in total fulfillment of the requirements of the degree of Doctor of Philosophy

January 2020

Department of Chemical Engineering

The University of Melbourne

Abstract

Attractive interactions between drops in which aggregation or adhesion occurs, rather than coalescence, govern the formation of microstructures that control the phase behaviour, stability, rheology and most importantly function of formulated products (e.g., food, personal care products, pharmaceutical formulations). These products are often multi-component emulsions where interactions between additives can mediate adhesion in complicated ways. The overarching objective of this thesis was to understand how polymer-surfactant (PS) complexes mediate adhesive interactions, with a focus given to the development of a novel microfluidic platform capable of investigating these systems using high throughput measurements. The attractive interactions between oil drops in poly(vinylpyrrolidone) (PVP) and sodium dodecyl sulphate (SDS) solutions were studied using both drop chaining in a microfluidic device and direct force measurements on an AFM. Links between the two methods were explored in detail with emphasis on understanding and establishing similarities in surface coverage and the structural composition of layers at the drops interface.

Through interfacial tension measurements, direct force measurements and microfluidic observations a detailed investigation into drop-drop interactions was performed. Interfacial tension measurements confirmed the formation of PS complexes and the concentration region in which they exist for the PVP/SDS system. Rigid force measurements showed via a quantitative model that depletion and electrical double layer (EDL) forces dominate the interactions between two hydrophobic surfaces. Force measurements between two deformable oil drops using the same systems displayed similar depletion behaviour. A model used to describe deformable systems, also accounting for depletion and EDL forces, used the depletion length and osmotic pressure fit from the rigid surface analysis and showed reasonable agreement with the force data. A small under prediction by the model suggested the existence of an additional steric force from the presence of adsorbed complexes at the interface. At velocities above 500 nm/s dynamic forces dominated the force data, such that it was no longer possible to observe the force features in the measurements. A microfluidic device designed with a drop collision region, allowing drops to come into close separation in the absence of hydrodynamic drainage forces was developed to form chains of oil drops. The persistence and length of a drop chain within a simple external flow was associated to the strength of adhesion across a range of solution compositions and concentrations, independently demonstrating the existence of attractive forces between drops in the PVP/SDS system. The interaction behaviour between the two techniques showed a strong

correlation, where the observed adhesion between drops in the microfluidics is sensitive to the drop deformation and Laplace pressure.

Microfluidic interfacial tension measurements were used to investigate the adsorption kinetics of the PVP/SDS system and surface chemistry of the drops in confined flow via the measurement of a drops deformation through a channel contraction. The continuous phase viscosities of the investigated systems were substantially lower than those used in previous studies, requiring much higher flowrates to be used to achieve measurable deformation. The interfacial tension values attained from microfluidic measurements agreed well with pendent drop experiments, showing characteristic features expected from polymer surfactant systems in interfacial tension measurements. A series of five contractions, where the interfacial tension was measured at increasing time intervals, showed that the interfacial tension reached a time invariant value within milliseconds. These results give reasonable evidence that the PS complex adsorbs to the interface in microfluidic flow at similar levels as the AFM measurements and within relevant timescales.

Droplet microfluidic SANS using a novel device provided information on the molecular structure of the complexes in solution and at the interface. Scattering from the single-phase solutions of PVP, SDS and their complex was successfully measured and showed characteristic intensity patterns expected from each condition based on reviews of the literature. Detailed quantitative analysis of each condition was performed, providing information on their confirmation and evidence of shear-induced transformations. Droplet microfluidic SANS was qualitatively assessed, showing clear differences to bulk single-phase data of equivalent solutions, suggesting evidence of changes to the scattering characteristics which is predicted to be due to an adsorbed layer. At this time the structure or composition of this layer beyond an estimated thickness were unable to be attained as models capable of fitting these specific measurements are not available. Nevertheless, these results provided a consistent picture of an adsorbed PS layer under flow as seen with the other techniques explored throughout this thesis.

Declaration

This is to certify that:

i. the thesis comprises only my original work towards the degree of Doctor of Philosophy except where indicated in the preface,
ii. due acknowledgment has been made in text to all other material used,
iii. the thesis is fewer than 100,000 words in length, exclusive of tables, maps, bibliographies and appendices.

Emily Jane Jamieson 17.01.2020

Preface

All work presented in this thesis was prepared during my enrolment as a PhD student at the University of Melbourne. Microfluidic experiments performed in Chapter 4 were completed with help from Christopher Fewkes. Initial image processing scripts prior to modification were designed and written by Christopher Bolton. I acknowledge the ARC, the Diane Lemaire Scholarship, the Robert Bage Memorial Scholarship, the University of Melbourne and Particulate Fluids Processing Centre for financial support during my PhD.

For Gramps, without whom I would never have been able to achieve this accomplishment.

Acknowledgements

The completion of this thesis has involved an incredible amount of joy, hard work, and if I'm honest pain, but most importantly an unbelievable experience that couldn't be reproduced in any other context. Throughout the journey a variety of people have been there to help me reach the point I'm at today, writing my acknowledgements.

First and foremost, I would like to thank my supervisors Ray Dagastine and Joseph Berry. Ray honestly couldn't have been a more ideal supervisor. He has been a great teacher, motivator, and ultimately mentor, while always being unbelievably supportive. Joe's wonderful support, expertise and friendship made everyday challenges a breeze. I'm particularly thankful for the Friday morning pep-talks. A huge acknowledgement should also go towards those I would name as my mentors when I first started my PhD and for many the on-going support that continued throughout the remainder of my degree. Christine Browne, Srinivas Mettu And Christopher Fewkes all provided me key knowledge and skills in AFM particularly, but also in how to conduct my research and approach a thesis. Christopher Bolton could almost make this list however I would prefer to acknowledge him as a key friend and office buddy who I would hope had just as much fun joking with me as I did listening to him. He was also incredibly helpful towards my work, not only providing me with image processing scripts, but also teaching and guiding me through coding such that I could develop the skills myself. Matthew Biviano and Alisa Bai were my thesis buddies, going through our degrees together was amazing and the support we gave each other through discussions on our work and friendship made the experience thousands of times easier. It was also a joy to spend time with Tanweepriya, Avinash and Dinesh my future group members, as well as Lucas, Ellen and Yuqi who spent extended stays with our group.

Throughout my time as a PhD I made a large effort in gaining as much out of it as possible, ensuring it was more than just research and the thesis that comes with it. Being on the committee of the Particulate Fluids Processing Centre (PFPC) was a joy, and I would like to thank all those involved for providing a distraction during the seminars. My time as the president of PACBER allowed me to engage with the entire department and meet people outside my group.

The people I have worked with through the Materials Characterisation and Fabrication Platform also played a vital role in the completion of this thesis. Lauren as the lead and my short-term boss, Dan at the Melbourne Centre for Nanofabrication (MCN) where I spent time fabricating cantilevers and microfluidic devices, as well as James and Tian as ongoing support in the lab and on the AFMs. Also, a massive thank you to Nick Ainger who helped integrate industrial work into my PhD, as well as a trip to Unilever a reality. It was a truly delightful and engaging experience.

Finally, I would like to do a massive shout out to all my family and friends who supported me through this experience and put up with all the joy and despair I had to offer over the 4 year journey. Your understanding and flexibility helped make the time fly!

Table of Contents

List of Figures

List of Tables

Chapter 1: Thesis Overview

1.1 Introduction to the Thesis

Attractive interactions between drops in which aggregation rather than coalescence occurs, govern the formation of microstructures that control the phase behaviour, stability, and ultimately the function of formulated products (*e.g.*, food, coatings, personal care products, pharmaceuticals). At concentrated volume fractions this behaviour can result in gelled networks which can be tailored to control the fluids rheological properties. Pioneering work on adhesive emulsions by Bibette *et al*. highlights the critical role adhesive mechanisms play in controlling the structure and morphology of these networks (1, 2). Products that require targeted functions such as deposition including shampoo, detergents or paint; also rely on adhesive interactions to perform their role (3). Therefore, understanding the pathways to drop adhesion is critical to advance the engineering of new complex fluids with superior functional properties.

These products are often multi-component emulsions where interactions between additives can mediate adhesion in complicated ways. Polymer-surfactant systems are commonly used for this purpose due to their ability to control both solution and surface properties with small changes to solution composition, as well as their potential to provide structure by forming aggregates (4-6). This also means any formulated system can have a larger parameter space and generalised predictive links between molecular composition and function remain elusive in many instances. The behaviour of polymer-surfactant (PS) systems in the bulk has been historically well studied, such that literature focus shifted to interfacial properties and mechanisms of adsorption over the last decade (7-10). Despite now having a greater understanding of how these systems behave at the interface and how this may influence colloidal interactions, links between surface properties and the adhesion between surfaces in colloidal systems is still unclear.

Connecting the adhesive behaviour of complex fluids to structure and molecular composition is challenging and time-consuming using current experimental methods. Techniques able to rapidly and accurately characterise a large number of new material formulations are not readily available, reducing the speed at which these formulation areas can be optimized and developed. Atomic force microscopy (AFM) provides exceptional accuracy and very detailed results at the nanoscale, yet experiments are costly and require a large distribution of measurements to be taken in order to appropriately analyse the system (11-13). Thus, linking the detailed quantitative results of AFM to a more easily performed platform such as microfluidics could potentially provide a means for rapidly and inexpensively probing the interactions and surface forces between adhesive and strongly interacting soft particles over a wide range of operating conditions.

Microfluidics is a commonly used technique for the generation and investigation of drops. This is largely owing to its capabilities in producing extremely controlled drops with precise volumes at high frequencies (14). Developments in the design and applications of microfluidics continue to progress, with examples of interfacial tension (15-18), drop sorting (19), micro-rheology (20-22) and scattering (23-25) presented in the literature. A number of groups have begun moving towards high throughput measurements in droplet microfluidic devices, yet most either probe or are governed by hydrodynamic interactions (26-30). In order to develop correlations between AFM and microfluidics, an understanding of both the molecules at the interface and the drop-drop interactions in these two scenarios is required.

1.2 Hypothesis

The aim of this thesis is to understand how adhesive interactions between soft particles (*i.e.* drops, bubbles and capsules) can be mediated and controlled by polymer surfactant complexes of various systems, and to correlate the behaviour with molecular composition. A common polymer-surfactant system; anionic surfactant, sodium dodecylsulphate (SDS), and neutral, water soluble polymer, poly(vinylpyrrolidone) PVP was selected for detailed investigation as it has been widely studied throughout the literature and is expected to have attractive properties, but its surface properties and interactions at interfaces is yet to be fully understood (31-35). Focus is given to exploring the development of a novel high-throughput microfluidic platform capable of measuring surface forces between drops. A microfluidic device designed with a drop collision region, allowing drops to come into close separation in the absence of hydrodynamic drainage forces was developed to form chains of oil drops. The persistence of a drop chain within external flow was explored as a means of identifying strength of adhesion across a range of solution composition and concentrations. Benchmarked against AFM force curves the following hypotheses were made:

1. Understanding drop interactions is a path to understanding adhesion mechanisms.
2. The maximum adhesion between drops is dependent on the polymer surfactant complex and composition ratios, but in the context of emulsions physical parameters are also critical factors.
3. Information that can be accessed through an AFM experiment can also be accessed using a microfluidic device, despite differences in fluid conditions.

It was found that the interaction behaviour between force measurements and microfluidic observations showed a strong correlation, where the observed adhesion between drops in the microfluidics is sensitive to the surfactant concentration, drop deformation and Laplace pressure. Given the existence of complexes in both the bulk and at the interface within the AFM

experiments, further work was dedicated to studying the surface properties of drops within the microfluidic system to corroborate the links made between the two techniques. The main hypotheses to support these links are:

4. The surface coverage of drops in an AFM is ultimately similar to what it is in a microfluidic channel, despite hydrodynamic effects.
5. The molecular structure and composition of layers at a drop interface in a microfluidic channel can be captured using small angle neutron scattering (SANS)

Microfluidic measurements of interfacial tension were performed and compared to pendant drop tensiometry to confirm the presence of the polymer-surfactant complex at the drops interface under flow. In addition, evidence of consistency in the surface chemistry of the drops within flow and in static conditions led to more detailed analysis of the interfacial coating as it is also important that the microstructure in both experimental conditions is understood. To obtain insight into the state of the interfacial coating microfluidic SANS for drops was developed to access information on the composition and structure of the interfacial coating.

1.3 Chapter Summaries

The work presented in this thesis is briefly summarised by chapter below.

Chapter 2 – Literature Review*:* This chapter explores relevant historical and recent literature on colloidal science that encompasses the study of adhesive emulsions, framing this thesis in a broader context. A discussion covering emulsion properties and drop interactions in the context of polymer surfactant systems and the methods developed to study them is presented. Through this review, a gap in available methods is presented and thus further explored throughout the thesis.

Chapter 3 – Experimental Methods: Details of the primary methods used throughout this thesis are presented, with focus given to procedures surrounding AFM and microfluidics. This includes steps for rigid and deformable AFM measurements, the analysis of their force curves, as well as the fabrication and operation of different microfluidic systems.

Chapter 4 – Forces between oil drops in polymer-surfactant systems: Linking direct force measurements to microfluidic observations: AFM and microfluidics were both used to quantify the forces between oil drops in the presence of complexes formed with SDS and PVP. From the AFM force curve analysis depletion, electrical double layer and steric forces were identified to dominate drop interactions. Correlation between the two techniques addresses hypothesis 1 through 3 by providing insight into the surface forces between drops in flowing systems.

Chapter 5 – Microfluidic Interfacial Tension: The surface chemistry of drops underflow is investigated to address hypothesis 4. We compare interfacial tension measurements of SDS and PVP collected from microfluidic and pendant drop tensiometry. The adsorption time within the microfluidics is considered to ensure surface coverage is occurring at timescales relevant to the drop chaining experiments presented in Chapter 4.

Chapter 6 – Droplet Microfluidic SANS: A novel microfluidic device designed for studying the composition of interfacial coatings in SANS is explored. Single-phase measurements of PVP, SDS and their complex is quantitatively analysed to provide insight into their bulk behaviour. Scattering data of bulk single-phases and two-phase drops systems was attained, with quantitative analysis of single-phases performed in more detail, addresses hypothesis 5.

Chapter 7 – Summary and Conclusions: The important outcomes of this thesis are concluded through a summary of the work presented.

1.4 List of Publications

The following is a list of publications resulting from the work presented in this thesis.

1. "Forces between oil drops in polymer-surfactant systems: Linking direct force measurements to microfluidic observations", E.J. Jamieson, C.J. Fewkes, J.D. Berry, R.R. Dagastine, J. Colloid Interface Sci., **2019**, 544, 130-143

Presented as Chapter 4

2. Manuscript in preparation: "Microfluidic tensiometry of polymer-surfactant systems in low viscosity fluids", E.J. Jamieson, C.G. Bolton, J.D. Berry, R.R. Dagastine.

Presented as Chapter 5

3. Manuscript in preparation: "Droplet microfluidic SANS for interfacial coatings of soft matter systems", E.J. Jamieson, C.G. Bolton, T. Das, T. Bai, A.E. Whitten, R.F. Tabor, R.R. Dagastine.

Presented as Chapter 6

Chapter 2: Literature Review

2.1 Introduction

A fundamental issue in colloidal and surface science is understanding how two surfaces interact across a medium, which is specifically relevant to a wide range of practical applications where the stability of colloidal objects, including particles, drops, bubbles and capsules, is a priority. In particular, the interactions between colloidal objects in formulated products are responsible for the aggregation, gel or microstructure formation that control the overall functionality of the system. The techniques available to explore colloidal systems and their behaviours range from the molecular to macro scale, however threading the acquired knowledge across the board to control and design these systems still presents in itself a challenge. This chapter explores the relevant literature covering emulsion properties and drop interactions in the context of polymer surfactant systems and the methods developed to study them. Through this review, a gap in available methods is presented and thus further explored throughout the thesis.

2.2 Drop and Emulsion Properties

2.2.1 Interfacial Tension

Interfacial tension is experienced when two immiscible fluids come into contact and is a measure of the free energy change per unit area required to create the interfacial area between them (36). The molecules experiencing self-interactions within the bulk have a lower energy state compared to those at the fluid-fluid interface, therefore it is energy intensive to move a molecule to the interface and by extension thermodynamically unfavourable. As a result, to reduce the number of exposed molecules and its energy state, the system will attempt to minimise its interfacial area to its smallest form. The interfacial tension of systems provides details on the shape, stability and formation of drops, which can also give insight into the surface composition of fluid interfaces in the presence of surface-active components (6, 37-39). The application of interfacial tension measurements and their implications is discussed across a range of topics throughout this thesis.

2.2.2 Laplace Pressure

The Laplace pressure is the difference in pressure between the inside and outside of a curved surface as a result of the force exerted by the interfacial tension on the interface. It is responsible for opposing external forces that result in deformation of the interface. According to the Young-Laplace equation it is a function of the interfacial tension and curvature of the interface. As the interfacial tension is a constant property for any given system, the Laplace pressure is essentially proportional to the dimensions of the interface. For spherical shapes and by extension drops this means that the radius plays a substantial role in dictating the magnitude of a systems Laplace pressure. This is relevant as the Laplace pressure has been shown to significantly impact the stability and formation of drops (40, 41). For interactions between drops or bubbles, Berry and

Dagastine defined a drop equilibrium stability criterion where a drop or bubble interaction with Laplace pressures less than the disjoining pressure would remain stable, as the film between the drops would not thin enough to reach attractive forces capable of inducing coalescence (42). Drop instability can also be introduced via a flow on effect known as Ostwald ripening. This phenomenon is the preferential diffusion of a discrete phase from smaller to larger drops via the continuous phase, which is driven by the higher Laplace pressure of the smaller drops (40). Taylor performed a detailed analysis on the effects of Ostwald ripening on emulsions stabilised with surfactant, finding that the droplet volume fraction, micellar solubilisation of the oil phase and overall oil solubility all play a crucial role in minimising its effects (43).

2.2.3 Thin Film Drainage

Drop contact or coalescence within an emulsion will occur only when the relative approach rate of the drops at collision is below a critical approach velocity. This is due to the hydrodynamic forces imparted by the surrounding fluid and deformability of the interfaces which will create a thin liquid film between the two drops as they approach. The rate at which the liquid film drains is dependent on the hydrodynamic pressure and can be modelled using the Reynolds lubrication approximation (44). The Reynolds lubrication approximation assumes that the film is thin enough such that the pressure from the film draining arises from radial flow from between the drops and ignores flow normal to the surfaces. There is an extensive body of literature dedicated to exploring the theory (45-48) and experimental (49-52) implications of thin film drainage and hydrodynamic pressures. Studies exploring the effects of static surface forces on dynamic drop interactions highlight the significance in the roll they also play on the overall drainage process due to their coupling to interfacial properties (13, 44, 53). In addition to this, a study by Yeo *et al*. investigating the impact of surfactant laden interfaces suggested that the hydrodynamic forces caused surfactant depleted regions which retarded the film drainage (49). While work by Manor *et al*. showed that film drainage between drops coated with adsorbed polymer layers is sensitive to flow through the polymer brush (54).

2.2.4 Osmotic Pressure

When a solution is separated from its pure solvent via a semipermeable membrane that is impermeable to its solute molecules, the pressure required to prevent the inward flow of the pure solvent into the solution is the osmotic pressure. The entropy of mixing within the solution reduces its chemical potential, driving the flow across the membrane in order to rebalance the chemical potential difference between the solvents. Once the osmotic pressure counteracts this difference the flow ceases. Kim *et al*. used this phenomenon to control the concentration of colloidal particles confined in double emulsion liquid capsules to modulate their photonic properties. By tuning the osmolarity of the continuous phase the flow of solvent across the

capsule (thin oil shell) membrane to the continuous phase was controlled and by extension the size of the droplet capsule (55). Osmotic pressure differences are also experienced during the collision of drops, bubbles or particles in solutions containing smaller colloids such as nanoparticles (56, 57), surfactant micelles (58, 59) or polyelectrolytes (60-62). When the excluded volumes of two approaching larger colloids overlap the smaller colloids confined within the space are expelled from the film, inducing an osmotic pressure difference between the now solute free film and bulk solution. As a result, the interacting entities typically experience an attractive force between the interfaces in the form of a depletion or structural force (12, 63).

2.3 Adhesive Emulsions (Forces)

There are conditions under which drop interactions are attractive over certain separation distances yet sufficiently stable at closer separations such that aggregation occurs, rather than coalescence. For drop interactions in emulsions, these attractive interactions between the drops underpin the properties of these systems and control processes such as gel formation, fluid microstructure, and the deposition of coatings. This has important applications in the formulation and processing of foods, personal care products, and pharmaceuticals. The term “adhesive emulsions”, first coined by Bibette (1), suggests that specific adhesive or attractive interactions are key to controlling or tuning the behaviour of these systems (2). At liquid-liquid or liquid-gas interfaces these types of attractive interactions are often attributed to a range of surface forces including electrostatic, Van der Waals, depletion and structural.

Bibette and co-workers studied the structure of strongly adhesive emulsions that do not coalesce, showing a complex interplay between the time evolution and strength of adhesion, and droplet volume fraction (1). Adhesion between silicon oil droplets stabilised with anionic surfactant was induced via the addition of sodium chloride and controlled using temperature variations. They found a small reduction in temperature resulted in a large increase in adhesive energy, which is analogous to observations of Newton black films (1). Films formed in solutions of ionic surfactants will reach an equilibrium thickness that is dictated by a balance between double layer repulsion and van der Walls attraction, which is theoretically described by Derjaguin-Landau-Verwey-Overbeek (DLVO) theory. However, in cases where high salt concentrations are present a secondary minimum film thickness can be formed due to strong electrostatic interactions between the discrete ions in the Stern layer of the two surfaces. (64-66). Both Huisman *et al.* and De Feijter *et al.* concluded that this stronger short-range attraction would explain the driving force for the formation of the second black film (66, 67).

2.3.1 Electrical Double Layer Force

Surfaces in solution will become charged due to either the dissociation of ionisable surface groups or by the adsorption of ions from solution onto an otherwise uncharged surface. The presence of these chargers creates an electric field that attracts counterions in an effort to neutralise the surface, which ultimately result in what is known as the electrical double layer (EDL) (36). The structure of an EDL consists of three sections; the Helmholtz or Stern layer where the counterions are transiently bound to the surface, a diffuse layer of ions in rapid thermal motion close to the surface and the bulk solution (68). The counterion distribution can be described by solving the Poisson-Boltzmann equation, which relates the charge density to the electric potential. For systems with low potentials and a single symmetrical electrolyte the Debye-Huckel approximation can be applied to give the simplified "linearised Poisson-Boltzmann equation" of:

$$\psi = \psi_o e^{-\kappa x} \tag{2.1}$$

where,

$$\kappa = \sqrt{\frac{e^2}{\varepsilon \varepsilon_o k_B T} \sum n_i z_i^2} \tag{2.2}$$

ψ is the local electric potential, ψ_o is the electric potential at the surface, e is the charge of an electron, ε is the dielectric constant of the solvent, ε_o is the permittivity of a vacuum, k_B is the Boltzmann constant, T is the temperature, n_i is the number density of each ion i, and z_i is the valence of ion i. The potential decreases exponentially from the surface and the decay length to the point at which the diffuse layer meets the bulk solution is referred to as the Debye length. The inverse of the decay parameter κ calculates this distance which is typically in the range of nanometres (69).

When two charged surfaces approach each other and their EDLs begin to overlap an electrostatic repulsion arises. If their Stern layers do not intersect this interaction is referred to as a weak overlap. The interactive force experienced between the interfaces is dependent on the surface charge, such that the potential energy between two planar surfaces with matching chemistry can be defined as (36):

$$E_{EDL} = \frac{64 k_b T n^o}{\kappa} tanh\left(\frac{e\psi_0}{4k_b T}\right)^2 e^{-\kappa h} \tag{2.3}$$

where n^o is the bulk ion number density and h is the separation.

2.3.2 Van der Waals Force

Van der Waals (vdW) forces arise from the induced dipole-dipole interactions in adjacent materials. For two objects of the same materials, separated by an intervening medium, these

forces are always attractive and the thermodynamic force drives dispersion aggregation or emulsion coalescence. Several theoretical models have been developed to describe these forces on the colloidal scale. The first, developed through the pairwise summation of molecular interactions for colloidal scale objects employs what is referred to as a Hamaker constant (A_H) (70). This is effectively a material property for combinations of two materials separated by a third. Examples are given in Table 2.1 for systems relevant to this thesis. For two planar surfaces separated by a third medium, the vdW interaction energy (E_{VDW}) can be represented by the following relation:

$$E_{VDW} = -\frac{A_H}{12\pi h^2} \tag{2.4}$$

To circumvent the pairwise assumption a more detailed theory was developed through electrodynamics which accounts for the many bodied interactions between molecules. Lifshitz theory, provides a more accurate path to calculate the Hamaker constant using the dielectric spectra of the materials involved (71, 72). Further, this theory also shows that the Hamaker constant is actually a function of separation, decreasing with increasing separation. The simple equation above is now:

$$E_{VDW} = -\frac{A_H(h)}{12\pi h^2} \tag{2.5}$$

where $A_H(h)$ is a more complicated calculation based on the dielectric properties of the three phases, often tabulated or parametrised in the literature (36, 73).

Table 2.1 Hamaker constants for systems relevant to this thesis (74).

Medium 1	Medium 2	Medium 3	Hamaker constant (A_H) x10^{-21} J
Tetradecane	Water	Tetradecane	7.80
Perfluorooctane	Water	Perfluorooctane	6.99

2.3.3 DLVO Theory

Derjaguin, Landau, Verwey and Overbeek (DLVO) theory provides detail on the stability of dispersions by describing the overall interaction between colloids given the impact of their EDL and vdW forces (75, 76). The net interaction energy is considered as the sum of the shorter range attractive vdW forces and longer range repulsive electrostatic force and is represented as a function of the surface separation between interacting colloids. The combination of these forces results in an energy profile which is dominated by an attractive well at close separation and maximum energy barrier at larger distances, as shown in Figure 2.1. The magnitude of the barrier provides insight into the system's stability as the interacting colloids need to have sufficient kinetic energy to overcome this energy barrier to form aggregates (36). For less simplistic

systems where DLVO theory fails to describe the interactions, such as colloids in the presence of polyelectrolytes or micelles, additional forces such as structural, steric or solvation need to be considered. In most cases these are incorporated by maintaining an additive approach, where the total interaction energy is still the summation of all individual forces involved (77).

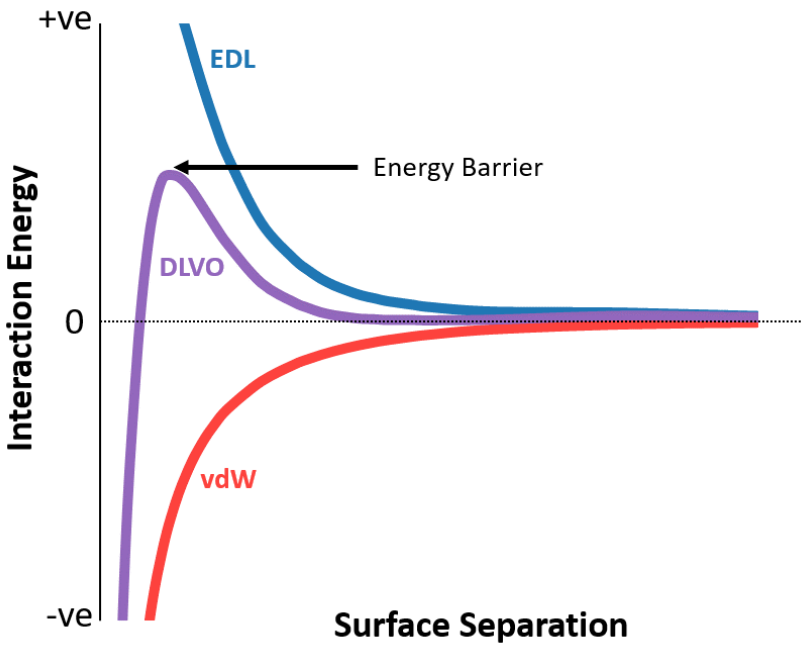

Figure 2.1 A schematic representation of the interaction energy between two colloids experiencing EDL forces, vdW forces and a combined DLVO interaction. The peak of the DLVO curve denotes the amount of energy required to form aggregates.

2.3.4 Depletion and Structural Forces

In the presence of smaller non-adsorbing colloidal species such as polyelectrolytes (60-62), surfactant micelles (58, 59) or nanoparticles (56, 57), larger emulsion droplets can experience aggregation due to a depletion attraction (78). This phenomenon is dictated by osmotic pressure and entropic arguments since smaller colloidal objects are subject to entropic tendencies that require them to equilibrate concentration throughout a solution. The physical driving force of the depletion interaction arises when the drops reach close separation distances forming a thin film, where it is no longer possible for the smaller colloids to fit within the space. This results in their expulsion from within the film creating an osmotic pressure difference between the interfaces and the bulk which drives the drops together (78). The separation distance at which this phenomenon occurs corresponds to around half the characteristic length of the depletant. Asakura and Oosawa *et al*. were the first to characterise the depletion between two interacting bodies, developing a model to describe the interactive force between them (79). In cases where higher concentrations of depletants are contained within the film stratification can occur (80).

The smaller colloids contained within the gap formed between two approaching drops can form structured layers that initially result in a repulsive interaction. As the surfaces approach further, a layer is expelled from within the film when they can no longer spatially arrange themselves inside resulting in an attractive force. This process continues with decreasing separation until all layers are removed and the final depletion force is experienced. This phenomenon results in a series of force oscillations which are referred to as structural forces (81, 82). Factors such as the charge of the interfaces or depletants (83), polydispersity (12) and micelle concentration (84) have all been shown to be important to the behaviour of depletion and structural forces.

2.3.5 Disjoining Pressure and Derjaguin Approximation

The disjoining pressure Π can be defined as the difference in pressure between a film confined between two surfaces, such as two interacting drops, and the bulk (85). It can also be calculated from the negative of the derivative of the interaction per unit area E of the interacting surfaces with respect to distance such that the following relationship can be made (86):

$$\Pi(h) = P_{film} - P_{bulk} = -\frac{\partial E(h)}{\partial h} \tag{2.6}$$

where P_{film} and P_{bulk} are the pressures in the film and the bulk respectively. As the disjoining pressure is related to the net interaction energy, it can be interpreted as the summation of all contributions from acting interfacial forces as shown in Equation 2.7 (86).

$$\Pi(h) = \Pi_{\mathrm{EDL}}(h) + \Pi_{\mathrm{vdW}}(h) + \Pi_{\mathrm{DEP}}(h) + \Pi_{\mathrm{other}}(h) \tag{2.7}$$

In order to relate two flat surfaces to surfaces with curved geometries, such as a spherical particle or oil drop, the Derjaguin approximation can be used. The relationship shown as Equation 2.6 utilises geometric arguments to scale the interaction energy per unit area E between two infinite flat plates to the force between two spheres F of radius R_1 and R_2 (87).

$$F(h) = 2\pi\left(\frac{R_1 R_2}{R_1 + R_2}\right)E(h) \tag{2.8}$$

If a sphere and flat plat configuration is used, this equation reduces to:

$$F(h) = 2\pi R_1 E(h) \tag{2.9}$$

To apply these relationships it is required that the separation distance between interacting surfaces h is far less than the radius of the spheres (86).

2.4 Polymer Surfactant Complexes

2.4.1 Critical Micelle Concentration

Surfactants are widely used to manipulate interfacial properties. There are various types of surfactants, but in general they are amphiphilic compounds that consist of a hydrophobic apolar tail attached to a hydrophilic polar head group. The tail is often a hydrocarbon chain of varying length, however is usually made up of 10-16 carbon atoms. If ionic, the head group is responsible for the charge of the compound and depending on the ion associated with its head group, the surfactant can either be anionic, cationic or non-ionic (88). Figure 2.2A shows the general form of a surfactant and some of the relevant properties.

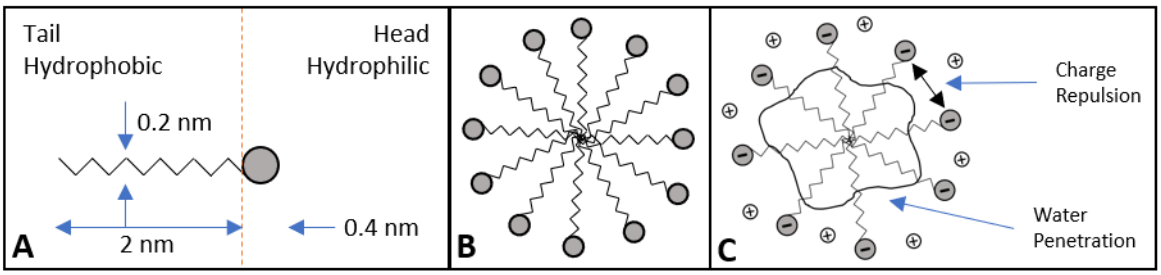

Figure 2.2 (A) General structure of a surfactant. Diagram of a surfactant micelle; (B) without and (C) with electrostatic repulsion due to head group charges.

Surfactants, at high enough concentrations in solution, will self-aggregate to form micelles, this concentration is known as the critical micelle concentration (88-90). The formation of micelles is driven as the surfactant concentration increases in the bulk according to the Gibbs free energy balance that results from the enthalpic contribution from head group repulsion and the increase in entropy from free solvent molecules around the hydrophobic tail as well as the aggregation of the hydrophobic tails (89-91). Figure 2.2B gives a schematic view of a micelle structure. The number of surfactant molecules per aggregation is not fixed and may vary with system condition (88). For example, anionic surfactants, as shown in Figure 2.2C, have charge repulsions between each of the head groups within the micelle that creates instability and hence puts geometric constraints on the structure (6, 90). The formation of micelles can be affected by parameters such as the hydrocarbon tail length, charge density and head to tail size ratio, which will consequently greatly affect the equivalent CMC and micelle shape (91). Based on these properties, micelle structures can take spherical, rod, disc, vesicle and infinitely branched bilayer forms.

2.4.2 Polymer Surfactant Aggregation

2.4.2.1 Bulk Behaviour

Adsorption of surfactants onto polymers can be the result of several types of interaction forces. The main interactions involved are the strong electrostatic forces between oppositely charged polyelectrolytes and surfactants or the reasonably weak dipolar interactions between the polymer chain and surfactant head group, in conjunction with hydrophobic interactions that are always present, and can occasionally be the principal interaction force (89, 92, 93). Many researchers have extensively investigated the interactive nature of these systems with useful reviews by Brackman and Engberts (94) and others (4, 5, 95).

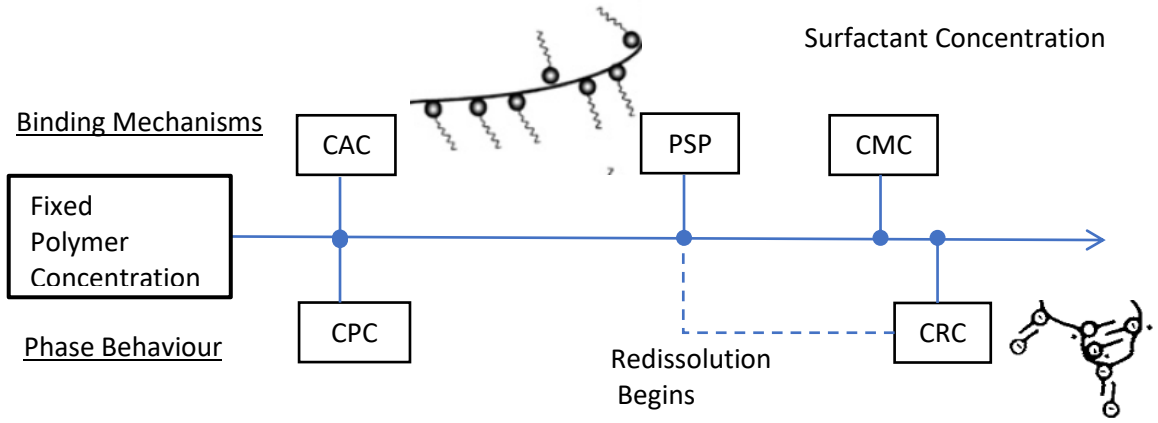

Figure 2.3 Diagram outlining the phase and binding mechanisms between polymers and surfactants with increasing surfactant concentration, where CAC refers to critical aggregation concentration, PSP refers to polymer saturation point, CMC refers to critical micelle concentration, CPC refers to critical precipitation concentration and CRC refers to critical redissolution concentration.

The binding mechanisms involved with PS complexes are generally reported to be proportional to the phase behaviour in such systems, as compared in Figure 2.3. In a system with fixed polymer concentration, binding of the surfactant to the polymer begins at the CAC, which is otherwise known as the critical aggregation concentration (10). This concentration is invariably lower than the CMC of the surfactant alone, as the binding is more energetically favourable than plain self-aggregation (6, 93). The polymer saturation point (PSP) will then occur at some concentration lower than the surfactant CMC (89). These defining concentrations create the start and endpoints for the region of phase separation. The point at which insoluble complexes begin to form is called the critical precipitation concentration (CPC) and is proportional to the system's CAC. Complete redissolution of the precipitate happens around the CMC at the critical redissolution concentration (CRC) as the result of admicelle formation and/or the adsorption of a second layer of surfactant on the polymer (6). Between the CPC and CRC there is a point of maximum

precipitation, frequently referred to as the CAC2 in literature, which corresponds to the PSP. This is when a single layer of surfactant is completely absorbed onto the polymer, and the redissolution phase begins (96, 97).

There are many factors that influence the interactions of polymers and surfactants, all of which must be taken into consideration for each unique system. These elements can influence the aggregative behaviour by hindering, helping or altering the interactions. Goddard (6) and Hannan (97) found that surfactants with longer hydrocarbon chains would more favourably interact with the polymer, which Thalberg extended to show would result in a larger two-phase region (98). Additional factors such as the addition of salt are discussed in further detail in relation to the specific systems, as the components and complexes aggregation behaviours influence the effects of such parameters. The main focus of this thesis is examining the behaviour of non-ionic polymers and anionic surfactants, discussed in more detail in the next section.

2.4.2.2 Non-ionic Polymer and Anionic Surfactant Systems

Non-ionic polymers and anionic surfactants are widely accepted to form what is known as a "necklace and bead" like complex structure (6, 8, 89-91, 93, 97). To understand the configuration, it is necessary to appreciate the interactions of anionic surfactant micelles. As previously noted the charged head groups repulse each other creating instability within the formation (6). Studies by Clifford and Pethica (99) implied that the first few carbons down from the surfactant head group in a pure micelle are in direct contact with water. Therefore to avoid these obviously unfavourable conditions, any alternative forms that reduce this will be favourable (8). When in contact with a polymer, the relatively weak dipolar interactions between the hydrophilic sites of the polymer chain and the anionic head of the surfactants can now be seen as the favourable form as they "insulate" the micelle (6, 8, 89). This partial neutralisation of the micelle sees a reduction in the number of necessary surfactants per aggregation as the effects of the repulsions are reduced (8). Thus, as described in the literature, once SDS begins to bind to PVP it forms 'clusters' with aggregation numbers below that of a standard surfactant micelle (8, 100-103).

Similar to oppositely charged systems, altering the properties and solution preparation will affect the resultant complex characteristics. Prasad et al. (35) more recently investigated the interactions between PVP and SDS with both forward and reverse component addition protocols. They found that PVP did not interact as effectively when added to pre-dissolved solutions of SDS. This could be attributed to the already formed (larger) surfactant micelles not aggregating as favourably to the PVP. Literature provided by as Khan et al. (92) and Minatti (104) say that from surface tension and binding ratio results, the presence of salt increases the binding ability of the complex. Sirivat et al. (105) also reported that the interactions are supported due to reducing the electrostatic repulsion between the ionic head groups, overall stabilising the complex.

Extensive research has been conducted on the surface tension of polymer-surfactant systems, specifically with non-charged polymers and anionic surfactants (8, 31, 35, 92). Not only are these results useful in understanding surface tension behaviour, but it can also be used as a general indicator for the two compounds interacting at the interface. Jones was the first to produce and rationalize such concepts by performing surface tension measurements on polyethylene oxide (PEO) and SDS. He deduced that at an initial transition point denoted T_1, adsorption of the surfactant onto the polymer abruptly occurs. At concentrations above T_1 there is no form of interaction. As the active polymer sites are filled the second transition T_2 occurs (39). Purcell and Thomas (31) completed research on the surface behaviour of a PVP-SDS system. They produced conclusive surface tension results over a range of concentrations where the T_1 and T_2 transition concentrations are clearly visible across a range of polymer concentrations.

2.4.3 Polyelectrolyte Scaling Theory

PS complexes formed between neutral polymers and charged surfactants have been observed to behave as pseudo-polyelectrolytes (106-110). Light scattering experiments performed by Minatti et al. claimed PVP and SDS aggregates have properties similar to polyelectrolytes, however due to the multiple equilibria that exists between the molecules the system exhibits higher complexity to that of a standard linear polyelectrolyte (111). Furthermore, Wu et al. used capillary electrophoresis to present direct evidence that PVP and SDS complexes should be treated as pseudo-polyanions as the apparent electrophoretic mobility of the complex decreases with increasing SDS aggregation (112). This behaviour has also been accounted for in studies observing the force between surfaces in systems containing neutral polymers and anionic surfactants. Using AFM, Tulpar et al. measured strong depletion forces between a silica particle and plate in the presence of Pluronic F108/SDS complexes, which they regarded as large polyelectrolytes (113). Work by Mondain-Monval credited an increase in repulsive electro-steric forces between emulsion droplets in solutions containing PVA/SDS complexes to their polyelectrolyte nature (114). In addition, a single foam stability study by Folmer *et al.*, using a thin film balance method, has observed stable films and stratification in the films with PVP/SDS at concentrations where they exhibit strong binding (115).

Pioneered by de Gennes *et al*. and Pfeuty (116-118), polyelectrolyte scaling theory has been extensively developed and used to describe trends across concentrations and molar mass variations of polyelectrolyte solutions in the dilute, semi-dilute or entanglement regimes (119-122). Incorporating Donnan equilibrium theory (123, 124) the total osmotic pressure of polyelectrolyte solutions can be obtained from the sum of the ionic and polymeric contributions of the system. The derived relationship is presented in the experimental methods chapter of this thesis.

2.4.4 Adsorption

In contrast to the more studied bulk phase behaviours, polymer surfactant mechanisms of adsorption on a surface are still under detailed investigation. Bulk associations are accepted to be key to ultimately controlling their behaviour, however molecule to surface associations such as diffusion and adsorption kinetics need to be understood to gain the full potential of such systems (10). Polymer adsorption onto surfaces is typically assessed in stagnant flow where mass transfer is suggested to be the rate determining step for adsorption (125, 126). Factors that influence the adsorption of PS complexes to a surface include surface hydrophobicity, surface charge, surface roughness and bulk salt concentration (10, 127, 128).

PVP and SDS have been shown in the literature to absorb at the silica-water interface as a complex brush (129, 130). Prescott *et al.* provided evidence of a three-stage binding process with increasing surfactant concentration, essentially comprising of initial surfactant binding, chain elongation and finally desorption of the adsorbed complex (130). From SANS and NMR experiments they demonstrate that around the CAC surfactants begin to aggregate to the adsorbed polymer, and at SDS concentrations above the CMC there is a barely discernible presence of a layer, concluding that desorption of the complex had occurred. Likewise, Chari *et al.* showed using radiotracers that PVP and SDS form two-dimensional aggregates similar in structure to those in the bulk phase at the air-water interface (34). Purcell *et al.* (31) furthered the investigation using neutron reflection to show the presence of both PVP and SDS at the interface between T_1 and T_2, demonstrating evidence of a surface interaction between PVP and SDS.

However, an interesting study by Fuller *et al.* looked at the effects of polymer adsorption to a surface under flow. The two possible effects considered to result from the influence of flow were; flow induced desorption and orientation/deformation of the polymer in line with the flow. Therefore the presence of flow has the potential to not only influence the transport of the polymers to the surface but also affect the intrinsic adsorption kinetics at the surface (131).

2.4.5 Adhesive Properties

Under certain conditions, polymer surfactant complexes have been shown in the literature to promote attractive forces between interfaces (132). When two surfaces covered with adsorbed polymer-surfactant complex come into close separation an adhesive force can be formed as a result of polymer bridging. Bridging can occur from the polymer interacting directly with the other surface or the adsorbed layer at its interface (133, 134). This means polymers with little to no surface activity can also exhibit similar behaviour as the chain does not have to occupy an adsorption site at the surface but simply interact with the layer (135). Bremmell *et al*. investigated the interaction forces between rigid surfaces in the presence of an oppositely charge polymer

surfactant system, which exhibited a bridging attraction between the surfaces (136). They proposed that a "patch-wise" bridging mechanism theorised by Gregory, where inhomogeneous aggregation of the polymer surfactant layer creates oppositely charged patches on approaching surfaces, was responsible for the results (137). Alternatively, attractive depletion forces caused by the formation of polymer-surfactant complexes in the bulk can be responsible for adhesive interactions between surfaces. Tulpar *et al*. showed that the complexation of a neutral polymer and anionic surfactant produced a significant adhesive force between a particle and plate (113). Their results demonstrated for the first time the synergistic nature of a polymer-surfactant complex on depletion forces, as when individually studied the components displayed repulsive forces between the surfaces.

2.5 Direct Force Measurements

To measure the forces of interaction between interfaces a range of established methods are available, primarily differing in their useability, sensitivity, resolution and scope of application. Typical apparatus used for direct force measurements include atomic force microscopes (AFM), surface force apparatus (SFA), thin film balance (TFB) and total internal reflection microscopes (TIRM). While each technique is capable of measuring surface forces, unique specifications dictate which method or combination of techniques is most suitable for a specific experiment (138).

Initially described in 1969 by Tabor and Winterton, the modern SFA is one of the most widely used surface force techniques, being the first of its kind to measure the force between two rigid surfaces at separation distances as small as 5-30 nm (139-141). Further modifications and developments to the method saw extensive advancement in the area, as can be seen through the work of Israelachvili and others (142-148). SFA studies commonly focus on the interactions of rigid surfaces in solution, typically using mica due to its molecularly smooth interface (140). However, the ability to adsorb soft matter systems such as polymers, polysaccharides, and biological materials to mica allows for a versatile range of systems to be measured (149-151). As seen in work by Argillier *et al.*, who used this technique to examine the interactions between absorbed polymer surfactant layers to help understand their suitability to hair and capacity to stabilise colloidal suspensions (152). Nevertheless, a considerable limitation of SFA measurements is its inability to study the interactions between deformable interfaces. Horn and co-workers have developed a modified surface force apparatus capable of measuring the interactions of a mercury droplet (53, 153, 154), or more recently bubble (155-157), and a flat surface. This is essentially achieved by incorporating white light interferometry in reflection and a cylindrical capillary, which is filled with either medium and fixed to the bottom of the chamber.

Yet extending these capabilities to allow measurements between two deformable interfaces still faces significant challenges.

The introduction of TIRM brought increased sensitivity and spatial resolution to direct force measurement techniques otherwise not seen with previous methods. Through a totally internal reflected laser beam the separation distance, and ultimately potential energy profile, between a glass plate and particle in solution can be detected via the formation of an evanescent wave at the plate/liquid interface. This wave causes particles within its range to scatter light, allowing nanometer z-axis separations and femtonewton forces to be quantified (158-160). Drop-solid measurements using TIRM to study oil-in-water emulsions are reported in the literature, each noting the potential influence of drop deformation on the quantitative analysis, particularly at zero separation (161-163). Despite this capability, like SFA, TIRM is unable to observe interactions between two deformable entities. Studies of direct force measurements between deformable surfaces of flat air-water and oil-water interfaces were first seen using thin film balances with a Scheludko cell (164), and then further modified versions of the technique (165-168). TFB methods interferometrically measure the thickness of a thin film as a function of the pressure difference across the film through which the disjoining pressure can be determined, but are limited to film radius of around 100 μm (167). Aveyard *et al.* developed a modified version, called the liquid surface force apparatus (LSFA), by integrating SFA functionality to attain measurements of films with radius of a few micrometers (169-171). These studies primarily focus on foam and film studies due to the nature of the experiment.

The introduction of AFM techniques capable of measuring deformable interfaces (172-178), encouraged the more recent development of various other devices with the ability to measure drop or bubble systems. These include the integration of interferometry with AFM and similar force measurement methods to simultaneously study the spatiotemporal separation and interaction force between a single bubble and flat plate (179). Xu's group have developed several novel larger length-scale techniques that utilise biomorph cantilevers to probe a single bubble or drop and either a flat surface or rigid particle, such as the integrated thin liquid film force apparatus (ITLFFA) and integrated thin film drainage apparatus (ITFDA) respectively (180-182). Notably, Frostad *et al.* established the cantilevered capillary force apparatus (CCFA), which uses cantilevered capillaries to examine the interaction between two drops with radii in the range of 50- 70 micrometers (183, 184). To measure the relevant forces between drops at length scales applicable to this project and by extension a vast majority of applied industrial or commercial colloidal systems, AFM techniques are essential.

2.5.1 Atomic Force Microscopy

Atomic force microscopy has been the foremost tool for imaging topology at the nanoscale since its invention by Binnig *et al.* in 1986 (185). By measuring the deflection of a cantilever equipped with a nanometer sharp tip scanned across the top of a surface, the AFM can produce a three-dimensional topographic image of the surface at a resolution of less than 1 Angstrom (185-187). Image contrast can be obtained as the force imparted on the cantilever is a function of both the tip-sample separation and surface chemistry of the tip and sample. This ability facilitates the AFM in also being used as a method for performing direct force measurements. In this case, the cantilever is driven towards and then away from the sample in the normal direction (188). The deflection of the cantilever is monitored as a function of its position in the z-direction, which through knowledge of the cantilever spring constant can be converted to a force verse distance plot known as a 'force curve' (188-190). However, limitations in poorly defined tip geometries and variability in surface chemistry prevented valid qualitative assessment (191-193). The introduction of the 'colloidal probe technique' saw major advancement in this area by providing a probe with known geometry.

2.5.1.1 Rigid Interfaces

In 1991, an AFM technique by which a rigid microsphere is attached to the end of a cantilever tip was independently announced by both Ducker *et al*. and Butt (187, 194). These initial experiments were performed between a silica substrate and glass bead with radii of around 3.5 and 120 microns respectively, and across a gradient of salt concentrations and pH conditions. In both cases the results agreed well with earlier literature and surface force theories. The colloidal probe technique is typically performed using attached rigid particles of approximately 2 to 20 microns in diameter, however variations in the size, shape and material can be made to explore a range of applications (195-197). For example, Vakarelski *et al.* developed a wet-chemistry technique capable of depositing 10 – 40 nm gold nanoparticles to the tips of cantilevers (198). While more recently Papastavrou's group have presented a novel approach for attaching particles of diameters as low as 500 nanometres using aspiration through hollow FluidFM cantilevers. This method is particularly convenient as it works independently of the particles surface chemistry and can be performed in situ (199). Otherwise, Huttl *et al.* offer an oxidation technique for adjusting the tips of commercial cantilevers to 2 microns with ideal spherical geometry and surface roughness (200). The accuracy and magnitude of the forces measured in colloidal probe studies is greatly influenced by the size and roughness of the particle, therefore access to devices such as SEM can be important to characterise the surface topography of the probe (201, 202). Alternatively, Neto and Craig developed a method for 'reverse imaging' the probe from a surface with very sharp features to extract its roughness, size and geometric regularity (203).

Since the introduction of colloidal probe measurements, the technique has been widely used for advancing the knowledge of a multitude of areas, including but not limited to; mineral processing, advanced materials, biological systems, product formulation, drug delivery and pharmaceuticals (188, 194). In particular, it has been used extensively in the exploration and characterisation of adhesive forces, which are vital in understanding the aggregation and dispersion of colloidal systems (197, 204). There is a large body of literature that focuses on the adhesive properties of polymer systems using colloidal probe techniques (136, 205, 206). Not limited to particle-substrate interactions, these measurements can also be performed between two particles allowing systems more representative of practical/industrial applications to be tested, as demonstrated in the work by Klitzing *et al.* who measured the forces between two silica particles and between a particle and a silicon wafer in the presence of a cationic surfactant (207). They observed different interaction forces between the two configurations, indicating that different aggregate morphologies exist at their surfaces. Furthermore, Gee *et al.* were able to show the change in adhesive behaviour between two cylindrical alumina fibres in the presence of an oppositely charged polymer-surfactant system with varying surfactant concentration and addition protocol (208). There have also been more applied types of materials including toner in particles (209), pieces of hair (210) and even mosquito limbs (211) to probe the adhesion between a material and a substrate.

2.5.1.2 Deformable Interfaces

Further developments into the colloidal probe technique saw the incorporation of deformable interfaces into direct force measurements, introducing the potential to unlock an even greater understanding of soft colloidal systems such as emulsions then previously obtainable. Independently performed by Butt and Ducker *et al*. in 1994, this initially involved measurements between a colloidal probe cantilever and an air bubble or water droplet fixed onto a substrate (172, 173). By 1996 additional variations by Mulvaney *et al.* led to the first force measurement between a rigid particle and oil droplet in water (176). Since then a large number of studies covering the interactions between rigid particles and bubbles (174, 212-214) or drops (175, 215-219) have been performed, including the development of methods for quantitative analysis of the experimental results of which further detail will be provided in the following sections (220-222).

Drop-drop interactions were realised in 2004 when Dagastine *et al*. and Gunning *et al.* both independently introduced a technique for attaching oil droplets to the end of a cantilever tip, allowing the first direct force measurements between oil drops to be attained (177, 178). Dagastine *et al.* demonstrated both pseudo-static (equilibrium) and dynamic interactions between n-decane drops in a range of SDS solutions, highlighting the strong link between surface forces, hydrodynamic drainage and interfacial deformation through theoretical analysis of the

measurements (44, 178). While Gunning *et al.* used protein or surfactant covered drops to investigate the effects of interfacial rheology on drop deformation and to monitor drop coalescence (177). To aide drop attachment and alleviate uncertainties in drop position, Lockie *et al.* further improved the technique by introducing a gold patch at the end of a tipless cantilever capable of hydrophobic surface modifications (13). A range of subsequent work has followed covering the interactions between drops in polyelectrolytes (223), surfactants (224), spherical and rod-like micelles (225, 226), microemulsions and nanoparticles (227), and asphaltenes (228) solutions to name a few. Through these studies depletion, structural and steric forces were able to be observed as a result of the surface active and non-active components in solution. Hydrodynamic forces have also been probed by Tabor *et al*. by employing high salt concentrations and oil drops that were refractive index matched with water (229). Furthermore, the same method cab been applied to bubble systems where by the bubbles are ultrasonically generated directly onto a glass substrate (12, 63, 230, 231). Further information into the application of AFM in studying deformable interactions can be found in the reviews by Tabor et al. (186, 229) and by Wang *et al*. (232).

Unlike other techniques such as SFA, standard AFM force measurements do not provide an absolute measurement of the separation between the two interacting bodies. For rigid measurements this can be attained via calibration of the point of hard contact, however in deformable systems where this does not exist alternative methods need to be applied. Tabor *et al*. combined confocal fluorescence microscopy with AFM to obtain a direct in-situ measurement of the initial separation between two drops prior to taking the force measurement (11). Similarly, Shi *et al*. utilised reflection interference contrast microscopy (RICM) to measure simultaneously the interaction force and spatiotemporal evolution of a water film between a bubble and mica surface (179). Alternatively, indirect theoretical predictions can be made through modelling of the experimental data, which also provide a pathway for quantitative analysis of the results (46, 233).

2.5.1.3 Modelling

When determining the separation of deformable entities in AFM force measurements, where drop or bubble sizes range from 10s of microns to hundreds of microns in radius, it is necessary to account for their potential for interfacial deformation. If the drops or bubbles do not coalescence when the surfaces are brought into close proximity, at the radial centre of the film between the surfaces, a minimum separation will exist at the point where the Laplace and disjoining pressure are balanced. Further approach will only result in further deformation of the entities surface and the intervening film growing radially, maintaining a constant film thickness at the axial centre. If the film thickness thins to separations (at either the centre of the film, or at the edges if a barrier

rim is formed) where attractive forces become dominant, either capillary wetting phenomena will dominate the behaviour in the case of a rigid and deformable measurement, or coalescence of the entities in a deformable-deformable measurement (42, 45, 234). The magnitude of the force is a function of the interacting area, therefore the force and degree of deformation with respect to the relative displacement also needs to be considered in a consistent way. In 2001, analysis accounting for these behaviours in equilibrium interactions between a drop or bubble and particle was achieved by various groups using a modified Young-Laplace equation (220-222). The separation is determined by fitting a predicted force curve from the theoretical model to the experimental force data. This was further developed to account for the interactions between bubble and drop pairs, which presents the variation of the Chan-Dagastine-White (CDW) model that is used throughout this thesis and is presented in further detail in the Methods Chapter (235). Furthermore, Manica et al. were able to produce a simplified analytical equation for improved curve fitting in the high force regime where typical surface forces are considered negligible (233).

Incorporating dynamic behaviour adds an additional degree of complexity to the analysis due to the introduction of hydrodynamic forces and film drainage. These forces will also deform an entities surface, but unlike the separation dependent disjoining pressure are a function of time. The Stokes-Reynolds equation can be used to model such behaviour, which in conjunction with the Young-Laplace equation gives the SRYL model, a solution capable of analysing the time-dependant interactions between two deformable entities (46, 47, 233, 236). Chan *et al*. offer a detailed summary of the development of this theory (45), while Tabor *et al*. covers an extensive review on their application and validation to a range of experimental systems using AFM (186).

2.6 Microfluidics

Since the early 2000's, microfluidics or 'lab-on-a-chip' technologies have stimulated rapid developments in both the fundamental understandings and applications of multiphase systems such as bubbles and drops (237). This has aided improvements in areas such as medical diagnostics and treatments, advanced material synthesis, biotechnology and cell culture, encouraging the production of several detailed review papers (237-239). The focus of this thesis is on microfluidic drop generation, however there are a vast number of other applications covered in the literature, ranging from the fabrication of microparticles for functional building blocks to the utilization of microfluidic reactors (240-244). The ability of microfluidic devices to provide precise control over flow rates, and subsequently droplet volume and production rate, is one example of many attributes that make them preferential for drop generation. Microfluidics offer high-throughput, low Reynolds numbers (ensuring laminar flow), and a high level of geometric accuracy providing excellent monodispersity (245).

Microfluidic devices are essentially arrays of micron sized channels, with their networks designed for the purpose of each unique project. A number of fabrication techniques are available to produce the devices including photolithography or etching methods. The most standard and widely used technique for fabricating devices is replica moulding polydimethylsiloxane (PDMS) onto a "master" structure produced via standard contact photolithography (238). Although this method is simple, cheap and efficient the surface chemistry and material properties of the channels is an important functionality of the device, thus PDMS is not always a viable material option (246). While there are procedures for altering the hydrophobicity of PDMS channels, additional factors such as the ability of PDMS to swell in organic solvents, need to be considered (247-249). Etching into silicon or silica wafers to create fused silicon-silica or silica-silica microchips offers mechanical and chemical stability, nanoscale precision and high levels of cleaning and modification flexibility, making them an ideal candidate for most microfluidic applications. However, their manufacturing process is more complicated and specialised, consequently increasing their cost in time and money. Kitamori's group has produced an extensive body of literature covering the fabrication and use of glass microfluidic devices, which includes specific attention to the difficulties in bonding/sealing the devices (250-253). Both techniques permit intricate designs to be created using CAD software, making spatial resolution of the selected fabrication method the greatest constraint to the design's complexity.

2.6.1 Drop Generation

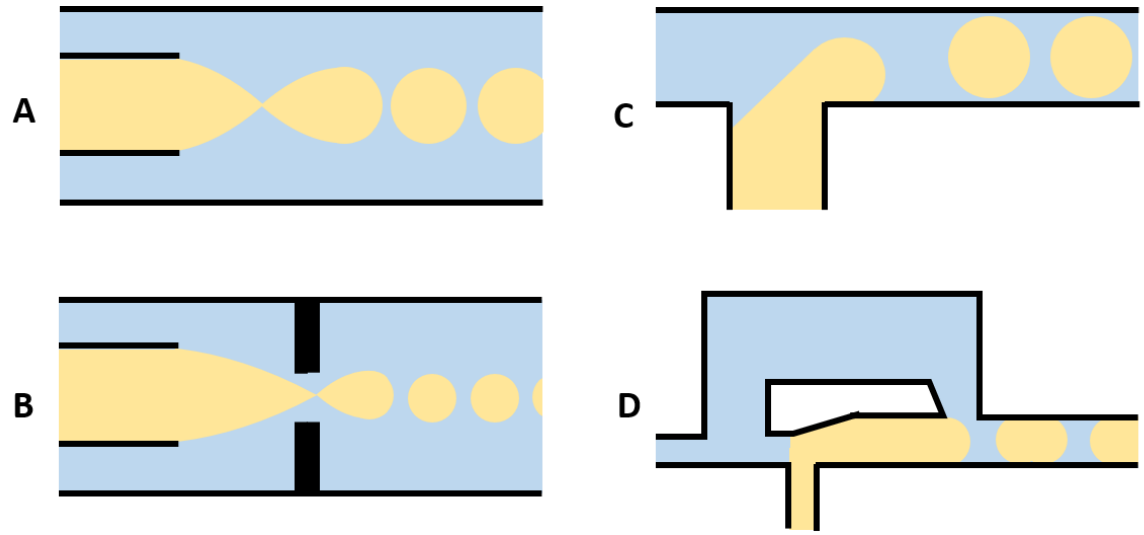

Figure 2.4 Schematic diagrams of popular passive drop generation geometries depicting (A) co-flow, (B) flow focusing, (C) T-junction/crossflow and (D) block-and-break designs. The dispersed (or oil) phase is shown in yellow and the continuous (or water) phase is shown in blue. The direction of flow is from left to right in all images.

There are a variety of different microfluidic methods that are employed to generate bubbles or drops. They can be categorised into either active or passive techniques, where the former utilises additional input energy to promote interfacial instabilities and the latter is dependent on the channel geometry. A brief description of the most popular passive geometries, as shown in Figure 2.4, is described below. For a deeper exploration of both passive and active methods, further information can be sourced from a large collection of review papers (238, 254-258).

2.6.1.1 Co-flow

A co-flow geometry incorporates two immiscible fluid streams which meet in parallel to flow together in the same direction. The continuous phase surrounds the dispersed phase, eventually causing the dispersed phase to taper off into droplets due to Rayleigh-Plateau instability (238). The geometry was originally presented by Umbanhowar *et al*. using a liquid-liquid system to generate monodisperse micro-emulsions (259). The size and polydispersity of the drops formed are dependent on the flow conditions, which can be predicted via the Capillary and Weber number of the fluids (260-262). The capillary number, Ca, is the dimensionless quantity representing the ratio of the viscous drag forces versus surface tension forces in a system given by:

$$Ca = \frac{\mu v}{\gamma} \tag{2.10}$$

where μ is the viscosity of the continuous phase, v is a characteristic velocity of the drop and γ is the interfacial tension between dispersed and continuous phases. The Weber number, We, is a dimensionless quantity representing the ratio effects from the continuous phase inertia to effects from the interfacial tension given by:

$$We = \frac{\rho v^2 l}{\gamma} \tag{2.11}$$

where l is the characteristic length scale, typically the droplet diameter. Utada *et al*. constructed a state diagram showing the dripping to jetting regime transition of a coflowing stream based on the capillary number of the continuous phase and weber number of the dispersed phase (260). Thus, the dimensional variables that ultimately define the size of the drops are the volumetric flowrates, viscosities and interfacial tension. A variation of the co-flow geometry is the step emulsification technique, which introduces a change in the aspect ratio of the channel from high to low, allowing the formation of highly monodispersed drops (263-265).

2.6.1.2 Flow Focusing

Similar to co-flow, a liquid is flowed both sides of a second immiscible fluid stream, however an orifice is now introduced which hydrodynamically focuses and accelerates the streams as they

are forced through the opening, elongating the inner fluid thread (254). This behaviour generates smaller drop sizes compared to a co-flow geometry with equivalent dimensions. Initially introduced by Ganan-Calvo to generate a steady microscopic liquid thread in a gas stream (266), it has since been used to produce a gas filled liquid jet (267), mono and polydisperse emulsions (268, 269), double emulsions (270) and encapsulated drops (271, 272). As the drop break-off is driven by pressure and viscous stresses the outer fluid places on the inner fluid, the drop size is now not only dependent on the flow regime but also the channel geometries. Therefore, investigation into the influence of volumetric flowrates (273), viscosities (274), interfacial tension (275) and channel dimensions on drop size have been covered to help characterise flow-focusing systems (276-278). To support the development of future designs, predictive models that describe drop formation based on these parameters have also been derived (279, 280).

2.6.1.3 T-Junction (Crossflow)

The T-junction geometry was first designed by Thorsen *et al*. to produce ordered complex patterns of drops under continuous operation (281). As seen in Figure 2.4 its configuration resembles a T in shape, where two channels meet at a 90-degree angle to create a crossflow. Due to its simplistic design, the T-junction geometry is easier to manufacture and operate compared to the more complex requirements of a co-flow or flow focusing design (238). As a result, numerous variables and parameters have been used to characterise drop formation in a T-junction in an effort to understand its mechanism of break-up (282-285). The two primary mechanisms of drop formation in a T-junction geometry are the filling and squeezing regimes. Ultimately an interface between the continuous and side channel fluids is established, which is then forced into filling the main channel by the side stream pressure. This is then directed downstream by the main channel flow. A build-up of the pressure gradient in the main channel forces the interface at the side stream inlet to be squeezed until the droplet pinches off (285-289). Based on this assertion, Garstecki *et al.* produced a simple scaling law for systems with low value capillary numbers to determine the length of a drop based on the flowrate ratio, channel width and a geometric parameter (286). Steijn *et al.* went on to develop are more detailed model capable of predicting the drop volume by individually accounting for the filling and squeezing regimes of the drop formation. The relationship is a function of the geometry of the microfluidic channels and channel flow rate ratios, and is based off fits to experimental results (287). The ability to produce such relationships effectively highlights the importance of the geometry and flow control in such devices and how they can play a vital role in the development of drop morphologies.

2.6.1.4 Block-and-Break

Although the previously discussed geometries are useful as they allow tuneable drops sizes via a variable parameter, there are cases where it is desired to produce monodisperse drops while also

having the flexibility to modify flowrates. This can be seen when using microfluidic mixers, or simply from the use of syringe pumps for flow control as they have a tendency to produce oscillatory fluctuations (290). To counteract this, Steijn *et al.* developed a new block-and-break configuration that allows the generation of fixed volume droplets solely based on the geometry of the device (291). As shown in Figure 2.4, the design consists of a classic T-junction with a bypass channel around it. This bypass allows the dispersed phase to fill up the channel to the exit of the bypass without being squeezed by the continuous phase as in a T-junction. Once the bypass exit is blocked the drop is then broken off by the continuous phase, thus consistently producing a drop of an equivalent size to the volume of the channel between the T-junction inlet and bypass exit (291).

2.6.2 Drop Interactions

To observe interactions between drops or bubbles in a microfluidic device it is necessary to bring them into contact. Various techniques are used to collide drops; however, they are all essentially designed to remove the continuous phase separating them by introducing a velocity difference between the drops. This can be achieved using specific channel geometries or by introducing active control over the drops using an external force field. Figure 2.5 shows schematic diagrams of common geometrically induced collision designs.

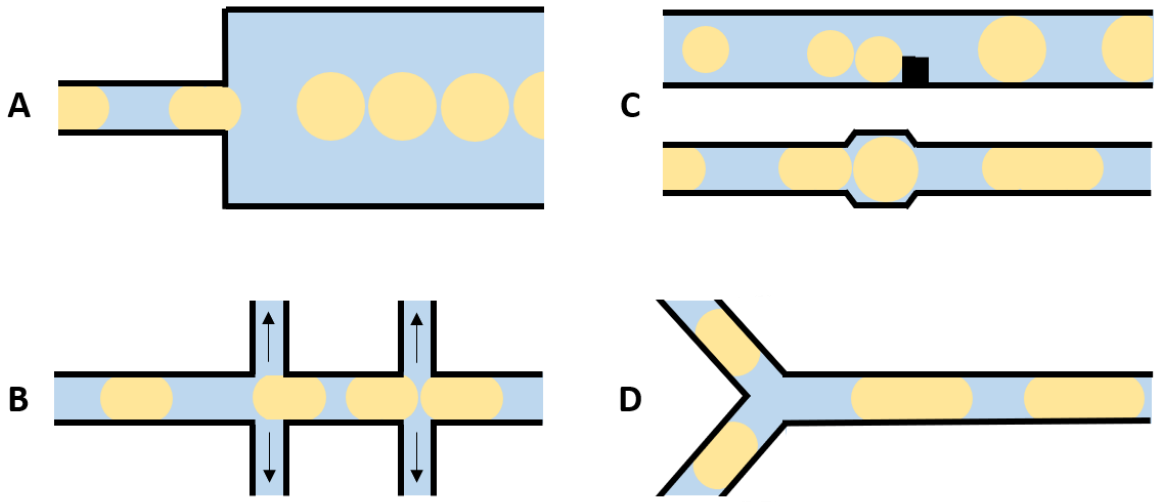

Figure 2.5 Schematic diagrams of microfluidic geometries used to induce drop collisions showing (A) a channel expansion, (B) withdrawing side channels, (C) droplet traps using a physical structure or local channel enlargement and (D) a Y-junction designs. The dispersed (or oil) phase is shown in yellow and the continuous (or water) phase is shown in blue. The direction of flow is from left to right in all images unless depicted by the direction of an arrow.

A typical approach used to achieve drop collisions is to add flow resistance by altering the flow properties of the surrounding fluid. Expanding the channel using either a rectangular (292, 293) or tapered (294) geometry is a basic tactic capable of achieving this. When the channel width increases, the velocity of the continuous phase reduces accordingly, ultimately slowing the drops down such that subsequent drops collide. Bremond *et al*. used this approach followed by an abrupt constriction of the channel to show that extensional flow triggers centre driven coalescence of droplets in close contact at the point of separation (26), and has subsequently been further investigated and used by others (28, 295). Introducing side channels to remove excess continuous phase has also been used to bring drops together (296). Tan *et al.* compared this technique to both a rectangular and tapered expansion, finding that the side channels provided greater flexibility in colliding drops as they have direct control over the separation through the controllable flowrates, while expansions have fixed rates based on the channel dimensions (297). Combinations of both expansions and side channels can further improve control over collisions, with Gunes *et al*. using an expansion followed by a series of side channels to systematically control the drainage time of the fluid separating the drops and ultimately the coalescence behaviour of a chain of drops (26, 27). Trapping droplets is another widely used method, which stops a drop in its path by way of a physical structure (298), local enlargement or change in asymmetry of the channel geometry (299, 300), or microwell (301, 302). The stationary drop is held in place until a secondary drop comes into contact, and either coalesces with the initial drop, displaces it from the trap, or passes it unperturbed.

Another geometric approach focuses on junction structure to achieve drop collision. This is typically attained using Y and T-Junctions although other geometries exist (303). Christopher *et al.* evaluated the influence of drop size and flowrate on the controlled collision of two drops at a T-junction (29). They found there was three kinds of primary phenomena after collision, namely splitting, slipping or coalescing, which has also been seen in microbubble studies of a similar nature (304, 305). A key variation in the Y-junction geometry compared to the T-junction is the angle at which the channels meet at the point of intersection. Both Wang *et al.* and Liu *et al*. studied the effect of channel intersection angle on drop collisions at a Y-junction, unanimously concluding that reducing the intersection angle can enhance coalescence efficiency (306, 307). These methods rely on precisely synchronising the arrival time of the drops in each channel, increasing the difficulty of the experiment and encouraging other passive techniques to be explored. Jin *et al*. investigated a technique using a difference in drop size or fluid viscosity to instigate drop collisions (308), while Fidalgo *et al*. used surface modification to pattern areas of the channel with hydrophilic properties which induced drop fusion (309).

Besides passive techniques a variety of active approaches have been developed to tackle the intricacies of controlling drop collisions. By incorporating an external force field, drops can be more easily manipulated to flow as desired. The most common method to do this is via an electric field or current (310-314). However, only aqueous or polar drops that are capable of carrying charge to form attractive dipoles can be used, limiting the application to drop systems with specific properties. Combining electric fields with passive geometries can also be useful, where the drops are bought into close separation by the channel geometry and collisions are instigated via the electric force (301, 315). Another method of active control is through thermal manipulation, which can be achieved by integrating thin film microheaters into the microfluidic device (299, 316), or via laser beams and subsequent thermocapillary effects that are able to pin the drops in selected locations (317-319). A novel method recently developed by Sesen *et al*. utilises surface acoustic waves to trap and merge drops with on-demand operation (320). Reviews on droplet coalescence in microfluidic systems conducted by both Shen *et al.* and Xu *et al.* provide a more detailed investigation into the drop collision techniques covered here (321, 322).

Given their variety of functionality in regard to drop formation, collision and control, microfluidic devices are an obvious candidate to systematically probe drop interactions, yet previous studies that have had such success have been limited to studying phenomena that are either dominated by hydrodynamic interactions between drops or exhibit some coupling of hydrodynamic behaviour and surface forces. The exciting studies previously mentioned by Bremond & Bibbette (26, 30), and Gunes *et al.* (27, 323), systematically explored drop coalescence in microfluidic devices, most notably where drops coalesced upon separation. However, the drop interaction outcomes in these studies were driven largely by hydrodynamic drainage effects until very close drop separations. Furthermore, the seminal work by Anna (29) into drop coalescence at T and Y shaped junctions specifically noted that the hydrodynamics of the surrounding fluid dominated any interaction, effectively masking equilibrium surface forces. A recent simulation study of drop and bubble collisions in AFM experiments, by Berry and Dagastine (42), mapped the rich phenomenological interplay between equilibrium surface forces, drop deformation and the hydrodynamic drainage effects, identifying collision velocities where hydrodynamic drainage effects play a small role in the collision outcomes. Thus, in order to study equilibrium surface forces with a microfluidic platform, it is necessary to create a geometry that removes or quantifiably controls the hydrodynamic interactions during soft particle collisions. An example of the latter can be seen in some recent work into microfluidic flow that used depletion forces to form drop aggregates, prior to photo-polymerisation, by controlling the channel flowrate through a channel expansion (242).

2.6.3 Other Applications

Drop-based microfluidic technologies provide a powerful tool for studying emulsion properties. In addition to drop interactions, they have also been used to investigate the interfacial properties of drops in flow. Standard drop volume techniques used to measure interfacial tension, such as the pendant drop method, are governed by the balance between gravity and interfacial tension forces. Xu *et al*. extended this theory to apply to microfluidic devices where shear force is instead responsible for drop formation (18). Initially developed for a coaxial geometry, they derived a relationship corelating the drop size to the two-phase flow ratio and capillary number, such that the dynamic interfacial tension could be calculated at the point of drop breakup. Luo's group went on to apply this theory to T-junction geometries (324), as well as use it to study the mechanism and kinetics of surfactant adsorption (325, 326). Wang *et al.* also published a pressure based technique, which measures the difference between Laplace pressure and the fluctuation pressure drop at the highest pressure drop point during drop generation to calculate the instantaneous interfacial tension (327). Schroen *et al*. have applied the same theory to Y-Junction geometries, however instead fit an empirical relationship to calibration data to relate drop area to the capillary number. They claim this method allows measurement at drop formation times of sub-millisecond timescales, compared to the millisecond range offered by other techniques (17, 328). As these measurements are performed during drop formation, they are far from providing equilibrium results.

Hudson and co-workers established a microfluidic method for assessing interfacial properties from the analysis of two-phase flow and drop-shape deformations. The technique tracks the deformation and time scale of recovery of a drop in an extensional flow field as a function of its displacement along the channel to extract the Taylors parameter of the drop, which can be used to regress its interfacial tension (329). It has been benchmarked against a range of systems with varying interfacial tensions and viscosities (329), as well as multi-component mixtures with adjustable compositions (16). Furthermore, through the addition of particle tracers they were able to assess the mobility of the interface from the droplet internal circulation velocity. A combination of the measurements demonstrated the ability to evaluate the interfacial tension, interfacial retardation and surfactant mass transfer in one experiment through direct correlation of the interfacial parameters (20, 330). Lee *et al*. adapted the method to incorporate localised temperature control such that temperature dependent interfacial tensions could also be measured (331). Another variation developed by Brosseau *et al*. works on a similar principle, where the maximum deformation of a drop hydrodynamically forced into an expansion is measured as a function of drop velocity and radius. Their work fits an empirical model to raw data to extract a relationship between the drop's deformation, geometry and capillary number in

order to determine the drop's interfacial tension. By introducing a series of expansions along the channels, they used this method to study surfactant adsorption kinetics (15).

More recently exploration into combined drop-based microfluidics and scattering techniques have emerged, introducing with it a new generation of microfluidic systems capable of measuring the structure, interactions and kinetic processes of the materials within emulsions. With continued advancements into the detection capabilities and speeds of scattering instruments such as Raman spectroscopy, small-angle X-ray scattering (SAXS), and small-angle neutron scattering (SANS) progress into novel approaches for sample preparation and formulation has become possible. Most of the literature currently available focuses on the proof of concept for these new techniques. Cristobal *et al*. introduced the use of Raman spectroscopy with drop-based microfluidics by probing *in situ* the composition and mixing of two-component drops (23). Cecchini *et al*. built on these ideas by incorporating surface-enhanced resonance Raman with improved temporal resolution such that multiple spectrums per drop could be taken (332). SAXS studies have been used to characterise the size, shape and concentration of gold particles encapsulated within water (24), as well as to investigate the assembly of weakly scattering protein vimentin within aqueous drops (333, 334). After refining microfluidic SANS techniques for the mixing of complex fluids in a continuous channel (25, 335), Adamo *et al.* moved onto droplet microfluidic SANS to create segmented flow as a means to circumvent flow dispersion (336). However, these studies have yet to focus on the interfacial behaviour of drops in flow, and are still focused on single phase, or the bulk phases of either the dispersed or continuous phase. Nevertheless, these novel approaches to characterising emulsions within microfluidic devices open the door to a new area of understanding for these systems in flow.

Chapter 3: Experimental Methods

3.1 Materials

Sodium dodecyl sulphate (SDS, >99% (GC)) was obtained from Sigma-Aldrich (New South Wales, Australia) and used as received. Deuterated sodium dodecyl sulphate (D25, 98%) was obtained from Cambridge Isotope Labs through Novachem and used as received. Polyvinylpyrrolidone (PVP, K90, MW = 360, 000 g/mol, analytical grade) was obtained from Fluka and used as received. Deuterium oxide (D- 99.9%) was obtained from Sigma-Aldrich (New South Wales, Australia) and used as received. Deionised water at 25°C (minimum resistivity 18.2 MΩ cm) was taken from a Milli-Q system. Tetradecane (98%) and perfluorooctane (98%) was obtained from Sigma-Aldrich (New South Wales, Australia). No adjustments were made to solution pH or ionic strength.

3.2 Cleaning Procedures

Glassware was cleaned using a standard 3-stage soaking process. The glassware was initially thoroughly rinsed with Milli-Q water, it was then soaked for 1 hr in 10% Ajax detergent (LabChem), followed by 1 hr in 10% sodium hydroxide solution, then 1 hr in 10% nitric acid (70%, Univar) solution, and finally thoroughly rinsed with Milli-Q water. A thorough rinse with Milli-Q water is performed between each stage, prior to drying.

AFM components, needles and other equipment containing metal were cleaned using 10% Ajax detergent (LabChem) alone to avoid corrosion and damage. AFM components such as screws, skirts and O-rings were stored in ethanol and sonicated along with the fluid cell if particularly contaminated with previous materials. The AFM tip holder was cleaned each time prior to use using a Kimwipe and ethanol. Syringes were cleaned using a series of rinses with ethanol, followed by water and finally the relevant solution for the experiment. The cleaning procedures for the microfluidic devices and their relevant components are provided in further detail in section 3.7.4 of this chapter.

3.3 Oil Purification

Oils were purified over packed silica via column chromatography. This was achieved by filling a glass column with a sintered disc at the base, with 10 – 15 cm of powdered silica (Florisil, Sigma-Aldrich, 100–200 mesh) and allowing the oils to pass through into a clean glass vial below. To ensure a high degree of purity, this process was performed a minimum of three times for each oil. The purity of the oils was also tested by measuring the interfacial tension in water using the pendant drop method, which was compared to previously recorded values (236, 337). Constant surface activity was maintained for around 2 weeks when stored in blacked-out sealed vials, after which additional passes were performed.

3.4 Interfacial Tension Measurements: Pendant Drop

Interfacial tensions were measured using pendant drop tensiometry with a Dataphysics OCA 20 Tensiometer. This involved generating a drop of oil in the aqueous solution within a clear quartz cuvette, using an inverted needle as the oil (721 kg/m3 @ 25°C) is less dense than water (998.9 kg/m3@ 25°C). The cell was sealed with Parafilm to avoid dust contamination. Care was taken to ensure the solutions or oil and syringe tip did not come into contact with the Parafilm. The drops were generated via a motor driven pump locked to the end of a syringe attached to the needle. Once a drop of appropriate size was formed the drop profile was captured using a CCD camera. The drop's deformation is dictated by a balance between interfacial tension forces and buoyancy which allows the interfacial tension to be determined (338). The curvature profile of the drop, needle diameter and fluid properties were then used to fit the Young-Laplace equation using the proprietary instrument software (SCA 202, Dataphysics) to calculate the interfacial tension between the fluids. Dynamic interfacial tension data was recorded over time on a log-log scale until a constant value was reached to account for surface adsorption kinetics.

3.5 Viscosity Measurements

Solution viscosities were measured using a shear-rate sweep with an Anton Paar MCR-702 Rheometer. This was performed using a bob in cup geometry, where the sample is filled to an indicated mark on the cup and a matched cylindrical measuring bob which is placed into the fluid under test. The Searle principle was employed, such that the cup was fixed securely to a measuring stage, while the cylindrical measuring bob was secured to a head containing a drive motor and encoder designed to measure and control the speed, torque and deflection angle of the bob. From these parameters, and knowledge of the bob and cup dimensions, the RheoCompass software uses the viscosity law to produce a viscosity curve by calculating the viscosity of the fluid from the shear stress at different shear rates. The allocated shear rate range was between 10 and 100 s^{-1}, which was selected by performing a water calibration curve prior to sample measurements to determine the torque and shear rate boundaries to avoid instrumental noise and inertial artefacts respectively. The stainless-steel cup and bob were cleaned before measurements by thoroughly rinsing in first ethanol, followed by Milli-Q and finally the sample to be tested.

3.6 AFM Force Measurements

A force measurement involves tracking the nanoscale movement of a cantilever being translated towards and away from a substrate to measure the force experienced by its probe as a function of its separation from the surface. A laser is focused onto the back of the cantilever tip which

reflects onto a position sensitive photodiode such that movement or a deflection in the cantilever can be detected as a difference in voltage (ΔV). Deflection is experienced when the cantilever approaches the surface as a reponse to the change in force experienced by the tip due to changes in surface interactions. The cantilever is translated in the z-direction towards and away from the surface via a piezo electric unit, with a distance that is recorded by a linear variable differential transformer (LVDT).

Force versus separation can be extracted from the raw data via several relationships and calibration variables, which is represented in Figure 3.1. The force (F) is equal to the cantilever spring constant (K) multiplied by its deflection, which in turn is defined as:

$$F = K \times d_s \times \Delta V \tag{3.1}$$

Where d_s is the deflection sensitivity and is measured from the slope of the voltage signal versus piezo translation when the cantilever is in contact with the surface. It is known as the inverse optical lever sensitivity but typically referred to as inVOLS in the AFM software. It is specific to the system conditions such as; the cantilever, laser position on the cantilever and the fluid medium and therefore must be calibrated for each experiment or for variations in conditions.

The spring constant is a property of the cantilever and is a function of its size, shape and material properties. Therefore, it is important to accurately measure each cantilever's spring constant individually. The calibration can be performed using a range of techniques including the Hutter and Bechhoefer method (339), the Cleveland method (340), and the Sader method (341). The Cleveland method requires the addition of a mass to the end of the cantilever, thus rendering the cantilever unusable afterwards, while the Sader method is tailored to rectangular cantilevers and has high degrees of inaccuracy associated with converting to non-rectangular shapes. Therefore, the Hunter and Bechhoefer method was used in this thesis, which fits a theoretical resonate response to the measured vibrations from the thermal noise created by the cantilever while in air. This is obtained using the AFM operating software, is easy to perform, non-destructive to the cantilever and doesn't require knowledge of its material properties or dimensions.

The change in separation (Δh) is not only a function of the piezo's displacement (Δz) but also the cantilevers deflection (Δd) and substrate deformation (Δs), therefore giving the following relation:

$$\Delta h = \Delta z - \Delta d - \Delta s \tag{3.2}$$

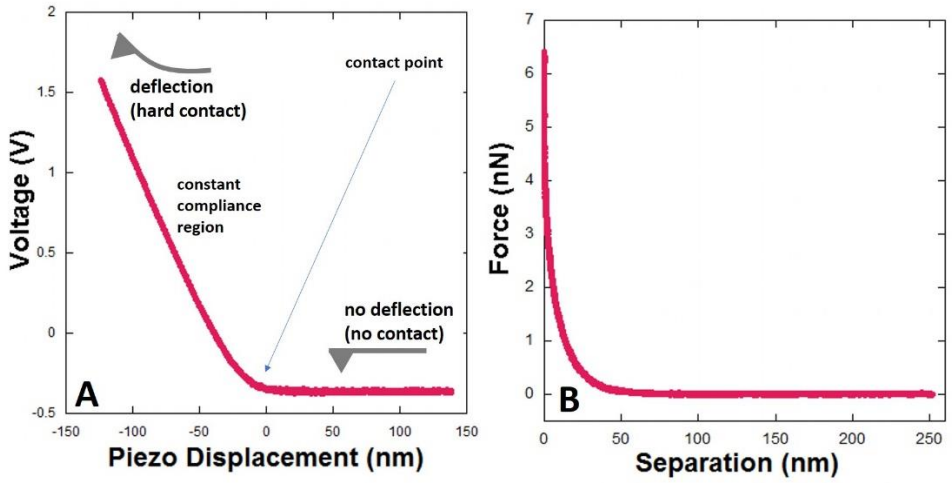

Figure 3.1 Standard force curves of a rigid force measurement before and after data conversion. A) Raw data curve of voltage vs piezo displacement highlighting at what points the cantilever is and is not in contact with the surface B) Converted force curve from applying the deflections sensitivity and cantilever spring constant

3.6.1 Colloidal Probe Measurement

Direct force measurements were performed on an Asylum MFP-3D (Asylum Research) mounted on an inverted microscope (Nikon Ti-2000) that was equipped with a CCD camera and positioned on an isolation table within an acoustic isolation hood. Asylum research fluid cells with interchangeable glass rounds for the bottom/ substrate were used in conjunction with 16" OD PTFE thin wall tubing (John Morris Scientific) connected to Female LuerTight locks (IDEX Health and Science LLC) which screwed directly onto 10 mL sterile syringes (Terumo) in order to perform fluid exchange. This cell is filled with around 3 mL of the initial solution and secured to the stage. The cantilevers were mounted into the head with a skirt attached and secured back to prevent fluid ingress into the head. Prior to lowering the cantilever into the solution contained within the fluid cell, a small amount of the same fluid is dropped onto the tip of the cantilever with a needle and syringe. This is done to avoid losing the particle due to the force applied to the tip as it breaks the liquid interface. The cantilever is manually brought down to the surface to measure the inVOLS for a minimum of three times to be averaged as a means to reduce error. This is obtained using the AFM software by measuring the gradient of the constant compliance region, which is highlighted in Figure 3.1. It should be measured regularly throughout an experiment to ensure a constant value is maintained. The spring constant calibration is preferably performed prior to measurements in case a tip is broken during the experiments, however where the probes surface is the point of interest it is conducted after the main experiments to avoid contamination.

In the asylum software several standard experimental parameters are available to control, which include; the drive velocity, the applied force or deflection limit that is controlled as the trigger point, and the force distance which is the distance the cantilever will travel towards and away

from the surface. Systematically changing these parameters over a range of conditions can provide detailed insight into the interactions between the surfaces. To explore the effects of a separated relaxation period or an extended contact time between the surfaces a dwell parameter can also be used. The dwell parameter will maintain the piezo's position for a specified period of time at either the moment after the trigger point has been reached or at the end of a force curve.

To change the fluid cells content to the next solution condition, fluid exchange is performed using two fluid pumps (NE-1000, NE-3000, New Era Pump Systems). These are set to identical flowrates of around 1 ml/min and operated in tandem, but one is set to push the new fluid into the device while the other is set to pull out the previous fluid into an empty syringe. Around 10 mL of fluid is exchanged to allow a minimum of 3 full volumes of the fluid cell to be exchanged. After the exchange is complete the system is given 30 minutes to thermally equilibrate prior to collecting the next set of data.

3.6.2 Cantilever and Substrate Preparation

3.6.2.1 Rigid Surfaces

Rigid AFM experiments used a triangular silicon nitride cantilever with a 5 μm diameter SiO_2 sphere attached at the tip (PT.SiO2.SN.5, Novascan, IA, USA), and a flat rigid glass round slide. The cantilevers and substrate used to measure the hydrophilic system were exposed to low concentration ozone (BioForce Nano-sciences, Inc., UV/Ozone ProCleaner Plus) prior to use. To functionalise the surfaces for hydrophobic measurements, the glass slide and both sides of the cantilever were sputter coated (Emitech K575X) with a thin layer of chromium (~7 nm) followed by a layer of gold (~30 nm) and then submerged in a 2 mM decanethiol solution for a minimum of 2 hrs. The spring constants of these cantilevers were measured to be in the range of 0.03-0.05 N m^{-1}.

To independently determine the size and roughness of the commercially purchased probes, an inverse imaging technique developed by Craig *et al.* was used prior to selecting each cantilever (203). When imaging a surface with a sharper point then the cantilever tip, the surface will instead image the AFM tip. Therefore, by using a commercial grating (TGT1, NT-MDT) containing an array of sharp spikes to image, a cross-section of the exposed portion of the sphere can be analysed to determine the probes characteristics. As seen in Figure 3.2, due to the repetitive pattern of the grating this produces a dense collection of the cantilever probe imaged multiple times. The characteristic width and height were extracted from the cross-section and used to calculate the particle radius. Visual inspection of the image in Figure 3.2 also shows that the probe is very smooth and free from debris.

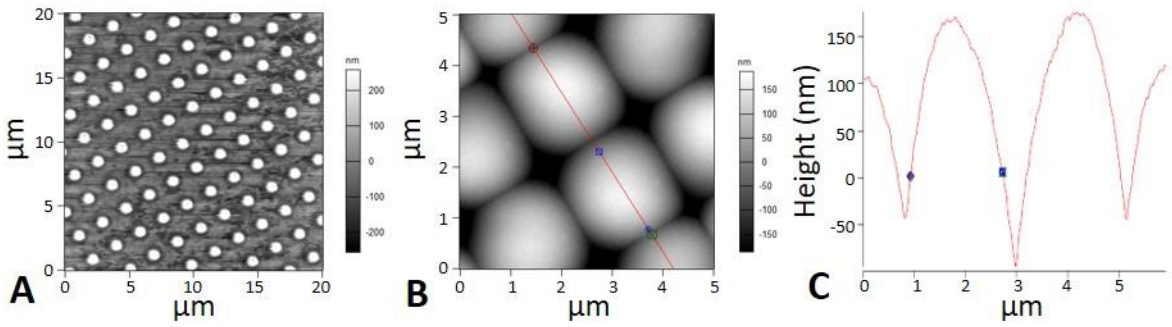

Figure 3.2 Image of (A) the commercial grating (TGT1, NT-MDT) used to reverse image the probe (B) a spherical probe attached to the end of a cantilever tip which is suitable for direct force measurements and (C) the height as a function of distance along the cross-sectional cut marked in (B) used to calculate the particle radius.

3.6.2.2 Deformable Surfaces

Drop experiments were performed using custom rectangular silicon cantilevers (450 µm x 50 µm x 2 µm) with a gold disk (radius of 45 µm) at the end, which were fabricated at the Victorian node of the Australian Nanofabrication Facility (ANFF), the Melbourne Centre for Nanofabrication (227, 342). The detailed design and fabrication process are described in Appendix A9.1. These cantilevers were submerged in a dilute 2 mM solution of decanethiol in ethanol to form a decanethiol monolayer on the gold disk to facilitate the drop attachment. A layer of chromium (~7 nm) followed by gold (~30 nm) was than sputter coated (Emitech K575X) onto the backside of the cantilever to ensure a sufficient laser signal was registered by the photodiode during AFM measurements. These steps are specifically performed in this order to prevent the thiols from attaching to the backside of the cantilever which can encourage oil to migrate there. The spring constants of these cantilevers were in the range of 0.1-0.3 N m^{-1}. As the oil is less dense then water it was necessary to make the glass round hydrophobic in order to immobilise the drops on the surface of the slide. This was achieved by boiling the slides in n-propanol for 2-5 h prior to use where the cantilevers were more hydrophobic then the substrate to aide drop attachment. A small amount of anti-bumping granules and an aluminium foil cover was used to prevent the n-propanol from over-boiling and loss of solution during the extended boiling time.

3.6.3 Deformable Measurements

The primary differences in deformable and rigid force measurements is the drop generation and characterisation. All other steps are otherwise essentially the same. Drops were generated by spray injection using a deformed hypodermic needle and submerged in solution using an O-ring technique outlined by Dagastine *et al.* (343). A small amount of oil was drawn into the needle with a folded tip introduced to create a barrier. This was than sprayed directly over the hydrophobically prepared glass round with an air-filled syringe to create a spattering of oil

droplets on the slide. A clean O-ring was then positioned into the centre of the substrate and gradually filled with Milli-Q water from 3 different points within the ring. This method helps retain the oil drops on the slide while positioning them in lines along the intersections of the contacting water drops. R_1

The deflection inVOLS was taken prior to drop attachment as the deformation of the drops interface will hinder an accurate measurement of the constant compliance region. It's important to find a drop free area on the surface to ensure there isn't any interference around the cantilever while taking the measurement. Using the optical microscope, a suitable drop was then located, and the cantilever was lowered over the drop such that the gold patch on the cantilever came into contact with its surface. By raising the cantilever, the drop would detach from the substrate and remain pinned to the gold patch at the cantilevers tip as seen in Figure 3.3.

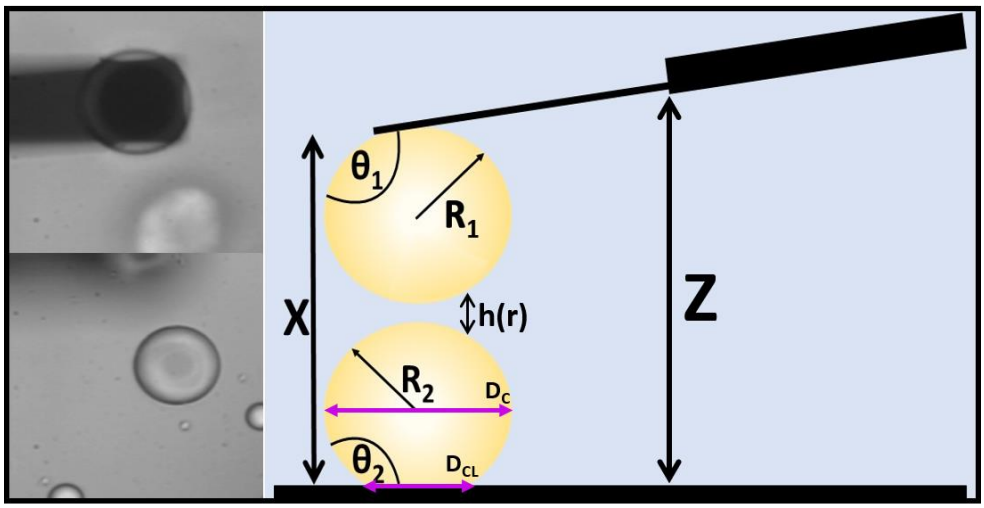

Figure 3.3 Schematic diagram of the experimental set-up during a drop-drop AFM force measurement. Images to the left show a drop attached to the gold patch at the end of a custom-made cantilever (TOP) and a drop immobilised on the hydrophobic substrate

A second drop, still immobilised on the surface and with a larger radius, was located for force measurements to be performed over. Using the camera connected to the microscope the diameter (D) of the drops was visually measured at both the centre (subscript C) and contact line (subscript CL) of each drop, highlighted in purple in Figure 3.3, in order to calculate the contact angels via:

$$\sin(\theta_c) = \frac{a}{R} \tag{3.3}$$

where θ_c is the contact angle of the drop, a is the contact area radius and R is the drop radius. A fluid exchange of the first experimental condition is then conducted. This step is performed last as introduction of surface-active components prior to attaching the drop to the cantilever can hinder the process. Finally, using the inverted microscope, the drops were aligned to be

axisymmetric as shown in Figure 3.3, allowing force measurements to be taken between the droplet pair.

3.6.4 Force Curve Analysis

3.6.4.1 Rigid Surfaces

Force versus piezo motion data between two rigid silica surfaces can be converted to force versus separation data by using the constant compliance region, the measured photodiode sensitivity and cantilever spring constant. This data is fitted to an analytical model for electrical double layer, van der Waals and depletion forces, where the total potential energy between two surfaces was modelled as the sum of these forces. The net interaction energy E between flat half spaces as a function of surface separation h is given by:

$$E(h) = E_{EDL} + E_{VDW} + E_{DEP}. \tag{3.4}$$

where E_{EDL} is the electrical double layer (EDL) potential energy, E_{VDW} is the van der Waals potential energy and E_{DEP} is the depletion potential energy. Assuming a weak overlap model, the EDL potential energy between two planar surfaces with matching chemistry can be modelled as (36):

$$E_{EDL} = \frac{64 k_b T n^o}{\kappa} tanh\left(\frac{e\psi_0}{4k_b T}\right)^2 e^{-\kappa h}, \tag{3.5}$$

where k_b is the Boltzmann constant, T is the absolute temperature, n^o is the bulk ion number density, κ is the inverse Debye length, e is the elemental charge, and ψ is the surface potential for each interacting surface. The Debye length and bulk ion number density for a given system can be calculated from the ionic strength. The van der Waals potential energy can be modelled using Lifshitz theory as (71, 72):

$$E_{VDW} = -\frac{A_H(h)}{12\pi h^2} \tag{3.6}$$

Where A_H is the Hamaker function, with values for $A_H(0)$ relevant to this thesis presented in Table 2.1. The depletion potential energy can be modelled with Asakura-Oosawa theory, according to (79):

$$E_{DEP} = \begin{cases} \Pi_{\mathrm{OSM}}(2\Delta - h) & for\ h < 2\Delta \\ 0 & for\ h \geq 2\Delta \end{cases} \tag{3.7}$$

where Π_{OSM} is the osmotic pressure and Δ is the depletion layer thickness. The Derjaguin approximation can then be used to relate the interaction energy of two flat surfaces to the force measured in the AFM measurements. This calculation scales the force of systems with curved

edges based on geometric arguments but is only applicable when the separation between the interacting surfaces is far less than the radius of the entities. For the interaction between two spheres of radius R_1 and R_2:

$$F(h) = 2\pi\left(\frac{R_1 R_2}{R_1 + R_2}\right)E(h) \tag{3.8}$$

Which reduces to,

$$F(h) = 2\pi R E(h) \tag{3.9}$$

For the force between a sphere and a flat plate. The fitted model is then used to determine the remaining unknown surface force parameters, the surface potential, osmotic pressure and depletion layer thickness, from the experimental data.

As mentioned in the previous chapter, non-ionic polymers and ionic surfactant complexes have been shown to reflect polyelectrolyte behaviour, and therefore it is possible to obtain an independent estimate of osmotic pressure using scaling theory analysis by approximating the PS complex as a polyelectrolyte. If one knows the number of bound micelles per polymer and the aggregation number of the micelle then it is possible to estimate the bound charge per monomer. The osmotic pressure for a polyelectrolyte system can be defined as the summation of the ionic and volume contribution of the depletant, defined by (121):

$$\frac{\Pi_{\mathrm{OSM}}}{kT} = \frac{C^2}{4A^2C_s + AC} + \frac{1}{\xi^3} \tag{3.10}$$

Where A is the number of monomers per charge, C is the polyelectrolyte monomer concentration and C_s is the concentration of additional electrolyte. The characteristic length ξ is related to the depletion layer thickness, being equal to twice its length.

3.6.4.2 Deformable Drops

The previously described CDW model was used to quantitatively analyse the forces between two deformable surfaces. This method uses a well-established theory that describes the interplay of changes in drop deformation, separation, surface forces and hydrodynamic drainage effects between drops/bubbles (45, 47, 221, 222, 344, 345), sometimes referred to as the Stokes-Reynolds-Young-Laplace (SRYL) model for drop and bubble interactions. The SRYL-model is a well described method that matches an inner numerical solution, which encompasses the drop or bubble interaction zone, to an outer analytical solution for the drop or bubble profile. This theory has been previously validated against measurements by a number of studies for both equilibrium surface forces measurements and conditions where hydrodynamic drainage is

significant (11, 179). The Reynolds lubrication approximation accounts for the thin film drainage between two drops or bubbles bought into close separation, describing the change in film thickness as a function of axial coordinate *r* with:

$$\frac{\partial h}{\partial t} = \frac{1}{12\mu r}\frac{\partial}{\partial r}\left(rh^3\frac{\partial \mathrm{P_H}}{\partial r}\right) \tag{3.11}$$

where μ is the viscosity of the liquid in the film and $\mathrm{P_H}$ is the hydrodynamic pressure in the film. Based on previous experimental studies and extensive modelling, the oil water interface is described with a tangentially immobile boundary condition (13, 45). The normal stress balance between the drop shape and disjoining pressure arising from the surface forces within the film is governed by a modified form of the Young-Laplace equation, with an additional term accounting for the effects of the hydrodynamic pressure:

$$\frac{\gamma}{2r}\frac{\partial}{\partial r}\left(r\frac{\partial h}{\partial r}\right) = \frac{2\gamma}{R} - \Pi(\mathrm{h}) - P_H(h) \tag{3.12}$$

Here γ is the interfacial tension of the system, $R = (2R_1R_2)/(R_1 + R_2)$ is the effective radius of the two drops and Π is the disjoining pressure. The force of interaction between the drops is defined by:

$$F(t) = 2\pi\int_o^\infty [\Pi(\mathrm{h}) + P_H(h)]r\,dr \tag{3.13}$$

In flow regimes where the system is considered to be in equilibrium such that hydrodynamic drainage is negligible, the system is modelled by the Young-Laplace equation without the hydrodynamic pressure contribution. In both cases, the disjoining pressure is defined as the negative of the derivative of the E(h):

$$\Pi(h) = -\frac{\partial E(h)}{\partial h} \tag{3.14}$$

The governing equation are solved numerically using four boundary conditions and one initial condition to find the shape of the film, total pressure and force over the entire drop-drop interaction. Two of the four boundary conditions occur in the inner region at $r = 0$, where it is assumed that the total pressure *P*, and gradient of the film is zero throughout the interaction, giving the boundary conditions:

$$\left.\frac{\partial P(r,t)}{\partial r}\right|_{r=0,t} = 0 \tag{3.15}$$

$$\left.\frac{\partial h(r,t)}{\partial r}\right|_{r=0,t} = 0 \tag{3.16}$$

Outside the interaction zone it is expected that the drops or bubbles have similar behaviour to rigid particles. Therefore, the pressure is inversely proportional to r^{-4} as $r \to \infty$ such that the third boundary condition becomes:

$$\left.\frac{\partial P(r,t)}{\partial r}\right|_{r=r_{max},t} = -\frac{4P(r,t)}{\mathrm{r}} \tag{3.17}$$

Where the inner and outer regions meet ($r = r_{max}$) it is assumed that the analytical approximation holds true, resulting in the final condition:

$$\left.\frac{\partial h(r,t)}{\partial t}\right|_{r=r_{max},t} = -\frac{d\Delta X(t)}{dt} + \frac{1}{K}\frac{dF(t)}{dt} - \frac{1}{2\pi\gamma} \times \frac{dF(t)}{dt}\left(\log\left(\frac{\mathrm{R}_2}{R_1}\right) + B(\theta_1) - B(\theta_2)\right) \tag{3.18}$$

Here ΔX is the displacement of the cantilever piezo head, K is the cantilever spring constant, θ_1 and θ_2 are the contact angles of drops on the cantilever and substrate respectively, and

$$\mathrm{B}(\theta) = 1 + \frac{1}{2}\log\left(\frac{1+cos\theta}{1-cos\theta}\right) \tag{3.19}$$

For a pinned contact line or,

$$\mathrm{B}(\theta) = 1 + \frac{1}{2}\log\left(\frac{1+cos\theta}{1-cos\theta}\right) - \frac{1}{2+cos\theta} \tag{3.20}$$

For a constant contact angle. To complete the model, it is predicted that the drops are far enough apart in their initial separation that neither body is deformed, giving the films a parabolic shape and yielding the initial condition:

$$h(r, \mathrm{t} = 0) = h_0 + \frac{r^2}{\mathrm{R}} \tag{3.21}$$

Where h_0 is the initial separation between the two drops at $r = 0$. The oil-water interface was described assuming a tangentially immobile boundary condition. This is consistent with previous experimental studies of the hydrodynamic drainage between oil drops in surfactant solutions, as well as early experimental and modelling studies showing very low levels of surface-active material is sufficient to describe the interfaces in the AFM with the no-slip boundary condition (13, 44, 54).

3.7 Microfluidics

3.7.1 Fabrication

As previously discussed in chapter two of this thesis, there are a range of materials and techniques available for fabricating microfluidic devices. In this project glass devices were used due to their chemical stability or in the case of SANS experiments high optical transmittance. Borosilicate was sufficient and used for the majority of experiments, however due to its potentially high boron content quartz devices were used for scattering measurements. Quartz has a high neutron transmission (up to 98%) and low scattering background ($\leq 10^{-2}\ cm^{-1}$) , whereas the boron content in borosilicate makes it a strong neutron absorber (25, 335).

Device fabrication was performed by the South Australia branch of the Australian Nanofabrication Facility (ANFF) using etching techniques. The channel geometries were designed as 2-dimentional images in Solidworks and exported as DXF files to be manufactured into chrome masks. Up to 4 devices were positioned onto a single wafer template. Using these masks, the designs are then lithographically patterned onto a glass 6" wafer (0.675 mm thickness) with SU-8, such that all non-channel areas are protected by a layer. Deep reactive ion etching (DRIE) using C_3F_8 as an etch gas is then used to directly etch out the channel dimensions. DRIE etching as opposed to wet HF etching occurs in a single perpendicular direction and provides straight rather than curved channel wall edges. Remaining SU-8 is removed from the glass substrate using selective etching and detailed cleaning processes. The individual devices are then cut out of the wafer using a dicing saw and paired with a second "lid" slide containing laser drilled holes at the desired port locations. The etched chip and lid are cleaned, chemically treated, aligned and pre-bonded before being fusion bonded at 1100 °C to create the completed microfluidic device. The etch depth of channels with width between 20 and 50 μm was around 51.8 μm, while widths greater than 60 μm were around 59.5 μm.

To secure tubing to the inlet ports of the devices, custom made clamps in conjunction with commercially available screw and ferrule fittings were used. A three-dimensional part was designed in Solidworks and used to cut the geometry from Delrin acetal resin blocks using a computer numerical control (CNC) machine (Figure 3.4). Holders to position the device and clamp assembly onto the microscopic stage were similarly designed in Solidworks and printed in RGD 720 on an Objet Eden 260V Polyjet printer. This also allowed the microfluidic assembly to be secured such that the microscope micromanipulators could be used for translation.

3.7.2 Experimental Setup

The experimental set-up, operation and cleaning is broken into two parts; general lab-based experiments, and SANS experiments. Due to the novel development of the microfluidic SANS studies, a custom rig was designed to integrate into the established equipment and is discussed in further detail.

3.7.2.1 General

Figure 3.4 shows a complete set-up of the microfluidic assembly used in general lab-based experiments. One end of 16" OD PTFE thin wall tubing (John Morris Scientific) was fit with a P-844x Vacutight PEEK screw and ferrule (IDEX Health and Science LLC) which was used in conjunction with the custom-made clamps to secure the tubing to the microfluidic device. The other end of the tube was fit with a Female LuerTight lock (IDEX Health and Science LLC) such that the tubing could be screwed directly into 500 µL glass (Hamilton Company), and 2.5 mL glass (Hamilton Company) luer lock syringes. The size of syringe used was dependant on the channel and experiment, where smaller volumes were preferable for sensitive flowrates due to an increased smoothness in fluid flow. The assembled device was then secured into the custom holder and positioned over the microscope's objective.

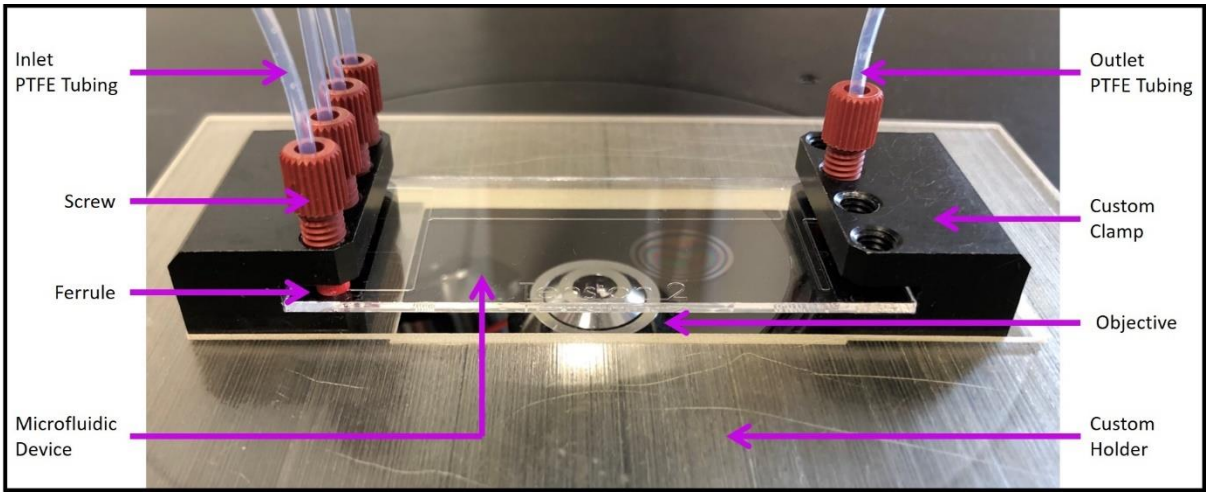

Figure 3.4 A photo of the microfluidic assembly used in general lab-based experiments

The experiments were performed on an inverted optical microscope (XJF400 Inverted and Reflected Fluorescence Microscope) with either a CMOS camera (Basler Ace acA720-520um, BASLER) or an Ultrahigh-speed camera (Phantom V1212, Vision Research) attached via the microscope/s C-mount to capture images of the channels. A 10x objective was used as it provided the necessary information required in the images while maintaining the desired camera frame rates. The syringes were driven by fluid pumps (NE-1000, NE-3000, New Era Pump Systems) that were controlled manually, while the outlet tubing was secured to a glass vial for waste collection. This is presented in the experimental set-up shown in Figure 3.5.

Figure 3.5 A photo of the experimental set-up used for general lab-based experiments

3.7.2.2 SANS

As required of standard SANS experiments, the instrument came pre-equipped with a sample stage, mounting plate and pedestal. Normally a 6 to 10 position sample changer is also provided to lock a series of banjo cells a top the pedestal in line with the neutron beam. Instead, for our experiments, an aluminium microfluidic device holder was designed to secure the microfluidic devices vertically into place. The previously described custom clamps used for securing tubing to the inlet and outlet ports of the devices were transformed to include a nut and bolt attachment allowing them an easy connection directly to the device holder. The photo in Figure 3.6 shows this set-up with and without a device secured in place. Recesses for the clamps to sit into were included to guide the clamps into place. The bottom recesses and taped holes were designed such that the device would consistently sit flush along the bottom of the holder. Inversely, the top recesses had a 3 cm vertical tolerance and slots built in to allow slight variations in clamp and device length, and any inconsistencies in device attachment. Tubing was connected to the device as previously described in the general section. Sample alignment is critical to the success of the measurement, therefore a tip, tilt and rotation stage for angle precision, and a lab jack for manual height adjustments were included between a sample changer plate and the device holder (Figure 3.6). The sample stage has the ability to translate horizontally by 170 mm and vertically by 500 mm with a precision of movement better than 100 μm. The sample changer plate was used to clamp the assembly directly to the pedestal.

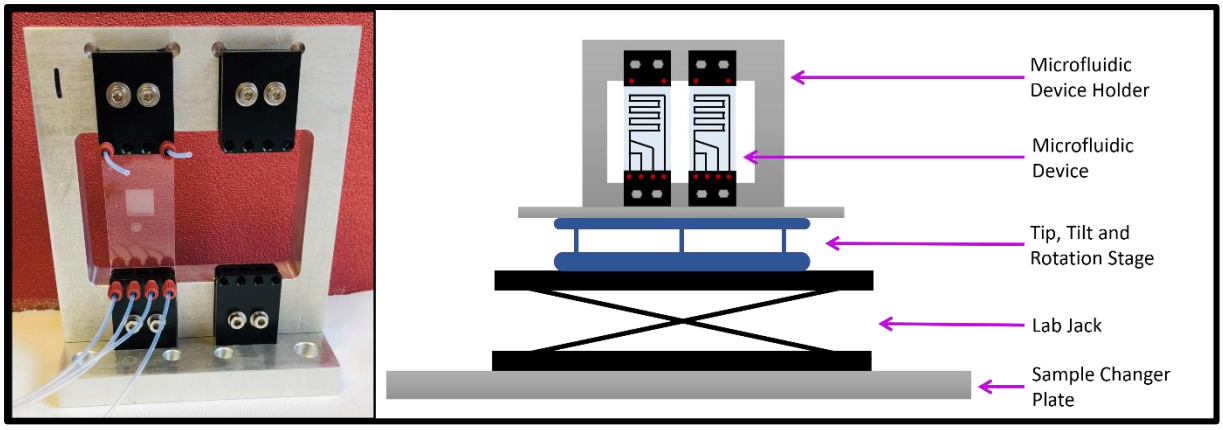

Figure 3.6 Left: a photo of the custom-made microfluidic device holder used to position the device vertically with the neutron beam. Right: A close up view of the alignment equipment used to ensure correct placement of the sample in the beamline.

To visualise drop generation during start-up procedures a horizontal microscope was constructed, as shown visually in Figure 3.7. A CMOS camera (Basler Ace acA720-520um, BASLER) connected directly to a 10x objective and LED light panel were secured to a set of translation stages providing coarse translation in the x, y and z directions. Additionally, the camera and objective had a fine manipulation in the direction towards the microfluidic device to use as a focus for the objective. The "microscope" was secured across the top of the microfluidic assembly using a crossbeam, which allowed it to be easily attached for drop generation start-up and removed for SANS measurements. The camera was connected to a laptop running the cameras proprietary software to visualise and capture the channels. Figure 3.7 shows a schematic diagram of the complete experimental rig required to perform drop microfluidics in line with SANS. A 500 µL (Hamilton Company) glass luer lock syringe was used to supply the dispersed phase, while 2.5 mL (Hamilton Company) glass luer lock syringes were used for the continuous phase. The syringes were driven by individual fluid pumps (PHD 22/2000, Advance Syringe Pump, Harvard Apparatus) that were controlled manually, while the outlet tubing was secured to a centrifuge tube for waste collection. The syringe pumps were placed atop the mounting plate and an additional shelf secured to the crossbeam such that they could remain undisturbed during the SANS measurements.

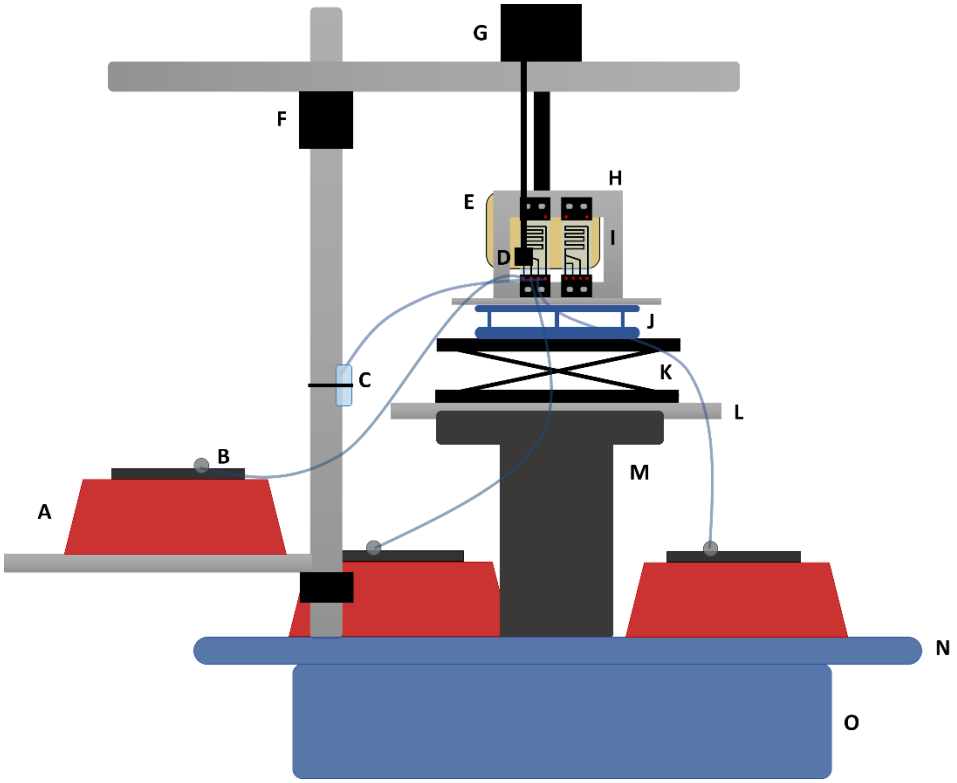

Figure 3.7 Schematic diagram of the experimental set-up used inline of the BILBY small-angle neutron scattering instrument. Equipment list: (A) Syringe pump (B) Syringe and PTFE tubing (C) Waste collection (D) Optical camera and 10x objective (E) Light source (F) Cross beam support junction (G) Translation stages with x, y and z control (H) Microfluidic device holder (In place of a standard sample holder) (I) Microfluidic device (J) Tip, tilt and rotation stage (K) Lab jack (L) Sample changer plate (M) Pedestal (N) Mounting plate (O) Sample stage

3.7.3 Experimental Operation

3.7.3.1 General

Every solution put through the device was first filtered using a 240 nm pore syringe filter. The devices were also initially primed with filtered Milli-Q water to remove the majority of air from the channels. Prior to attaching the tubing to the device each line was primed with its respective solution and secured into the syringe pumps, such that the fluid would directly contact the device and no trapped air or bubbles would enter. To align the clamps and device so that the tubing directly overlaps with the inlet holes, the device is pushed flush against the back of the clamp and edges tracked smoothly to each other. Once in place and securely fastened the syringe pumps were started, with channels directly responsible for drop generation started first. After steady-state drop generation was achieved under the desired flow conditions the system was allowed to run for around 30 minutes to ensure equilibrium conditions. When changing solutions, the tubing was disconnected at the device to repeat the above procedure for each condition.

Pictures of the microfluidic channels at specific viewpoints were taken for 3 second intervals and collected for image processing and further analysis. When using the CMOS camera, pictures were captured and spooled to an external hard drive via a circular ram buffer on the computer, with frame rates limited to 2469 per second. However, the Phantom camera allowed observations to be taken at 10,000 frames per second, permitting larger flowrates to be tested.

3.7.3.2 SANS

The microfluidic devices were set-up and connected in a similar fashion to the general method outlined above, however slight variations were made to accommodate the logistics of the SANS experiments. The devices were primed with deuterium oxide (D_2O) or a matched solvent consisting of a balanced ratio of H_2O to D_2O. To initially transfer microfluidic devices to the beamline, they were completely connected with primed tubing to the clamps and secured into a device holder at a laboratory bench. Once safely transferred to the beamline and connected to the sample changer assembly, the tubing was loosely unscrewed to secure the syringes into the syringe pumps set-up on the mounting plate. Alignment of the device was performed optically using a laser mounted to the guard-aperture of the SANS instrument. Solutions were changed over using the general method above, with syringes pre-primed in the laboratory and transferred to the beamline ready for connection.

The horizontal microscope was connected to visualise and capture drop formation for the start-up of each system. To efficiently produce stable drop formation the discontinuous, continuous, then additional spacer feed was turned on at the pumps. Once drop generation was constant, images at the junction where the drops enter the main channel were captured, such that the drop radius and frequency could be analysed. After stable conditions were sufficiently met the horizontal microscope was removed and the SANS measurement was performed. Following the SANS measurement, the horizontal microscope was reattached to also capture the drops post measurement.

3.7.4 Cleaning

3.7.4.1 General

Upon receiving the devices, a 5% w/w NaOH solution was passed through the device for at least 10 minutes followed by Milli-Q for at least 30 minutes to remove excess oil and contamination left over from the fabrication process. After each use the devices were rinsed through with ethanol followed by Milli-Q water. This procedure was successful at removing excess oil and the majority of contaminates trapped in the channels or to the walls, however a more thorough cleaning method was required to remove stubborn contaminates. This involved flushing the device with 10% Ajax detergent, Milli-Q water, 5% w/w NaOH solution and then a final rinse with

Milli-Q water in the reverse direction to normal operation at high flowrates. To aide this process, manually pushing and pulling a syringe connected at either end of the device would help dislodge particularly bad blockages.

3.7.4.2 SANS

Due to the sensitivity of the SANS experiments, materials other than those required for the measurements were avoided as much as possible. However as before, upon receiving the devices a NaOH solution was passed through but was rinsed for at least several hours afterwards with Milli-Q water. Particular care was taken during every use of the SANS devices to avoid contaminates at all cost as further use of NaOH or Ajax detergent was extremely undesirable. Prior to the official SANS measurements all devices were passed through with filtered ethanol, Milli-Q and finally D_2O to cleanse the channels of materials with the potential to scatter.

Chapter 4: Forces Between Oil Drops in Polymer-Surfactant Systems – Linking Direct Force Measurements to Microfluidic Observations

Abstract

Hypothesis

Linking atomic force microscopy and microfluidics opens up the possibility of probing adhesive interactions between drops in a high-throughput context. A microfluidic device designed to form, and subsequently break-up, chains of drops, where the drop break-up is sensitive to the underlying surface forces between drops, not hydrodynamic drainage forces, would play a key role in developing this link.

Experiments

Both techniques have been used to quantify the forces between oil drops in the presence of complexes formed with anionic surfactant, sodium dodecylsulphate, and neutral, water soluble polymer, poly(vinylpyrrolidone). Measurement and modelling of the interaction forces between both rigid and deformable surfaces demonstrated that the attraction between the drops is due to depletion forces, whereas the repulsive force is a combination of electrical double layer and steric forces, indicating complexes exist both in the bulk and at the drop interface.

Findings

The interaction behaviour between the force measurements and the microfluidic observations showed a strong correlation, where the observed adhesion between drops in the microfluidics is sensitive to the drop deformation and Laplace pressure. Correlation between the two techniques provides insight into the surface forces between drops in flowing systems and has potential utility in the formulation of emulsions.

Keywords

Microfluidics; Atomic force microscopy; Drops; Deformable; Hydrodynamics; Depletion forces; Surface forces

Abbreviations

AFM, atomic force microscopy; CMC, critical micelle concentration; PS, polymer-surfactant; SDS, sodium dodecylsulphate; PVP, poly(vinylpyrrolidone); CAC, critical aggregation concentration; EDL, electrical double layer;

4.1 Introduction

Studies of interactions between drops and bubbles usually focus on the transition between repulsion and attraction, defining precise conditions whereby drops/bubbles may coalesce. These measurements are usually made using direct force measurement methods such as atomic force microscopy (AFM) (42, 44, 177, 179, 186, 234, 346, 347), larger capillary based drop and

bubble methods sensitive to interfacial separation (48, 169, 181, 183, 348), insightful and novel microfluidic devices (26, 27, 29, 30, 323), or other geometries yielding elongational flow such as the four roll mill (349). However, there are conditions under which drop/bubble interactions are attractive over certain separation distances yet sufficiently stable at closer separations such that aggregation occurs, rather than coalescence (1). For drop interactions in emulsions, these attractive interactions between the drops underpin the properties of these systems and control processes such as gel formation, fluid microstructure, and the deposition of coatings. This has important applications in the formulation and processing of foods, personal care products, and pharmaceuticals.

The term "adhesive emulsions", first coined by Bibbette (1), suggests that specific adhesive or attractive interactions are key to controlling or tuning the behaviour of these systems (2). At liquid-liquid or liquid-gas interfaces these types of attractive interactions, often attributed to a range of surface forces including depletion and structural forces, were initially measured in systems of flat air-water and oil-water interfaces using thin film balances in the seminal work of Langevin (4, 135, 350, 351), as well as Wasan's work using the Scheludko cell technique (352, 353). More recently, a series of AFM studies investigated aggregation in drop and bubble systems, as the AFM can probe both attractive and repulsive interactions, whereas thin film studies require a stable film for any observation. In addition, AFM studies have elucidated the importance of the interplay between drop/bubble deformation and these structural or depletion forces in foams or emulsions (12, 44, 63, 225-227).

One class of adhesive emulsion systems, common to formulated products, is formed by the complexation of long-chained polymers with various surfactants (4, 5). Over a range of surfactant concentrations, often spanning from below to well above the critical micelle concentration (CMC), the surfactant and polymer form molecular complexes due to the association of the surfactant with the polymer. This association is based on interactions of the surfactant head group with the polar or hydrophilic regions of the polymer, as well as the hydrophobic association of the surfactant tail with the less polar or hydrophobic regions of the polymer (31, 35, 354). Thus, even for a hydrophilic polymer showing little surface activity, the polymer-surfactant (PS) complex is often surface-active over a significant range of surfactant concentrations (7, 8, 31, 355). The PS complex and resultant attractive interaction is influenced by many factors including surfactant concentration, added electrolytes, polymer backbone flexibility, polymer charge, and surfactant-polymer associations (often based on charge or hydrophobic interaction). This sensitivity and flexibility is one of the reasons why PS complexes are used so widely in formulated products (356). This has led to an extensive understanding of PS complex behaviour in the bulk (4, 8, 89, 355). However, there are still uncertainties related to the interaction between PS complexes and

surfaces, summarised in numerous reviews on the topic (4, 10, 95, 350), and in particular the interactions between surfaces coated with the complexes. Thus, quantifying the forces involved between two interacting surfaces coated with PS complexes is important to understanding the fundamental nature of PS systems.

PS complexes coated on hydrophobic solid surfaces have been found to exhibit attractive adhesive forces between the surfaces due to polymer bridging or depletion forces (10, 113, 136, 357-360). The characterisation of such systems is limited not only in the choice of surface, polymer and surfactant but concentration variation and the effect of added components. As mentioned above, thin film balance methods have been used to explore the forces between flat air-water interfaces where both bridging and stratification of the PS complex layers have been observed (4, 115, 135, 350, 351, 361), however these forces have not been explored with drop/bubble systems exhibiting curvature and deformation in the same detail. Depletion and structural forces have been previously studied in drop/bubble pair interactions using AFM in a number of systems where strong attractions are observed, but not coalescence. Gromer *et al.* measured the effect of a non-adsorbing polyelectrolyte on the structural forces between two oil drops in food systems, notably sugar beet pectin (223). Other studies using AFM have probed the behaviour of oil drop-pair interactions in the presence of surfactant micelles, microemulsions, nanoparticles and rod-like surfactants (225-227). In addition, the interaction of a bubble and a particle was studied in the presence of non-adsorbing nanoparticles (362), and structural and depletion forces in the presence of non-adsorbing polyelectrolytes was observed between bubble pairs for both monodisperse and polydisperse polyelectrolytes (12, 63). The detailed modelling in many of these studies showed that the interplay of the structural and depletion forces with the deformation of the drops/bubbles lead to significant attractive interactions at small separations not present with equivalent sized rigid particles. In these studies, the force behaviour showed a clear dependence on the Laplace pressure of the drops (227). However, PS complexes have not yet been explored using AFM with drops/bubbles. The only direct force measurements with nanometer resolution in separation we are aware of involving PS complexes are the elegant studies by Mondain-Monval and co-workers using the magnetic field induced chaining technique (MCT), which offers some insight into these systems, but are limited to femto-Newton forces, micron to sub-micron drops that exhibit little if any deformation and struggle to probe attractive forces (114).

PS complexes are often difficult to study in a direct force measurement context over a large surfactant concentration range as many PS complexes induce phase separation, especially when the polymer and surfactant are oppositely charged (359). The bulk phase behaviour of the common anionic surfactant sodium dodecylsulphate (SDS) and non-ionic polymer

poly(vinylpyrrolidone) (PVP) has been covered in detail throughout the literature (8, 35, 101, 355), and is used in this study as the complex is water soluble and does not induce phase separation (363, 364). It is understood that once SDS begins to bind to PVP it forms 'clusters' with aggregation numbers below that of a standard surfactant micelle (8, 100-103). (See Appendix A9.4 for further details)

Interactions between SDS and PVP at an air-water interface have also been observed using several techniques such as pendant drop tensiometry and neutron scattering (31, 32, 34). For neutral polymers and charged surfactants, it is widely accepted in the literature that the interfacial tension behaviour for a polymer-surfactant system with constant polymer concentration and varying surfactant concentration can be described by 3 regions, delineated by the points of discontinuity in the interfacial tension versus concentration curve. The initial change, denoted as T_1, is the result of the onset of surfactant aggregation to the polymer also known as the critical aggregation concentration (CAC) (39). At T_2 the polymer is considered to be completely saturated, such that further addition of surfactant does not increase the amount on the interface or polymer, but instead results in the formation of surfactant only micelles (100, 101, 354, 365). This point occurs at interfacial tension values similar to those of a pure surfactant system at its CMC, which is due to the availability of free surfactant molecules competing with the polymer-surfactant complex for adsorption at the interface (95). Observations from literature report CAC values for 0.5% PVP and SDS in a SDS concertation range of 1-3 mM, by using a range of techniques, such as conductivity (366), surface tension measurements (31, 354) and capillary electrophoresis (367). The saturation of the polymer is reported over a much larger SDS concentration range, from 15-25 mM, attributed to the dependence on polymer molecular weight and concentration (95).

PS complexes formed between neutral polymers and charged surfactants have been observed to behave as pseudo-polyelectrolytes (106-110). Light scattering experiments performed by Minatti et al. claimed PVP and SDS aggregates have properties similar to polyelectrolytes, however due to the multiple equilibria that exists between the molecules the system exhibits higher complexity to that of a standard linear polyelectrolyte (111). Furthermore, Wu *et al.* used capillary electrophoresis to present direct evidence that PVP and SDS complexes should be treated as pseudo-polyanions as the apparent electrophoretic mobility of the complex decreases with increasing SDS aggregation (112). This behaviour has also been accounted for in studies observing the force between surfaces in systems containing neutral polymers and anionic surfactants. Using AFM, Tulpar *et al*. measured strong depletion forces between a silica particle and plate in the presence of Pluronic F108/SDS complexes, which they regarded as large polyelectrolytes (113). The previously mentioned work by Mondain-Monval credited an increase

in repulsive electro-steric forces between emulsion droplets in solutions containing PVA/SDS complexes to their polyelectrolyte nature (114). In addition, a single foam stability study by Folmer *et al.*, using a thin film balance method, has observed stable films and stratification in the films with PVP/SDS at concentrations where they exhibit strong binding (115). To our knowledge there is a gap in the literature covering the direct forces between rigid or deformable surfaces in a PVP/SDS system to probe the attractive forces in this system.

It is possible to investigate PS complexes or any emulsion system by examining the drop pair interactions using direct force measurement methods such as AFM, larger scale methods such as the Integrated Thin Film Drainage Apparatus (IFTDA)(181, 182) or the cantilevered capillary apparatus (183, 368). However, these studies require extensive sub-discipline expertise and are unable to perform measurements at a timescale comparable to other emulsion characterisation methods. Thus, potential advancements can be made by developing methods that probe soft particle attraction and adhesive forces in a high-throughput context over a wide range of operating conditions. Microfluidic devices are an obvious candidate to systematically probe drop interactions, yet previous studies that have had such success have been limited to studying phenomena that are either dominated by hydrodynamic interactions between drops or exhibit some coupling of hydrodynamic behaviour and surface forces. The exciting studies by Bremond & Bibbette, (26, 30) and Gunes *et al.*,(27, 323) systematically explored drop coalescence in microfluidic devices, most notably where drops coalesced upon separation. However, the drop interaction outcomes in these studies were driven largely by hydrodynamic drainage effects until very close drop separations. Furthermore, the seminal work by Anna (29) into drop coalescence at T and Y shaped junctions specifically noted that the hydrodynamics of the surrounding fluid dominated any interaction, effectively masking equilibrium surface forces. A recent simulation study of drop and bubble collisions in AFM experiments, by Berry and Dagastine (42), mapped the rich phenomenological interplay between equilibrium surface forces, drop deformation and the hydrodynamic drainage effects, identifying collision velocities where hydrodynamic drainage effects play a small role in the collision outcomes. Thus, in order to study equilibrium surface forces with a microfluidic platform, it is necessary to create a geometry that removes or quantifiably controls the hydrodynamic interactions during soft particle collisions. An example of the latter can be seen in some recent work into microfluidic flow that used depletion forces to form drop aggregates, prior to photo-polymerisation, by controlling the channel flowrate through a channel expansion (242).

The current investigation focuses on the strong attractions between oil drops in the presence of complexes formed with anionic surfactant and neutral, water soluble polymers. Both direct force measurements between two oil drops measured with AFM and microfluidic observations of the

formation and then breakup of chains of oil drops were studied via systematically varying surfactant concentration at constant polymer concentrations. The two techniques were used to better correlate the behaviour of droplets in flowing systems such as microfluidics with the underlying surface forces. Doing so works towards the possibility of developing a novel technique for measuring the adhesive interactions between oil drops and has the potential to enable screening and optimal selection of new components and additives for advanced materials.

4.2 Experimental Section

4.2.1 Materials

Sodium dodecylsulphate (SDS, >99% (GC)) was obtained from Sigma-Aldrich (New South Wales, Australia) and used as received. Polyvinylpyrrolidone (PVP, K90, MW = 360, 000 g/mol, analytical grade) was obtained from Fluka and used as received. Deionised water at 25 °C (minimum resistivity 18.2 MΩ cm) was taken from a Milli-Q system. Tetradecane (98%) was obtained from Sigma-Aldrich (New South Wales, Australia) and purified over silica (Florisil, Sigma-Aldrich, 100–200 mesh) via column chromatography. No adjustments were made to solution pH or ionic strength.

4.2.2 Interfacial Tension

Interfacial tensions were measured using pendant drop tensiometry with a Dataphysics OCA 20 Tensiometer. This involved generating a drop of oil in the aqueous solution within a clear quartz cuvette, using an inverted needle as the oil (721 kg/m3 @ 25°C) is less dense than water (998.9 kg/m3@ 25°C). The cell was sealed with Parafilm to avoid dust contamination with care taken to ensure the solutions did not come in contact with the Parafilm. The drops were generated manually by depressing a syringe attached to the needle. Once a drop of desired size was produced, the drop profile was photographed with the needle diameter used as a reference and then fit to the Young-Laplace equation using the proprietary instrument software based on the deformation of the drop and fluid properties input into the calculations. The balance between interfacial tension forces and buoyancy allowed for the interfacial tension to be calculated (338). To account for surface adsorption kinetics the interfacial tension was tracked over time until it was considered to be stable on a log-log scale.

4.2.3 AFM

All experiments were performed on an Asylum MFP-3D AFM. The procedure for drop-drop (deformable) and particle-slide (rigid) AFM measurements has been covered in detail in previous literature (44, 186, 226, 227). All slides were cleaned prior to use by soaking for 1 hr in 10% Ajax detergent (LabChem), followed by 1 hr in 10% sodium hydroxide solution, then 1 hr in 10% nitric

acid (70%, Univar) solution, and finally thoroughly rinsed with Milli-Q water. Spring constants were measured using the method of Hutter and Bechhoefer.(339)

Rigid AFM experiments used a triangular silicon nitride cantilever with a 5 μm diameter SiO_2 sphere attached at the tip (PT.SiO2.SN.5, Novascan, IA, USA), and a flat rigid glass round slide. The cantilevers used to measure the hydrophilic system were exposed to low concentration ozone (BioForce Nano-sciences, Inc., UV/Ozone ProCleaner Plus) prior to use. To functionalise the surfaces for hydrophobic measurements, the glass slide and both sides of the cantilever were sputter coated (Emitech K575X) with a thin layer of chromium (~7 nm) followed by a layer of gold (~30 nm) and then submerged in a 2mM decanethiol solution for a minimum of 2 hrs. The spring constants of these cantilevers were measured to be in the range of 0.03-0.05 N m^{-1}.

Drop experiments were performed using custom rectangular silicon cantilevers (450 μm x 50 μm x 2 μm) with a gold disk (radius of 45 μm) at the end, which were fabricated at the Victorian node of the Australian Nanofabrication Facility (ANFF), the Melbourne Centre for Nanofabrication.(227, 342) These cantilevers were submerged in a dilute 2mM solution of decanethiol in ethanol to form a decanethiol monolayer on the gold disk to facilitate the drop attachment. A layer of chromium (~7 nm) followed by gold (~30 nm) was than sputter coated (Emitech K575X) onto the backside of the cantilever to ensure a sufficient laser signal was registered by the photodiode during AFM measurements. The spring constants of these cantilevers were in the range of 0.1-0.3 N m^{-1}. As the oil is less dense then water it was necessary to make the glass round hydrophobic in order to immobilise the drops on the surface of the slide. This was achieved by boiling the slides in n-propanol for 2-5 h prior to use where the cantilevers were more hydrophobic then the substrate to aide drop attachment. Drops were generated by spray injection using a deformed hypodermic needle and submerged in solution using an O-ring technique outlined by Dagastine *et al.*(343). Drop radii were measured before and after a set of experiments using optical microscopy. Raw data was recorded as photodiode voltage versus linear variable differential transformer (LVDT) position. Force curves were taken at a scan speed of 100 and 200 nm s^{-1} unless otherwise stated.

4.2.4 Force Curve Analysis:

4.2.4.1 Rigid Surfaces

Force versus piezo motion data between two rigid silica surfaces in the SDS-PVP system were converted to force versus separation data by using the constant compliance region, the measured photodiode sensitivity and cantilever spring constant. These data were fitted to an analytical model for electrical double layer and depletion forces, where the total interaction energy between two surfaces was modelled as the sum of these forces. For this study, the net interaction energy E between flat half spaces as a function of surface separation h is given by:

$$E(h) = E_{EDL} + E_{DEP}. \tag{4.1}$$

where E_{EDL} is the electrical double layer (EDL) interaction energy and E_{DEP} is the depletion interaction energy. Assuming a weak overlap model, the EDL interaction energy between two planar surfaces with matching chemistry can be modelled as (36):

$$E_{EDL} = \frac{64 k_b T n^o}{\kappa} tanh\left(\frac{e\psi_0}{4k_b T}\right)^2 e^{-\kappa h}, \tag{4.2}$$

where k_b is the Boltzmann constant, T is the absolute temperature, n^o is the bulk ion number density, κ is the inverse Debye length, e is the elemental charge, and ψ is the surface potential for each interacting surface. The depletion interaction energy can be modelled with Asakura-Oosawa theory, according to (79):

$$E_{DEP} = \begin{cases} \Pi_{\mathrm{OSM}}(2\Delta - h) & for\ h < 2\Delta \\ 0 & for\ h \geq 2\Delta \end{cases} \tag{4.3}$$

where Π_{OSM} is the osmotic pressure and Δ is the depletion layer thickness. The Debye length and bulk ion number density for a given system can be calculated from the ionic strength. The Derjaguin approximation was used to relate the interaction energy of two flat surfaces to the force measured in the AFM measurement for a sphere and a flat plate. The fitted model was then used to determine the remaining unknown surface force parameters, the surface potential, osmotic pressure and depletion layer thickness, from the experimental data.

4.2.4.2 Deformable Drops

To quantitatively model the forces between two deformable surfaces we used a well-established theory that describes the interplay of changes in drop deformation, separation, surface forces and hydrodynamic drainage effects between drops/bubbles (45, 47, 221, 222, 344, 345), sometimes referred to as the Stokes-Reynolds-Young-Laplace (SRYL) model for drop and bubble interactions. This theory has been previously validated against measurements by both the authors and others for both equilibrium surface forces measurements and conditions where hydrodynamic drainage is significant (11, 179). The Reynolds lubrication approximation accounts for the thin film drainage between two drops or bubbles bought into close separation, describing the change in film thickness as a function of axial coordinate *r* with:

$$\frac{\partial h}{\partial t} = \frac{1}{12\mu r}\frac{\partial}{\partial r}\left(rh^3\frac{\partial \mathrm{P_H}}{\partial r}\right) \tag{4.4}$$

where μ is the viscosity of the liquid in the film and $\mathrm{P_H}$ is the hydrodynamic pressure in the film. Based on previous experimental studies and extensive modelling discussed in Chapter 3, the oil water interface is described with the no-slip boundary condition. The normal stress balance between the drop shape and disjoining pressure arising from the surface forces within the film is governed by a modified form of the Young-Laplace equation, with an additional term accounting for the effects of the hydrodynamic pressure:

$$\frac{\gamma}{2r}\frac{\partial}{\partial r}\left(r\frac{\partial h}{\partial r}\right) = \frac{2\gamma}{R} - \Pi(\mathrm{h}) - P_H(h) \tag{4.5}$$

Here γ is the interfacial tension of the system, $R = (2R_1R_2)/(R_1 + R_2)$ is the effective radius of the two drops and Π is the disjoining pressure. The force of interaction between the drops is defined by:

$$F(t) = 2\pi\int_o^\infty [\Pi(\mathrm{h}) + P_H(h)]r\,dr \tag{4.6}$$

In flow regimes where the system is considered to be in equilibrium such that hydrodynamic drainage is negligible, the system is modelled by the Young-Laplace equation without the hydrodynamic pressure contribution. In both cases, the disjoining pressure is defined as the negative of the derivative of the E(h):

$$\Pi(h) = -\frac{\partial E(h)}{\partial h} \tag{4.7}$$

The governing equations can be solved using appropriate boundary conditions for both equilibrium and dynamic cases to calculate the expected force measured using the AFM. These boundary conditions and further details of the modelling can be found in Chapter 3.

4.2.5 Microfluidics

The microfluidic devices were manufactured from borosilicate glass by the South Australia node of ANFF using deep reactive ion etching (DRIE). The experiments were conducted on an inverted optical microscope (XDS-2 Inverted Biological Microscope, Daintree Scientific, St. Helens, Tasmania, Australia). The syringes used for these experiments were 500 µL glass (Hamilton Company), and 100 µL glass (Hamilton Company) luer lock syringes. The 500 µL syringes were

used for the fluid injection channels and the 100 µL syringes were used for the withdraw channels, as this needed very fine control and does not have problems with fluid dead zones or water in the line. Syringes were driven by fluid pumps (NE-1000, NE-3000, New Era Pump Systems, New York, United States of America) that were controlled manually.

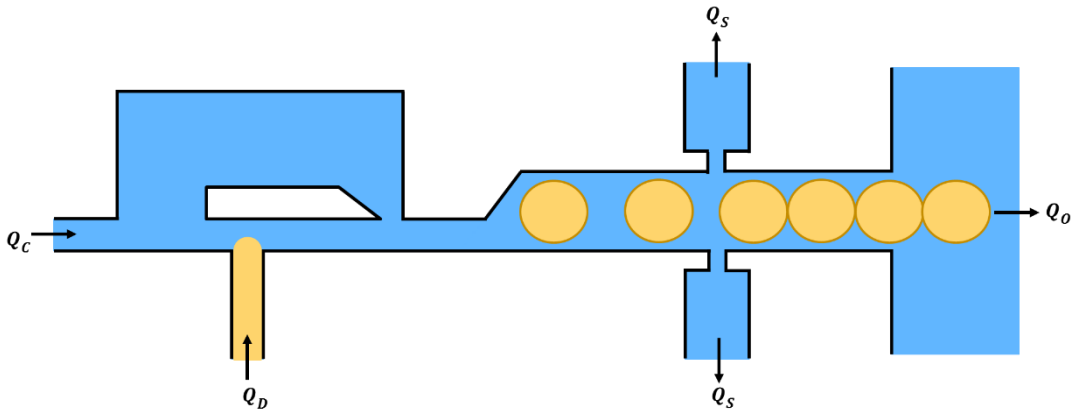

Figure 4.1 Simplified top down schematic diagram of the microfluidic geometry designed to generate drop chains. A block and break junction is used to generate the drops and then two side channels are used to collide and bunch the drops together by removing the excess continuous phase. The droplet chains then flow into solution. Flowrates were set on the fluid pumps as Q_C = 30 µL/hr, Q_D = 10 µL/hr, and Q_S = 11 µL/hr, resulting in Q_O =18 µL/hr, giving drops with an equivalent spherical radius of ~ 28 µm and a drop velocity of ~2 mm/s.

Figure 4.1 demonstrates a simplified schematic for the drop chaining microfluidic device with drop generation, collision, and release. This device combines a block and break junction for droplet generation with two side channels to initiate drop collisions by removing excess continuous phase (291). A detailed schematic outlining channel dimensions can be found in the Appendix (See A9.2). The apparatus was designed such that the drops exited the microfluidic device into solution within a large Petri-dish as shown in Figure A9.3. To avoid drop build-up at the exit, and to demonstrate the existence of an attractive force between drops as a resistance to drop separation in the fluid flow, an external flow was generated near the exit of the microfluidic device. This was generated by adding solution above the microfluidic device so that it would flow over the exit port due to gravity (See A9.2). This flow was added by drawing 3 mL of solution from the Petri-dish into a 3 mL syringe and manually dropping the solution onto the top of the microfluidic device. The pool of solution was positioned so that it would flow over the surface of the device and out over the exit of the channel in the same direction as the flow out of the device. The speed that the solution was added was changed to obtain situations where the drops would be travelling slower in the device than the surrounding solution. This involved dispensing the entire syringe over approximately 10 seconds.

4.3 Results and Discussion

4.3.1 Interfacial Tension

By measuring interfacial tension with concentration, it is possible to observe the concentration regions where polymer-surfactant complexes are formed based on adsorption at the oil-water interface. The values of T_1 and T_2 can vary with molecular weight and length of the polymer chain, thus it was important to measure the specific characteristics for the system used (369). The interfacial tension for tetradecane in pure water was measured as 48.4 mN/m and tetradecane with 0.5% PVP was measured as 33 mN/m, indicating that PVP molecules are absorbed at the oil-water interface in the absence of surfactant. The literature value for tetradecane in water is often reported to be slightly higher, where a small amount of an autoxidation product may be present. Previous AFM measurements suggest with surfactant systems this is unlikely to impact these force data, unless at very low surfactant concentrations (13, 44, 370).

Figure 4.2 shows the variation of interfacial tension with SDS concentration at the oil-water interface for tetradecane with SDS aqueous solutions with no PVP and 0.5% PVP, respectively. The PVP with SDS curve demonstrates a shape similar to that of other polymer-surfactant complexes; an overall decreasing interfacial tension, with two clear points of discontinuity either side of the CMC of SDS (roughly 8 mM) and a final plateau equivalent to that of the SDS curve at an interfacial tension of 8 mN/m (355). The points of discontinuity for the system are observed at roughly 2.5 mM SDS and 30 mM SDS, encompassing the region at which it is expected that polymer-surfactant complexes are formed and exist on the interface. PVP and SDS have previously been shown by Chari *et al.* using radiotracers to form two-dimensional aggregates similar in structure to those in the bulk phase at the air-water interface (34). Purcell *et al.* (31) furthered the investigation using neutron reflection to show the presence of both PVP and SDS at the interface between T_1 and T_2, demonstrating evidence of a surface interaction between PVP and SDS. Using these data and previous studies on the adsorption at the air-water interface, the concentration range 2.5 – 30 mM SDS was selected for investigating the adhesion between drops using direct force measurements and microfluidics.

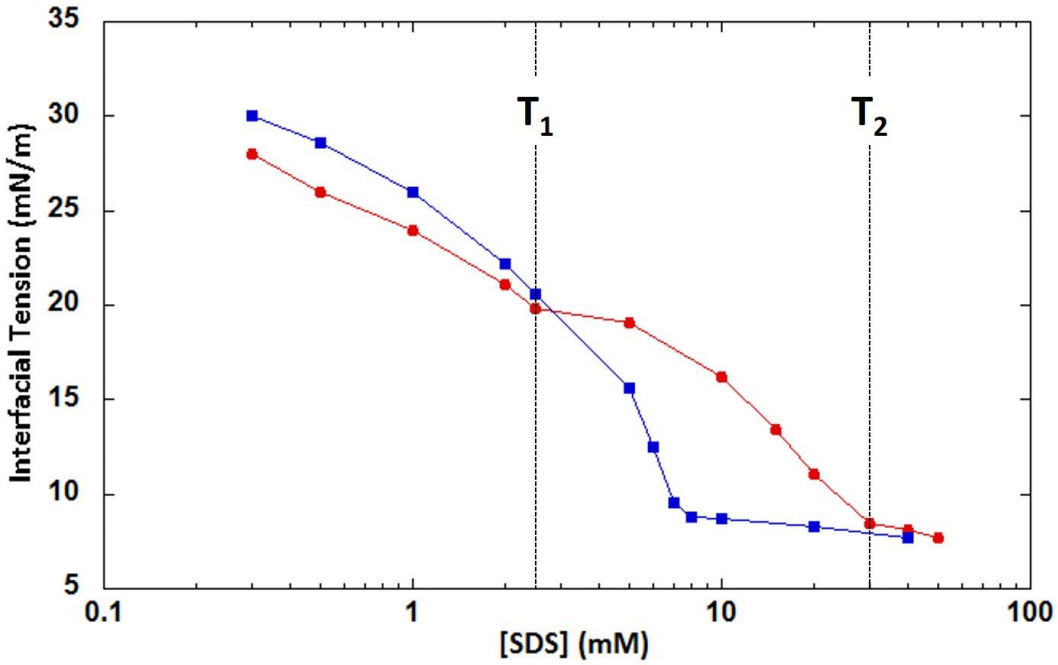

Figure 4.2 The interfacial tension between tetradecane SDS aqueous solutions (blue squares), and interfacial tension between tetradecane SDS aqueous solutions with 0.5% PVP (red circles), across a range of SDS concentrations. The points T_1 and T_2 highlight the concentration region between which PVP/SDS complexes are expected to have formed and be located at the oil-water interface.

4.3.2 Direct Force Measurements

4.3.2.1 Rigid Surfaces

AFM direct force measurements between a silica particle and glass slide in aqueous solution were conducted to quantify the attractive forces observed between oil drops in the presence of the PVP/SDS complex, but in the absence of interfacial deformation. Previous AFM studies between rigid interfaces in the presence of polyelectrolytes have accurately measured depletion forces and successfully fitted osmotic pressure models to the data (60-62, 371, 372).

Hydrophobic and hydrophilic surfaces were studied to determine the effective osmotic pressure for the SDS and PVP polymer-surfactant complexes across a range of SDS concentrations between T_1 and T_2. The AFM force curves measured between two hydrophilic silica surfaces (See A9.3) exhibit increasing repulsion at close separation, consistent with the presence of a steric brush. The presence of a steric force obscures any attractive forces attributed between the surfaces, thus hydrophobically modified surfaces were used.

Force measurements between a hydrophobically modified 5 μm silica particle and glass slide in solutions of 0.5% PVP and SDS concentrations of 2 mM, 10 mM and 30 mM are shown in Figure 4.3A. At 2 mM SDS, below the CAC, the force curve exhibits a repulsive force attributed to electrical double layer repulsion, due to surfactant adsorption to the hydrophobic surfaces.

However, at surfactant concentrations above the CAC an attractive force is observed, attributed to a depletion force where the magnitude of the attractive minima increases with increasing surfactant concentration. As additional surfactant is added to the system the number of surfactants bound to the polymer grows, effectively increasing the number of ions associated with the polymer. As discussed above, by treating the PVP/SDS complex as a pseudo-polyanion, this force behaviour is consistent with polyelectrolyte scaling theory, where the magnitude of the depletion force is primarily dependent on solution ionic strength and the ionic density of the polymer (119).

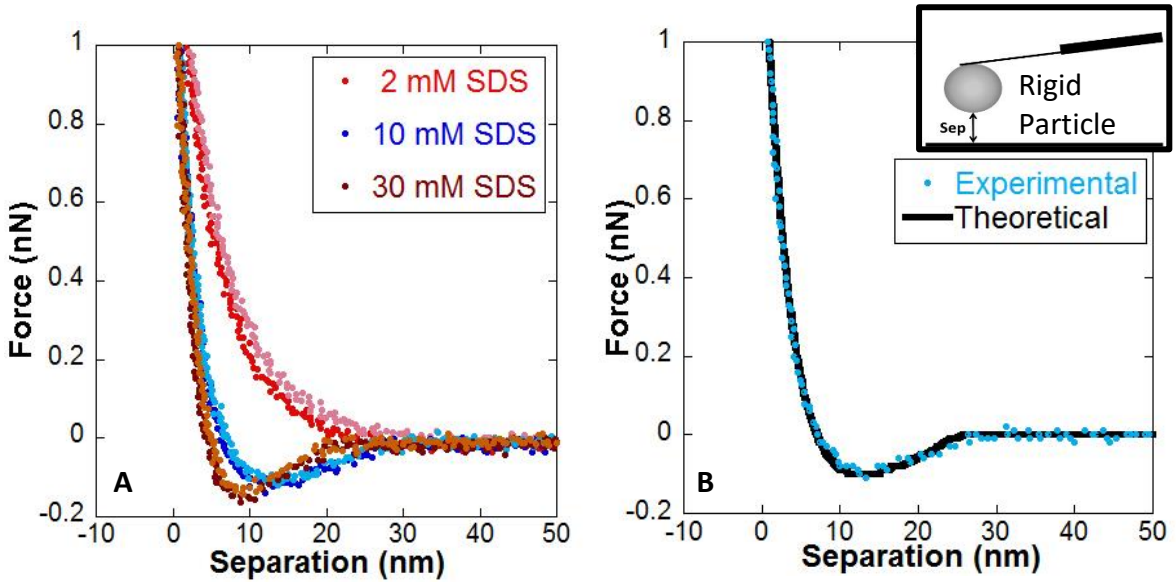

Figure 4.3 (A) The approach and retract AFM force curves between a silica particle and glass slide coated with gold and hydrophobically modified with decanethiol in an aqueous solutions of 0.5% PVP with 2 mM SDS (red), 10 mM SDS (blue) and 30 mM SDS (brown) (B) A comparison between experimental data and the fitted model that describes the interaction force for this geometry in the presence of an EDL and depletion force for the case of an aqueous solution with 0.5% PVP and 10 mM SDS.

The surface force model to describe the EDL and depletion forces (equations 4.1 – 4.3) was fitted to the experimental data to determine the effective osmotic pressures, surface potential and depletion lengths for different SDS concentrations. In this system, there was no added electrolyte, thus the ionic strength was determined from the SDS concentration. Using the aggregation numbers and number of bound micelles per monomer, the dissociation of SDS molecules in bound micelles, free micelles or as free molecules in solution, were calculated via a mass balance in order to determine the ionic strength of the system (See Appendix A9.4 for further details).

As seen in Figure 4.3B, a comparison between the output of the model and experimental data for 10 mM SDS demonstrates the force data is well described as an EDL repulsion and depletion attraction. Based on the calculated ionic strength, the fitted depletion length and osmotic

pressure are reported in Table 4.1 for SDS concentrations of 10 mM, 15 mM, 20 mM and 30 mM of SDS with 0.5% PVP. The depletion length generally decreases with increasing ionic strength. The length scale of the depletion layer is closely related to the characteristic length of the PVP/SDS complex in solution. As the number of SDS molecules increases within the system, the number of bound SDS molecules to the complex increases. This can increase the charge of the complex, but given the discussion of surfactant association above, this results in a weak dependence on concentration. However, the ionic strength also increases with the addition of surfactant, resulting in an increase in the amount of charge screening effects of the bound SDS molecules on the PVP, and thus reducing the effective characteristic length of the PVP/SDS pseudo-polyelectrolyte complex.

The surface potential shows a weak dependence on SDS concentration, which is not surprising given the partial dissociation of the SDS layer on a hydrophobic surface (44, 370). The fitted osmotic pressure is relatively constant within experimental error for 10 & 15 mM SDS concentrations and then increases with SDS concentration at higher concentrations. In addition to fitting the osmotic pressure, by treating the PVP/SDS complex as a pseudo-polyelectrolyte complex or pseudo-polyanion, we can estimate an independent value for osmotic pressure using polyelectrolyte scaling theory defined by (121):

$$\frac{\Pi_{\mathrm{OSM}}}{kT} = \frac{C^2}{4A^2C_s + AC} + \frac{1}{\xi^3} \tag{4.8}$$

where A is the number of monomers per charge, C is the polyelectrolyte monomer concentration and C_s is the concentration of additional electrolyte. The characteristic length ξ is related to the depletion layer thickness, equal to twice its length. Accounting for micelle disassociation, the number of monomers per charge can be calculated from the bound micelle aggregation numbers and number of PVP monomers per micelle. For the concentration range of 10-30 mM the number of monomers per charge was found to vary between 19.5 and 11.6. The concentration of additional electrolyte was determined in the SDS molecule mass balance (Appendix A9.4). Combining these values with the depletion length obtained from the rigid force measurements, enables calculation of the osmotic pressure directly from Eq. 8, providing a comparative value to those determined from the fitted model in Table 4.1. The calculated values show a similar trend but are systemically higher than the fitted model values. The difference between these values is most likely due to polydispersity effects that are not considered in the scaling theory analysis (Eq. 4.8), which specifically assumes a homogeneous system (119). Previous direct force measurements between bubbles or rigid surfaces using both AFM and total internal reflection microscopy measurements (12, 60, 373) have observed a reduction in the measured osmotic pressure due to the polydispersity of the depletant for both charged and neutral depletants. In

these instances, it was found that the larger size fraction of the depletant set the length scale of the depletion length, but the small size fraction of the depletant was not excluded from the gap, leading to a reduction in the osmotic pressure measured via force measures measurement compared to the osmotic pressure calculated based on scaling theory. These data and force model, describing the depletion force between rigid hydrophobic surfaces will be used in the analysis framework that accounts for interfacial deformation for the force data between two oil drops discussed below.

Table 4.1 Summary of the depletion length and osmotic pressure determined by fitting an EDL and depletion model to AFM force curve data between rigid hydrophobic surfaces as well as the Osmotic Pressure calculated via polyelectrolyte scaling theory.

[SDS] (mM)	Ionic Strength (mM)	Calculated Debye Length (nm)	Fitted Surface Potential (mV)	Fitted Depletion Length (nm)	Fitted Osmotic Pressure (Pa)	Osmotic Pressure (Pa) (Scaling Theory)
10	7.2 $\pm$ 0.3	3.6	-15 $\pm$ 2	12.8 $\pm$ 0.9	667 $\pm$ 65	879 $\pm$ 202
15	9.1 $\pm$ 0.7	3.2	-15 $\pm$ 2	11.5 $\pm$ 0.8	572 $\pm$ 51	1017 $\pm$ 285
20	11.7 $\pm$ 0.5	2.8	-15 $\pm$ 2	11.4$\pm$ 0.6	738 $\pm$ 63	1141 $\pm$ 280
30	13.94	2.6	-16 $\pm$ 2	9.7$\pm$ 1.0	1117$\pm$ 109	1397 $\pm$ 75

4.3.2.2 Deformable Surfaces

4.3.2.2.1 Equilibrium

Force curves for the interactions between two tetradecane drops in 0.5 wt% PVP over a range of SDS concentrations are shown in Figure 4.4. To facilitate a qualitative comparison between drop pairs, the force has been normalised by the average drop radius to account for variations in drop size across different measurements. These measurements were performed at piezo drive velocities of 100 nm/s as hydrodynamic effects are expected at higher piezo drive velocities, which is explored further in the following section.

The force curve for the 0.5 wt% PVP and 2 mM SDS solution exhibits a small hysteresis between the approach and retract curves with a small repulsive force at close range attributed to EDL forces. This behaviour is consistent with that observed in a control measurement of 0.5 wt% PVP without SDS and is not attributed to a depletion force from the PVP/SDS complex (Appendix A9.5). When the concentration of SDS is increased to 5 mM, the force behaviour changes to an attractive profile on both approach and retract. At close separation, the attractive region exhibits a small hysteresis consistent with the presence of an attractive surface force, but the drops do not coalesce (221, 344).

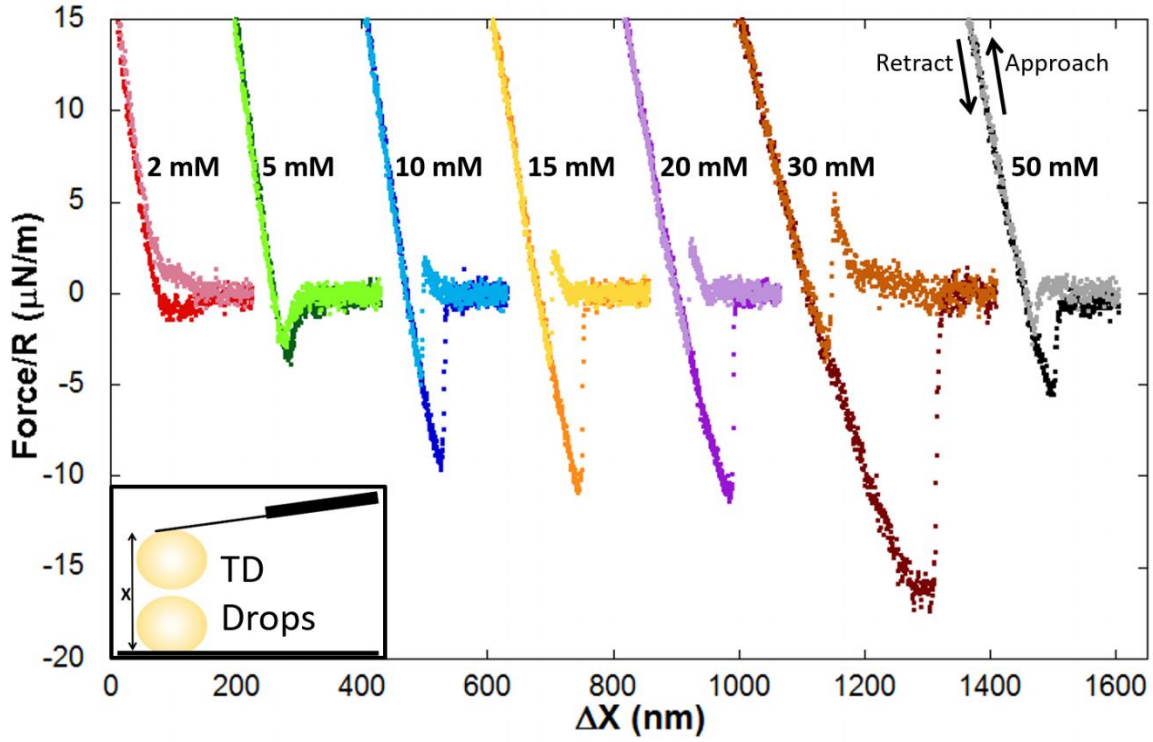

Figure 4.4 The interaction force between two tetradecane drops in aqueous solution measured by AFM normalised by average drop radius versus ΔX in the presence of 0.5% PVP and a range of SDS concentrations. These data are translated on a relative ΔX scale for ease of viewing. The SDS concentration spanned below T_1 at 2 mM SDS (light red approach, dark red retraction), above T_1 at 5 mM SDS (light green approach, dark green retraction), 10 mM SDS (light blue approach, dark blue retraction), 15 mM SDS (yellow approach, orange retraction), 20 mM SDS (light purple approach, dark purple retraction), and 30 mM SDS (light brown approach, dark brown retract) and above T_2 at 50 mM SDS (grey approach, black retract). These curves were taken with a piezo drive velocity of 100 nm/s.

The 10 mM solution exhibits significant hysteresis between approach and retraction without drop coalescence. On approach there is a small but significant repulsion followed by a jump in to an attractive force region. The retraction is defined by a significant attractive force followed by a jump off as the drops move apart without coalescence. The jump in behaviour in attractive force fields from depletion or structural force between drops and bubbles has been observed previously, for polyelectrolytes, micelles, nanoparticles, or microemulsion depletants, and modelled in some detail (223, 226). Thus, the presence of the jumps on approach and retract and the increasing hysteresis is attributed to the drop deformation caused by the equilibrium disjoining pressure. The 15 to 30 mM SDS solutions exhibit force behaviour very similar to the 10 mM case. However, there are two significant changes observed in the force profiles with increasing surfactant concentration. Firstly, there is an increase in the magnitude of the repulsion on approach, which is noticeably larger at a concentration of 30 mM. Moreover, there is a gradual increase in the attractive force seen in the retract curve until a large jump in magnitude at 30 mM

SDS. At 50mM there is no longer any evidence of a repulsive force on approach, demonstrating behaviour more similar to that seen at 5 mM SDS. A large reduction in the attractive force compared to the 10-30 mM concentrations is also measured.

Qualitatively, the changes in the attractive force are attributed to changes in the PVP/SDS complex mediating a depletion force, whereas the changes in the repulsive force are associated with the adsorption and then desorption of the PVP/SDS complex from the oil-water interface with increasing SDS concentration. As discussed above, at 2 mM SDS, the repulsive force is attributed to the presence of an EDL force, similar to the control measurements. From 5 mM to 30 mM, depletion interactions are present and increase in size with added surfactant. Similar to the rigid force measurements at these concentrations, SDS and PVP aggregate in the bulk resulting in a complex that effectively acts as a pseudo-polyelectrolyte leading to a depletion force between the drops. The increase in depletion force is due to the accumulation of adsorbed SDS molecules to the PVP, resulting in an increasing counter ion density of the pseudo-polyelectrolyte. At 50 mM, depletion is still prevalent although it is greatly reduced in magnitude. Despite the fact that SDS is still adsorbed to the PVP, the polymer is now expected to be completely saturated such that any additional SDS will act effectively as added electrolyte, increasing the ionic strength and ultimately reducing the osmotic pressure via screening of the repulsive SDS/PVP complex intra- and inter-actions, and thus the depletion force. To further support this analysis and explain the origins of the hysteresis in the approach and retract force curves, a comparison of these force data to the SRLY model is presented below.

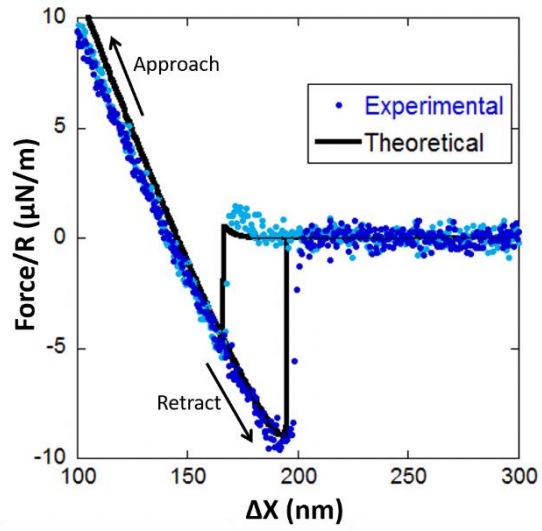

Figure 4.5 Force divided by average drop radius versus ΔX for the interaction between two tetradecane drops comparing experimental data and theoretical output for 0.5 wt% PVP with 10 mM SDS.

These AFM force measurements were analysed using the SRYL model outlined above, assuming no significant hydrodynamic drainage effects, but accounting for the presence of EDL and depletion forces, as well as the deformation of the interface, in order to determine the separation between the drops. The osmotic pressure, depletion length, ionic strength and Debye length were defined using the values determined from the rigid force fit measurements such that the only adjustable parameter in the model was the surface potential of the drops. Figure 4.5 shows a comparison of the modelling results to the experimental results for an SDS concentration of 10mM. The agreement between the model and the experiment supports the use of the depletion parameters and ionic strength calculations determined in the rigid measurements. Independently measured values for the drop radii, interfacial tension, drop-substrate and drop-cantilever contact angles, and cantilever spring constant were also used. A list of parameters used for the analysis in Figure 4.5 and their associated uncertainties are given in Appendix A9.6.

For the 10 mM data in Figure 4.5, there is an under prediction in the model of the repulsion on approach, suggesting that the EDL forces are not sufficient to describe the entire repulsive force. The EDL force does not account for a contribution from a steric force due to adsorbed PVP/SDS complex. Based on the interfacial tension measurements in Figure 4.2, and previous neutron scattering of the PVP/SDS complexes adsorbed at an air water interface (31), adsorption of the PVP/SDS complex is expected at the drop interface. The steady growth of repulsion in the approach force curves for SDS concentrations from 10 to 30 mM in Figure 4.4 is attributed to the increase of SDS within the complex. Similar to the bulk behaviour, as the amount of SDS increases in the complex, the number of bound micelles and the aggregation number of these micelles grows, creating more intra- and inter-complex repulsion within the adsorbed complex layer. This leads to the layer swelling, resulting in an electro-steric repulsion between the drops at close separations as seen in Figure 4.5. Thus, the details that would need to be captured to include an electro-steric contribution in the surface forces, such as the potential for asymmetric binding of SDS molecules to the bound polymer and its associated implications on differing ion binding and micelle disassociation, go well beyond a simple steric model and are not included in the implementation of the SRYL model used here. At 50 mM there is no longer any evidence of a repulsive force. At this surfactant concentration the solution is above T_2, where the polymer is completely saturated with surfactant, and it is expected that the complex has desorbed from the interface. The attractive well observed during retract is well described by the model (Figure 4.5). The magnitude of the adhesion corresponds to attractive depletion but is also affected by the deformation of the drops at close separation. Previous studies of depletion and structural forces between drops using simpler depletants have shown that the interfacial deformation makes the

probe more sensitive to these attractive interactions than a rigid sphere of the same radius (63, 225-227). In addition, the interfacial deformation is the origin of the large hysteresis between the approach and retract, as the drops flatten by the point of maximum force, thus there is a larger interaction area when the drops are separated and sampling the attractive depletion force. At 30 mM SDS, there is a significant increase in both the electro-steric repulsion and the adhesion due to the onset of desorption and swelling of the complex from the interface (130, 374).

4.3.2.2.2 Dynamic

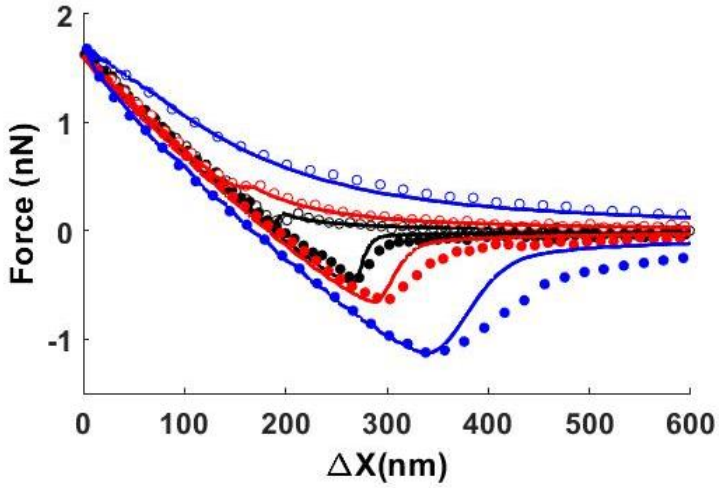

Figure 4.6 Comparison of the force vs displacement between two tetradecane drops in 10 mM of SDS and 0.5% PVP at velocities of (black) 1 μm/s, (red) 3 μm/s and (blue) 10 μm/s. The graph shows both the experimental results (dots) and the theoretical prediction of the Stokes-Reynolds-Young-Laplace model (lines). For the experimental results, the approach curve is shown as open dots and the retract curve as filled dots.

A comparison of the dynamic interactions between two tetradecane drops in 10 mM SDS and 0.5 wt% PVP over nominal velocities of 1-10 μm and a maximum force of approximately 2 nN is shown in Figure 4.6. The increase in the velocity dependent hysteresis is attributed to hydrodynamic drainage effects. This is consistent with previous studies using drop radii between 10 and 100 μm, where strong coupling between hydrodynamic and surface force interactions is observed (42, 44, 186). Similar to earlier studies of drops/bubbles in the presence of depletion and/or structural forces -- with either surfactants or polyelectrolytes (12, 63, 225) -- it is clear that as the velocity increases, the depletion behaviour apparent in the equilibrium measurements shown in Figure 4.4 is overwhelmed by hydrodynamic effects. The increasing effect of hydrodynamic drainage is evident in the increasing hysteresis, which eventually softens the well-defined sharp features from the repulsion and attraction to a smooth transition as a result of the large hydrodynamic pressure within the film. The current work differs to previous studies, where we have used the SRYL model to describe these force data, shown in Figure 4.6, using the osmotic

pressure, surface potential and characteristic depletion length extracted from fitting the equilibrium measurements given in Table 4.1 or in the Appendix, Table A9.3. Noticeably, there is a strong agreement between the model and the experimental results over the range of velocities. However, although the approach curve is tracked well by the model, there is a visible under-prediction of the attractive force on the retract curve. A study by Manor *et al.* explored the effects of film drainage through a steric polymer brush at the interface between two decane drops (54). They highlighted that the film drainage through an adsorbed polymer layer should not be treated as a simple interface, showing through continuum modelling that the film drainage between drops is sensitive to flow through the brush. Thus, the deviation between the model and measurement in Figure 4.6 is consistent with the presence of a steric layer, where a portion of the hydrodynamic drainage occurs within the absorbed PS complex layer on the drops. The dynamic results highlight the importance of controlling hydrodynamic drainage effects when measuring the interfacial forces between drops in polymer-surfactant systems. Thus, in drop collisions, to accurately observe the equilibrium surface forces, such as adhesion between drops in a microfluidic device it is therefore necessary to mitigate hydrodynamic interference.

4.3.3 Microfluidics: Equilibrium Interactions

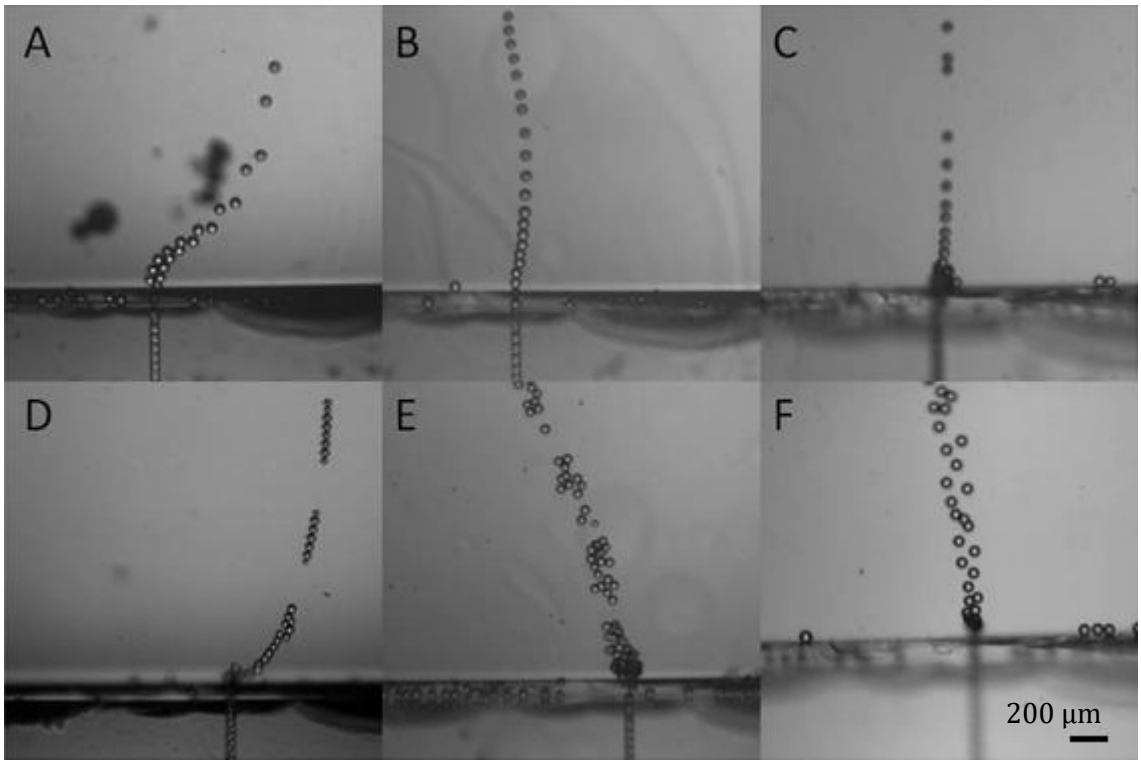

Figure 4.7 Representative images of the breakup of tetradecane drop chains at the exit of the microfluidic device due to external flow. Solutions used are a) 10 mM SDS, b) 2 mM SDS and 0.5% PVP, c) 5 mM SDS and 0.5% PVP, d) 10 mM SDS and 0.5% PVP, e) 15 mM SDS and 0.5% PVP, and f) 20 mM SDS and 0.5% PVP. Flowrates were set on the fluid pumps as Q_C = 30 µL/hr, Q_D = 10 µL/hr, and Q_S = 11 µL/hr, resulting in Q_O =18 µL/hr,

giving drop with an equivalent spherical radius of ~28 μm and a drop velocity of ~2 mm/s.

A microfluidic device was developed, schematically shown in Figure 4.1 and in more detail in Appendix A9.2, to probe the attractive or adhesive interactions between drops. The goal of this work was to form chain-like structures of drops held together via equilibrium surfaces forces and then exit a microfluidic channel into a bulk, sweeping flow. In any drop based microfluidic device where drop collisions occur, hydrodynamic drainage forces occur, and as discussed above in the study by Anna and co-workers (29), often dictate the outcomes of the collisions masking surface force effects. As shown in Figure 4.6, even a relative velocity difference of 5 μm/s is sufficient for hydrodynamic drainage effects to mask the depletion forces encountered from the PVP/SDS complex. We developed a device where the drops come into close contact via the introduction of side channels, similar to those used in drop coalescence studies by Gunes et al. (27), enabling the removal of excess continuous phase, driving the drops into close separation with the same relative velocity, but without coalescence. The drops continue in this geometry moving through the device and exit the device where the persistence of the drop chain is expected to correlate with the attractive interactions between the drops.

The formation of drop chains in solutions covering a range of SDS concentrations in the absence and presence of 0.5% w/w PVP was studied using the microfluidic device, where frames from movies of the operation of the device are shown in Figure 4.7. A control measurement for 10 mM SDS in Figure 4.7A shows the drops momentarily bunch near the exit of the microfluidic device before breaking apart into individual drops downstream. This is understandable as a small region near the microfluidic device is likely protected from the external flow due to the thickness of the device allowing the drops to bunch up in this area and push against each other. Once the drops move past this area the external flow is much stronger and the drops break apart due to the lack of any adhesive or strong attractive forces.

For the 2 mM SDS 0.5% w/w PVP solution shown in Figure 4.7B the drops maintain contact upon exiting the microfluidic device and form a single line of touching drops in the direction of fluid flow unlike the control measurement that separated immediately. Once the drops move into the region of significant external fluid velocity they break apart immediately into individual drops without exception. This is expected from the force curves as no strong attractive forces were observed for this SDS concentration. The 5 mM SDS 0.5% w/w PVP solution shown in Figure 4.7C behaves in a similar fashion, where very occasionally double or triple drop chains persist moving into the external flow field. This is attributed to a possible drop adhesion consistent with the increasing attraction observed in the AFM data at this concentration. It is important to note that in the region outside of the device, forces from both drag due to fluid motion and buoyancy act on

the drops opposing the adhesive force between them. The approximate nature of the sweeping flow is difficult to quantify, but the buoyancy force, based on the drop radii is of the order of 1 nN.

The 10 mM SDS 0.5% w/w PVP solution shown in Figure 4.7D demonstrates significantly more drop aggregation. In this solution the drops would exit the microfluidic device and maintain contact as they moved into the stronger flow field. Unlike the previous solutions the drops moved significantly farther into bulk solution with neighbouring drops moving over each other while maintaining contact to align in the flow. The drops would then break off into stable groups of roughly between 6 and 10 drops depending on the flowrate. This implies that the adhesive forces between each drop are strong enough such that the drag and buoyancy force on each drop is not enough to break the chain into individual drops.

The 15 mM SDS 0.5% w/w PVP solution shown in Figure 4.7E exhibits behaviour that is less adhesive than the 10 mM SDS solution but still demonstrates attractive forces between drops. The drops do not form the desired chains, instead forming loose clumps at the exit of the device that break apart into individual drops after a short time. The 20 mM SDS 0.5% w/w PVP solution shown in Figure 4.7F demonstrates no signs of adhesive forces between the drops. The drops in this solution break apart very quickly upon leaving the microfluidic device and spread out into two alternating streams of drops.

Each solution was run within the device a number of times with the rate that the added solution was dispensed intentionally varied to try and ensure that the drops experienced a variety of different flow fields so that the exact conditions needed to just break the drops apart could be observed. If the flow was too gentle the drops would pool near the channel exit but if the flow was too strong the drops would break apart rapidly. The presented results are indicative of the strongest aggregation between drops that was observed for each solution.

An important factor to consider regarding the adhesive forces between the drops is the length of time that the drop spends within the microfluidic channel. The observation of adhesive forces is dependent on the adsorption of the PVP/SDS complex onto the drop interface. This is influenced by both drop lifetime and surfactant concentration. Depending on the flow rates, the time between drop generation and collision will vary but is normally on the scale of seconds. Post drop collision, the time the drops maintain close proximity in the device, is again on the scale of seconds (up to 10 seconds). Describing the transport and adsorption process in this device quantitatively will be a focus of subsequent work, however we note here that the adsorption time scales within the channel are expected to be faster than bulk measurements such as dynamic pendant drop tensiometry (375).

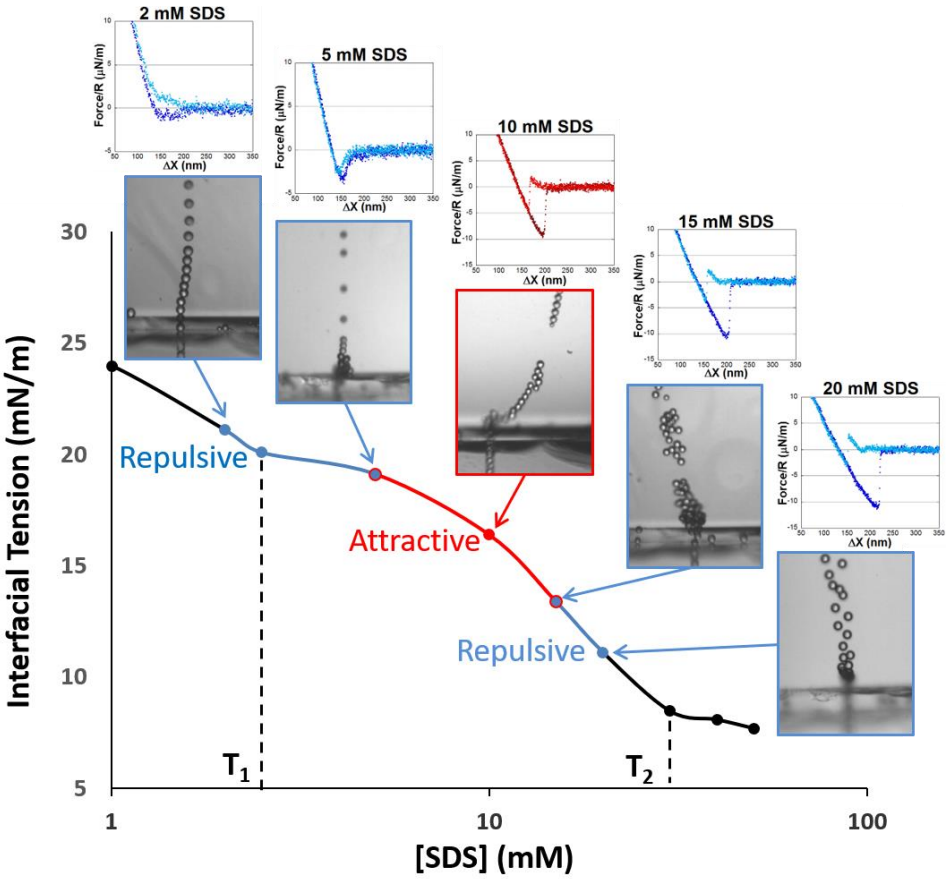

Figure 4.8 A diagram comparing the results from the interfacial tension measurements (defining the T_1 and T_2 region), microfluidic observations and drop-drop AFM measurements. The results highlighted in blue illustrate the data that returned an overall repulsive behaviour in the microfluidic observations as the drops in the microfluidic device did not sample the forces observed in the retract curve, while the red demonstrates the data that returned an overall attractive behaviour where the drops did sample the attraction observed in the retract curve.

4.3.4 Linking AFM and Microfluidic Observations

Figure 4.8 shows an overview of the microfluidic observations and direct force measurements with respect to their corresponding concentration on the interfacial tension isotherm. Our original hypothesis was that drop adhesion would occur between the T_1 and T_2 concentrations (at 2.5 mM and 30 mM respectively). In the AFM force measurements, large adhesive wells were observed between these concentrations. However, drop chaining was only observed at 10 mM SDS in the microfluidic experiments with some drop adhesion observed at 5 mM and 15 mM. In contrast to the AFM measurements, the microfluidic observations give insight into the stability of the drop chains. Upon exiting the channel into bulk solution, the stability of the drop chains is governed by a balance between drag, buoyancy, and the adhesive forces between the drops. If the adhesive forces between the drops are too weak, the drop chains break up upon exiting the channel. Further, for surfactant concentrations experiencing sufficient attractive forces, drops

will detach from the drop chain until the external force acting on the chain is low enough such that a stable length is reached.

The comparison of the AFM results to the microfluidics also demonstrates that the microfluidics is primarily path dependent, such that the attractive forces at close separation can only be experienced when the Laplace pressure is high enough to overcome the repulsive barrier encountered as the drops approach each other. In the microfluidic device drops move together due to the removal of continuous phase, and as a consequence the collision is not as controlled as a collision measured using AFM, where one drop is driven towards another by a prescribed distance and velocity. Thus, it is reasonable to expect that a drop collision in the microfluidic device may not be of sufficient force to overcome the repulsive barrier upon approach. Berry and Dagastine (42) defined a drop equilibrium stability criterion such that if the Laplace pressure is less than the repulsive force, the film between the drops will not drain enough to reach attractive forces capable of inducing coalescence or stable adhesion. It is therefore likely that as the steric repulsion gets bigger at 20 mM, despite an obviously larger attraction present in the force curve, the necessary force of collision required to overcome repulsion as the drops approach each other is not achieved and thus drop chains are not observed. Therefore, the longest stable drop chain correlates with the SDS concentrations in the AFM measurements (~5 - 15 mM) when the repulsive force on approach is low enough, and the attractive force at close separation is high enough, to keep the drops in adhesive contact. This suggests that the droplet interactions in the microfluidic channel can identify at what SDS concentrations the attractive force dominates for that specific drop size. Thus, for this technique to be broadly used to probe surface forces between drops, it is necessary to produce drops with a range of sizes in order to sample a range of Laplace pressures. Smaller drops with higher Laplace pressures can potentially push through the repulsive barrier, move closer together and thus be able to encounter the attractive forces also present at higher concentrations.

This study demonstrates the clear potential for using microfluidic devices to investigate surface forces, specifically net adhesive interactions. Clearly there are many areas that could benefit from greater control and more accurate measurements; in particular the flowrate of external fluid near the observation region. The variation in internal flow rates from the fluid syringe pumps also limited the ability to model the drop breakup or adsorption kinetics in this instance. An additional concern is understanding the impact of wall effects on the observed behaviour. It is important to note in this work, and the work by Shen *et al.*, where they formed drop aggregates for photo-polymerisation, the structure was formed and persisted outside of a confined channel (242). In Shen's work, a large expansion with a controlled co-flow, a desirable attribute in our next design, was used. In our work, the drop chains were observed in a gentle co-flow region completely

outside of the device. Effects from internal circulation of the drop are often minimized by high coverage of surface-active materials, low flow rates and when the continuous phase viscosity is much less than the drop phase, as it is in this instance (376).

4.4 Conclusion

For polymer-surfactant (PS) complexes and poly(vinylpyrrolidone) (PVP)/ sodium dodecylsulphate (SDS) in particular, there is a large understanding of bulk behaviour in terms of surfactant binding to the polymer, micelle dissociation, the size of the PS complex, phase separation boundaries and the solution viscosity. There are also substantial studies on interfacial properties including surface and interfacial tension, however far fewer measures of the adsorption and structure of the complex at an interface. For the PVP/SDS systems, characterisation was made possible through years of study using scattering methods in the bulk and the interface, calorimetric studies of phase behaviour and binding, fluorescence solubilisation studies, and surface and interfacial tension measurements (8, 31, 32, 34, 35, 100-103, 112, 354, 363, 364, 366, 367). These studies are fundamental in understanding how the solution bulk and interfacial behaviours link to functions this PS complex might enable in a colloid suspension or complex fluid.

For the case of a PS complex, one pathway to link the function of a colloidal fluid to its structure is through the surface forces between colloids, which are highly dependent on the bulk and interfacial properties of the PS complex. Yet, in comparison to bulk and interfacial characterisation, there is a paucity of data in surface force measurements. This is often due to the complexity and time required for surface force measurements, limiting the concentrations and solution conditions practical to observe (359). In this study, accessing attractive surface forces in a microfluidic device takes the first step towards developing a surface force platform capable of exploring solution conditions on a similar scale to other characterisation methods. At the same time, this study, on what is a smaller subset of concentrations has already shown insight into the force behaviour, not accessible or likely to extrapolate from bulk and interfacial characterisation. For example, the concentration at which the strongest adhesive interactions between drops were observed have a complicated interplay between drop deformation, the PS complex adsorption and surfactant saturation of the complex in a way that cannot be predicted from interfacial adsorption and bulk characterisation measurements.

Through interfacial tension measurements, direct force measurements and microfluidic observations we have provided a detailed investigation into drop-drop interactions in a sodium dodecylsulphate (SDS) and poly(vinylpyrrolidone) (PVP) solution. Rigid force measurements in 0.5% w/w PVP and SDS concentrations between 2.5 mM and 30 mM, showed via a quantitative

model that depletion and electrical double layer forces dominate the interactions between two hydrophobic surfaces. Force measurements between two deformable oil drops using the same systems displayed similar depletion behaviour. A model used to describe deformable systems, also accounting for depletion and EDL forces, used the depletion length and osmotic pressure fit from the rigid surface analysis and showed reasonable agreement with the force data. A small under prediction by the model of the repulsive force on the approach curve suggests the existence of an additional steric force from the presence of adsorbed PS complexes at the interface. At velocities above 500 nm/s, dynamic forces, caused by film drainage between the drops, dominated the force data, such that it was no longer possible to observe the depletion or EDL force features in the measurements. A microfluidic device that minimized the influence of hydrodynamic drainage effects between drops was developed and shown to create short drop chains held together by surface forces, independently demonstrating the existence of attractive forces between drops in the PVP/SDS systems. Of the concentrations tested, the 10 mM SDS concentration successfully showed significant drop adhesion and chain formation.

The evidence presented here provides a detailed insight into the force behaviour between drops and how the PVP/SDS complex in the bulk and at the interface can mediate the forces between both rigid and deformable interfaces. This conclusion supports the findings of both Chari and Purcell (31, 34), however also provides greater insight into the characterisation of SDS and PVP between and on oil-water interfaces. Correlating the AFM and microfluidic results suggest that attractive forces observed in the AFM lead to the formation of drop chains when the repulsive force on approach is low enough to allow the drops to move into close separation, and when the attractive force is sufficient to hold the drops in a secondary attractive minimum. Increasing the Laplace pressure by generating smaller drops could allow for a wider range of adhesion to be observed, potentially enabling the development of a matrix of conditions for which adhesive emulsions can be formed across different system concentrations and drop sizes. Similar to developments in high throughput rheology using microfluidic devices, further developing this device could provide a novel technique for screening through a range of systems with ease, aiding formulation development where adhesive emulsions are important in areas such as pharmaceuticals, coatings and personal care products (21).

Acknowledgements

This work was performed in part at the Melbourne Centre for Nanofabrication (MCN) in the Victorian Node of the Australian National Fabrication Facility (ANFF). This work was performed in part at the South Australian node of the Australian National Fabrication Facility, a company established under the National Collaborative Research Infrastructure Strategy to provide nano and micro-fabrication facilities for Australia's researchers. This work was performed in part in the Materials Characterisation and Fabrication Platform (MCFP) at the University of Melbourne. We thank the ARC for funding and the PFPC for providing infrastructure support.

Chapter 5: Microfluidic Measurements of Interfacial Tension

5.1 Introduction

The interfacial tension between two immiscible fluids is related to minimisation of the surface free energy and provides important information on the interface's stability, morphology and structure. In the presence of surface-active components this physico-chemical property can be measured dynamically to give insight into their adsorption kinetics and mass transfer mechanisms. By extension it is also therefore possible to deduce the surface chemistry at the interface. Under flow the activity of molecules such as polymers and surfactants can be predicted to behave differently compared to static systems (131). From the previous chapter, the adhesive or attractive interactions between the drops provide strong evidence that the oil drops are coated in PS complexes. Yet, this lacks an independent measure of the surface coverage or adsorption. More critical, the hypothesis made on the surface chemistry of the drops within the microfluidic device was primarily drawn from AFM measurements under static conditions. The adsorption dynamics and relevant time scales that occur within the microfluidic device are obviously different than the AFM environment. Therefore, to corroborate if the surface chemistry of the drops under flow reach a similar state as the AFM measurements by the time they reach the final stage of the microfluidic device in the previous chapter, it is important to analyse the chemistry at the drops interface at similar flow conditions as the previous chapter.

Microfluidics have been used to investigate the interfacial properties of drops in flow using a range of methods. These include designs focused on the relationship between drop size, two-phase flow ratio and capillary number at drop break-up. Work by Luo's group benchmarked the theory behind this via a balance between shear forces and interfacial tension forces at drop formation, utilizing a range of channel geometries and solution conditions to enforce the measurements (18, 324-326). Schroen *et al*. have applied the same theory to Y-Junction geometries, however they instead fit an empirical relationship to calibration data to relate drop area to the capillary number. They claim this method allows measurement at drop formation times of sub-millisecond timescales, compared to the millisecond range offered by other techniques (17, 328). These measurements are performed during drop formation, which prevents the collection of dynamic data over longer timescales. An alternative method established by Hudson *et al*. relies on drop deformation due to the introduction of channel contractions to extract the interfacial tension of drops. The technique tracks the deformation and time scale of recovery of a drop in an extensional flow field as a function of its displacement along the channel to extract a theoretically derived parameter of the drop, which can be used to regress its interfacial tension (329). It has been benchmarked against a range of systems with varying interfacial tensions and viscosities (329), as well as multi-component mixtures with adjustable compositions (16, 330). Lee *et al*. adapted the method to incorporate localised temperature

control such that temperature dependent interfacial tensions could also be measured (331). Another variation developed by Brosseau *et al*. works on a similar principle, where the maximum deformation of a drop hydrodynamically forced into an expansion is empirically modelled as a function of drop velocity and radius. By introducing a series of expansions along the channels, they used this method to study surfactant adsorption kinetics (15).

In this chapter the interfacial tension of drops formed in a microfluidic device from SDS and PVP solutions is measured to characterise their surface chemistry under flow. The technique described by *Hudson et al*. has been adapted, where a series of five contractions has been introduced along a straight channel at specific separation distances to obtain dynamic measurements over time scales relevant to the drop chaining experiments. Unlike the conditions previously investigated using this approach, the solutions in this study have low viscosities and to our knowledge are the first example of a two-component surface active system. This is relevant as the measurable value of interfacial tension is dependent on the viscosity and drop radius. Additionally, the value of the capillary number plays a crucial role in determining the extent of quantifiable deformation, therefore requiring a larger velocity to compensate for reduced fluid viscosities.

5.2 Methods

5.2.1 Design and Operation

The schematic diagram in Figure 5.1 highlights where the drops are generated, introduced to the enlarged main channel and deformed. Drops were generated using the same block-and-break geometry described in the previous chapter to produce drops of equivalent sizes (Figure 5.1A). This geometry produces drops with consistent sizes, however due to the narrow channel and high friction its size is only partially set by the channel geometry as seen in Figure A9.7 in the appendix (377). When measuring the drop's deformation, it is important that the drops are free from hydrodynamic interactions and interference from the channel walls that could alter their deformation and relaxation behaviour. Therefore, after forming, the drops were introduced to a larger channel for measurements to take place. Increasing the channel width from 20 to 350 μm causes a large decrease in drop velocity. Consequently, to avoid drop collisions two symmetric streams were introduced at a 30° angle either side of the primary channel to help accelerate the drops (Figure 5.1B). Five channel contractions were placed sequentially along the main channel in order to induce extensional flow and deformation in the drops. The contraction width was set to 116 μm, which is around one third of the main channels, and tapered or enlarged at a 110° angle to induce rapid changes in the flow conditions (Figure 5.1C). The spacing between contractions was gradually increased, ranging from 900 – 13500 μm in length, with associated timescales specific to the experiment's flowrates.

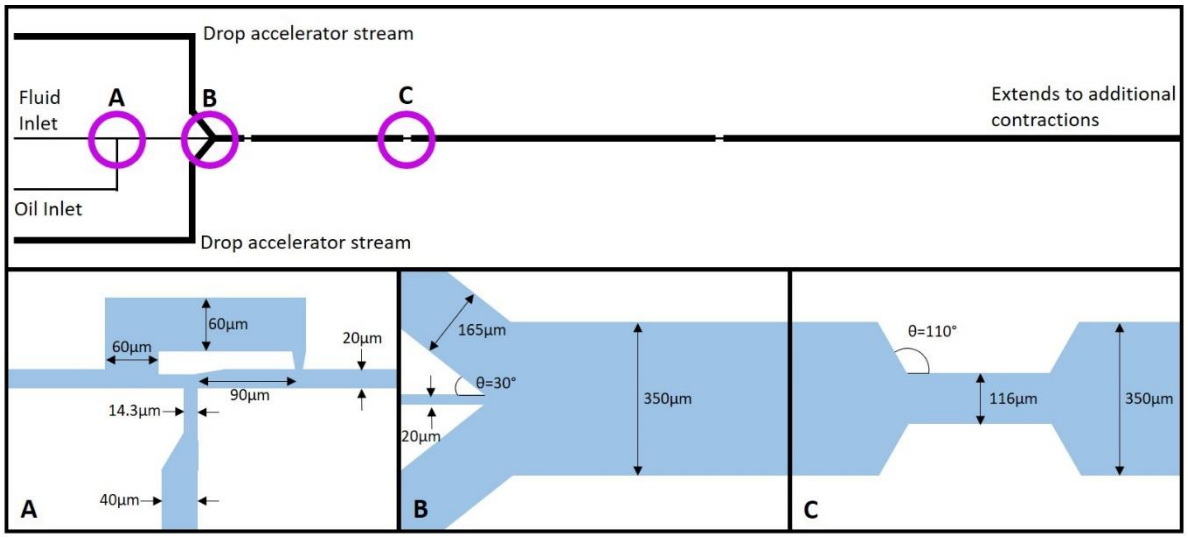

Figure 5.1 Schematic diagram of the microfluidic design used for measuring the interfacial tension of drops in flow showing an overview of the device and specific details of the channels geometries at the (A) block-and-break drop generation, (B) expansion into the main channel, and (C) channel contraction were drop deformation is observed.

The general experimental set-up and operation of the device is covered in detail in Chapter 3 of this thesis. Due to the low viscosities that change with the SDS concentration of the solutions tested, the flowrates were different for each of the concentrations and ranged from 4 – 20 ml/hr, which corresponds to velocities of 55 – 820 mm/s. Flowrates were increased to achieve deformation in low viscosity solutions but reduced at higher viscosities to alleviate the increased pressure as a result of the larger viscous forces. Two different cameras were used to capture the deformation of the drops depending on the specified flowrate. For flowrates in the main channel of 4.5 ml/hr or less a CMOS camera (Basler Ace acA720-520um, BASLER) provided ideal acquisition conditions. The camera offered a high pixel resolution of 0.647 px/µm and at lower flowrates a high enough frame rate (2469 fps) to capture enough observations per drop along the observation window required to produce sufficient clarity and detail for data analysis. However, at higher flow rates the acquisition rate was no longer acceptable and image integration times were reduced such that the drops appeared to be blurred when captured. Therefore, an Ultrahigh-speed camera (Phantom V1212, Vision Research) was used to capture drop deformation at flowrates above 4.5 ml/hr. The Phantom increased the frame rate capacity by four times to 10000 fps, allowing larger drop velocities to be investigated. This permitted the very low viscosity solutions to be tested and the potential for larger deformation in the higher viscosity systems for smoother analysis. However, a reduced resolution of 0.267 px/µm lowered the accuracy of capturing the drops interface which neared the smallest accessible resolution in the image processing capabilities. To reduce/prevent blurring of the drops, exposure times were set to the

smallest value possible (30 μs for the Basler and 1 μs for the Phantom) which were optimised as a trade-off between the illuminating intensity and the cameras specifications. Images were captured with the contraction of interest centred in the middle of the frame, allowing the drop deformation entering and exiting the contraction to be observed.

5.2.2 Image Processing and Data Analysis

An image processing script was compiled in MATLAB to extract the drop shape and position along the channel from the images. The background was estimated using a morphological dilation on an image stack of around 2000 images, with a structuring element oriented along the frame dimension. After thresholding the image using Otsu's method (378) the drops are identified from the binary image, where entities below a specified pixel size are removed as noise. A bounding box was then placed around each drop to aide edge association for the pixels comprising the interface. Due to the blocky resolution of the drops and large pixel sizes, edge detection using intensity gradients rather than pixel-level image morphology was used. Pixel-level approaches for edge finding such as derivative, zero-crossing and local maxima of intensity techniques provide similarly low-resolution results as they rely on drop-pixel morphology (379, 380). There are a variety of sub-pixel level edge detection approaches that instead focus on edge finding which can be used to avoid this. Direct curve-fitting, where a curve is fit to a point cloud, is simple to perform however is sensitive to outliers and noise (381, 382). Reconstructive techniques use a Gaussian function to model the vertical or horizontal gradient profile at the edge to find the peak or intensity maxima to identify it (383). However, despite being less sensitive to noise compared to other gradient based methods, it can be computationally expensive to perform. Moment-based methods look at a range of geometric moments to extract the edge location (384). While many of these use an intensity step function to determine the moments relationship to the edge location, Christian showed that using a ramp function and Zernike moments reduces the effect of noise and is the most accurate technique for detecting isolated edges (385). For a more robust fitting technique capable of highly accurate edge extraction irrelevant of noise, blurred edges, contrast areas or proximity of edges, Trujillo-Pino *et al*. produced a method derived from the partial area effect (PAE) (386). It is based on the observation that since light emanating from each side of an edge will truly subtend only a specific fraction of an edge pixel, the intensity observed at that pixel site logically must be a function of the patrial areas that are subtended. It is thereby able to locally approximate edges with second-order curves, and produce useful estimates on the local edge normal, curvature and intensity gradients. Christian acknowledged the accuracy of this method, citing it as the best performing technique of the pre-existing methods tested in the study (385). Thus, the PAE method described by Trujillo-Pino *et al*. was implemented to extract the drop edges.

As seen in Figure 5.2, the drops edge is a relatively thick black area, therefore to avoid speculating the location of the edge, an average contour (red outline in Figure 5.2) was extracted from a fitted inner and outer cusp (blue outlines in Figure 5.2). The averaged contour is smoothed using local regression lines to obtain the best estimate of the cusp's centreline. Discussion on the appropriate contour for data analysis is discussed further in the following section. Assuming a global symmetry line, a minimum bounding box orthogonal to the global coordinate axis, as seen in Figure 5.2, was fit to each drop to extract the midpoint and major/minor axis. These parameters were then used to assist computation of the volume of the drop by mirroring one half of the drops edge across the centreline to obtain a solid of revolution whose volume was computed using a disc integration method. The equivalent sphere radius of the drop is calculated directly from the computed volume.

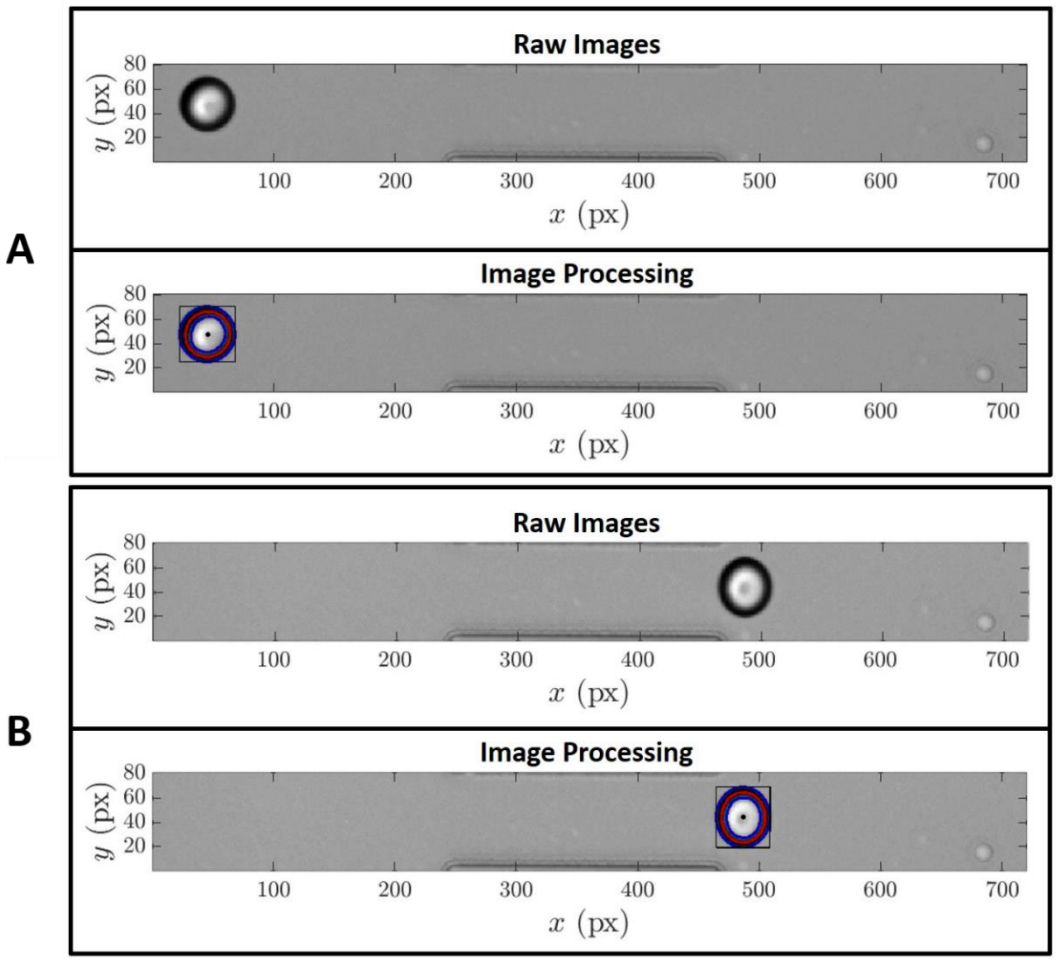

Figure 5.2 Example of processed images showing drops in a (A) relaxed and (B) deformed state. A raw image (Top) and processed image (Bottom) with the centre point, minimum bounding box and inner, outer and average contours is shown for each condition.

Work performed by Taylor on the deformation of an isolated drop in an extensional flow field, experimentally and theoretically established the characteristic dynamics of a dispersed phase from the viscous forces associated with the surrounding continuous phase (387, 388). Rallison extended this theory to apply to small viscous drops and bubbles allowing a variety of systems to be defined by the model (389). Assuming a low Reynolds number, the time dependant deformation of a spherical drop in extensional flow is defined as:

$$\frac{\partial D}{\partial t} = \frac{5}{2\hat{\mu}+3}\dot{\varepsilon} - \gamma\frac{D}{\alpha\mu_c a_0} \tag{5.1}$$

where D describes the deformation as the difference between the major and minor radii divided by their sum,

$$D = \frac{a-b}{a+b} \tag{5.2}$$

t is time, γ is the interfacial tension, a_0 is the equilibrium drop radius, $\hat{\mu}$ is the relative viscosity between the dispersed phase (μ_d) and continuous phase (μ_c), and α is the equivalent viscosity described by:

$$\alpha = \frac{(2\hat{\mu}+3)(19\hat{\mu}+16)}{40(\hat{\mu}+1)} \tag{5.3}$$

For non-instantaneous deformation, where the accelerating flow rapidly increases or decreases, the extension rate of the surrounding fluid ($\dot{\varepsilon}$) is equal to the spatial derivative of the velocity (u),

$$\dot{\varepsilon} = \frac{du}{dx} \tag{5.4}$$

where x is the relative spatial displacement of the drop along the channel. Given that:

$$\frac{\partial D}{\partial t} = \frac{\partial D}{\partial x}\frac{\partial x}{\partial t} = \frac{\partial D}{\partial x}u \tag{5.5}$$

Equation 5.1 can be rewritten as:

$$\alpha\mu_c\left(\frac{5}{2\hat{\mu}+3}\dot{\varepsilon} - \frac{\partial D}{\partial x}u\right) = \gamma\left(\frac{D}{a_0}\right) \tag{5.6}$$

which linearly relates what is referred to as the Taylors parameter to a radially normalised deformation with a gradient equal to the interfacial tension of the system. The first term of the left-hand side of Equation 5.6 encompasses the steady state deformation, while the second incorporates the time dependence of the drop deformation. The solution viscosities and deformation data were directly obtained through rheological measurements and image processing in order to produce a Taylor's plot where the interfacial tension was extracted from the slope of a linear fit.

Viscosities of the polymer-surfactant solutions were measured using a shear-rate controlled rotational test as described in the Methods Chapter of this thesis, while the dispersed phase (tetradecane) viscosity was obtained from the supplier. Image analysis was performed batchwise in MATLAB on the data obtained from image processing. As multiple drops are regularly present within each grabbed image, drops were tracked across images and assigned a drop index using paramsTracking. This also allowed the information of individual drops as they pass along the observation window to be linked. Depending on the velocity, each drop was observed 12 - 25 times in Basler experiments and 22 – 50 times in Phantom experiments. The difference in displacement x is taken as the distance between two linked sequential midpoints, of which the change in deformation $\frac{\partial D}{\partial x}$ can be found. The velocity is also than computed from the drops relative transit time within the observation window which is converted from the difference in frames to time using the relevant fps acquired by the camera. The extension rate is obtained from the change in velocity and relative mean position within the channel. A Taylors plot is finally produced from a data set of at least 200 drops to obtain a statistically relevant linear fit, of which the slope directly provides the interfacial tension.

5.3 Results and Discussion

5.3.1 Dynamic Viscosity

The dynamic viscosity of solutions containing 0.5% w/w PVP and the 2 – 50 mM range of SDS concentrations at 21.5 °C is presented in Figure 5.3. A water calibration performed prior to the measurements gave a 0.4% offset, which values were adjusted to accordingly. At low concentrations of SDS below the critical aggregation concentration (CAC), the viscosity is relatively constant at around 1.6 mPa.s. Increasing the concentration above the CAC sees a sharp increase in viscosity until 20 mM of SDS where the viscosity begins to gradually reduce. These results are relatively consistent with the pendant drop interfacial tension measurements presented in the previous chapter, where the points of discontinuity at 2.5 mM SDS and 30 mM SDS encompasses the region polymer surfactant complexes are expected to form and then become saturated. As seen in the AFM measurements 30 mM SDS and 0.5% w/w PVP is expected to be at the cusp of polymer saturation, therefore slight changes in solution conditions could result in a shift to the point of saturation, which explains the reduction in viscosity prior to 30 mM SDS.

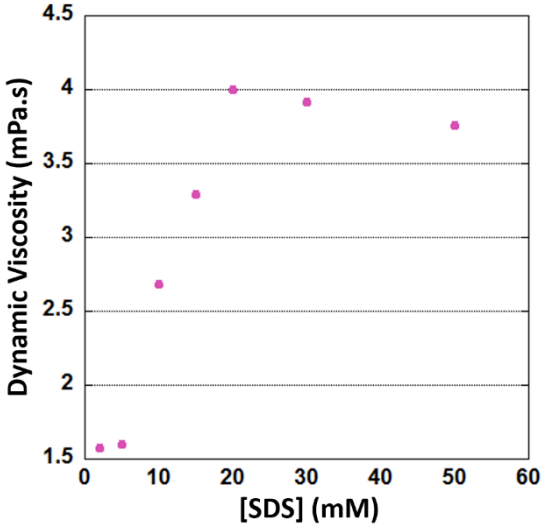

Figure 5.3 The dynamic viscosity vs SDS concentration of solutions containing 0.5% w/w PVP and SDS. The error bars, based on the uncertainty of the shear-rate controlled rotational test, are just visible above and below the data marker.

The capillary number ($Ca = \frac{\mu_c u}{\gamma}$) plays a key role in dictating the extent of deformation experienced by the drop during contraction. As seen by Rallison and others, an increase in the capillary number directly correlates to an increase in deformation as the viscous forces dominate the interfacial tension to distort the drop (388-390). Therefore the 2 and 5 mM SDS solutions would require a larger velocity to achieve deformations equivalent to the higher concentrations given their smaller viscosities. In addition to lower viscosities, the interfacial tension has an inverse behaviour where 2 and 5 mM SDS are comparably larger, thus requiring an even greater compensation in velocity to maintain a measurable drop deformation.

5.3.2 Interfacial Tension

The interfacial tension can be measured from the deformation of a drop entering or exiting a contraction. As the deformation parameter D is simply a measure of the difference between the major and minor radii and their sum, inverting the assigned axis also produces a positive deformation for exiting drops. Drop flow into the contraction was visibly offset from the channel centreline (Figure 5.4), potentially distorting the deformation and deviating the system from theoretically predicted behaviour. Therefore, the drop deformation exiting the contraction was chosen for all further analysis.

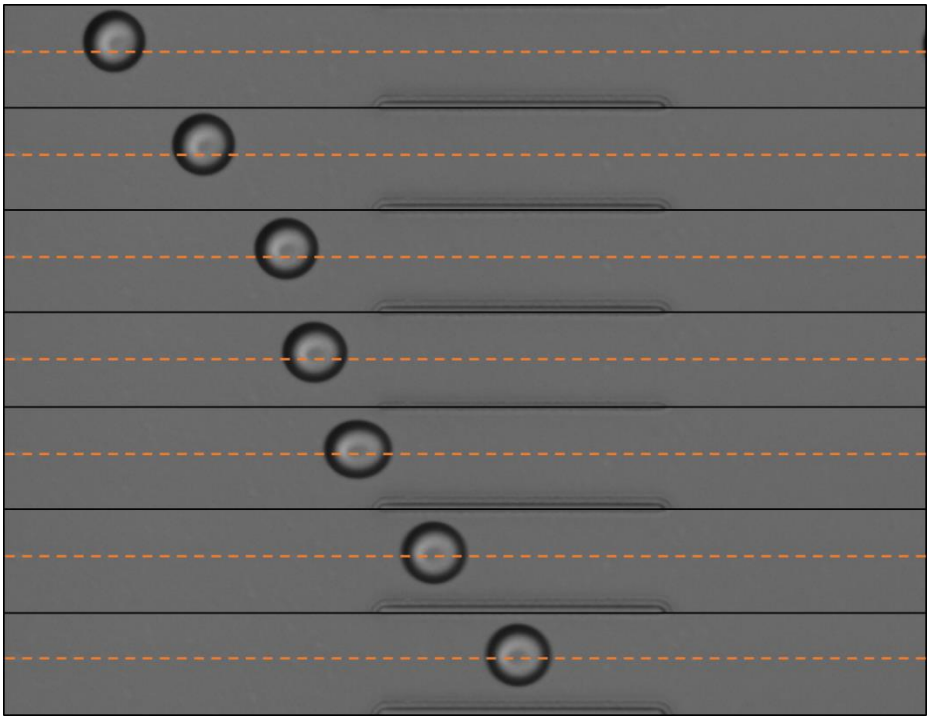

Figure 5.4 Image of a drop tracking across the channel into a contraction highlighting the deviation of the drops position from the centreline. The orange line is positioned through the centre of the channel as a visual aide.

Figure 5.5 shows the data obtained from 225 tetradecane drops with average radius of 29.2 μm formed in 50 mM SDS and 0.5% w/w PVP used to determine the systems interfacial tension. This data was acquired using the Basler camera and a combined main channel flowrate of 8430 μL/hr, such that each drop was observed around 20 times each over the allotted time frame. The deformation data in Figure 5.5A begins at the point of maximum deformation to isolate the relevant change as it transitions from high to low velocity or ellipsoidal to spherical morphology. After around 150 μm the drop has transitioned back to its equilibrium form. The drop transit time as a function of relative spatial displacement (Figure 5.5B) captures the drop velocity, which quickly decelerates upon exiting the contraction. Syringe pumps have been shown to induce oscillatory fluctuations in microfluidic flow due to the driving mechanism of the stepper motors (290, 391, 392). The impact of this can be clearly seen in Figure 5.5B, were transience in the drop flow results in pulse rather than smooth transitions in displacement. The overlapping times at a single position suggest a stick-slip behaviour in the pumps drive. The extension rate (Figure 5.5C) is unaffected by this behaviour and highlights the rapid transition the drops velocity experiences from the contraction. Figure 5.5D shows the final Taylors plot fit with a linear model that is forced through the origin as required by the theory. The slope of the fit and thus interfacial tension for this system is 8.42 mN/m with a 95% confidence interval of 0.103. The population of data points is denser at lower D values as the drops more frequently exist in a relaxed morphology,

unaffected by extensional flow. As *D* gets smaller for cases of spherical non perturbed drops, the errors from image extraction become larger, which leads to systematic increase in random error. Therefore, the data was cut-off at small *D* values, effectively when the drop is meant to be a sphere and return a Taylors parameter of 0, to remove the associated uncertainty from the image analysis.

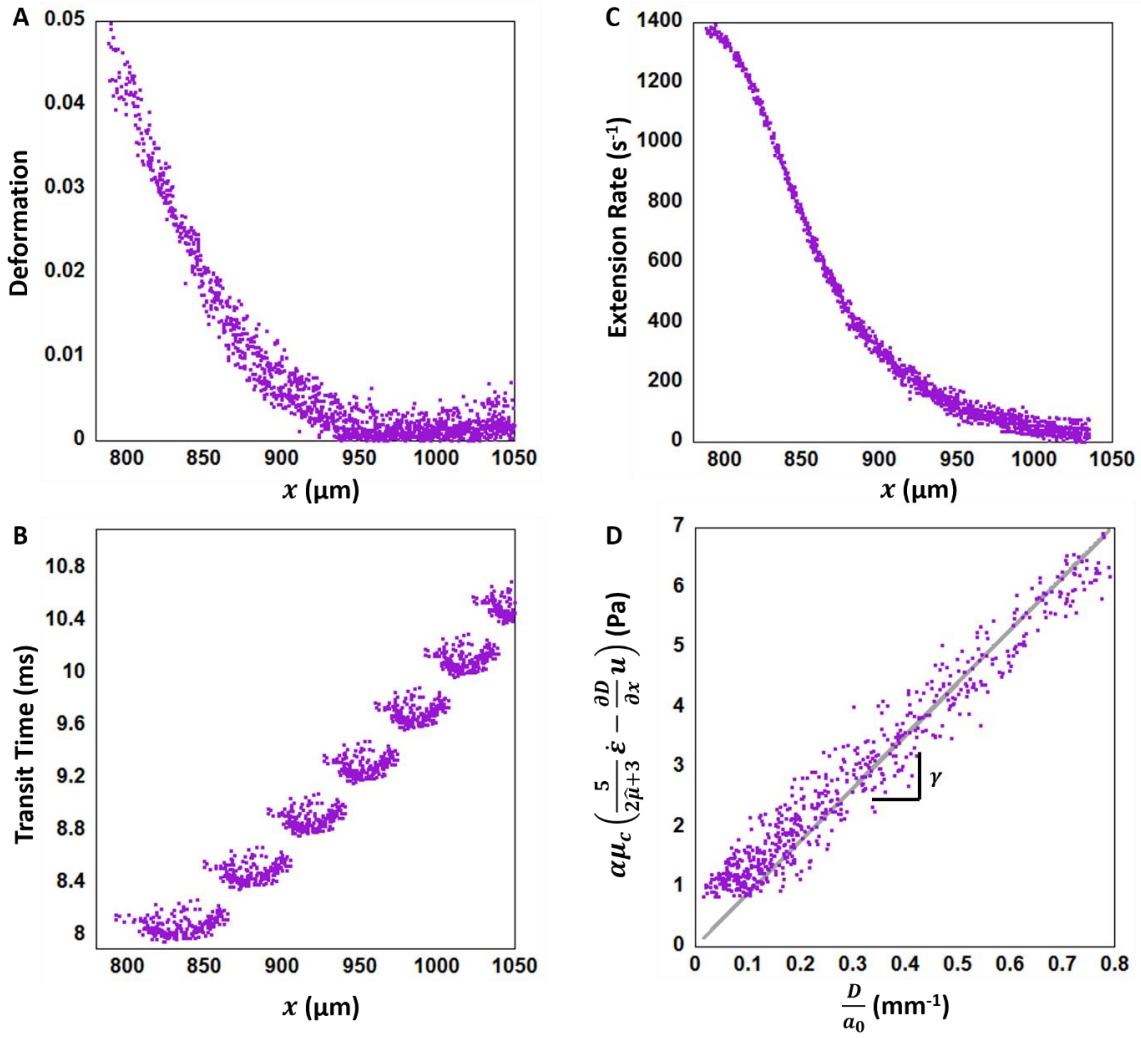

Figure 5.5 Results obtained from a data set of 225 tetradecane drops ($a_0 \approx 29.2$ μm) formed in 50 mM SDS and 0.5% w/w PVP expressing the (A) dimensionless deformation parameter D, (B) transit time t and (C) extension rate $\dot{\varepsilon}$ as a function of channel displacement. (D) The Taylors parameters is plot as a function of a radially normalised deformation with a linear regression passing through the origin (grey line) fit to extract the interfacial tension from the slope.

As previously mentioned, two aspects of the image processing required careful attention to detail. The approaches to ensure reliable edge detection were outlined above. The second was the decision of which edge to use in the drop profiles as the drop shape was not defined by a thin, sharp edge, but instead a dark ring creating an ambiguous perception of where the edge lay (Figure 5.2). Therefore, to investigate the appropriate edge location a contour was extracted at

both the inner and outer cusp of the dark ring, which were then used to construct an average contour (Figure 5.2). The averaged contour was also smoothed using local regression lines to obtain the best estimate of the cusp's centreline. The inner contours gave non-sensible results which greatly underpredicted drop radius (≈ 18.9 μm) and produced unusable Taylors plots, see Appendix A9.7. The inner contours also appeared to not always be circular due to the lensing of the drop and the background lights, as can be seen in Figure 5.2. Figure 5.6 compares the Taylors plot of the outer, averaged and smoothed contours of drops formed in 10 mM SDS and 0.5% w/w PVP. It is visually clear from the plots that the data taken from the averaged contours are considerably more disperse than the outer contour, which is further evident in the R-squared values obtained from the linear regression. The interfacial tension increases with decreasing data dispersity, where the outer cusp typically produced values equivalent to those obtained from pendant drop measurements. In addition, the average contour is likely to still be affected by the distortions from lensing and lighting that the inner contour was affected by, but to a larger extent. Therefore, the outer cusp was selected to represent the true edge of the drops interface and used for data analysis at each concentration.

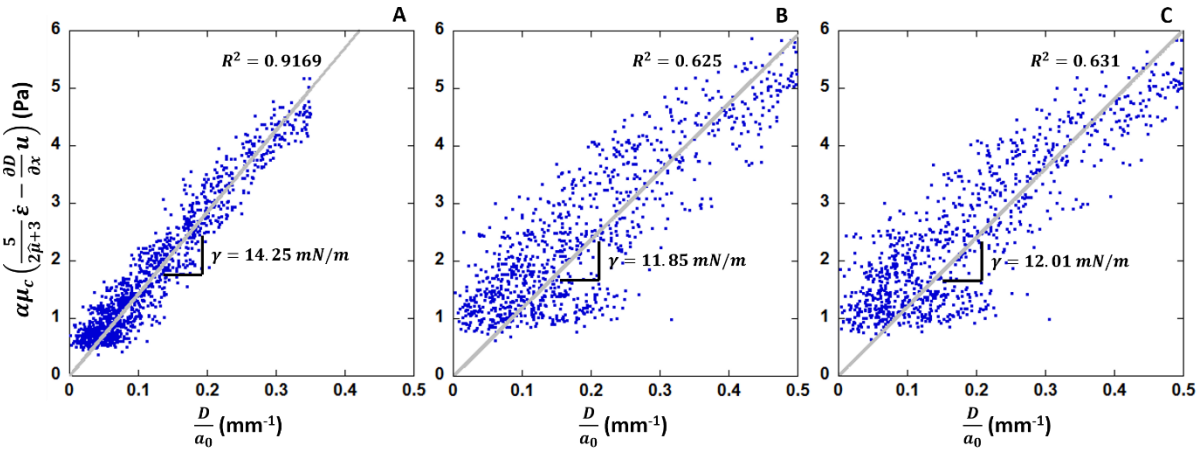

Figure 5.6 Taylor plots obtained from a data set of 353 tetradecane drops formed in 10 mM SDS and 0.5% w/w PVP comparing the results from using the (A) outer, (B) averaged or (C) smoothed contour. The respective slope, interfacial tension and R-squared value of the linear regression (grey line) is included for each contour.

A sensitivity analysis was performed on the minimum number of drops required for image analysis to provide a statistically relevant fit to the data. Table 5.1 shows the results of principal parameters obtained from analysing an increasing number of drops in a 2 mM SDS and 0.5% w/w PVP system. The number of observations per drop and equilibrium radius are essentially unaffected by the number of drops analysed. From 108 drops the interfacial tension remains relatively constant at around 22.7 mN/m. However, predictively the 95% confidence interval of the interfacial tension continues to decline with an increase in data points. The number of drops analysed is directly proportional to the computational expense of the analysis, where up until

around 400 drops, doubling the number of drops correlates to approximately 2 s in additional processing time. Therefore, a minimum of 200 drops was analysed for each data set based on a compromise between the achievable accuracy and time to process a single condition, where there are seven conditions at five different residence times with a number of repeat experiments.

Table 5.1 Parameter list of the primary observables taken from an increasing number of analysed drops in a 2 mM SDS and 0.5% w/w PVP solution where time refers to the image analysis processing time.

Drops	Observations/Drop	Radius a_0 (um)	IFT (mN/m)	95% Confidence Interval	Time (s)
28	36.8	24.3	24.3	1.61	7.79
55	36.4	24.4	22.7	1.14	8.72
108	37.0	24.4	22.8	0.840	10.8
213	37.6	24.4	22.8	0.610	12.9
424	37.7	24.4	22.9	0.430	15.1
851	37.6	24.3	22.6	0.310	22.1
1498	37.5	24.3	22.5	0.240	46.6

With this information, the interfacial tension of tetradecane drops in 0.5% w/w PVP and a range of SDS concentrations was measured across five contractions in the microfluidic device. Figure 5.7 shows a comparison of the average interfacial tension values measured in the microfluidic device with those obtained from Pendant Drop experiments for both SDS and SDS/PVP. The average was used over residence times greater than 0.1 s as the data did not show a dynamic dependence over this time, details of which are discussed below. While Pendant drop measurements reach equilibrium values in static conditions with drop ages of minutes to hours, the microfluidic measurements are captured in less than a second, with smaller drop sizes and in flow. The critical aggregation concentration, critical micelle concentration and critical redissolution are incorporated for clarity of the points at which interaction between the surfactant and polymer are expected. The microfluidic values agree well with the pendant drop experiments, where the largest deviation of 2.14 mN/m is seen at 10 mM SDS. Additionally, the shape of the curve is clearly characteristic of polymer surfactant complexation and not just surfactant adsorption (grey SDS curve). Thus, given the strong agreement between the two techniques there is reasonable evidence that the polymer surfactant complex is at the interface and underflow can reach comparable interfacial tensions values as the Pendant drop and AFM measurements.

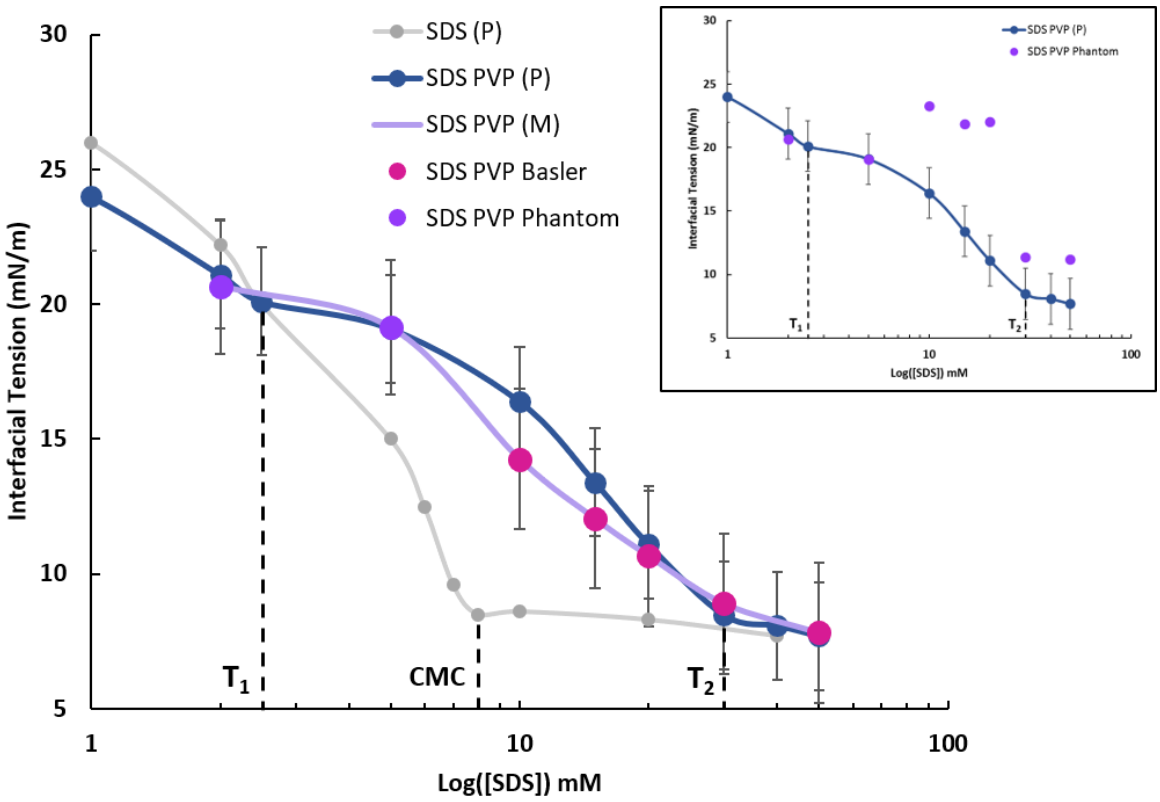

Figure 5.7 A comparison of interfacial tension measured using the microfluidic device (M) and the Pendant Drop (P) method. The pink and purple points denote data acquired using the Basler and Phantom cameras, respectively. (Inset) Interfacial tension values acquired using the Phantom camera across all SDS concentrations.

There are several factors that can contribute to the accuracy of the measurement including the microscope focus, edge detection threshold limits and drop radius. The focal plane of the microscope should be set to the centreline of the microfluidic channel were the drops are theoretically centred for accurate measurement of the drop's morphology. Deviation from this point can cause the drops to appear out of focus, being either smaller of larger than their true form. Therefore, to minimise its impact the microscope was re-focused prior to each measurement, using imperfections in the glass surface at the top and bottom walls and stationary drops as a guide. The threshold input for PAE edge detection sets the minimum difference in intensity at both sides of a pixel required to be considered as an edge. Consequently, for the outer contour, low values would increase the apparent drop size while high values would reduce it. However, in this case the threshold limit could be refined between two or three values as edge detection would quickly return broken edges (no edge detection) or extra pixels clearly outside the contours range if limits were set inadequately. Hudson *et al*. found that insufficient threshold settings affected the accuracy of the measurement by at most 5% (16). Confinement of the drops from the channel walls has the potential to affect the relative interfacial tension via several paths, typically resulting in a underpredicted value (16, 330, 331). At drop sizes close to the height of

the channel wall, where a thin layer of the continuous phase separates the drop from the wall, lubrication forces are likely to become applicable and cause the drops relaxation to slow. Further confinement, where the drops are equal to or larger than the channel height, will not only alter the drop's morphology but also potentially affect the path of the external flow field to which the theory is based. Hudson *et al*. showed that the interfacial tension remained constant below drop diameters at 80% of the channel height (16). Also, when considering adsorption of surface-active components confinement can impact how the molecules interact at the interface.

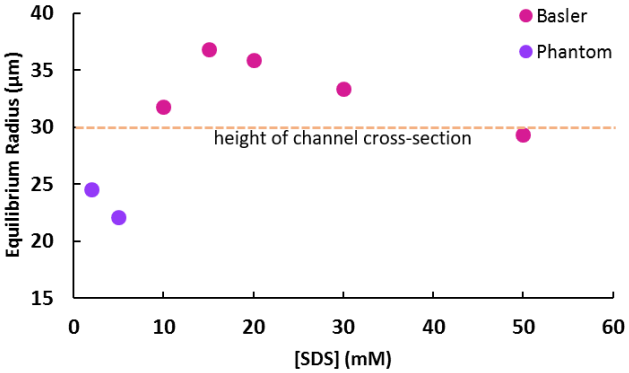

Figure 5.8 The average equilibrium radius as a function of SDS concentration. The height of the channel cross-section is included to clearly indicate where the drop would be in contact with the channel walls.

A block-and-break geometry was used to maintain a consistent droplet size to avoid issues surrounding wall interference and drop confinement. Although this can be effective without surface active components, the incorporation of surface-active components resulted in the formation of drops with sizes dictated by surface properties as opposed to channel geometries or input flow conditions (Figure A9.7). The resulting drop radius at each SDS concentration is shown in Figure 5.8 and are compared to the relative height of the channel's cross-section to demonstrate at what concentrations the drop size is constrained by the walls. Between 10 and 30 mM SDS the drops are larger than the channel height, where 15mM has the largest drop size. These values do not correlate directly with the differences observed in the interfacial tension measurements, suggesting that the error induced due to larger drop sizes aren't necessarily as important as expected and other factors could be responsible for the variance in results. In these cases, the measured radius is likely to be larger than the actual radius as the size is determined from the images as previously described in the image processing method. If the drops are in contact with the wall, they will become "pancaked" altering their morphology such that radius extracted from the derived spherical volume will be perceived as larger than expected. It is also worth noting that due to the density difference in the continuous phase (ρ = 998.9 kg/m3 @ 25 °C) and the dispersed phase (ρ =762 kg/m3 @ 25 °C) without including an additional inlet to adjust

the height drops will sit at the top wall of the channel and create confinement anyway. This effect could ultimately be responsible for the larger than expected drop sizes.

The interfacial tension data presented in Figure 5.7 was obtained using both the Basler and Phantom cameras, as represented by the purple and pink markers. As previously discussed, 2 and 5 mM SDS have comparably smaller viscosities and larger interfacial tensions, thus requiring higher drop velocities and by extension flowrates to achieve measurable drop deformation. Based on measurements performed on the higher SDS concentrations, a minimum capillary number of around 0.009 was necessary to detect and measure the drops deformation during image processing. At the acquisition speeds and image integration times achievable using the Basler camera, the channel flowrate was limited to around 4.5 ml/hr before image quality and the number of observations per drop were unacceptable. At this flowrate, based on the previously measured dynamic viscosities and pendant drop interfacial tensions, the capillary numbers of the 2 and 5 mM SDS systems were substantially below the minimum threshold. Attempted measurements supported the criteria as they did not produce appreciable deformation which could be detected in the image processing. Therefore, the Phantom was used to explore higher flowrates, allowing increases in the capillary number of up to five times and the interfacial tension at 2 and 5 mM to be measured. Table 5.2 summarises these values for clarity.

Table 5.2 Summary of capillary numbers at each SDS concentration given flowrates below (Basler) and above (Phantom) 4.5 ml/hr

SDS Concentration mM	2	5	10	15	20	30	50
Viscosity (mPa.s)	1.58	1.60	2.68	3.29	4.00	3.92	3.76
Interfacial Tension (mN/m)	21.1	19.1	16.4	13.4	11.1	8.5	7.7
Capillary Number Ca (Basler)	0.004	0.005	0.009	0.013	0.020	0.025	0.027
Capillary Number Ca (Phantom)	0.014	0.023	0.045	0.041	0.050	0.052	0.054

Together the interfacial tensions at each of the five contractions can be used as a direct indication of the dynamic behaviour of the polymer and surfactant systems under flow. Figure 5.9 plots the interfacial tension of the five SDS and PVP systems (10 to 50 mM SDS) measured using the Basler camera against the drops residence time from the point of drop formation. The average interfacial tension for each system has been included as a guide. From the first to the last point of measurement, all five systems remain predominantly constant. This suggests that they have already reached their equilibrium configuration by the first contraction at a time corresponding to approximately 18.2 ms. The time between drop generation and collision in the drop chaining experiments is around 4.49 s, therefore adsorption times are well and truly within appreciable timescales during the measurements. With this in mind, a reasonable assumption that the drop interface has a high degree of coverage from surface-active materials at the point of collision can

be made, supporting the hypothesis of an immobile interface which typically arrests internal circulation of the drop (330, 376).

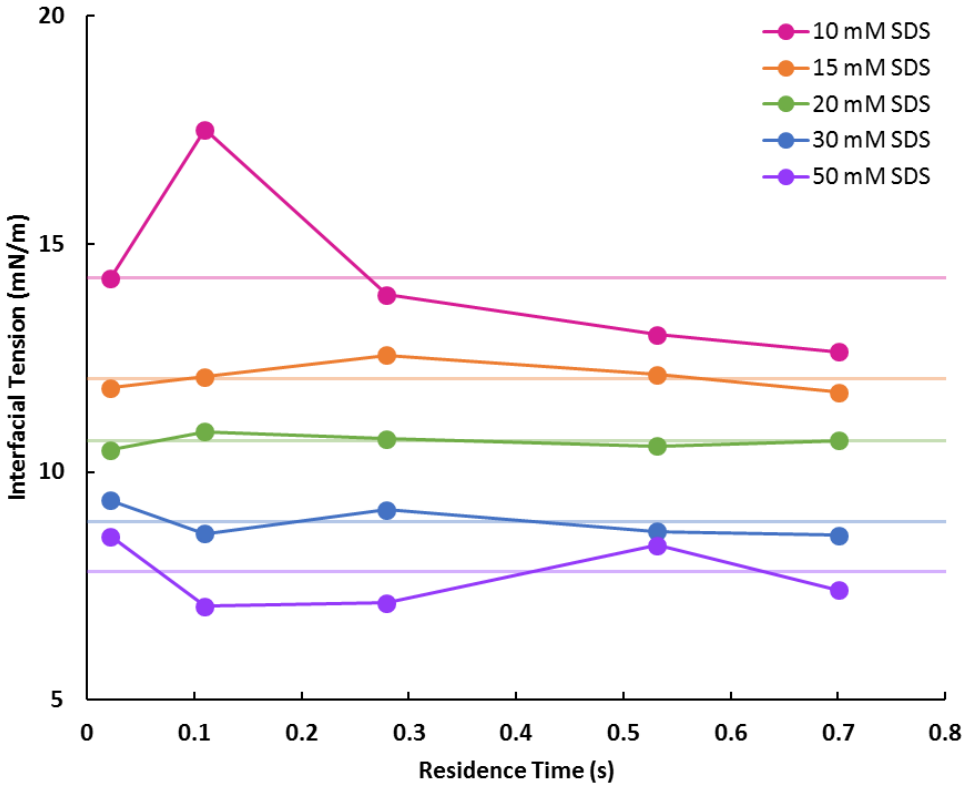

Figure 5.9 Interfacial tension measured as a function of residence time from the point of drop generation. The markers represent the value obtained at each contraction. The faded horizontal lines indicate the average interfacial tension at each SDS concentration.

The Phantom camera was also used to measure SDS concentrations from 10 to 50 mM in order to probe larger deformation and quicker time scales. The average interfacial tensions are shown in the inset of Figure 5.7 and show a clear deviation from the values obtained through Pendant Drop measurements. This discrepancy can be explored by instead presenting the data as a function of residence time as shown in Figure 5.10. While 2 and 5 mM of SDS present equilibrium behaviour as seen in the Basler measurements, 10 to 20 mM exhibit dynamic results where the interfacial tension declines over time. By 30 mM the results again appear to have reached steady state and are relatively constant between each contraction. Due to a minimum 2-fold increase in flowrate, the results were taken at a fraction of the time seen in the Basler experiments, equivalent to microsecond timescales. While complexes have begun to form at 5 mM of SDS and 0.5% w/w PVP, as seen in the AFM experiments the complexes at the interface do not appear to have adsorbed at an appreciable amount. While at 30 mM it is expected that complexes have begun to desorb from the interface, with SDS preferentially absorbing. Therefore, it is possible that the dynamic behaviour between these concentrations is the result of delayed absorption of the surface-active complexes at these smaller timescales. Alternatively, the high-speeds could be altering the

adsorption kinetics entirely and provide evidence of a scenario where the activity of the molecules in flow has deviated from static behaviour.

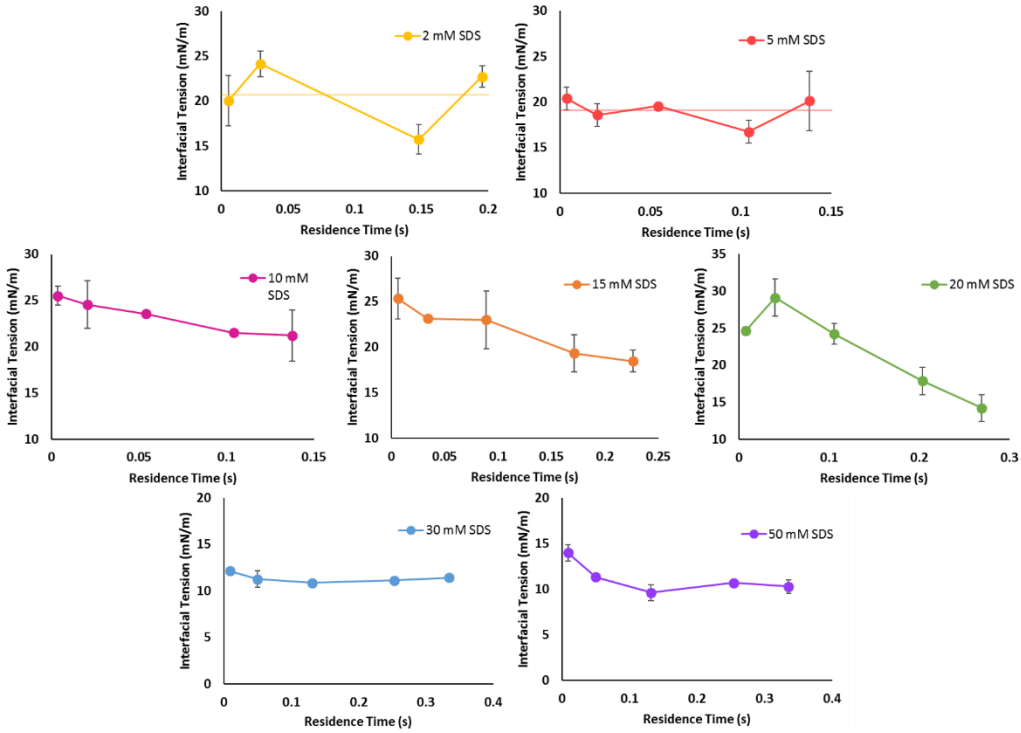

Figure 5.10 Dynamic interfacial tension from experiments using the Phantom. The interfacial tension vs residence time from the point of drop generation are presented for solutions of 0.5% w/w PVP and SDS concentrations ranging from 2 to 50 mM. The faded horizontal lines in the 2 and 5 mM SDS plots indicate the average interfacial tension at each SDS concentration.

5.4 Conclusion

The interfacial tension of tetradecane drops in the presence of SDS ranging between 2 and 50 mM and 0.5% w/w PVP was measured in flow using a microfluidic device. The continuous phase viscosities of the investigated systems were substantially lower than those used in previous studies (16, 329-331), requiring much higher flowrates to be used to achieve measurable deformation. Investigation into the drop's edge, showed that the outer contour of a dark ring outlining the drop provides the most accurate data. In addition, a sensitivity analysis on the number of drops analysed per data set suggests that 200 drops is a sensible value to attain statistically significant results. The interfacial tension values attained from microfluidic measurements agreed well with the pendent drop experiments, with a maximum deviation within uncertainty of the measurements at 10 mM SDS, where most SDS concentrations were in close agreement. Additionally, they showed characteristic features expected from polymer surfactant systems in interfacial tension measurements. These results provide reasonable

evidence that the polymer surfactant complex is adsorbing to the interface in microfluidic flow at similar levels as the pendant drop and AFM measurements. A series of five contractions, where the interfacial tension was measured at increasing time intervals showed that at flowrates below 4.5 ml/hr, solutions containing SDS concentrations between 10 and 50 mM reached equilibrium within 21.9 ms. This suggests that adsorption is occurring at timescales well below those used in the previous drop chaining experiments. Measurements using substantially higher drop velocities were either able to observe dynamic absorption of the polymer surfactant complexes or exhibited a scenario where the activity of the molecules in flow has deviated from static behaviour at small residence times.

This chapter ultimately corroborates the potential links drawn between the AFM and microfluidic studies performed in the previous chapter. The results provide physical chemistry-based evidence that the surface chemistry of the drop within flow at the conditions used for drop-chaining experiments are equivalent to the static environment of the AFM. Further insight into the molecular structure of the complexes in solution and at the interface in microfluidic conditions would provide a greater understanding of how they affect drop interactions.

Chapter 6: Droplet Microfluidic SANS

6.1 Introduction

To further explore the adsorbed PS complex on the drop interface, studied via force measurements in Chapter 4, droplet interaction measurements (Chapter 4) and interfacial tension measurements (Chapter 5) in microfluidic devices, we extend this study to probe this layer on a molecular scale. The structural properties of polymer-surfactant complexes at interfaces have traditionally been studied using neutron reflectivity (393-395). Applying these measurements to liquid-liquid interfaces is non-trivial which has limited its application primarily to air-water interfaces. Although pioneering work by Zarbakhsh *et al*. using a microscopic frozen alkane layer and further derivations have seen its use in observing a variety of surface-active components at the oil-water interface (396-400). Using SANS to study these systems was introduced by Staples *et al*. to investigate the absorption of mixed surfactants at an oil-water interface (401). The measurement was performed on a well-defined and stable oil-in-water emulsion with sub-micron droplet sizes. This approach was again used by Penfold *et al*. on non-ionic surfactants with varying degree of ethoxylation and by Bumajdad *et al*. for the case of water-in-oil emulsions (402, 403). The only cited case of a polymer-surfactant mixture was research performed by Tucker *et al*., who measured the impact of the addition of two cationic polymers on the adsorption of SDS at the droplet interface (404). From these they were able to obtain the structure, compositions and adsorbed amounts of each component at the interface as well as identify entities within the bulk.

More recently exploration into combined drop-based microfluidics and scattering techniques have emerged, introducing with it a new generation of microfluidic systems capable of measuring the structure, interactions and kinetic processes of the materials within emulsions. With continued advancements into the detection capabilities and speeds of scattering instruments such as Raman spectroscopy, small-angle X-ray scattering (SAXS), and small-angle neutron scattering (SANS) progress into novel approaches for sample preparation and formulation has become possible. Most of the literature currently available focuses on the proof of concept for these new techniques. Cristobal *et al*. introduced the use of Raman spectroscopy with drop-based microfluidics by probing *in situ* the composition and mixing of two-component drops (23). Cecchini *et al*. built on these ideas by incorporating surface-enhanced resonance Raman with improved temporal resolution such that multiple spectrums per drop could be taken (332). SAXS studies have been used to characterise the size, shape and concentration of gold particles encapsulated within water (24), as well as to investigate the assembly of weakly scattering protein vimentin within aqueous drops (333, 334). After refining microfluidic SANS techniques for the mixing of complex fluids in a continuous channel (25, 335), Adamo *et al.* moved onto droplet microfluidic SANS to create segmented flow as a means to circumvent flow dispersion

(336). These novel approaches to characterising emulsions within microfluidic devices open the door to a new area of understanding for these systems in flow. However, these studies have yet to focus on the interfacial behaviour of drops in flow, and are still focused on single phase, or the bulk phases of either the dispersed or continuous phases. Thus, there is an opportunity and need to probe the presences and adsorption of materials at the drop interface under flow as this has implications for both the hydrodynamic circulation within the drop and inter-droplet interactions in microfluidic devices.

In this chapter we explore the use of a novel microfluidic device for performing droplet microfluidic SANS with the purpose of analysing the adsorbed layers at the drops interface and their structural confirmation while under flow. SDS and PVP in single and two-phase flow is analysed to understand the molecular structuring of the molecules with increasing degrees of complexity.

6.2 Methods

6.2.1 Design

A schematic diagram of the microfluidic channels is illustrated in Figure 6.1, where the drop generation, introduction into an enlarged main channel and position within a SANS observation window is emphasized. The etch depth for every channel and therefore associated sample path-length was 51.2 μm. Maximising the scattering volume was considered the highest priority factor for channel design. With this in mind and to remain consistent across experiments, channel geometries were planned for a drop diameter of 50 μm. Drops were generated using a T-junction, which was designed based off a predictive model for drop volume made by Steijn *et al*., with tolerances considered to consistently produce drops smaller than the channel walls (287). As discussed in the previous chapter, drop confinement can produce a range of complications in not only drop morphology but also adsorption of surface-active components. Furthermore, contact of the drop interface with the channel wall could produce obscure scattering and introduce uncharacteristic behaviour into the data. As seen in the literature, to remain within the squeezing regime for drop formation in a T-junction, where break-up is solely dependent on the ratio of the volumetric flowrates, the Capillary number needs to be below 0.01 (286, 288). Thus, for consistency in drop formation across surfactant concentrations, decisions on preliminary flowrates and channel geometries were bound by this criteria. The final channel dimensions are shown in Figure 6.1A. A T-junction was used instead of a block-and-break geometry to avoid channel dimensions below 30 μm, as lengths below this are more likely to trap contaminants, which is highly undesirable for SANS experiments due to their sensitivity to foreign materials.

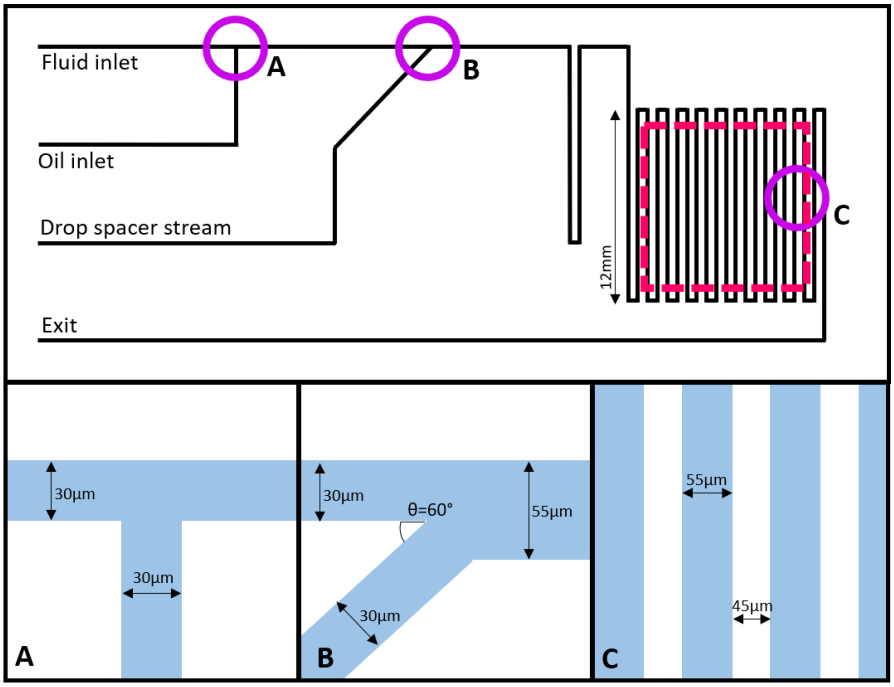

Figure 6.1 Schematic diagram of the microfluidic design used for SANS measurements showing an overview of the device and specific details of the channels geometries at the (A) T-junction drop generation, (B) expansion into the main channel, and (C) region of repeating parallel channels; SANS observation window where the beamline (pink dashed box) is aimed.

In the squeezing regime, drops are formed by filling the main channel and blocking the upstream continuous phase flow. Therefore, after generation the droplet slugs were introduced into an enlarged main channel liberating them from wall constrictions and allowing them to become spherical. Increasing the channel width from 30 to 50 µm causes a decrease in drop velocity, which significantly reduces the spacing between the drops by as much as 80%. Consequently, to avoid drop collisions, a second continuous phase stream was introduced at a 60° angle to the main channel to help accelerate the drops and control their separation (Figure 6.1B). For example, the space between droplets formed with a continuous phase flow of 135 µL/hr and dispersed phase flow of 45 µL/hr decreases from 68.5 µm to 16 µm after entering the expansion. Introducing an additional 100 µL/hr via the drop spacer stream increases this space back up to around 49 µm, roughly to the same size as the drop.

A 12 x 12 mm observation window where the main channel is looped back repeatedly creates an illumination zone made up of 121 parallel channels for the neutron beam to be aimed towards. Using a 10 X 10 mm beam cross section, this will illuminate 100 channels or 69% of the cross-sectional area. The dimensions and design of the illumination zone was determined from a calculation of the expected scattering volume from absorbed layers of PS complexes at the interface of an estimated number of drops that would exist within the zone at any one point in time. The calculated scattering volume fraction of the layers was compared to the scattering

volume fraction of micelles from a typical highly scattering static SDS SANS measurement using a standard path-length to determine the viability of the design. Details of the analysis is presented in the Appendix (A9.8) and highlights the necessity for the dimensions and number of channels included within the design in order to obtain a scattering volume fraction at a similar order of magnitude to an SDS micelle measurement. Figure 6.1C shows the pattern and geometry of the channel and it's spacing within this region. The total channel length is roughly 1.45 m, giving a total volume of 4.14 µL within the observation window. To increase contact time and ensure complete adsorption of the polymer and surfactant an additional 24 mm of channel was introduced prior to the main observation window.

6.2.2 Experimental Systems

Perfluorooctane (PFO) was used as the drop phase fluid due to its immiscibility and low SANS background (≈ 0.02 cm^{-1}) as identified by Adamo *et al*. in their analysis of appropriate carrier fluids for droplet microfluidic SANS (336). Drops were generated in solutions of D_2O/H_2O mixtures to contrast match the solvent/continuous phase to the PFO drops, such that scattering from the surface-active components in the bulk or at the interface could be isolated. The ratio of D_2O to H_2O was calculated by balancing the scattering light density (SLD) of the D_2O/H_2O mixture to the SLD of PFO (≈3.683), giving a mixture of 63.4/36.6% w/w respectively. Figure 6.2 shows the scattering from the D_2O/H_2O mixture and a drop measurement in 0.1 mM of SDS and equivalent D_2O/H_2O solution. The two sets of data are in good agreement, particularly in the high q-range where future measurements are focused.

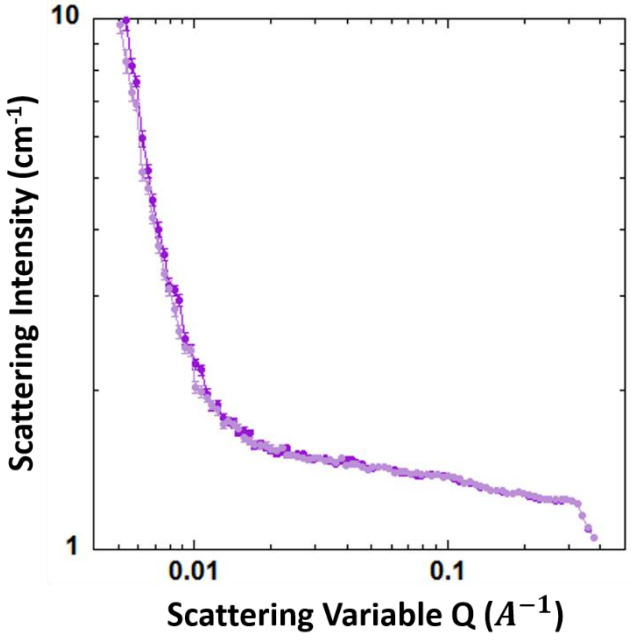

Figure 6.2 Normalised scattering intensity as a function of the scattering vector Q for a D_2O/H_2O mixture at ratios 63.4/36.6% w/w (light purple) and PFO drops in a 0.1 mM SDS and equivalent D_2O/H_2O solution (dark purple).

6.2.3 Operation

The general experimental set-up and operation of the microfluidic device is covered in detail in Chapter 3 of this thesis. Small angle neutron scattering (SANS) was performed on BILBY, a time-of-flight instrument operated by the Australian Centre for Neutron Scattering at the Australian Nuclear Science and Technology Organisation (ANSTO), Lucas Heights, Australia. Measurements were conducted at room temperature, which ranged from 18 to 21 °C, with an incident neutron wavelength of $\lambda = 6$ Å ($\Delta\lambda/\lambda = 10\%$) and a sample-detector distance of 6 m to attain an effective Q range of 0.004 – 0.4 $Å^{-1}$. A 10 x 10 mm square-beam footprint was created using a cadmium diaphragm, which when aimed at the illumination zone covered 100 channels with a 51.2 µm path-length and a total sample volume of 3.42 µL. Figure 6.1 demonstrates the position of the beam in relation to the microfluidic device by means of a pink dashed box. The raw data was reduced into 1D scattering spectra by subtracting the scattering from an empty device before radially averaging the resulting spectrum assuming isotropic scattering using standard procedures described in the literature by Sokolova *et al*. (405, 406). Data reduction was performed using the Mantid software suite (407), where errors on the scattering data came from uncertainty analysis performed in Mantid, and the data was modelled using the SasView 4.0.1 software (http://www.sasview.org/). Both the single-phase and two-phase data were normalised by subtracting the scattering of the solvent (either D_2O or mixed D_2O/H_2O) in the device as background.

6.2.4 Data Analysis

6.2.4.1 Micelles

For ellipsoidal micelles in solution, the scattering intensity I(Q) as a function of scattering vector Q is related to their form factor $P(Q)$ and effective structure factor $S'(Q)$ through the following equation (227, 408):

$$I(Q) = \frac{scale}{V} P(Q)S'(Q) + background \tag{6.1}$$

Where scale incorporates the volume fraction of scattering objects, V is the volume of a micelle, and background accounts for contributions from incoherent background scattering (cm^{-1}). The form factor corresponds to intraparticle interactions, which for prolate ellipsoids can be expressed as:

$$P(Q) = \int_0^1 F(Q,\alpha)^2 \, d\alpha \tag{6.2}$$

Where α is the cosine of the angle between the scattering vector (Q) and major axis of the ellipsoid, and the function $F(Q,\alpha)$ is defined as:

$$F(Q,\alpha) = 3V\Delta p\ \frac{\sin(x) - x\cos(x)}{x^3} \tag{6.3}$$

and

$$x = Q\sqrt{R_e^2\alpha^2 + R_p^2(1-\alpha)} \tag{6.4}$$

The two radii, R_e and R_p, denote the radius along the equatorial and polar axis of the ellipsoid respectively, and Δp is the contrast created by the difference in scattering length density (SLD) between the micelle (p_m) and solvent (p_s). The interparticle interactions are captured by the structure factor $S(Q)$, which for spheroidal objects in a dielectric medium can be evaluated analytically with the Hayter-Penfold rescaled mean spherical approximation (RMSA) to account for interference effects from screened Coulomb potentials between charged particles (409, 410). The effective structure factor $S'(Q)$, orientationally averages the structure factor to account for anisotropic particles and is related to $S(Q)$ through the expression:

$$S'(Q) = 1 + \frac{P(Q)^2}{\langle |P(Q)|^2 \rangle}(S(Q) - 1) \tag{6.5}$$

6.2.4.2 Polymers

The Guinier-Porod model (411) fits small angle scattering data from spherical and anisotropic objects, such as rods or platelets, and any intermediate shape in-between using the functional form:

$$I(Q) = \begin{cases} \dfrac{G}{Q^s} exp\left[\dfrac{-Q^2R_g^2}{3-s}\right] & Q \le Q_1 \\ \dfrac{M}{Q^m} & Q \ge Q_1 \end{cases} \tag{6.6}$$

Where G and M are the Guinier and Porod scale factors respectively, R_g is the radius of gyration, s is a parameter used to account for anisotropic objects, and m is the Porod exponent. To analyse the Guinier and Porod regions with a smooth transition a continuity criteria arises where their functions and resulting derivatives must be continuous at a value of Q_1. Enforcing this requirement yields the following relationships:

$$Q_1 = \frac{1}{R_g}\sqrt{\frac{(m-3)(3-s)}{2}} \tag{6.7}$$

and

$$M = G\ exp\left[\frac{-Q_1^2R_g^2}{3-s}\right]Q^{m-s} \tag{6.8}$$

$$= \frac{G}{R_g^{m-s}} \, exp\left[\frac{-(m-s)}{2}\right]\left(\frac{(m-s)(3-s)}{2}\right)^{\frac{m-s}{2}}$$

Q_1 is iteratively calculated through Equation 6.8 and is therefore not a set value.

6.2.4.3 Polymer-Surfactant Complexes

An empirical model for scattering data characterised by a broad peak was used to fit the bulk scattering measurements of polymer-surfactant complexes. The model accounts for a broad Lorentzian-type peak and a power law decay using the relationship(412):

$$I(Q) = \frac{M}{Q^m} + \frac{C}{1 + (|Q - Q_o|\xi)^g} + background \tag{6.9}$$

Where C is the Lorentzian scale factor, Q_o is the scattering vector at the position of the peak, ξ is a characteristic length and g is the exponent of Q. Details of this model can be found in the software documentation of the SasView 4.0.1 software.

6.2.4.4 Droplet Interfaces

An empirical model incorporating two Lorentzian-type functions was fit to scattering data obtained from drop systems in polymer-surfactant solutions. This model fits for two characteristic lengths using the following equation (412, 413):

$$I(Q) = \frac{A}{1 + (Q\xi_1)^f} + \frac{C}{1 + (Q\xi_2)^g} + background \tag{6.10}$$

Details of this model can be found in the software documentation of the SasView 4.0.1 software

6.2.5 Image Processing

Images of the drops at the junction where they enter the main channel (shown in Figure 6.1B) were captured before and after each SANS measurement. Basic image processing techniques were performed on the images using MATLAB to extract the drop dimensions and frequency. The background was estimated using a morphological dilation on an image stack of around 1000 images, with a structuring element oriented along the frame dimension. Binary thresholding using Otsu's method was applied to identify the drops and their morphologies, with an additional thresholding factor incorporated to allow modifications. An in-built MATLAB function, regionprops, which returns a range of properties for each object within a binary image, was used to fit the drops dimensions and identify their location within the image/channel. Drops were tracked across images and assigned a drop index using paramsTracking. The frequency was than obtained by assigning an arbitrary datum position along the channel with each drops crossing time either interpolated or extrapolated to depending on the available information of each drop. Figure 6.3 shows an example image summarising the information taken from each frame.

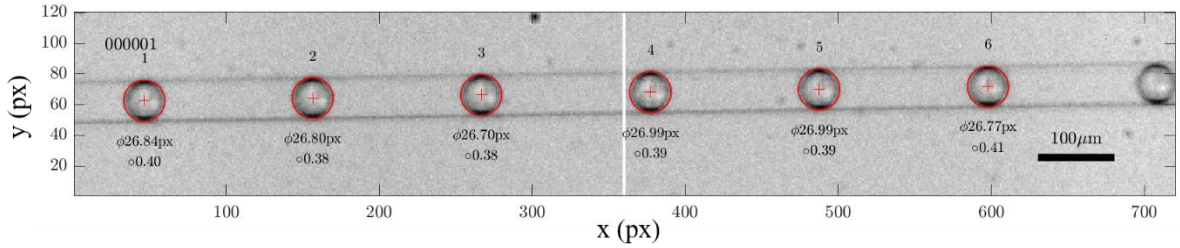

Figure 6.3 Example image of the drops within the main section of the channel. The centre point (red cross), drop edge (red circle), diameter, eccentricity and drop index are shown for each drop. The white line through the centre of the image denotes the location of the datum point used to determine drop frequency.

6.3 Results and Discussion

6.3.1 Single Component

To verify the validity of our microfluidic device in place of a typical SANS cell the scattering from a 50 mM SDS solution in D_2O was captured. Figure 6.4 compares the normalised scattering intensity as a function of scattering vector between a static measurement of 20 mM of SDS in D_2O taken from a 2 mm path-length quartz cell, and the flow measurement obtained from our 51.2 μm path-length channels. The flow measurement was performed with a total channel flowrate of 270 μL/hr, giving a fluid velocity of 26.6 mm/s within the main channel. Both sets of scattering profiles clearly present behaviour analogous to the presence of micelle structures. The characterisation of SDS with SANS has been extensively covered in the literature, however the reported shape of the micelle is highly variable with samples described as spheres (414-416), prolate (227, 417-419) or oblate (335, 336, 420-422) ellipsoids and rods (422, 423). In this case a prolate ellipsoidal model with Hayter-Penfold structure factor has been used to fit the data following an analysis from a range of shape dependent models and is shown as a solid line in the data presented in Figure 6.4 (424). The SLD of the headgroup portion of the micelle is assumed to be equivalent to the solvent due to its ability to penetrate the area (418, 419). Therefore, the static system was fit with the equatorial axis constrained to be 16.7 Å , the length of a fully extended dodecyl chain (425). The resulting fitted parameters were the polar radius, micelle charge and volume fraction of micelles present. To obtain a model with a best fit that can accommodate changes in structure that may occur due to flow conditions, the equatorial radius in the microfluidic results was unbounded and thus included as a fitted parameter. As seen in Figure 6.4, the corresponding fits are in strong agreement across the entire *q* range for both sets of experimental data.

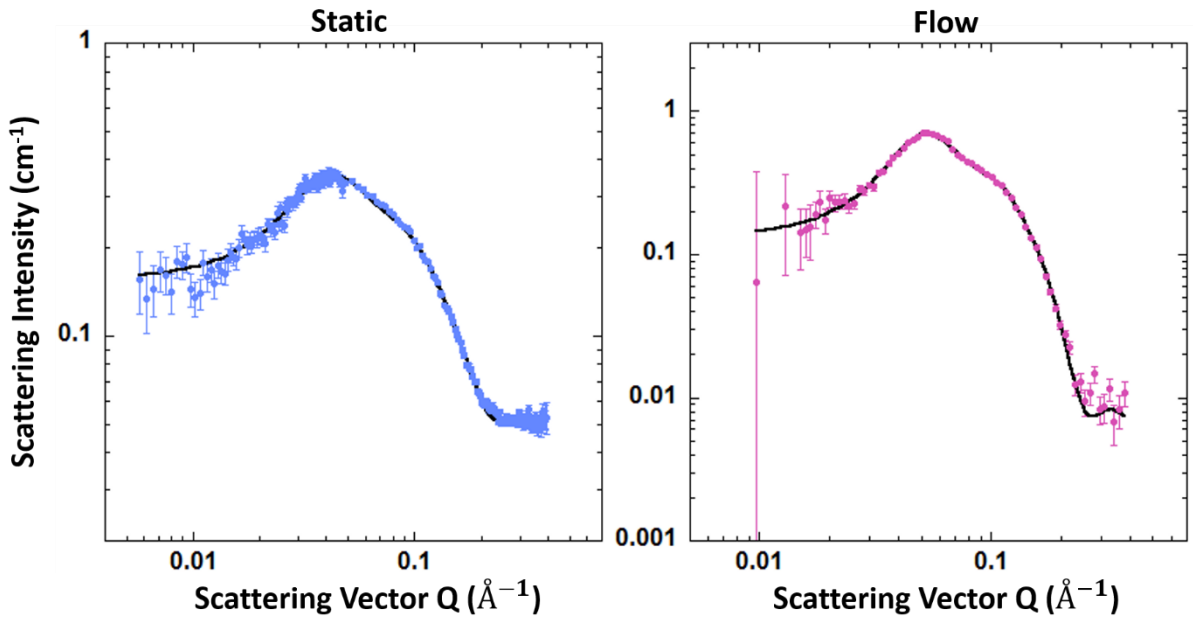

Figure 6.4 Normalised scattering intensity as a function of the scattering vector Q for SDS at concentrations above the CMC (roughly 8 mM). Static data (left) from a 20 mM SDS in D_2O solution (424). Flow data (right) is for a 50 mM SDS in D_2O solution obtained from the microfluidic studies. The markers represent the experimental scattering data, while the solid lines show the theoretical fits obtained from an ellipsoidal model with a Hayter-Penfold structure factor.

The structural parameters obtained from the fits are summarised in Table 6.1, with a full list of fitting parameters located in the Appendix (A9.9.1). The axial ratio can be used as an indication of the degree of elongation of a prolate ellipsoid, where an increase in value corresponds to an increase in elongation. Comparing values of the axial ratio obtained from the flow data to the static data, it can be seen that the micelle under flow is more elongated, presumably due to shear forces induced by the flow conditions within the microfluidic channels. However, an increase in salt concentration will also elongate charged micelles due to screening of head group repulsions, which alters the geometric packing of the micelle to become more cylindrical. Nevertheless, comparison to data obtained from Tabor *et al.* (227) for a 50 mM of SDS static system suggests that the micelle elongation is in fact a result of the microfluidic flow conditions, as the axial ratio increases from 1.37 to 1.49 when flowing the equivalent solution through the microfluidic device. The aggregation number of the micelles was determined by dividing the micellar volume by the molecular volume of a single surfactant tail, where V_{tail} is equivalent to 351 Å (227). As expected, increasing surfactant concentration results in an increase in aggregation number. Despite changes in the micelle geometry between the static and flow data at 50 mM of SDS, the micelle volume and by extension aggregation number remains essentially constant. This is reasonable given the micelles elongation is a result of shear force.

Table 6.1 Summary of structural parameters determined from fitting an ellipsoidal model with a Hayter Penfold structure factor to SDS in D_2O solutions in static and flow conditions. $\boldsymbol{R_e}$ and $\boldsymbol{R_p}$ denote the equatorial and polar radii of an ellipsoidal micelle respectively, $\boldsymbol{N_{agg}}$ is the number of surfactants per micelle, $\boldsymbol{D_m}$ is the average distance between two micelles and $\boldsymbol{S(Q_{max})}$ is the scattering intensity at the first peak of the structure factor plot.

	Static		Flow
	20 mM SDS	**50 mM SDS***	**50 mM SDS**
$\boldsymbol{R_e}$ **(Å)**	16.7	16.7	16.1 ± 0.17
$\boldsymbol{R_p}$ **(Å)**	21.2 ± 0.2	22.9	24.0 ± 0.5
Axial Ratio	1.27	1.37	1.49
Salt Concentration (mM)	11.2	19.3	19.3
$\boldsymbol{N_{agg}}$	70	75	74
$\boldsymbol{D_m}$ **(Å)**	152	108	122
$\boldsymbol{S(Q_{max})}$	1.06	1.15	1.15

*From reference (227)

The structure factor S(Q) defines the interference of scattering from multiple particles and can therefore provide information on the interaction between the micelles (426, 427). Figure 6.5 shows the structure factor as a function of the scattering vector Q for the static and flow systems. The position of the first structure factor peak Q_{max} is related to the average distance between two micelles D_m by the relationship $D_m = 2\pi/Q_{max}$ (57, 428), which is summarised for each system in Table 6.1. As expected, the average intermicellar distance decreases with increasing concentration, as a physical increase in the number of micelles must bring them closer together. When comparing the flow to the static data at 50 mM of SDS the D_m value is larger. For a spherical system this would suggest the micelle spacing would increase when subjected to flow. Yet, the concentration has not changed, nor has the electrotactic repulsion between head groups. Further, the magnitude of the first peak $S(Q_{max})$, which characterises the degree of the local structure around a given micelle remains constant (427, 428) also suggesting no significant changes to the head group interactions. As the micelle is now more prolate in flow, the simple model of average spacing for spherical objects implicit in D_m is not strictly appropriate. If the prolate micelle has a random orientation, the average distance would be expected to be similar to spherical micelle case. As the prolate micelle shape is induced from shear it is reasonable to assume the prolate axis is at least partially aligned with the flow direction. An alignment of longer axis with flow would result in a lager separation between micelles in the direction perpendicular to flow, where the smaller ellipsoidal axis is aligned. Thus, the increase in D_m could be a result of the change in geometry of the micelle to more elongated ellipsoids, requiring an increase in spacing to accommodate the local packing structure at that concentration, or the orientational re-alignment of the micelles in the direction of the flow.

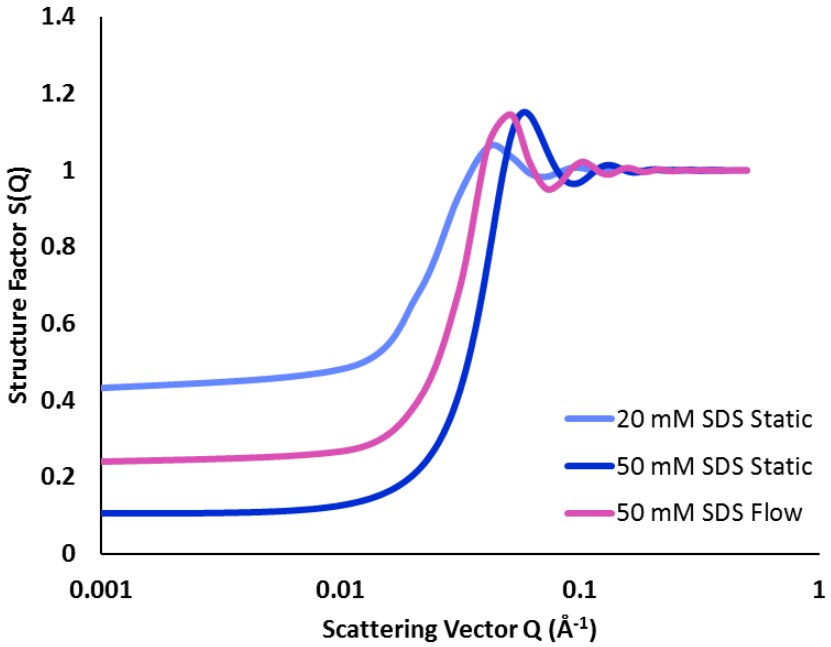

Figure 6.5 Structure factor S(Q) as a function of the scattering vector Q obtained from a Hayter-Penfold fit for charged colloidal dispersions to a 20 mM and 50 mM of SDS static system and 50 mM of SDS flow system. The magnitude and position of the peak in the curve indicates the degree of local structuring and intermicellar distance within the solutions respectively.

Investigation into the structural behaviour of micelles in flow using Rheo-SANS techniques have covered a variety of systems including those containing worm-like micelles (429, 430), rod-like micelles (431-433) and Pluronics (434-436). Reoccurring comments consistent across these studies include the observation of rod to cylinder transitions in micelle structures with increasing shear force and the orientational alignment of the micelles with flow. Notably, Penfold and co-workers have produced an extensive body of literature on the behaviour of common surfactants (such as SDS, $C_{16}E_6$, CTAB and DDACI) and their mixtures, but in high salt concentrations such that the systems formed rod-like micelles, which agree with these observations (437-440). By measuring the scattering with the beam positioned orthogonal and normal to the flow direction they showed that the anisotropy of micelles in a 50 mM of SDS solution with 1.3 M of NaCl would increase with increasing shear until reaching a constant value at a minimum shear threshold of around 8000 s^{-1} (441). This behaviour is indictive of rigid, non-deformable particles.

Cabral and co-workers have previously studied the structure and alignment of SDS systems using microfluidic SANS (25, 335, 336). In their initial report introducing the new technique they measured the alignment and spacing of an SDS/octanol/d-brine mixture at ratios 17.4/62.6/20 wt%, which form multilamellar vesicles. These were performed on a device with channel depths/a path-length of 540 μm and a scattering volume of just 0.1 μL (25). Their second paper exploring the use of microfluidic SANS for rapid contrast matching measured the scattering of a

10% w/v SDS solution in varying ratios of D_2O/H_2O solvents at a fluid velocity of 16.7 mm/s in a device with a 250 μm path-length and 16.5 μL scattering volume. An ellipsoidal model with a Hayter-Penfold structure factor was used to model the data, providing a fit of 14 Å and 24 Å for the minor and major axis respectively and therefore axial ratio of 2.5. This geometry is questionable given the largest reported axial ratio for SDS without added salt in the literature is 1.84 and their fluid velocity is around 40% less than the velocity within our measurements (227). Nevertheless, these results support our findings that the micelle structures are elongated in flow.

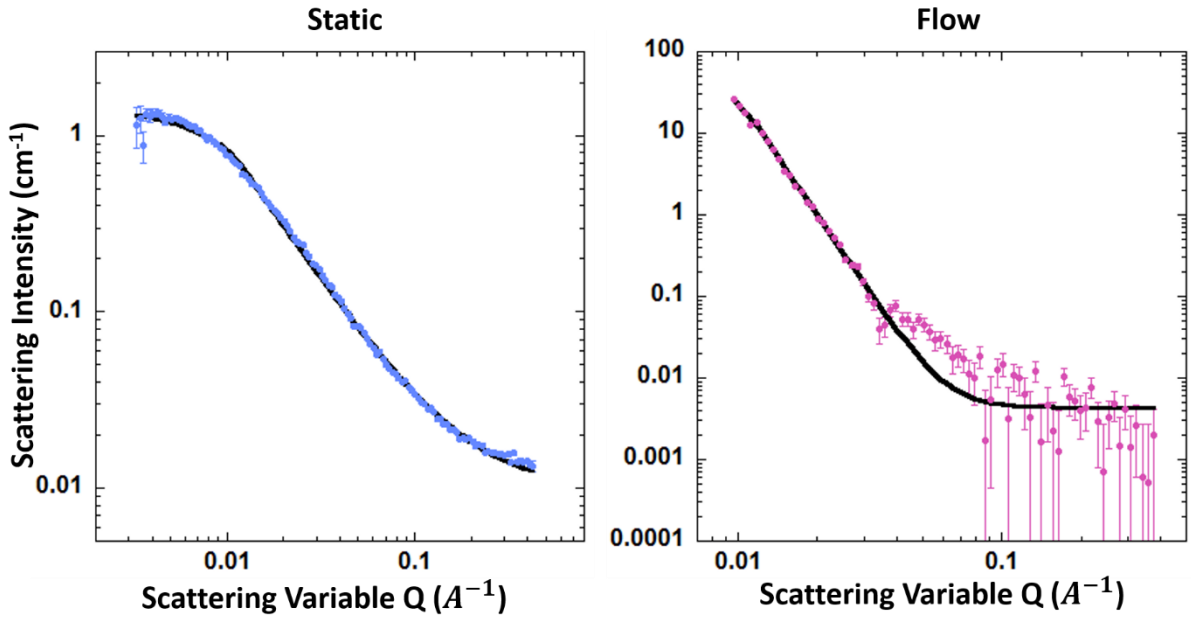

Figure 6.6 Normalised scattering intensity as a function of the scattering vector Q for 0.5% w/w PVP in D_2O solutions. Static data (left) were provided by a collaborator[1]. Flow data (right) was obtained from the microfluidic studies. The markers represent the experimental scattering data, while the solid lines show the theoretical fits obtained from a Guinier-Porod model.

For additional substantiation, the same approach was applied to a 0.5% w/w PVP solution as presented in Figure 6.6. This time the flow measurement was performed with a total channel flowrate of 450 μL/hr, giving a fluid velocity of 44.4 mm/s within the main channel. These data show that the microfluidic experiments also provide enough signal to observe polymeric objects within the device. The characteristic structures of polymers can be extracted from SANS measurements using a range of models, where PVP has been specifically fit using both an excluded volume model and the Beaucage model (413, 442-445). For our data a generalised

[1] Thanks to Mark Vidallon and Rico Tabor

Guinier-Porod model was fit to the data and is shown alongside the data presented in Figure 6.6 (411). This method is similar to the Beaucage model, however as shown in a comparative study by Hammouda it outperforms the model across most geometries, where the Beaucage model only matched up for Gaussian coil fits (446). The static data is in strong agreement with the Guinier-Porod model across the entire q-range measured. For the flow data, at low q-range where the Guinier region exists the model fits well. However, at higher q-values where the spread of data is larger and the statistical quality also reduces, the agreement obviously suffers but the general shape is tracked.

Table 6.2 lists the parameters computed by the Guinier-Porod function for each of the experiments. A complete summary of fitting parameters is located in the Appendix (A9.9.2). The radius of gyration R_g should be considered as an apparent value as it does not necessarily represent the properties of a single chain. An R_g value of 114 Å for PVP K-90 in static conditions is in good agreement with the literature, where Knappe et al. reported an R_g value of 121 Å from fitting SAXS data with a Guinier model (447). Comparing this result to the same system under flow the PVP chains appear to be larger in size, recording an R_g value of 159 Å. The Porod exponent m and dimensionality parameter $(3 - s)$ both provide information on the structure and dimensions of the scattered objects. The dimensionality parameter was introduced into the Guinier-Porod model to account for non-spherical objects and consequently offers information on the structure (411). An s parameter of 0 suggests that the static data is taken from a globular object such as a sphere, while a value of 1 tells us that the polymer in flow takes the form of a rod. This sphere-to-rod transition is hypothetically responsible for the increase in the apparent size of the polymer observed in the radius of gyration. The Porod exponent is measured in the high q-region where the scattering intensity begins to decay as a power law and is related to the dimensions of a fractal. A value of 1.67, as calculated for the static data, represents scattering from a mass fractal and more specifically a fully swollen chain in a good solvent with dimension equal to m (411, 413). An exponent larger than 3 corresponds to a surface fractal, where the dimension is equivalent to $6 - m$ (448). Therefore, the value of 4.81 for the flow data suggests that the polymer in flow is scattering as a 1D rod. This is in agreement with results obtained by Hammouda for 0.5% P85/d-water solutions at 343 K, which form cylindrical micelles, and report a Porod exponent of 4.82 and s parameter of 0.94, which are directly equivalent to the values calculated from the flow data (411). Given this analysis it is reasonable to suggest that the PVP structure also elongates whilst in flow.

Table 6.2 Summary of structural parameters determined from fitting a Guinier-Porod model to 0.5% w/w PVP solutions in static and flow conditions. R_g is the radius of gyration, s defines the dimensionality parameter $(3 - s)$ and m is the Porod exponent.

	Static	Flow
R_g (Å)	114 ± 0.7	159 ± 1.2
s	0.05 ± 0.002	0.95 ± 0.007
m	1.58 ± 0.004	4.81 ± 0.030

The corroboration between the scattering intensity patterns of our microfluidic SANS experiments and standard static measurements provides a basic proof that we are able to successfully see a self-interacting soft matter system and polymeric object in our 50 μm path-length device covering 100 channels. This is further strengthened by the ability to perform detailed quantitative analysis on the data which is in good agreement with the literature.

6.3.2 Two-Component: Polymer-Surfactant Complexes

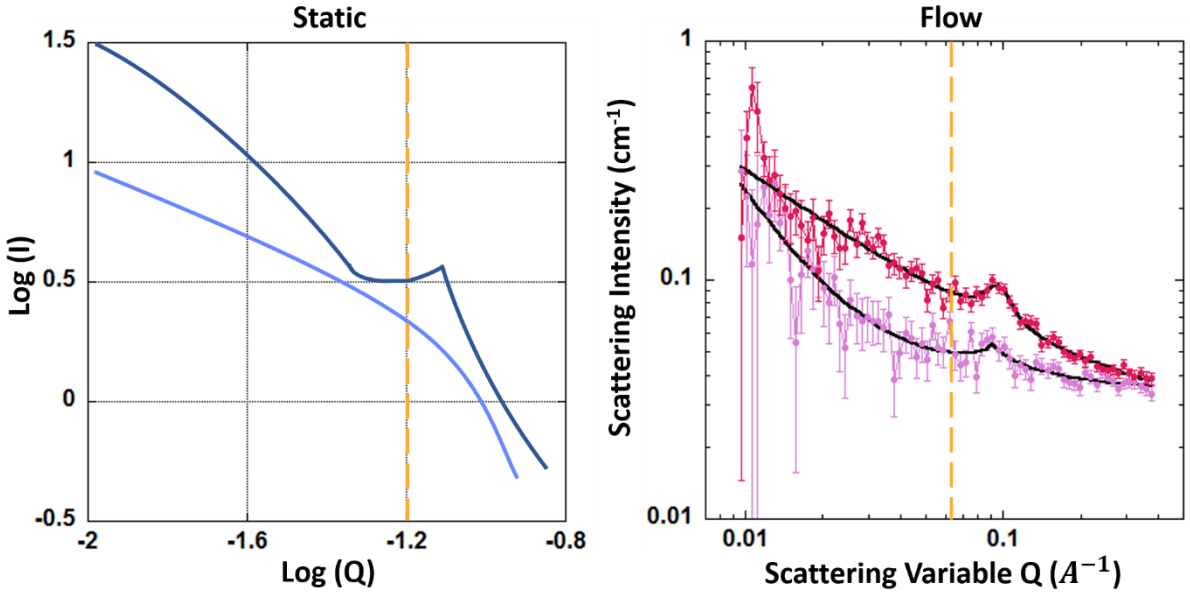

Figure 6.7 Left: Prediction of scattering curves from polymer in a dilute surfactant solution (light blue) and polymer in a concentrated surfactant solution (dark blue) based on linear response theory in static conditions. This graph has been reproduced from reference (449). Right: Normalised scattering intensity as a function of the scattering vector Q for 0.5% w/w PVP with 10 mM of SDS (light pink) and 30 mM of SDS (dark pink) D_2O/H_2O solutions in flow. Here the markers represent the experimental scattering data, while the solid lines show the theoretical fits obtained from a broad peak empirical model. The dashed orange line is included to visually aide the comparison of features between the two conditions.

To investigate the nature of polymer-surfactant complexes in flow, the scattering of two-component mixtures consisting of PVP and SDS were measured using microfluidic SANS. The flowrate was held constant at 270 μL/hr (fluid velocity of 26.6 mm/s) for solutions containing 0.5% w/w PVP and 10 or 30 mM of SDS. Figure 6.7 shows the results from these measurements, where increasing the SDS concentration shows an increase in the scattering intensity. The intensity patterns are reminiscent of the polymer curves presented in Figure 6.6, however are characterised by a peak in the high q-range which increases in magnitude with increasing SDS concentration. Cabane and co-workers were the first to study the structures of polymer surfactant complexes in the bulk using SANS, covering a range of systems and polymer concentration regimes (393, 449-453). The plot on the right hand side in Figure 6.7 is reproduced from one of their papers investigating mixtures of non-ionic polymer poly(ethylene oxide) (PEO) and SDS (449). It is a schematic of scattering curves of a polymer in dilute or concentrated surfactant solution predicted from linear response theory for the coupling between two weakly interacting systems. Comparing these to our experimental results, the peaks seen in the high q-range are clearly predicted in the polymer with concentrated surfactant curve and correspond to closely the same *q* value. This peak can be linked to intermicellar correlations from within the polymer-surfactant complexes (449). Claesson *et al*. have explored oppositely charged polymer-surfactant complexes in some detail, however these systems have different aggregation pathways which tend to form precipitates and therefore different intensity patterns (9, 454, 455).

Table 6.3 Summary of structural parameters determined from fitting a broad peak empirical model to 0.5% w/w PVP solutions with SDS in flow conditions. $\boldsymbol{\xi}$ is the correlation length, $\boldsymbol{R_g}$ is the radius of gyration, $\boldsymbol{d_0}$ is a characteristic distance between scattering objects and $\boldsymbol{p}$ is the Porod exponent.

	10 mM SDS	**30 mM SDS**
$\boldsymbol{m}$	1.76 ± 0.224	0.80 ± 0.044
$\boldsymbol{\xi}$ **(Å)**	32.9 ± 27.5	71.2 ± 16.1
$\boldsymbol{R_g}$ **(Å)**	46.5 ± 38.9	101 ± 22.8
$\boldsymbol{d_0}$ **(Å)**	68.9 ± 4.1	65.6 ± 1.2

A well-known broad peak feature is seen in SANS measurements of polyelectrolytes (456-458). As discussed in Chapter 4 of this thesis, polymer-surfactant complexes formed between neutral polymers and charged surfactants have been shown to behave as pseudo-polyelectrolytes. The similarities in intensity patterns between them was therefore unsurprising and the use of a broad peak empirical model to fit the scattering data from these measurements was deemed reasonable. The fits from this model are shown as a solid line in Figure 6.7 and a summary of the fitted structural parameters are listed in Table 6.3. The model accounts for a Lorentzian type peak and power law decay, and has a similar form to the correlation length model used by Hammouda *et*

al. to fit PEO polymers (459, 460). It Is adjusted to fit for the peak position which corresponds to the d-spacing ($d_0 = \frac{2\pi}{Q_o}$), a characteristic spacing between scattering objects which is a feature of a range of soft matter systems such as polyelectrolytes, layered structures and multiphase systems.

The Porod exponents suggest that at 10 mM of SDS with 0.5% w/w PVP the complex structure is in the form of a fully swollen chain in a good solvent, as seen in the static PVP measurements. While at 30 mM a value of around 1 represents the scattering from a stiff rod or thin cylinder (411). In comparison to the PVP data under flow in the absences of surfactant, the presence of the surfactant causes configuration chances. At 10 mM SDS, the conformation of the polymers is more of a globular nature. This is surprising as this configuration is similar to the PVP in the absence of surfactant without flow. At the higher surfactant concentration of 30 mM, the PVP is more rod like in nature, also consistent with a charged polyelectrolyte. The addition of 10 mM of SDS is expected to restrict the structural configuration of the polymer due to both accommodating the bound micelles as well as charge repulsions, reducing its freedom to form more extended geometries. While at 30 mM of SDS the system is predicted to be around the point of saturation with a higher ionic strength increasing charge screening effects which could allow more flexibility in flow. However, without static measurements of the polymer-surfactant complexes it is hard to say whether the change in geometry is due to aggregation of more SDS molecules or shear forces elongating it in flow. It should also be noted that the flow measurement of PVP was performed at flowrates around 1.7 times faster than these polymer-surfactant complex measurements, thus smaller degrees of elongation due to flow would be likely.

The correlation length **ξ** is equal to the end-to-end distance for very dilute polymer systems and can be related to the radius of gyration by $R_g = \sqrt{2}\xi$ for such cases (459). The overlap concentration c^* corresponds to the point where polymers begin to interact, signifying the transition from dilute to semi-dilute systems and can be calculated from the relationship $c^* = \frac{3M_w}{4\pi R_g^3 N_A}$ (461). Given the radius of gyrations extracted from the PVP measurements, the overlap concentrations are 9.6% w/w and 3.56% w/w for the static and flow system respectively. Therefore, as our solutions of 0.5% w/w PVP alone are significantly dilute, it is reasonable to assume that the system remains within the dilute regime despite the addition of SDS molecules. The R_g values suggest that the polymer undergoes a compression or reduction in size with the initial addition of SDS. This is expected from the PVP chains as they wrap around the SDS micelles, effectively reducing their available free contour length (453). This is in contrast to the polymer surfactant complexes, which R_g values increase in size with the further addition of SDS. This is likely the result of increasing the number of bound SDS molecules to the PVP chain (102), which

by doing so effectively increases the size of the complex due to an increase in the objects molecular weight. This increase in complex size correlates well to the decrease in the d-spacing value, where the relationship between the size of the object and the spacing between scattering objects is roughly a cubed root difference.

In Chapter 4 of this thesis a depletion layer thickness was determined for these systems from fitting AFM curves with a depletion and EDL force model. A characteristic length was related to it, being equal to twice its value, and used to apply polyelectrolyte scaling theory in order to estimate an independent value for the osmotic pressure. Although the characteristic lengths share similarities in their description, the absolute values are difficult to compare based on their use in context. The AFM depletion length accounts for the size of the object plus the EDL surface forces and the EDL from the complexes. Due to this they are sensitive to surface charge and therefore are a function of the number of absorbed charged molecules at the surface. Essentially the depletion characteristic lengths are not defined by the physical length scale but by the force length scale. The characteristic lengths described here, based on neutron scattering contrast, don't see the solvent or double layer behaviour and are therefore considerably smaller than the values presented in the AFM analysis.

6.3.3 Droplet Interfaces (Two Phases)

Having validated and analysed the microfluidic device using single phases of SDS and PVP solutions the measurement was applied to droplet systems to investigate scattering of the complexes at the interface. Drops were generated using different flowrates in order to provide consistent drop generation at sizes smaller than the channel dimensions. Drop generation depends on the fluid properties, such as capillary number, which are variable across solution components and concentrations. Key parameters obtained using the image processing steps described in the methods section of this chapter on images taken before and after the SANS measurements is shown in Table 6.4. A complete list is provided in the Appendix (Table A9.8). The drops were produced at frequencies ranging from 111 to 227 Hz at an average drop diameter of around 51 μm. The measured drop diameters were dependent on the degree of thresholding applied to the images. Due to variability in the clarity of drop edges across some frames, there was a thresholding limit for each system at which all drops could be well defined and not result in nonsensible fits. Examples of a fit with thresholding below this limit are shown in the Appendix (Figure A9.8). For drops with a clear edge, thresholding at the limit typically caused fits larger than observed, thus the drop diameters reported here are on average greater than the actual expected sizes. Cyclic fluctuations in the drop frequency was observed, which is likely due to pump transience as discussed in Chapter 5 of this thesis. This makes direct comparisons between the magnitude of scattering intensities at different concentrations difficult, however on average

a volume fraction of around 0.85 for the aqueous phase was measured for the SDS and PVP systems.

Table 6.4 Summary of the key parameters surrounding drop generation. The values measured through image processing analysis are provided both before and after the SANS measurements.

	50 mM SDS		20 mM SDS/PVP		30 mM SDS/PVP	
	Before	**After**	**Before**	**After**	**Before**	**After**
Dispersed Phase Flowrate (µL/hr)	50		45		45	
Continuous Phase Flowrate (µL/hr)	175		135		115	
Spacer Flowrate (µL/hr)	50		40		30	
Drop Diameter (µm)	49.6	52.6	51.6	50.4	51.9	50.2
Frequency (Hz)	151	227	111	149	-	166
Volume Fraction of Aqueous Phase	0.87	0.77	0.87	0.84	-	0.79

In Figure 6.8 the scattering measured from drops generated in a 50 mM of SDS and D_2O/H_2O solution is shown alongside the single-phase scattering data presented previously in Figure 6.4 of 50 mM of SDS in D_2O in flow. To directly compare the results, variances in the measurements need to be considered. Due to the presence of the dispersed oil phase a reduction in scattering volume in the drop measurements will reduce the overall scattering intensities. Using the approach used by Cabral *et al*., the volume fraction of the dispersed phase was quantified from the drop frequency and size and subsequently used to rescale the data (336). As both data sets were normalised by subtracting the scattering of their respective solvent, potential differences due to the incoherent scattering of water introduced by the mixed solvent are not applicable. Despite the obvious differences in the magnitude of scattering intensities the two scattering patterns are relatively alike. However, a fit to the drop data with an ellipsoidal model and Hayter-Penfold structure factor, as previously used (Figure 6.4), poorly describes the data (solid line in Figure 6.8). To such a point that the structural parameters attained from the fit are subject to error equivalent to the value of the property, which are shown in the Appendix (Table A9.6). This inability to fit a micelle structure to the scattering suggests that there is another object that is clearly being scattered, which we hypothesis to be a coating of SDS at the drop interface. SANS measurements previously performed on emulsions stabilised by surfactants or polymer-surfactant complexes have used core shell models to measure the adsorbed layer thickness at the interface (401, 402, 404). These were typically performed on emulsions with drop radii of around 200 nm, such that in the model the core is represented by the drop and the shell as the layer. This method is therefore impractical for our system given the average drop diameter of around 50 µm. At this time, there is no available model appropriate to fit our data for a layer at the interface and further work dedicated to this specific system is recommended for the future. However, the differences outlined here provides strong evidence that we have a coating on the surface of the drops.

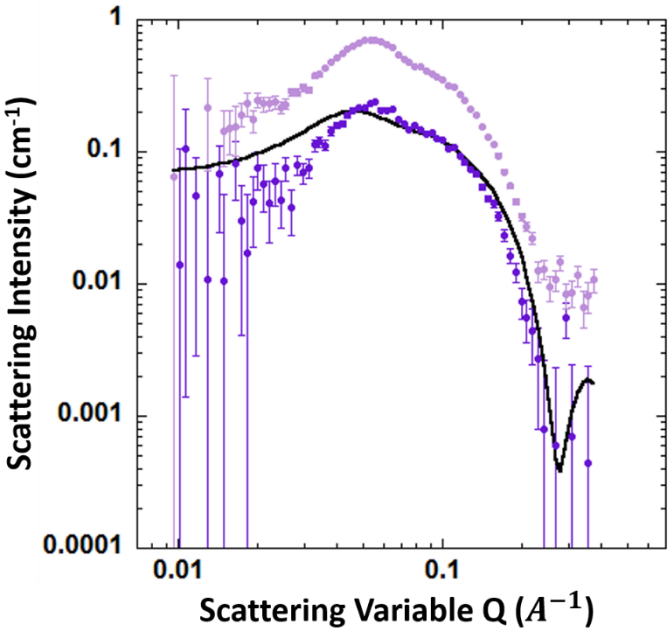

Figure 6.8 Normalised scattering intensity as a function of the scattering vector Q from a 50 mM of SDS and D_2O solution obtained from the single-phase microfluidic studies (light purple) and droplet microfluidic measurements using a 50 mM of SDS and D_2O/H_2O solution (dark purple). Here the markers represent the experimental scattering data, while the solid lines show the theoretical fits obtained from an ellipsoidal model with a Hayter-Penfold structure factor.

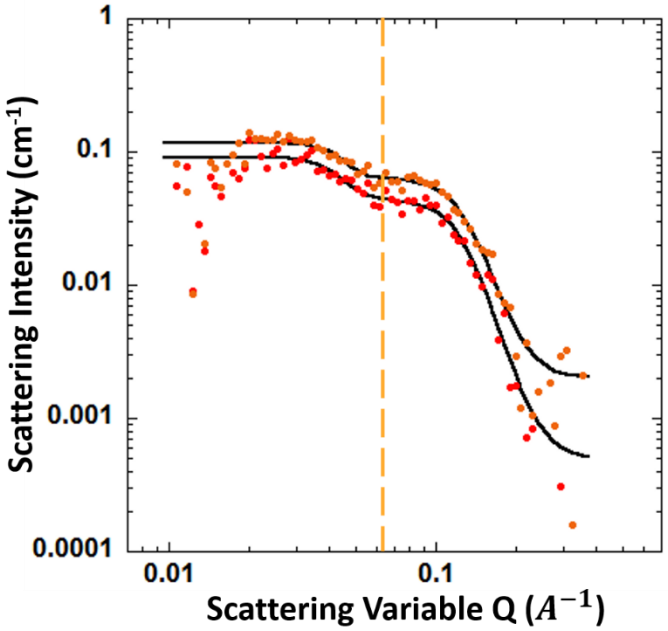

Figure 6.9 Normalised scattering intensity as a function of the scattering vector Q from droplet microfluidic measurements using a 0.5% w/w PVP with 20 mM of SDS (red) or 30 mM of SDS (orange) and D_2O/H_2O solution. Here the markers represent the experimental scattering data, while the solid lines show the theoretical fits obtained from a two Lorentzian-type function. The dashed orange line is included to visually aide the comparison of features between the two-component data with drops in this figure to the key peak location for the two-component system without drops in Figure 6.7.

Drops formed in polymer-surfactant solutions show dramatically different scattering patterns compared to their single-phase equivalence (as shown in Figure 6.7). The broad peak seen in the single-phase data at a q-value of around 0.1 is no longer visible in the droplet measurements of 0.5% w/w PVP and 20 or 30 mM of SDS provided in Figure 6.9. There are however two clear characteristic shapes in the curves, which can be fit to a two-Lorentzian type function to extract two characteristic lengths. A larger and smaller length scale is obtained, where the values of each length at the SDS concentrations measured are relatively similar as shown in Table 6.5. The increased level of scattering reflects the increasing concentration of SDS and does not appear to affect the value of the lengths. The SANS studies performed by Tucker *et al*. on polymer-surfactant mixtures at an oil-water interface fit adsorbed layers of 10 to 15 Å from the slope of the scattering at higher q-values (404). The values of $\xi 1 \approx 23$ Å are therefore of a length scale that can be reasonably associated to a layer of adsorbed complex at the oil water interface, which has already been predicted by the work presented in Chapter 4 and 5 of this thesis. Although further development into a theoretical model is necessary to draw true qualitative analysis from the droplet microfluidic SANS, from a semi-quantitative approach we have extracted a length scale that is consistent with the literature suggesting that there is scattering signal from the interface.

Table 6.5 Characteristic lengths (ξ) fit from a two-Lorentzian type function to scattering from drop measurements using a 0.5% w/w PVP with 20 mM of SDS (red) or 30 mM of SDS (orange) and D_2O/H_2O solution

	20 mM SDS and PVP	**30 mM SDS and PVP**
ξ1 (Å)	23.3 ± 1.2	22.8 ± 0.87
ξ2 (Å)	7.9 ± 0.2	7.9 ± 0.2

6.4 Conclusion

The use of a novel microfluidic device with a 51.2 μm path-length in SANS measurements was validated through the use of single-phase and two-phase experiments. Corroboration between the scattering intensity patterns of the single-phase microfluidic SANS measurements and standard static measurements showed that soft matter systems at the concentrations explored could be successfully seen with the technique. Detailed quantitative analysis on these systems was in strong agreement with the literature. It was also able to provide evidence of shear-induced transformations in the micelle structure of 50 mM SDS solutions and the polymer confirmation of 0.5% w/w PVP solutions, as well as information on the shape and size of their complexes in flow. Droplet microfluidic SANS was qualitatively assessed, showing clear differences to the bulk single-phase data of equivalent solutions, suggesting evidence of changes to the scattering characteristics which is predicted to be due to an adsorbed layer. Future work into a theoretical model designed to fit these specific experiments is necessary to attain detailed qualitative

information on the structures present beyond an estimated thickness of the layer. Nevertheless, these SANS data provide a consistent picture with the AFM measurements and both sets of microfluidic droplet studies, that there is adsorption of the PVP-SDS complex to the drop interface under flow.

Acknowledgements

This work benefited from the use of the SasView application, originally developed under NSF award DMR-0520547. SasView contains code developed with funding from the European Union's Horizon 2020 research and innovation programme under the SINE2020 project, grant agreement No 654000. This work was performed in part at the South Australian node of the Australian National Fabrication Facility, a company established under the National Collaborative Research Infrastructure Strategy to provide nano and micro-fabrication facilities for Australia's researchers. We thank the ARC for funding and the PFPC for providing infrastructure support.

Chapter 7: Conclusions

The overarching objective of this thesis was to understand how polymer-surfactant complexes mediate adhesive interactions, with a focus given to the development of a novel microfluidic platform capable of investigating these systems using high throughput measurements. The attractive interactions between oil drops in PVP and SDS solutions were studied using both drop chaining in a microfluidic device and direct force measurements on an AFM. Links between the two methods was explored in detail with emphasis on understanding and establishing similarities in surface coverage and the structural composition of layers at the drops interface. Microfluidic interfacial tension was used to study the surface coverage and adsorption time scales, while droplet microfluidic SANS was developed as a technique to access information on the composition and structure of the layers.

PVP and SDS complexes have been shown previously to aggregate in the bulk and exist as similar structures at the surface of rigid particles (130) and air-water interfaces (31, 34). To link these structures to the function of colloidal fluids, such as gel formation and deposition, identification of the force behaviour was required as it is not accessible or plausible to extrapolate this information from these bulk and interfacial characterisation studies. Direct force measurements were performed using both rigid and deformable interfaces to capture a complete quantitative understanding of the interactive forces present within the system. The concentrations of SDS at which the force studies were performed was identified using pendant drop interfacial tension measurements, which defined a clear region where complex formation occurs.

Hydrophobic and hydrophilic rigid particles were first measured to quantify the attractive forces between surfaces in the presence of the PVP/SDS complexes, but in the absence of interfacial deformation. The force curves between hydrophilic particles exhibited force behaviour consistent with the presence of a steric brush, as observed previously (130). The presence of a steric force obscured any attractive forces attributed between the surfaces, thus hydrophobically modified surfaces were used. The measurements conducted between hydrophobic particles demonstrated that depletion and electrical double layer forces dominate the force behaviour between two hydrophobic surfaces in this system. An increase in the magnitude of the attractive minima in the force curves was observed with increasing surfactant concentration, signifying an increase in adhesion. The interactions were modelled using a surface force model and polyelectrolyte scaling theory, given the reported pseudo-polyelectrolyte nature of the complexes (112, 462). An osmotic pressure was calculated from both approaches with differences in values attributed to polydispersity effects unaccounted for within scaling theory analysis (119). Thus, data collected directly from the analysis of the rigid force measurements was used in the fits for deformable surfaces.

Force measurements between two deformable oil drops using the same SDS concentrations displayed similar depletion behaviour. With increasing SDS an increase in adhesion was seen between the drops with a maximum attractive pull-off force reached close to the polymer saturation concentration. Additionally, a repulsive force that appeared on the approach also increased in magnitude with increasing SDS concentration. The Chan-Dagastine-White model adapted for depletion and EDL forces, used the depletion length and osmotic pressure fit from the rigid surface analysis to fit the curves, showing reasonable agreement with the data. A small under prediction by the model of the repulsive force on the approach curve suggests the existence of an additional steric force from the presence of adsorbed PS complexes at the interface as well as the bulk. Dynamic measurements of the drops with increasing collision velocities was performed to investigate the effects of hydrodynamic interactions. At velocities above 500 nm/s, dynamic forces, caused by film drainage between the drops, dominated the force data, such that it was no longer possible to observe the depletion or EDL force features in the measurements.

Observations of drop chains formed via a microfluidic device independently demonstrated the existence of attractive forces between drops in the PVP/SDS systems. Upon exiting the channel into bulk solution, the stability of the drop chains is governed by a balance between drag, buoyancy, and the adhesive forces between the drops. Thus, the persistence of a drop chain was used to identify the strength of adhesion across the range of SDS concentrations. Of those tested, the 10 mM SDS concentration successfully showed significant drop adhesion and chain formation. While concentrations close to this value occasionally exhibited the retention of pairs and triplets, no attractive interactions were seen at either end of the SDS concentration region where complexes were identified to exist.

Correlating the AFM and microfluidic results suggest that attractive forces observed in the AFM lead to adhesive drop chains when the repulsive force on approach is low enough to allow the drops to move into close separation, and when the attractive force is sufficient to hold the drops in a secondary attractive minimum. The ability to draw this conclusion suggests that the study of drop interactions has provided a detailed insight into the adhesive mechanisms controlling these complex fluids. While the maximum adhesive force was identified to directly correlate to the composition of the complex via direct force measurements, the microfluidics showed the importance of physical parameters such as the Laplace pressure in enabling the drops to experience the adhesive interactions. Despite differences in the physical properties and fluid conditions of microfluidic and AFM measurements, an understanding of adhesive interactions between drops in polymer surfactant systems could be grasped via both avenues.

Further developing the microfluidic platform could provide a novel technique for screening through a range of systems with ease. The flowrate of the external fluid near the observation

region, responsible for extending the drop chains away from the exit, would benefit from a design with greater control. Implementing a large expansion chamber with controlled channel co-flow, as seen in the work by Shen *et al*., into future designs would help address this (242). Additionally, with known fluid velocities the implementation of computational fluid dynamics to quantify the drag and buoyancy forces affecting the droplet chains would be possible, paving the way to a means for extending the microfluidic platform capabilities into directly measuring the adhesive forces between drops.

The interfacial tension of oil drops flowing through a microfluidic channel was measured using a technique first developed by Hudson *et al*. (329). Image processing allowed the drops deformation through a contraction to be tracked and related to the Taylors parameter, which was used to regress its interfacial tension. Comparison to pendant drop measurements showed strong agreement, suggesting that the surface chemistry at the drop interfaces are equivalent across both methods despite differences in fluid conditions. Analysing the drop's deformation across a series of contractions provided insight into the adsorption kinetics, which were shown to occur at timescales well below those used in the drop chaining experiments having reached a time invariant value within the first channel constriction. Measurements using substantially higher drop velocities were either able to observe dynamic absorption of the PS complexes or exhibited a scenario where the activity of the molecules in flow has deviated from static behaviour at small residence times.

To gain further insight into the molecular structure of the complexes in solution and at the interface SANS was performed on a novel microfluidic device. Scattering from the single-phase solutions of PVP, SDS and their complex was successfully measured and showed characteristic intensity patterns expected from each condition based on reviews of the literature. Quantitative analysis of each condition provided information on the confirmation and structure of the soft matter materials, with clear evidence of shear-induced transformations in the micelle structure of SDS and chain of PVP realised. Drop based measurements qualitatively showed differences in scattering characteristics compared to the bulk single-phase measurements, alluding to the presence of an adsorbed layer at the drops interface. At this time the detail of structure or composition of this layer beyond an estimated thickness was unable to be attained from the data as models capable of fitting these specific measurements are not available. Future work should focus on developing a theoretical model relevant to this measurement in order to access the necessary information required to extract details on the molecular structure of layers at the interface.

This thesis has explored the surface forces responsible for colloidal adhesion in polymer surfactant systems through a range of methods. However, it was primarily achieved through the

introduction of prelimary work into a novel microfluidic device capable of measuring the adhesive forces between drops. Through developing this techique a greater understanding of the links between surface properties and drop adhesion in polymer surfactant systems was achieved. Practically, this work provides a strong first step towards creating a novel technique for screening through a range of systems with ease. Being able to screen formulations with the microfluidics to probe adhesion or gel formation would go towards revolutionising product development. For example, we see the extensive work required to characterise HEC PS complexes (4, 356, 357, 463, 464), where the methods developed here would enable an equivalent parameter space to be covered on a scale of months rather than years.

Chapter 8: References

1. Bibette J, Mason TG, Gang H, Weitz DA, Poulin P. Structure of adhesive emulsions. Langmuir. 1993;9(12):3352-6.
2. Bibette J, Calderon FL, Poulin P. Emulsions: basic principles. Reports on Progress in Physics. 1999;62(6):969.
3. Poulin P, Bibette J. Adhesion between Pure and Mixed Surfactant Layers. Langmuir. 1999;15(14):4731-9.
4. Bain CD, Claesson PM, Langevin D, Meszaros R, Nylander T, Stubenrauch C, et al. Complexes of surfactants with oppositely charged polymers at surfaces and in bulk. Advances in Colloid and Interface Science. 2010;155(1):32-49.
5. Chiappisi L, Hoffmann I, Gradzielski M. Complexes of oppositely charged polyelectrolytes and surfactants - recent developments in the field of biologically derived polyelectrolytes. Soft Matter. 2013;9(15):3896-909.
6. Goddard ED. Polymer/surfactant interaction—Its relevance to detergent systems. Journal of the American Oil Chemists' Society. 1994;71(1):1-16.
7. Goddard ED. Polymer Surfactant Interaction .2. Polymer and Surfactant of Opposite Charge. Colloids and Surfaces. 1986;19(2-3):301-29.
8. Goddard ED. Polymer Surfactant Interaction .1. Uncharged Water-Soluble Polymers and Charged Surfactants. Colloids and Surfaces. 1986;19(2-3):255-300.
9. Claesson PM, Bergström M, Dedinaite A, editors. Surfce Force Studies of Polymer-Surfactant Complexes at the Solid-Liquid Interface: Relation to Structure of Bulk Complexes. 3rd International Symposium on Food Rheology and Structure; 2003.
10. Nylander T, Samoshina Y, Lindman B. Formation of polyelectrolyte–surfactant complexes on surfaces. Advances in Colloid and Interface Science. 2006;123–126:105-23.
11. Tabor RF, Lockie H, Mair D, Manica R, Chan DYC, Grieser F, et al. Combined AFM-Confocal Microscopy of Oil Droplets: Absolute Separations and Forces in Nanofilms. The Journal of Physical Chemistry Letters. 2011;2:961-5.
12. Browne C, Tabor RF, Grieser F, Dagastine RR. Direct AFM force measurements between air bubbles in aqueous polydisperse sodium poly(styrene sulfonate) solutions: Effect of collision speed, polyelectrolyte concentration and molar mass. J Colloid Interface Sci. 2015;449:236-45.
13. Lockie HJ, Manica R, Stevens GW, Grieser F, Chan DYC, Dagastine RR. Precision AFM Measurements of Dynamic Interactions between Deformable Drops in Aqueous Surfactant and Surfactant-Free Solutions. Langmuir. 2011;27(6):2676-85.
14. Shah RK, Shum HC, Rowat AC, Lee D, Agresti JJ, Utada AS, et al. Designer emulsions using microfluidics. Materials Today. 2008;11(4):18-27.
15. Brosseau Q, Vrignon J, Baret J-C. Microfluidic Dynamic Interfacial Tensiometry (μDIT). Soft Matter. 2014;10(17):3066-76.
16. Cabral JT, Hudson SD. Microfluidic approach for rapid multicomponent interfacial tensiometry. Lab on a Chip. 2006;6(3):427-36.
17. Muijlwijk K, Hinderink E, Ershov D, Berton-Carabin C, Schroën K. Interfacial tension measured at high expansion rates and within milliseconds using microfluidics. Journal of Colloid and Interface Science. 2016;470:71-9.
18. Xu JH, Li SW, Lan WJ, Luo GS. Microfluidic Approach for Rapid Interfacial Tension Measurement. Langmuir. 2008;24(19):11287-92.
19. Xi H-D, Zheng H, Guo W, Gañán-Calvo AM, Ai Y, Tsao C-W, et al. Active droplet sorting in microfluidics: a review. Lab on a Chip. 2017;17(5):751-71.
20. Martin JD, Marhefka JN, Migler KB, Hudson SD. Interfacial Rheology Through Microfluidics. Advanced Materials. 2011;23(3):426-32.
21. Schultz KM, Furst EM. High-throughput rheology in a microfluidic device. Lab on a Chip. 2011;11(22):3802-9.
22. Sharma V, Jaishankar A, Wang Y-C, McKinley GH. Rheology of globular proteins: apparent yield stress, high shear rate viscosity and interfacial viscoelasticity of bovine serum albumin solutions. Soft Matter. 2011;7(11):5150-60.

23. Cristobal G, Arbouet L, Sarrazin F, Talaga D, Bruneel J-L, Joanicot M, et al. On-line laser Raman spectroscopic probing of droplets engineered in microfluidic devices. Lab on a Chip. 2006;6(9):1140-6.
24. Stehle R, Goerigk G, Wallacher D, Ballauff M, Seiffert S. Small-angle X-ray scattering in droplet-based microfluidics. Lab on a Chip. 2013;13(8):1529-37.
25. Lopez CG, Watanabe T, Martel A, Porcar L, Cabral JT. Microfluidic-SANS: flow processing of complex fluids. Scientific Reports. 2015;5:7727.
26. Bremond N, Thiam AR, Bibette J. Decompressing Emulsion Droplets Favors Coalescence. Physical Review Letters. 2008;100(2):024501.
27. Gunes DZ, Bercy M, Watzke B, Breton O, Burbidge AS. A study of extensional flow induced coalescence in microfluidic geometries with lateral channels. Soft Matter. 2013;9(31):7526-37.
28. Gunes DZ, Clain X, Breton O, Mayor G, Burbidge AS. Avalanches of coalescence events and local extensional flows – Stabilisation or destabilisation due to surfactant. Journal of Colloid and Interface Science. 2010;343(1):79-86.
29. Christopher GF, Bergstein J, End NB, Poon M, Nguyen C, Anna SL. Coalescence and splitting of confined droplets at microfluidic junctions. Lab on a Chip. 2009;9(8):1102-9.
30. Bremond N, Bibette J. Exploring emulsion science with microfluidics. Soft Matter. 2012;8(41):10549-59.
31. Purcell IP, Lu JR, Thomas RK, Howe AM, Penfold J. Adsorption of Sodium Dodecyl Sulfate at the Surface of Aqueous Solutions of Poly(vinylpyrrolidone) Studied by Neutron Reflection. Langmuir. 1998;14(7):1637-45.
32. Purcell IP, Thomas RK, Penfold J, Howe AM. Adsorption of SDS and PVP at the air/water interface. Colloids and Surfaces A: Physicochemical and Engineering Aspects. 1995;94(2):125-30.
33. Chari K. The structure of the PVP ・ SDS complex in water. Journal of Colloid and Interface Science. 1992;151(1):294-6.
34. Chari KH, T. Z. Adsorption at the Air/Water Interface from an Aqueous Solution of Poly(vunyl pyrollidone) and Sodium Dodecly Sulfate. J Phys Chem. 1991;95:3302-5.
35. Prasad M, Palepu R, Moulik SP. Interaction between sodium dodecyl sulfate (SDS) and polyvinylpyrrolidone (PVP) investigated with forward and reverse component addition protocols employing tensiometric, conductometric, microcalorimetric, electrokinetic, and DLS techniques. Colloid and Polymer Science. 2006;284(8):871-8.
36. Israelachvili JN. Intermolecular and surface forces. 3rd ed. ed: Academic Press; 2011.
37. Eggers J. Nonlinear dynamics and breakup of free-surface flows. Reviews of Modern Physics. 1997;69(3):865-930.
38. Eggers J, Villermaux E. Physics of liquid jets. Reports on Progress in Physics. 2008;71(3):036601.
39. Jones MN. The interaction of sodium dodecyl sulfate with polyethylene oxide. Journal of Colloid and Interface Science. 1967;23(1):36-42.
40. Bibette J, Morse DC, Witten TA, Weitz DA. Stability criteria for emulsions. Physical Review Letters. 1992;69(16):2439-42.
41. Walstra P. Principles of emulsion formation. Chemical Engineering Science. 1993;48(2):333-49.
42. Berry JD, Dagastine RR. Mapping coalescence of micron-sized drops and bubbles. Journal of Colloid and Interface Science. 2017;487(Supplement C):513-22.
43. Taylor P. Ostwald ripening in emulsions. Advances in Colloid and Interface Science. 1998;75(2):107-63.
44. Dagastine RR, Manica R, Carnie SL, Chan DYC, Stevens GW, Grieser F. Dynamic Forces Between Two Deformable Oil Droplets in Water. Science (Washington, DC, United States). 2006;313(5784):210-3.
45. Chan DYC, Klaseboer E, Manica R. Theory of non-equilibrium force measurements involving deformable drops and bubbles. Advances in Colloid and Interface Science. 2011;165(2):70-90.
46. Chan DYC, Klaseboer E, Manica R. Film drainage and coalescence between deformable drops and bubbles. Soft Matter. 2011;7(6):2235-64.

47. Carnie SL, Chan DYC, Lewis C, Manica R, Dagastine RR. Measurement of Dynamical Forces between Deformable Drops Using the Atomic Force Microscope. I. Theory. Langmuir. 2005;21(7):2912-22.
48. Klaseboer E, Chevaillier JP, Gourdon C, Masbernat O. Film Drainage between Colliding Drops at Constant Approach Velocity: Experiments and Modeling. Journal of Colloid and Interface Science. 2000;229(1):274-85.
49. Yeo LY, Matar OK, Perez de Ortiz ES, Hewitt GF. Film drainage between two surfactant-coated drops colliding at constant approach velocity. Journal of Colloid and Interface Science. 2003;257(1):93-107.
50. Joye J-L, Hirasaki GJ, Miller CA. Asymmetric Drainage in Foam Films. Langmuir. 1994;10(9):3174-9.
51. Aston DE, Berg JC. Thin-film hydrodynamics in fluid interface. - Atomic force microscopy. Industrial & Engineering Chemistry Research. 2002;41(3):389-96.
52. Horn RG, Asadullah M, Connor JN. Thin Film Drainage: Hydrodynamic and Disjoining Pressures Determined from Experimental Measurements of the Shape of a Fluid Drop Approaching a Solid Wall. Langmuir. 2006;22(6):2610-9.
53. Connor JN, Horn RG. The influence of surface forces on thin film drainage between a fluid drop and a flat solid. Faraday Discuss. 2003;123:193-206.
54. Manor O, Chau TT, Stevens GW, Chan DYC, Grieser F, Dagastine RR. Polymeric Stabilized Emulsions: Steric Effects and Deformation in Soft Systems. Langmuir. 2012;28(10):4599-604.
55. Kim S-H, Park J-G, Choi TM, Manoharan VN, Weitz DA. Osmotic-pressure-controlled concentration of colloidal particles in thin-shelled capsules. Nature Communications. 2014;5(1):3068.
56. Tulpar A, Walz JY. Simultaneous measurement of structural and hydrodynamic forces between colloidal surfaces in complex fluids. Colloid Surface A. 2007;300:268-80.
57. Klapp SHL, Zeng Y, Qu D, von Klitzing R. Surviving Structure in Colloidal Suspensions Squeezed from 3D to 2D. Physical Review Letters. 2008;100(11):118303.
58. Sober DL, Walz JY. Measurement of long-range depletion energies between a colloidal particle and a flat surface in micellar solutions. Langmuir. 1995;11(7):2352-6.
59. Richetti P, Kékicheff P. Direct measurement of depletion and structural forces in a micellar system. Phys Rev Lett. 1992;68(12):1951.
60. Biggs S. Direct measurement of the depletion interaction in binary solutions of polyelectrolytes. Physical Chemistry Chemical Physics. 2010;12(16):4172-7.
61. Biggs S, Burns JL, Yan Yd, Jameson GJ, Jenkins P. Molecular Weight Dependence of the Depletion Interaction between Silica Surfaces in Solutions of Sodium Poly(styrene sulfonate). Langmuir. 2000;16(24):9242-8.
62. Milling AJ. Depletion and Structuring of Sodium Poly(styrenesulfonate) at the Silica-Water Interface. J Phys Chem. 1996;100(21):8986-93.
63. Browne C, Tabor RF, Grieser F, Dagastine RR. Direct AFM force measurements between air bubbles in aqueous monodisperse sodium poly(styrene sulfonate) solutions. J Colloid Interface Sci. 2015;451:69-77.
64. Jones MN, Mysels KJ, Scholten PC. Stability and some properties of the second black film. Transactions of the Faraday Society. 1966;62(0):1336-48.
65. Aronson MP, Princen HM. Contact angles in oil-in-water emulsions stabilized by ionic surfactants. Colloids and Surfaces. 1982;4(2):173-84.
66. Huisman F, Mysels KJ. Contact angle and the depth of the free-energy minimum in thin liquid films. Their measurement and interpretation. The Journal of Physical Chemistry. 1969;73(3):489-97.
67. De Feijter JA, Vrij A. Contact angles in thin liquid films: III. Interaction forces in Newton black soap films. Journal of Colloid and Interface Science. 1979;70(3):456-66.
68. Stern O. Theory of a double-electric layer with the consideration of the adsorption processes. Z Electrochem. 1924;30(21-22):508-16.
69. H.-J. Butt KG, M. Kappl. Physics and Chemistry of Interfaces. Ed. S, editor. Germany: Wiley-VCH Verlag GmbH & Co.; 2003.

70. Hamaker HC. The London—van der Waals attraction between spherical particles. Physica. 1937;4(10):1058-72.
71. Dzyaloshinskii IE, Lifshitz EM, Pitaevskii LP. The general theory of van der Waals forces. Adv Phys. 1961;10(38):165-209.
72. Lifshitz EM. The theory of molecular attractive forces between solids. Sov Phys JETP. 1956;2:73.
73. Dagastine RR, Prieve DC, White LR. The Dielectric Function for Water and Its Application to van der Waals Forces. J Colloid Interface Sci. 2000;231(2):351-8.
74. Butt HJ, Kappl M. Surface and Interfacial Forces: Wiley; 2018.
75. Derjaguin BV, Landau L. Acta Physicochim URS. 1941;14:633-62.
76. Verwey EJW, Overbeek JTG. Theory of the STability of Lyophobic Colloids. Amsterdam: Elsevier; 1948.
77. Ninham BW. On progress in forces since the DLVO theory. Advances in Colloid and Interface Science. 1999;83(1):1-17.
78. Jenkins P, Snowden M. Depletion flocculation in colloidal dispersions. Adv Colloid Interface Sci. 1996;68(0):57-96.
79. Asakura S, Oosawa F. On Interaction between Two Bodies Immersed in a Solution of Macromolecules. J Chem Phys. 1954;22(7):1255-6.
80. Wasan DT, Nikolov AD, Kralchevsky PA, Ivanov IB. Universality in film stratification due to colloid crystal formation. Colloids and Surfaces. 1992;67:139-45.
81. Chu XL, Nikolov AD, Wasan DT. Thin liquid film structure and stability: The role of depletion and surface-induced structural forces. The Journal of Chemical Physics. 1995;103(15):6653-61.
82. Henderson D, Lozada-Cassou M. A simple theory for the force between spheres immersed in a fluid. Journal of Colloid and Interface Science. 1986;114(1):180-3.
83. Exerowa D, Kolarov T, Esipova NE, Yankov R, Zorin ZM. Foam and Wetting Films from Aqueous Cetyltrimethylammonium Bromide Solutions: Electrostatic Stability1. Colloid Journal. 2001;63(1):45-52.
84. Wasan D, Nikolov A. Thin liquid films containing micelles or nanoparticles. Curr Opin Colloid Interface Sci. 2008;13(3):128-33.
85. Derjaguin BV, Churaev NV. Structural component of disjoining pressure. J Colloid Interface Sci. 1974;49(2):249-55.
86. Berg JC. An Introduction to Interfaces and Collids: The Bridge to Nanoscience. Singapore: World Scientific Printers; 2010.
87. Derjaguin BV. Friction and adhesion. IV: The theory of adhesion of small particles. Kolloid Z. 1934;69(155):155-64.
88. Fendler JH. The colloidal domain: Where physics, chemistry, biology, and technology meet. By D. Fennell Evans and Hakån Wennerström. VCH Publishers, New York 1994, XXXII, 515 pp, DM 980, ISBN 1–56081–525–6. Advanced Materials. 1996;8(3):260-.
89. Taylor DJF, Thomas RK, Penfold J. Polymer/surfactant interactions at the air/water interface. Advances in Colloid and Interface Science. 2007;132(2):69-110.
90. Kalwarczyk E, Gołoś M, Hołyst R, Fiałkowski M. Polymer-induced ordering and phase separation in ionic surfactants. Journal of Colloid and Interface Science. 2010;342(1):93-102.
91. Piculell L, Lindman B. Association and segregation in aqueous polymer/polymer, polymer/surfactant, and surfactant/surfactant mixtures: similarities and differences. Advances in Colloid and Interface Science. 1992;41:149-78.
92. Khan MY, Samanta A, Ojha K, Mandal A. Interaction between aqueous solutions of polymer and surfactant and its effect on physicochemical properties. Asia-Pacific Journal of Chemical Engineering. 2008;3(5):579-85.
93. Chatterjee S, Prajapati R, Bhattacharya A, Mukherjee TK. Microscopic Evidence of "Necklace and Bead"-Like Morphology of Polymer–Surfactant Complexes: A Comparative Study on Poly(vinylpyrrolidone)–Sodium Dodecyl Sulfate and Poly(diallyldimethylammonium chloride)–Sodium Dodecyl Sulfate Systems. Langmuir. 2014;30(32):9859-65.

94. Brackman JC, Engberts JBFN. Polymer-micelle interactions: physical organic aspects. Chemical Society Reviews. 1993;22(2):85-92.
95. Guzmán E, Llamas S, Maestro A, Fernández-Peña L, Akanno A, Miller R, et al. Polymer–surfactant systems in bulk and at fluid interfaces. Advances in Colloid and Interface Science. 2016;233(Supplement C):38-64.
96. Yamaguchi Y, Inaba Y, Uchiyama H, Kunieda H. Anomalous phase behavior of water-soluble polyelectrolyte and oppositely charged surfactants. Colloid and Polymer Science. 1999;277(12):1117-24.
97. Goddard ED, Hannan RB. Polymer/surfactant interactions. Journal of the American Oil Chemists' Society. 1977;54(12):561-6.
98. Thalberg K, Lindman B, Karlstroem G. Phase behavior of systems of cationic surfactant and anionic polyelectrolyte: influence of surfactant chain length and polyelectrolyte molecular weight. The Journal of Physical Chemistry. 1991;95(8):3370-6.
99. Clifford J, Pethica BA. The Self-Diffusion Coefficient of Sodium Dodecyl Sulfate Micelles. The Journal of Physical Chemistry. 1966;70(10):3345-6.
100. Wan-Badhi WA, Wan-Yunus WMZ, Bloor DM, Hall DG, Wyn-Jones E. Equilibrium and kinetic studies associated with the interaction between sodium dodecyl sulfate and polyvinylpyrrolidone in aqueous solution. Journal of the Chemical Society, Faraday Transactions. 1993;89(15):2737-42.
101. Fishman M, R. Elrich F. Interactions of aqueous poly(N-vinylpyrrolidone) with sodium dodecyl sulfate. II. Correlation of electric conductance and viscosity measurements with equilibrium dialysis measurements1975. 2740-4 p.
102. Zana RL, J.; Lianos, P. Fluorescence probe studies of the aggregation state of sodium dodecul-sulfate in aqueous solutions of polioxyethylenegycol and poly-N-vinylpirrolidone. Polym Prepr Am Chem Soc Div Polym Chem. 1982;23(39).
103. Bales BL. A Definition of the Degree of Ionization of a Micelle Based on Its Aggregation Number. The Journal of Physical Chemistry B. 2001;105(29):6798-804.
104. Minatti E, Zanette D. Salt effects on the interaction of poly(ethylene oxide) and sodium dodecyl sulfate measured by conductivity. Colloids and Surfaces A: Physicochemical and Engineering Aspects. 1996;113(3):237-46.
105. Suksamranchit S, Sirivat A. Influence of ionic strength on complex formation between poly(ethylene oxide) and cationic surfactant and turbulent wall shear stress in aqueous solution. Chemical Engineering Journal. 2007;128(1):11-20.
106. Chen J, Gong X, Yang H, Yao Y, Xu M, Chen Q, et al. NMR Study on the Effects of Sodium n-Dodecyl Sulfate on the Coil-to-Globule Transition of Poly(N-isopropylacrylamide) in Aqueous Solutions. Macromolecules. 2011;44(15):6227-31.
107. Francois J, Dayantis J, Sabbadin J. Hydrodynamical behaviour of the poly(ethylene oxide)-sodium dodecylsulphate complex. European Polymer Journal. 1985;21(2):165-74.
108. Xia J, Dubin PL, Kim Y. Complex formation between poly(oxyethylene) and sodium dodecyl sulfate micelles: light scattering, electrophoresis, and dialysis equilibrium studies. The Journal of Physical Chemistry. 1992;96(16):6805-11.
109. Jiang WH, Han SJ. Viscosity of Nonionic Polymer/Anionic Surfactant Complexes in Water. Journal of Colloid and Interface Science. 2000;229(1):1-5.
110. Sorci GA, Reed WF. Electrostatic and Association Phenomena in Aggregates of Polymers and Micelles. Langmuir. 2002;18(2):353-64.
111. Minatti E, Norwood DP, Reed WF. Surfactant/Polymer Assemblies. 2. Polyelectrolyte Properties. Macromolecules. 1998;31(9):2966-71.
112. Wu Y, Chen J, Fang Y, Zhu M. Polyvinylpyrrolidone-sodium dodecylsulfate complex is a family of pseudo-polyanions with different charge densities: Evidence from capillary electrophoresis, capillary viscosimetry and conductometry. Journal of Colloid and Interface Science. 2016;479:34-42.
113. Tulpar A, Tilton RD, Walz JY. Synergistic Effects of Polymers and Surfactants on Depletion Forces. Langmuir. 2007;23(8):4351-7.

114. Philip J, Prakash GG, Jaykumar T, Kalyanasundaram P, Mondain-Monval O, Raj B. Interaction between Emulsion Droplets in the Presence of Polymer-Surfactant Complexes. Langmuir. 2002;18(12):4625-31.
115. Folmer BM, Kronberg B. Effect of Surfactant–Polymer Association on the Stabilities of Foams and Thin Films: Sodium Dodecyl Sulfate and Poly(vinyl pyrrolidone). Langmuir. 2000;16(14):5987-92.
116. De Gennes PG, Pincus P, Velasco RM, Brochard F. Remarks on polyelectrolyte conformation. Journal de Physique. 1976;37(12):1461-73.
117. de Gennes P-G. Scaling Concepts in Polymer Physics. New York: Cornell University Press; 1979.
118. Pfeuty P. Conformation of polyelectrolytes order in polyelectrolyte solutions. J Phys Colloques. 1978;39(C2):C2-149-C2-60.
119. Dobrynin AV, Colby RH, Rubinstein M. Scaling Theory of Polyelectrolyte Solutions. Macromolecules. 1995;28(6):1859-71.
120. Dobrynin AV, Rubinstein M. Hydrophobic Polyelectrolytes. Macromolecules. 1999;32(3):915-22.
121. Dobrynin AV, Rubinstein M. Theory of polyelectrolytes in solutions and at surfaces. Prog Polym Sci. 2005;30(11):1049-118.
122. Shusharina NP, Rubinstein M. Scaling Theory of Polyelectrolyte and Polyampholyte Micelles. In: Zvelindovsky AV, editor. Nanostructured Soft Matter. NanoScience and Technology: Springer Netherlands; 2007. p. 301-26.
123. Hill TL. A fundamental studies on the theory of the Donnan membrane equilibrium. Discussions of the Faraday Society. 1956;21(0):31-45.
124. Hill TL. Electrolyte Theory and the Donnan Membrane Equilibrium. J Phys Chem. 1957;61(5):548-53.
125. Dijt JC, Stuart MAC, Hofman JE, Fleer GJ. Kinetics of polymer adsorption in stagnation point flow. Colloids and Surfaces. 1990;51:141-58.
126. Grant WH, Smith LE, Stromberg RR. Adsorption and desorption rates of polystyrene on flat surfaces. Faraday Discussions of the Chemical Society. 1975;59(0):209-17.
127. Rojas OJ, Ernstsson M, Neuman RD, Claesson PM. Effect of Polyelectrolyte Charge Density on the Adsorption and Desorption Behavior on Mica. Langmuir. 2002;18(5):1604-12.
128. Rojas OJ, Neuman RD, Claesson PM. Desorption of Low-Charge-Density Polyelectrolyte Adlayers in Aqueous Sodium n-Dodecyl Sulfate Solution. Journal of Colloid and Interface Science. 2001;237(1):104-11.
129. Thibaut A, Misselyn-Bauduin AM, Broze G, Jérôme R. Adsorption of Poly(vinylpyrrolidone)/Surfactant(s) Mixtures at the Silica/Water Interface: A Calorimetric Investigation. Langmuir. 2000;16(25):9841-9.
130. Cattoz B, Cosgrove T, Crossman M, Prescott SW. Surfactant-Mediated Desorption of Polymer from the Nanoparticle Interface. Langmuir. 2012;28(5):2485-92.
131. Lee J-J, Fuller GG. Adsorption and desorption of flexible polymer chains in flowing systems. Journal of Colloid and Interface Science. 1985;103(2):569-77.
132. Claesson PM, Poptoshev E, Blomberg E, Dedinaite A. Polyelectrolyte-mediated surface interactions. Adv Colloid Interface Sci. 2005;114-115:173-87.
133. Claesson PM, Dedinaite A, Blomberg E, Sergeyev VG. Polyelectrolyte-surfactant association at solid surfaces. Berichte der Bunsengesellschaft für physikalische Chemie. 1996;100(6):1008-13.
134. Rojas OJ, Claesson PM, Berglund KD, Tilton RD. Coadsorption and surface forces for selective surfaces in contact with aqueous mixtures of oppositely charged surfactants and low charge density polyelectrolytes. Langmuir. 2004;20(8):3221-30.
135. Bergeron V, Langevin D, Asnacios A. Thin-Film Forces in Foam Films Containing Anionic Polyelectrolyte and Charged Surfactants. Langmuir. 1996;12(6):1550-6.
136. Bremmell KE, Jameson GJ, Biggs S. Forces between surfaces in the presence of a cationic polyelectrolyte and an anionic surfactant. Colloids and Surfaces A: Physicochemical and Engineering Aspects. 1999;155(1):1-10.

137. Gregory J. Rates of flocculation of latex particles by cationic polymers. Journal of Colloid and Interface Science. 1973;42(2):448-56.
138. Claesson PM, Ederth T, Bergeron V, Rutland MW. Techniques for measuring surface forces. Advances in Colloid and Interface Science. 1996;67:119-83.
139. Craig VSJ. An historical review of surface force measurement techniques. Colloids and Surfaces A: Physicochemical and Engineering Aspects. 1997;129-130:75-93.
140. Israelachvili J, Min Y, Akbulut M, Alig A, Carver G, Greene W, et al. Recent advances in the surface forces apparatus (SFA) technique. Reports on Progress in Physics. 2010;73(3):036601.
141. Tabor D, Winterton RHS. The direct measurement of normal and retarded van der Waals forces. Proceedings of the Royal Society of London A Mathematical and Physical Sciences. 1969;312(1511):435-50.
142. Israelachvili JN, Adams GE. Direct measurement of long range forces between two mica surfaces in aqueous KNO3 solutions. Nature. 1976;262(5571):774-6.
143. Israelachvili JN, Pashley RM. Measurement of the hydrophobic interaction between two hydrophobic surfaces in aqueous electrolyte solutions. Journal of Colloid and Interface Science. 1984;98(2):500-14.
144. Israelachvili JN, Tabor D. Measurement of van der Waals Dispersion Forces in the Range 1.4 to 130 nm. Nature Physical Science. 1972;236:106.
145. Israelachvili JN, McGuiggan PM. Adhesion and short-range forces between surfaces. Part I: New apparatus for surface force measurements. Journal of Materials Research. 1990;5(10):2223-31.
146. Briscoe WH, Horn RG. Direct Measurement of Surface Forces Due to Charging of Solids Immersed in a Nonpolar Liquid. Langmuir. 2002;18(10):3945-56.
147. Klein J. Forces between mica surfaces bearing layers of adsorbed polystyrene in cyclohexane. Nature. 1980;288(5788):248-50.
148. Tonck A, Georges JM, Loubet JL. Measurements of intermolecular forces and the rheology of dodecane between alumina surfaces. Journal of Colloid and Interface Science. 1988;126(1):150-63.
149. Kulcsar A, Lavalle P, Voegel JC, Schaaf P, Kekicheff P. Interactions between Two Polyelectrolyte Multilayers Investigated by the Surface Force Apparatus. Langmuir. 2004;20(2):282-6.
150. Chen N, Maeda N, Tirrell M, Israelachvili J. Adhesion and Friction of Polymer Surfaces: The Effect of Chain Ends. Macromolecules. 2005;38(8):3491-503.
151. Marra J. Controlled deposition of lipid monolayers and bilayers onto mica and direct force measurements between galactolipid bilayers in aqueous solutions. Journal of Colloid and Interface Science. 1985;107(2):446-58.
152. Argillier JF, Ramachandran R, Harris WC, Tirrell M. Polymer Surfactant Interactions Studied with the Surface Force Apparatus. J Colloid Interface Sci. 1991;146(1):242-50.
153. Horn RG, Bachmann DJ, Connor JN, Miklavcic SJ. The effect of surface and hydrodynamic forces on the shape of a fluid drop approaching a solid surface. J Phys-Condens Mat. 1996;8(47):9483-90.
154. Connor JN, Horn RG. Measurement of Aqueous Film Thickness between Charged Mercury and Mica Surfaces: A Direct Experimental Probe of the Poisson-Boltzmann Distribution. Langmuir. 2001;17(23):7194-7.
155. Pushkarova RA, Horn RG. Surface forces measured between an air bubble and a solid surface in water. Colloid Surface A. 2005;261(1-3):147-52.
156. Pushkarova RA, Horn RG. Bubble - Solid Interactions in Water and Electrolyte Solutions. Langmuir. 2008;24(16):8726-34.
157. Del Castillo LA, Ohnishi S, Carnie SL, Horn RG. Variation of Local Surface Properties of an Air Bubble in Water Caused by Its Interaction with Another Surface. Langmuir. 2016;32(30):7671-82.
158. Prieve DC, Frej NA. Total internal reflection microscopy: a quantitative tool for the measurement of colloidal forces. Langmuir FIELD Full Journal Title:Langmuir. 1990;6(2):396-403.

159. Prieve DC. Measurement of colloidal forces with TIRM. Adv Colloid Interface Sci. 1999;82(1-3):93-125.
160. Bevan MA, Eichmann SL. Optical microscopy measurements of kT-scale colloidal interactions. Current Opinion in Colloid & Interface Science. 2011;16(2):149-57.
161. Odiachi PC, Prieve DC. Removing the effects of additive noise from TIRM measurements. Journal of Colloid and Interface Science. 2004;270(1):113-22.
162. Lockie HJ, McLean S, Dagastine RR. Hindered Diffusion of an Oil Drop Under Confinement and Surface Forces. J Phys Chem Lett. 2011;2:2472-7.
163. Haughey D, Earnshaw JC. Studies of colloidal interactions using total internal reflection microscopy. Colloids and Surfaces A: Physicochemical and Engineering Aspects. 1998;136(1-2):217-30.
164. Scheludko A, Exerowa D. Instrument for interferometric measurements of the thickness of microscopic foam films. CR Acad Bulg Sci. 1959;7:123-32.
165. Gupta A, Sharma MM. Stability of thin aqueous films on solid surfaces: I. Ellipsometric measurement of disjoining pressure isotherms for aqueous films bounded by glass and mercury. Journal of Colloid and Interface Science. 1992;149(2):392-406.
166. Bergeron V, Radke CJ. Equilibrium measurements of oscillatory disjoining pressures in aqueous foam films. Langmuir. 1992;8(12):3020-6.
167. Stubenrauch C, Klitzing Rv. Disjoining pressure in thin liquid foam and emulsion films—new concepts and perspectives. Journal of Physics: Condensed Matter. 2003;15(27):R1197-R232.
168. Yang F, Tchoukov P, Qiao P, Ma X, Pensini E, Dabros T, et al. Studying demulsification mechanisms of water-in-crude oil emulsions using a modified thin liquid film technique. Colloids and Surfaces A: Physicochemical and Engineering Aspects. 2018;540:215-23.
169. Aveyard R, Binks BP, Cho WG, Fisher LR, Fletcher PDI, Klinkhammer F. Investigation of the Force-Distance Relationship for a Small Liquid Drop Approaching a Liquid-Liquid Interface. Langmuir. 1996;12(26):6561-9.
170. Binks BP, Cho WG, Fletcher PDI. Disjoining Pressure Isotherms for Oil-Water-Oil Emulsion Films. Langmuir. 1997;13(26):7180-5.
171. Cho W-G, Fletcher PDI. Investigation of the force–distance relationship for a small liquid drop approaching an adhesive liquid/liquid interface. J Chem Soc, Faraday Trans. 1997;93(7):1389-95.
172. Ducker WA, Xu Z, Israelachvili JN. Measurements of Hydrophobic and DLVO Forces in Bubble-Surface Interactions in Aqueous Solutions. Langmuir. 1994;10(9):3279-89.
173. Butt H-J. A technique for measuring the force between a colloidal particle in water and a bubble. Journal of Colloid and Interface Science. 1994;166(1):109-17.
174. Fielden ML, Hayes RA, Ralston J. Surface and Capillary Forces Affecting Air Bubble-Particle Interactions in Aqueous Electrolyte. Langmuir. 1996;12(15):3721-7.
175. Snyder BA, Aston DE, Berg JC. Particle-Drop Interactions Examined with an Atomic Force Microscope. Langmuir. 1997;13(3):590-3.
176. Mulvaney P, Perera JM, Biggs S, Grieser F, Stevens GW. The Direct Measurement of the Forces of Interaction between a Colloid Particle and an Oil Droplet. J Colloid Interface Sci. 1996;183(2):614-6.
177. Gunning AP, Mackie AR, Wilde PJ, Morris VJ. Atomic Force Microscopy of Emulsion Droplets: Probing Droplet-Droplet Interactions. Langmuir. 2004;20(1):116-22.
178. Dagastine RR, Stevens GW, Chan DYC, Grieser F. Forces between two oil drops in aqueous solution measured by AFM. Journal of Colloid and Interface Science. 2004;273(1):339-42.
179. Shi C, Cui X, Xie L, Liu Q, Chan DYC, Israelachvili JN, et al. Measuring Forces and Spatiotemporal Evolution of Thin Water Films between an Air Bubble and Solid Surfaces of Different Hydrophobicity. ACS Nano. 2015;9(1):95-104.
180. Zhang X, Tchoukov P, Manica R, Wang L, Liu Q, Xu Z. Simultaneous measurement of dynamic force and spatial thin film thickness between deformable and solid surfaces by integrated thin liquid film force apparatus. Soft Matter. 2016;12(44):9105-14.

181. Wang L, Sharp D, Masliyah J, Xu Z. Measurement of Interactions between Solid Particles, Liquid Droplets, and/or Gas Bubbles in a Liquid using an Integrated Thin Film Drainage Apparatus. Langmuir. 2013;29(11):3594-603.
182. Zhang X, Manica R, Tchoukov P, Liu Q, Xu Z. Effect of Approach Velocity on Thin Liquid Film Drainage between an Air Bubble and a Flat Solid Surface. The Journal of Physical Chemistry C. 2017;121(10):5573-84.
183. Frostad JM, Collins MC, Leal LG. Cantilevered-Capillary Force Apparatus for Measuring Multiphase Fluid Interactions. Langmuir. 2013;29(15):4715-25.
184. Frostad JM, Seth M, Bernasek SM, Leal LG. Direct measurement of interaction forces between charged multilamellar vesicles†. Soft Matter. 2014;10(39):7769-80.
185. Binnig G, Quate CF, Gerber C. Atomic Force Microscope. Physical Review Letters. 1986;56(9):930-3.
186. Tabor RF, Grieser F, Dagastine RR, Chan DYC. Measurement and analysis of forces in bubble and droplet systems using AFM. Journal of Colloid and Interface Science. 2012;371(1):1-14.
187. Butt H-J. Measuring electrostatic, van der Waals, and hydration forces in electrolyte solutions with an atomic force microscope. Biophysical Journal. 1991;60(6):1438-44.
188. Butt H-J, Cappella B, Kappl M. Force measurements with the atomic force microscope: Technique, interpretation and applications. Surface Science Reports. 2005;59(1):1-152.
189. Butt H-J, Berger R, Bonaccurso E, Chen Y, Wang J. Impact of atomic force microscopy on interface and colloid science. Adv Colloid Interface Sci. 2007;133(2):91-104.
190. Cappella B, Dietler G. Force-distance curves by atomic force microscopy. Surf Sci Rep. 1999;34(1–3):1-104.
191. Drummond CJ, Senden TJ. Examination of the geometry of long-range tip—sample interaction in atomic force microscopy. Colloid Surface A. 1994;87(3):217-34.
192. Senden TJ, Drummond CJ. Surface chemistry and tip-sample interactions in atomic force microscopy. Colloid Surface A. 1995;94(1):29-51.
193. Senden TJ. Force microscopy and surface interactions. Curr Opin Colloid Interface Sci. 2001;6(2):95-101.
194. Ducker WA, Senden TJ, Pashley RM. Direct measurement of colloidal forces using an atomic force microscope. Nature. 1991;353(6341):239-41.
195. Bonaccurso E, Kappl M, Butt H-J. Thin liquid films studied by atomic force microscopy. Curr Opin Colloid Interface Sci. 2008;13(3):107-19.
196. Larson I, Drummond CJ, Chan DYC, Grieser F. Direct force measurements between titanium dioxide surfaces. J Am Chem Soc. 1993;115(25):11885-90.
197. Kappl M, Butt HJ. The colloidal probe technique and its application to adhesion force measurements. Part Part Sys Char. 2002;19(3):129-43.
198. Vakarelski IU, Higashitani K. Single-Nanoparticle-Terminated Tips for Scanning Probe Microscopy. Langmuir. 2006;22(7):2931-4.
199. Helfricht N, Mark A, Dorwling-Carter L, Zambelli T, Papastavrou G. Extending the limits of direct force measurements: colloidal probes from sub-micron particles. Nanoscale. 2017;9(27):9491-501.
200. Hüttl G, Klemm V, Popp R, Simon F, Müller E. Tailored colloidal AFM probes and their TEM investigation. Surface and Interface Analysis. 2002;33(2):50-3.
201. van Zwol PJ, Palasantzas G, van de Schootbrugge M, de Hosson JTM, Craig VSJ. Roughness of Microspheres for Force Measurements. Langmuir. 2008;24(14):7528-31.
202. Yang S, Zhang H, Hsu SM. Correction of Random Surface Roughness on Colloidal Probes in Measuring Adhesion. Langmuir. 2007;23(3):1195-202.
203. Neto C, Craig VSJ. Colloid Probe Characterization: Radius and Roughness Determination. Langmuir. 2001;17(7):2097-9.
204. Drelich J, Mittal KL. Atomic Force Microscopy in Adhesion Studies: CRC Press; 2005.
205. Biggs S. Steric and Bridging Forces between Surfaces Bearing Adsorbed Polymer: An Atomic Force Microscopy Study. Langmuir. 1995;11(1):156-62.

206. Biggs S, Spinks G. Atomic force microscopy investigation of the adhesion between a single polymer sphere and a flat surface. Journal of Adhesion Science and Technology. 1998;12(5):461-78.
207. Lüderitz LAC, v. Klitzing R. Interaction forces between silica surfaces in cationic surfactant solutions: An atomic force microscopy study. Journal of Colloid and Interface Science. 2013;402:19-26.
208. Muir I, Meagher L, Gee M. Interaction Forces between α-Alumina Fibers with Coadsorbed Polyelectrolyte and Surfactant. Langmuir. 2001;17(16):4932-9.
209. Aston DE, Berg JC. Fluid interfacial separations for secondary fiber recovery as probed with atomic force microscopy. Journal of Pulp and Paper Science. 1998;24(4):121-4.
210. Max E, Häfner W, Wilco Bartels F, Sugiharto A, Wood C, Fery A. A novel AFM based method for force measurements between individual hair strands. Ultramicroscopy. 2010;110(4):320-4.
211. Pashazanusi L, Lwoya B, Oak S, Khosla T, Albert JNL, Tian Y, et al. Enhanced Adhesion of Mosquitoes to Rough Surfaces. ACS Applied Materials & Interfaces. 2017;9(28):24373-80.
212. Preuss M, Butt H-J. Direct Measurement of Particle-Bubble Interactions in Aqueous Electrolyte: Dependence on Surfactant. Langmuir. 1998;14(12):3164-74.
213. Nguyen AV, Nalaskowski J, Miller JD. A study of bubble-particle interaction using atomic force microscopy. Minerals Engineering. 2003;16(11):1173-81.
214. Nguyen AV, Nalaskowski J, Miller JD. The dynamic nature of contact angles as measured by atomic force microscopy. Journal of Colloid and Interface Science. 2003;262(1):303-6.
215. Nespolo SA, Chan DYC, Grieser F, Hartley PG, Stevens GW. Forces between a Rigid Probe Particle and a Liquid Interface: Comparison between Experiment and Theory. Langmuir. 2003;19(6):2124-33.
216. Dagastine RR, Chau TT, Chan DYC, Stevens GW, Grieser F. Interaction forces between oil-water particle interfaces - Non-DLVO forces. Faraday Discussions. 2005;129:111-24.
217. Webber GB, Manica R, Edwards SA, Carnie SL, Stevens GW, Grieser F, et al. Dynamic Forces between a Moving Particle and a Deformable Drop. J Phys Chem C. 2008;112(2):567-74.
218. Hartley PG, Grieser F, Mulvaney P, Stevens GW. Surface Forces and Deformation at the Oil-Water Interface Probed Using AFM Force Measurement. Langmuir. 1999;15(21):7282-9.
219. Gillies G, Prestidge CA, Attard P. An AFM Study of the Deformation and Nanorheology of Cross-Linked PDMS Droplets. Langmuir. 2002;18(5):1674-9.
220. Aston DE, Berg JC. Quantitative Analysis of Fluid Interface-Atomic Force Microscopy. J Colloid Interface Sci. 2001;235(1):162-9.
221. Bhatt D, Newman J, Radke CJ. Equilibrium Force Isotherms of a Deformable Bubble/Drop Interacting with a Solid Particle across a Thin Liquid Film. Langmuir. 2001;17(1):116-30.
222. Chan DYC, Dagastine RR, White LR. Forces between a Rigid Probe Particle and a Liquid Interface. I. The Repulsive Case. J Colloid Interface Sci. 2001;236(1):141-54.
223. Gromer A, Penfold R, Gunning AP, Kirby AR, Morris VJ. Molecular basis for the emulsifying properties of sugar beet pectin studied by atomic force microscopy and force spectroscopy. Soft Matter. 2010;6(16):3957-69.
224. Mettu S, Wu C, Dagastine RR. Dynamic forces between emulsified water drops coated with Poly-Glycerol-Poly-Ricinoleate (PGPR) in canola oil. Journal of Colloid and Interface Science. 2018;517:166-75.
225. Fewkes CJ, Tabor RF, Dagastine RR. Sphere to rod transitions in self assembled systems probed using direct force measurement. Soft Matter. 2015;11(7):1303-14.
226. Tabor RF, Chan DYC, Grieser F, Dagastine RR. Structural Forces in Soft Matter Systems. J Phys Chem Lett. 2011;2(5):434-7.
227. Tabor RF, Lockie H, Chan DYC, Grieser F, Grillo I, Mutch KJ, et al. Structural forces in soft matter systems: unique flocculation pathways between deformable droplets. Soft Matter. 2011;7(24):11334-44.
228. Shi C, Zhang L, Xie L, Lu X, Liu Q, Mantilla CA, et al. Interaction Mechanism of Oil-in-Water Emulsions with Asphaltenes Determined Using Droplet Probe AFM. Langmuir. 2016;32(10):2302-10.

229. Tabor RF, Grieser F, Dagastine RR, Chan DYC. The hydrophobic force: measurements and methods. Phys Chem Chem Phys. 2014;16(34):18065-75.
230. Vakarelski IU, Lee J, Dagastine RR, Chan DYC, Stevens GW, Grieser F. Bubble Colloidal AFM Probes Formed from Ultrasonically Generated Bubbles. Langmuir. 2008;24(3):603-5.
231. Browne C, Tabor RF, Chan DYC, Dagastine RR, Ashokkumar M, Grieser F. Bubble Coalescence during Acoustic Cavitation in Aqueous Electrolyte Solutions. Langmuir. 2011;27:12025–32.
232. Wang W, Li K, Ma M, Jin H, Angeli P, Gong J. Review and perspectives of AFM application on the study of deformable drop/bubble interactions. Advances in Colloid and Interface Science. 2015;225:88-97.
233. Manica R, Connor JN, Dagastine RR, Carnie SL, Horn RG, Chan DYC. Hydrodynamic forces involving deformable interfaces at nanometer separations. Phys Fluids. 2008;20(3):032101/1-/12.
234. Vakarelski IU, Manica R, Tang X, O'Shea SJ, Stevens GW, Grieser F, et al. Dynamic interactions between microbubbles in water. Proceedings of the National Academy of Sciences. 2010;107(25):11177.
235. Carnie SL, Chan DYC, Manica R. Modelling drop-drop interactions in an atomic force microscope. ANZIAM J. 2005;46(E):C805--C19.
236. Tabor RF, Wu C, Lockie H, Manica R, Chan DYC, Grieser F, et al. Homo- and hetero-interactions between air bubbles and oil droplets measured by atomic force microscopy. Soft Matter. 2011;7(19):8977-83.
237. Anna SL. Droplets and Bubbles in Microfluidic Devices. Annual Review of Fluid Mechanics. 2016;48(1):285-309.
238. Seemann R, Brinkmann M, Pfohl T, Herminghaus S. Droplet based microfluidics. Reports on Progress in Physics. 2012;75(1):016601.
239. Whitesides GM. The origins and the future of microfluidics. Nature. 2006;442(7101):368-73.
240. Křenková J, Foret F. Immobilized microfluidic enzymatic reactors. ELECTROPHORESIS. 2004;25(21-22):3550-63.
241. Nie Z, Xu S, Seo M, Lewis PC, Kumacheva E. Polymer Particles with Various Shapes and Morphologies Produced in Continuous Microfluidic Reactors. Journal of the American Chemical Society. 2005;127(22):8058-63.
242. Shen B, Ricouvier J, Malloggi F, Tabeling P. Designing Colloidal Molecules with Microfluidics. Advanced Science. 2016;3(6):1600012-n/a.
243. Franke TA, Wixforth A. Microfluidics for Miniaturized Laboratories on a Chip. ChemPhysChem. 2008;9(15):2140-56.
244. Song H, Chen DL, Ismagilov RF. Reactions in Droplets in Microfluidic Channels. Angewandte Chemie International Edition. 2006;45(44):7336-56.
245. Wang J-T, Wang J, Han J-J. Fabrication of Advanced Particles and Particle-Based Materials Assisted by Droplet-Based Microfluidics. Small. 2011;7(13):1728-54.
246. Li W, Nie Z, Zhang H, Paquet C, Seo M, Garstecki P, et al. Screening of the Effect of Surface Energy of Microchannels on Microfluidic Emulsification. Langmuir. 2007;23(15):8010-4.
247. Bauer W-AC, Fischlechner M, Abell C, Huck WTS. Hydrophilic PDMS microchannels for high-throughput formation of oil-in-water microdroplets and water-in-oil-in-water double emulsions. Lab on a Chip. 2010;10(14):1814-9.
248. Hemmilä S, Cauich-Rodríguez JV, Kreutzer J, Kallio P. Rapid, simple, and cost-effective treatments to achieve long-term hydrophilic PDMS surfaces. Applied Surface Science. 2012;258(24):9864-75.
249. Lee JN, Park C, Whitesides GM. Solvent Compatibility of Poly(dimethylsiloxane)-Based Microfluidic Devices. Analytical Chemistry. 2003;75(23):6544-54.
250. Hibara A, Tokeshi M, Uchiyama K, Hisamoto H, Kitamori T. Integrated Multilayer Flow System on a Microchip. Analytical Sciences. 2001;17(1):89-93.

251. Hibara A, Iwayama S, Matsuoka S, Ueno M, Kikutani Y, Tokeshi M, et al. Surface Modification Method of Microchannels for Gas−Liquid Two-Phase Flow in Microchips. Analytical Chemistry. 2005;77(3):943-7.
252. Björn RK, Sato; Takehiko, Tsukahara; Kazuma, Mawatari; Takehiko, Kitamori. Hands on: thermal bonding of nano- and microfluidic chips. Microchim Acta. 2009;166(1-2):177-81.
253. Wang C, Gao X, Mawatari K, Kitamori T. Clogging-Free Irreversible Bonding of Polycarbonate Membranes to Glass Microfluidic Devices. Journal of The Electrochemical Society. 2017;164(5):B3087-B90.
254. Christopher GF, Anna SL. Microfluidic methods for generating continuous droplet streams. J Phys D Appl Phys. 2007;40(19):R319.
255. Zhu P, Wang L. Passive and active droplet generation with microfluidics: a review. Lab on a Chip. 2017;17(1):34-75.
256. Teh SY, Lin R, Hung LH, Lee AP. Droplet microfluidics. Lab on a Chip. 2008;8(2):198-220.
257. Baroud CN, Gallaire F, Dangla R. Dynamics of microfluidic droplets. Lab Chip. 2010;10(16):2032-45.
258. Zhao C-X, Middelberg APJ. Two-phase microfluidic flows. Chem Eng Sci. 2011;66(7):1394-411.
259. Umbanhowar PB, Prasad V, Weitz DA. Monodisperse Emulsion Generation via Drop Break Off in a Coflowing Stream. Langmuir. 2000;16(2):347-51.
260. Utada AS, Fernandez-Nieves A, Stone HA, Weitz DA. Dripping to Jetting Transitions in Coflowing Liquid Streams. Physical Review Letters. 2007;99(9):094502.
261. Castro-Hernández E, Gundabala V, Fernández-Nieves A, Gordillo JM. Scaling the drop size in coflow experiments. New Journal of Physics. 2009;11(7):075021.
262. Gordillo JM, Sevilla A, Campo-Cortés F. Global stability of stretched jets: conditions for the generation of monodisperse micro-emulsions using coflows. Journal of Fluid Mechanics. 2014;738:335-57.
263. Chokkalingam V, Herminghaus S, Seemann R. Self-synchronizing pairwise production of monodisperse droplets by microfluidic step emulsification. Appl Phys Lett. 2008;93(25):3.
264. Priest C, Herminghaus S, Seemann R. Generation of monodisperse gel emulsions in a microfluidic device. Appl Phys Lett. 2006;88(2):024106.
265. Mittal N, Cohen C, Bibette J, Bremond N. Dynamics of step-emulsification: From a single to a collection of emulsion droplet generators. Physics of Fluids. 2014;26(8):082109.
266. Gañán-Calvo AM. Generation of Steady Liquid Microthreads and Micron-Sized Monodisperse Sprays in Gas Streams. Physical Review Letters. 1998;80(2):285-8.
267. Gañán-Calvo AM, Gordillo JM. Perfectly Monodisperse Microbubbling by Capillary Flow Focusing. Phys Rev Lett. 2001;87(27):274501.
268. Anna SL, Bontoux N, Stone HA. Formation of dispersions using "flow focusing" in microchannels. Appl Phys Lett. 2003;82(3):364-6.
269. Tan Y-C, Cristini V, Lee AP. Monodispersed microfluidic droplet generation by shear focusing microfluidic device. Sensor Actuat B-Chem. 2006;114(1):350-6.
270. Huang S-H, Tan W-H, Tseng F-G, Takeuchi S. A monolithically three-dimensional flow-focusing device for formation of single/double emulsions in closed/open microfluidic systems. Journal of Micromechanics and Microengineering. 2006;16(11):2336-44.
271. Takeuchi S, Garstecki P, Weibel DB, Whitesides GM. An Axisymmetric Flow-Focusing Microfluidic Device. Adv Mater. 2005;17(8):1067-72.
272. Ugrinic M, Zambrano A, Berger S, Mann S, Tang TYD, deMello A. Microfluidic formation of proteinosomes. Chemical Communications. 2018;54(3):287-90.
273. Garstecki P, Stone HA, Whitesides GM. Mechanism for Flow-Rate Controlled Breakup in Confined Geometries: A Route to Monodisperse Emulsions. Phys Rev Lett. 2005;94(16):164501.
274. Nie Z, Seo M, Xu S, Lewis PC, Mok M, Kumacheva E, et al. Emulsification in a microfluidic flow-focusing device: effect of the viscosities of the liquids. Microfluidics and Nanofluidics. 2008;5(5):585-94.
275. Anna SL, Mayer HC. Microscale tipstreaming in a microfluidic flow focusing device. Phys Fluids. 2006;18(12):121512.

276. Lashkaripour A, Rodriguez C, Ortiz L, Densmore D. Performance tuning of microfluidic flow-focusing droplet generators. Lab on a Chip. 2019;19(6):1041-53.
277. Cubaud T, Mason TG. Capillary threads and viscous droplets in square microchannels. Physics of Fluids. 2008;20(5):053302.
278. Lee W, Walker LM, Anna SL. Role of geometry and fluid properties in droplet and thread formation processes in planar flow focusing. Phys Fluids. 2009;21(3):032103.
279. Dupin MM, Halliday I, Care CM. Simulation of a microfluidic flow-focusing device. Phys Rev E. 2006;73(5):055701.
280. Chen X, Glawdel T, Cui N, Ren CL. Model of droplet generation in flow focusing generators operating in the squeezing regime. Microfluid Nanofluid. 2015;18(5-6):1341-53.
281. Thorsen T, Roberts RW, Arnold FH, Quake SR. Dynamic Pattern Formation in a Vesicle-Generating Microfluidic Device. Physical Review Letters. 2001;86(18):4163-6.
282. Guillot P, Colin A. Stability of parallel flows in a microchannel after a T junction. Physical Review E. 2005;72(6):066301.
283. Zhao Y, Chen G, Yuan Q. Liquid-liquid two-phase flow patterns in a rectangular microchannel. AIChE Journal. 2006;52(12):4052-60.
284. Xu JH, Luo GS, Li SW, Chen GG. Shear force induced monodisperse droplet formation in a microfluidic device by controlling wetting properties. Lab on a Chip. 2006;6(1):131-6.
285. Christopher GF, Noharuddin NN, Taylor JA, Anna SL. Experimental observations of the squeezing-to-dripping transition in T-shaped microfluidic junctions. Physical Review E. 2008;78(3):036317.
286. P. Garstecki MJF, H.A. Stone, G.M. Whitesides. Formation of Droplets and Bubbles in a Microfluidic T-junction - Scaling and Mechanism of Break-up. Lab Chip. 2006;6:437-46.
287. van Steijn V, Kleijn CR, Kreutzer MT. Predictive model for the size of bubbles and droplets created in microfluidic T-junctions. Lab On A Chip. 2010;10(19):2513-8.
288. Xu JH, Li SW, Tan J, Luo GS. Correlations of droplet formation in T-junction microfluidic devices: from squeezing to dripping. Microfluidics and Nanofluidics. 2008;5(6):711-7.
289. De Menech M, Garstecki P, Jousse F, Stone HA. Transition from squeezing to dripping in a microfluidic T-shaped junction. Journal of Fluid Mechanics. 2008;595:141-61.
290. Korczyk PM, Cybulski O, Makulska S, Garstecki P. Effects of unsteadiness of the rates of flow on the dynamics of formation of droplets in microfluidic systems. Lab on a Chip. 2011;11(1):173-5.
291. van Steijn V, Korczyk PM, Derzsi L, Abate AR, Weitz DA, Garstecki P. Block-and-break generation of microdroplets with fixed volume. Biomicrofluidics. 2013;7(2):024108.
292. Krebs T, Schroën CGPH, Boom RM. Coalescence kinetics of oil-in-water emulsions studied with microfluidics. Fuel. 2013;106:327-34.
293. Baret J-C, Kleinschmidt F, El Harrak A, Griffiths AD. Kinetic Aspects of Emulsion Stabilization by Surfactants: A Microfluidic Analysis. Langmuir. 2009;25(11):6088-93.
294. Ming-Yu Zhang HZ, Jian-Hong Xu and Guang-Sheng Luo. Controlled coalescence of two immiscible droplets for Janus emulsions in a microfluidic device. RSC Advances. 2015;5:32768-74.
295. Chokkalingam V, Weidenhof B, Krämer M, Maier WF, Herminghaus S, Seemann R. Optimized droplet-based microfluidics scheme for sol–gel reactions. Lab on a Chip. 2010;10(13):1700-5.
296. Tan Y-C, Ho YL, Lee AP. Droplet coalescence by geometrically mediated flow in microfluidic channels. Microfluidics and Nanofluidics. 2007;3(4):495-9.
297. Tan Y-C, Fisher JS, Lee AI, Cristini V, Lee AP. Design of microfluidic channel geometries for the control of droplet volume, chemical concentration, and sorting. Lab on a Chip. 2004;4(4):292-8.
298. Niu X, Gulati S, Edel JB, deMello AJ. Pillar-induced droplet merging in microfluidic circuits. Lab on a Chip. 2008;8(11):1837-41.
299. Köhler JM, Henkel T, Grodrian A, Kirner T, Roth M, Martin K, et al. Digital reaction technology by micro segmented flow—components, concepts and applications. Chemical Engineering Journal. 2004;101(1):201-16.

300. Shen F, Li Y, Wang G, Liu Z. Mechanisms of rectangular groove-induced multiple-microdroplet coalescences. Acta Mechanica Sinica. 2017;33(3):585-94.
301. Wang W, Yang C, Li CM. On-demand microfluidic droplet trapping and fusion for on-chip static droplet assays. Lab on a Chip. 2009;9(11):1504-6.
302. Bithi SS, Vanapalli SA. Collective dynamics of non-coalescing and coalescing droplets in microfluidic parking networks. Soft Matter. 2015;11(25):5122-32.
303. Wang K, Lu Y, Tostado CP, Yang L, Luo G. Coalescences of microdroplets at a cross-shaped microchannel junction without strictly synchronism control. Chemical Engineering Journal. 2013;227:90-6.
304. Wu Y, Fu T, Zhu C, Ma Y, Li HZ. Bubble coalescence at a microfluidic T-junction convergence: from colliding to squeezing. Microfluidics and Nanofluidics. 2014;16(1):275-86.
305. Yang L, Wang K, Tan J, Lu Y, Luo G. Experimental study of microbubble coalescence in a T-junction microfluidic device. Microfluidics and Nanofluidics. 2012;12(5):715-22.
306. Wang K, Lu Y, Yang L, Luo G. Microdroplet coalescences at microchannel junctions with different collision angles. AIChE Journal. 2013;59(2):643-9.
307. Liu Z, Cao R, Pang Y, Shen F. The influence of channel intersection angle on droplets coalescence process. Experiments in Fluids. 2015;56(2):24.
308. Jin BJ, Kim YW, Lee Y, Yoo JY. Droplet merging in a straight microchannel using droplet size or viscosity difference. Journal of Micromechanics and Microengineering. 2010;20(3):035003.
309. Fidalgo LM, Abell C, Huck WTS. Surface-induced droplet fusion in microfluidic devices. Lab on a Chip. 2007;7(8):984-6.
310. Link DR, Grasland-Mongrain E, Duri A, Sarrazin F, Cheng Z, Cristobal G, et al. Electric Control of Droplets in Microfluidic Devices. Angewandte Chemie International Edition. 2006;45(16):2556-60.
311. Chabert M, Dorfman KD, Viovy J-L. Droplet fusion by alternating current (AC) field electrocoalescence in microchannels. ELECTROPHORESIS. 2005;26(19):3706-15.
312. Tan W-H, Takeuchi S. Timing controllable electrofusion device for aqueous droplet-based microreactors. Lab on a Chip. 2006;6(6):757-63.
313. Thiam AR, Bremond N, Bibette J. Breaking of an Emulsion under an ac Electric Field. Physical Review Letters. 2009;102(18):188304.
314. Zagnoni M, Le Lain G, Cooper JM. Electrocoalescence Mechanisms of Microdroplets Using Localized Electric Fields in Microfluidic Channels. Langmuir. 2010;26(18):14443-9.
315. Schoeman RM, Kemna EWM, Wolbers F, van den Berg A. High-throughput deterministic single-cell encapsulation and droplet pairing, fusion, and shrinkage in a single microfluidic device. ELECTROPHORESIS. 2014;35(2-3):385-92.
316. Miralles V, Huerre A, Malloggi F, Jullien M-C. A Review of Heating and Temperature Control in Microfluidic Systems: Techniques and Applications. Diagnostics. 2013;3(1):33-67.
317. Cordero ML, Burnham DR, Baroud CN, McGloin D. Thermocapillary manipulation of droplets using holographic beam shaping: Microfluidic pin ball. Applied Physics Letters. 2008;93(3):034107.
318. Jung JH, Lee KH, Destgeer G, Lee KS, Cho H, Ha BH, et al. In situ seriate droplet coalescence under an optical force. Microfluidics and Nanofluidics. 2015;18(5):1247-54.
319. Baroud CN, Robert de Saint Vincent M, Delville J-P. An optical toolbox for total control of droplet microfluidics. Lab on a Chip. 2007;7(8):1029-33.
320. Sesen M, Alan T, Neild A. Microfluidic on-demand droplet merging using surface acoustic waves. Lab on a Chip. 2014;14(17):3325-33.
321. Shen F, Li Y, Liu Z-M, Cao R-T, Wang G-R. Advances in Micro-Droplets Coalescence Using Microfluidics. Chinese Journal of Analytical Chemistry. 2015;43(12):1942-54.
322. Xu B, Nguyen N-T, Neng Wong T. Droplet Coalescence in Microfluidic Systems. Micro and Nanosystems. 2011;3(2):131-6.
323. Gunes DZ, Clain X, Breton O, Mayor G, Burbidge AS. Avalanches of coalescence events and local extensional flows - Stabilisation or destabilisation due to surfactant. Journal of Colloid and Interface Science.343(1):79-86.

324. Wang K, Lu YC, Xu JH, Luo GS. Determination of Dynamic Interfacial Tension and Its Effect on Droplet Formation in the T-Shaped Microdispersion Process. Langmuir. 2009;25(4):2153-8.
325. Xu JH, Dong PF, Zhao H, Tostado CP, Luo GS. The Dynamic Effects of Surfactants on Droplet Formation in Coaxial Microfluidic Devices. Langmuir. 2012;28(25):9250-8.
326. Wang K, Zhang L, Zhang W, Luo G. Mass-Transfer-Controlled Dynamic Interfacial Tension in Microfluidic Emulsification Processes. Langmuir. 2016;32(13):3174-85.
327. Wang X, Riaud A, Wang K, Luo G. Pressure drop-based determination of dynamic interfacial tension of droplet generation process in T-junction microchannel. Microfluidics and Nanofluidics. 2015;18(3):503-12.
328. Steegmans MLJ, Warmerdam A, Schroën KGPH, Boom RM. Dynamic Interfacial Tension Measurements with Microfluidic Y-Junctions. Langmuir. 2009;25(17):9751-8.
329. Hudson SD, Cabral JT, Goodrum WJ, Beers KL, Amis EJ. Microfluidic interfacial tensiometry. Applied Physics Letters. 2005;87(8):081905.
330. Martin JD, Hudson SD. Mass transfer and interfacial properties in two-phase microchannel flows. New Journal of Physics. 2009;11(11):115005.
331. Lee D, Fang C, Ravan AS, Fuller GG, Shen AQ. Temperature controlled tensiometry using droplet microfluidics. Lab on a Chip. 2017;17(4):717-26.
332. Cecchini MP, Hong J, Lim C, Choo J, Albrecht T, deMello AJ, et al. Ultrafast Surface Enhanced Resonance Raman Scattering Detection in Droplet-Based Microfluidic Systems. Analytical Chemistry. 2011;83(8):3076-81.
333. Saldanha O, Graceffa R, Hémonnot CYJ, Ranke C, Brehm G, Liebi M, et al. Rapid Acquisition of X-Ray Scattering Data from Droplet-Encapsulated Protein Systems. ChemPhysChem. 2017;18(10):1220-3.
334. Silva BFB. SAXS on a chip: from dynamics of phase transitions to alignment phenomena at interfaces studied with microfluidic devices. Physical Chemistry Chemical Physics. 2017;19(35):23690-703.
335. Adamo M, Poulos AS, Miller RM, Lopez CG, Martel A, Porcar L, et al. Rapid contrast matching by microfluidic SANS. Lab on a Chip. 2017;17(9):1559-69.
336. Adamo M, Poulos AS, G. Lopez C, Martel A, Porcar L, Cabral JT. Droplet microfluidic SANS. Soft Matter. 2018;14(10):1759-70.
337. Neeson MJ, Tabor RF, Grieser F, Dagastine RR, Chan DYC. Compound sessile drops. Soft Matter. 2012;8(43):11042-50.
338. Berry JD, Neeson MJ, Dagastine RR, Chan DYC, Tabor RF. Measurement of surface and interfacial tension using pendant drop tensiometry. Journal of Colloid and Interface Science. 2015;454:226-37.
339. Hutter JL, Bechhoefer J. Calibration of Atomic-Force Microscope Tips. Rev Sci Instrum. 1993;64(7):1868-73.
340. Cleveland JP, Manne S, Bocek D, Hansma PK. A nondestructive method for determining the spring constant of cantilevers for scanning force microscopy. Rev Sci Instrum. 1993;64(2):403-5.
341. Sader JE, Chon JWM, Mulvaney P. Calibration of rectangular atomic force microscope cantilevers. Rev Sci Instrum. 1999;70(10):3967-9.
342. Manor O, Vakarelski IU, Tang X, O'Shea SJ, Stevens GW, Grieser F, et al. Hydrodynamic Boundary Conditions and Dynamic Forces between Bubbles and Surfaces. Phys Rev Lett. 2008;101(2):024501.
343. Dagastine RR, Prieve DC, White LR. Forces between a rigid probe particle and a liquid interface III. Extraction of the planar half-space interaction energy E(D). Journal of Colloid and Interface Science. 2004;269(1):84-96.
344. Dagastine RR, White LR. Forces between a Rigid Probe Particle and a Liquid Interface. II. The General Case. Journal of Colloid and Interface Science. 2002;247(2):310-20.
345. Chan DYC, Klaseboer E, Manicac R. Dynamic deformations and forces in soft matter. Soft Matter. 2009;5:2858-61.
346. Tabor RF, Chan DYC, Grieser F, Dagastine RR. Anomalous Stability of Carbon Dioxide in pH-Controlled Bubble Coalescence. Angew Chem Int Ed. 2011;123(15):3516-8.

347. Xie L, Shi C, Cui X, Zeng H. Surface Forces and Interaction Mechanisms of Emulsion Drops and Gas Bubbles in Complex Fluids. Langmuir. 2017;33(16):3911-25.
348. Clasohm LY, Connor JN, Vinogradova OI, Horn RG. The "Wimple": Rippled Deformation of a Fluid Drop Caused by Hydrodynamic and Surface Forces during Thin Film Drainage. Langmuir. 2005;21(18):8243-9.
349. Borrell M, Yoon Y, Leal LG. Experimental analysis of the coalescence process via head-on collisions in a time-dependent flow. Physics of Fluids. 2004;16(11):3945-54.
350. Langevin D. Polyelectrolyte and surfactant mixed solutions. Behavior at surfaces and in thin films. Adv Colloid Interface Sci. 2001;89–90(0):467-84.
351. Asnacios A, Langevin D, Argillier J-F. Complexation of Cationic Surfactant and Anionic Polymer at the Air−Water Interface. Macromolecules. 1996;29(23):7412-7.
352. Nikolov AD, Wasan DT. Ordered micelle structuring in thin films formed from anionic surfactant solutions: I. Experimental. Journal of Colloid and Interface Science. 1989;133(1):1-12.
353. Kumar K, Nikolov AD, Wasan DT. Effect of Film Curvature on Drainage of Thin Liquid Films. Journal of Colloid and Interface Science. 2002;256(1):194-200.
354. Chari K, Lenhart WC. Effect of polyvinylpyrrolidone on the self-assembly of model hydrocarbon amphiphiles. Journal of Colloid And Interface Science. 1990;137(1):204-16.
355. Goddard ED. Polymer/surfactant interaction: Interfacial aspects. Journal of Colloid and Interface Science. 2002;256(1):228-35.
356. Clauzel M, Johnson ES, Nylander T, Panandiker RK, Sivik MR, Piculell L. Surface Deposition and Phase Behavior of Oppositely Charged Polyion–Surfactant Ion Complexes. Delivery of Silicone Oil Emulsions to Hydrophobic and Hydrophilic Surfaces. ACS Applied Materials & Interfaces. 2011;3(7):2451-62.
357. Svensson AV, Huang L, Johnson ES, Nylander T, Piculell L. Surface Deposition and Phase Behavior of Oppositely Charged Polyion/Surfactant Ion Complexes. 1. Cationic Guar versus Cationic Hydroxyethylcellulose in Mixtures with Anionic Surfactants. ACS Applied Materials & Interfaces. 2009;1(11):2431-42.
358. Svensson AV, Johnson ES, Nylander T, Piculell L. Surface Deposition and Phase Behavior of Oppositely Charged Polyion−Surfactant Ion Complexes. 2. A Means to Deliver Silicone Oil to Hydrophilic Surfaces. ACS Applied Materials & Interfaces. 2010;2(1):143-56.
359. Anthony O, Marques CM, Richetti P. Bulk and Surface Behavior of Cationic Guars in Solutions of Oppositely Charged Surfactants. Langmuir. 1998;14(21):6086-95.
360. Zimin D, Craig VSJ, Kunz W. Adsorption and desorption of polymer/surfactant mixtures at solid-liquid interfaces: Substitution experiments. Langmuir. 2004;20(19):8114-23.
361. Cohen-Addad S, di Meglio J-M. Stabilization of aqueous foam by hydrosoluble polymers. 2. Role of polymer/surfactant interactions. Langmuir. 1994;10(3):773-8.
362. Zeng Y, von Klitzing R. Structuring of colloidal suspensions confined between a silica microsphere and an air bubble. Soft Matter. 2011;7(11):5329-38.
363. Wang G, Olofsson G. Titration Calorimetric Study of the Interaction between Ionic Surfactants and Uncharged Polymers in Aqueous Solution. The Journal of Physical Chemistry B. 1998;102(46):9276-83.
364. Shen Q, Wei H, Wang L, Zhou Y, Zhao Y, Zhang Z, et al. Crystallization and Aggregation Behaviors of Calcium Carbonate in the Presence of Poly(vinylpyrrolidone) and Sodium Dodecyl Sulfate. The Journal of Physical Chemistry B. 2005;109(39):18342-7.
365. Lange H. Wechselwirkung zwischen Natriumalkylsulfaten und Polyvinylpyrrolidon in wäßrigen Lösungen. Kolloid-Zeitschrift und Zeitschrift für Polymere. 1971;243(2):101-9.
366. Fadnavis N, Engberts JBFN. Surfactant-polymer interactions and their effects on the micellar inhibition of the neutral hydrolysis of 1-benzoyl-1,2,4-triazole. Journal of the American Chemical Society. 1984;106(9):2636-40.
367. Öztekin N, Erim FB. Determination of Critical Aggregation Concentration in the Poly-(vinylpyrrolidone)–Sodium Dodecyl Sulfate System by Capillary Electrophoresis. Journal of Surfactants and Detergents. 2013;16(3):363-7.
368. Frostad JM, Walter J, Leal LG. A scaling relation for the capillary-pressure driven drainage of thin films. Physics of Fluids. 2013;25(5):052108.

369. Mészáros R, Varga I, Gilányi T. Effect of Polymer Molecular Weight on the Polymer/Surfactant Interaction. The Journal of Physical Chemistry B. 2005;109(28):13538-44.
370. Nespolo SA, Bevan MA, Chan DYC, Grieser F, Stevens GW. Hydrodynamic and Electrokinetic Properties of Decane Droplets in Aqueous Sodium Dodecyl Sulfate Solutions. Langmuir. 2001;17(23):7210-8.
371. Milling AJ, Kendall K. Depletion, Adsorption, and Structuring of Sodium Poly(acrylate) at the Water-Silica Interface. 1. An Atomic Force Microscopy Force Study. Langmuir. 2000;16(11):5106-15.
372. Biggs S, Dagastine RR, Prieve DC. Oscillatory Packing and Depletion of Polyelectrolyte Molecules at an Oxide-Water Interface. J Phys Chem B. 2002;106(44):11557-64.
373. Edwards TD, Bevan MA. Depletion-Mediated Potentials and Phase Behavior for Micelles, Macromolecules, Nanoparticles, and Hydrogel Particles. Langmuir. 2012;28(39):13816-23.
374. Braem AD, Prieve DC, Tilton RD. Electrostatically Tunable Coadsorption of Sodium Dodecyl Sulfate and Poly(ethylene oxide)-b-poly(propylene oxide)-b-poly(ethylene oxide) Triblock Copolymer to Silica. Langmuir. 2001;17(3):883-90.
375. Alvarez NJ, Walker LM, Anna SL. Diffusion-limited adsorption to a spherical geometry: The impact of curvature and competitive time scales. Physical Review E. 2010;82(1).
376. Ma S, Sherwood JM, Huck WTS, Balabani S. On the flow topology inside droplets moving in rectangular microchannels. Lab on a Chip. 2014;14(18):3611-20.
377. Fewkes CJ. Droplet interactions in structured fluids and charged colloidal systems2016.
378. Otsu N. A Threshold Selection Method from Gray-Level Histograms. IEEE Transactions on Systems, Man, and Cybernetics. 1979;9(1):62-6.
379. Sharifi M, Fathy M, Mahmoudi MT, editors. A classified and comparative study of edge detection algorithms. Proceedings International Conference on Information Technology: Coding and Computing; 2002 8-10 April 2002.
380. Shrivakshan GT, Chandrasekar C. A comparison of various edge detection techniques used in image processing. International Journal of Computer Science Issues. 2012;9(5):269-76.
381. Coope ID. Circle fitting by linear and nonlinear least squares. Journal of Optimization Theory and Applications. 1993;76(2):381-8.
382. Fitzgibbon A, Pilu M, Fisher RB. Direct least square fitting of ellipses. IEEE Transactions on Pattern Analysis and Machine Intelligence. 1999;21(5):476-80.
383. Fabijańska A. Subpixel edge detection in blurry and noisy images. 2015;12:1-19.
384. Ghosal S, Mehrotra R. Orthogonal moment operators for subpixel edge detection. Pattern Recognition. 1993;26(2):295-306.
385. Christian JA. Accurate Planetary Limb Localization for Image-Based Spacecraft Navigation. Journal of Spacecraft and Rockets. 2017;54(3):708-30.
386. Trujillo-Pino A, Krissian K, Alemán-Flores M, Santana-Cedrés D. Accurate subpixel edge location based on partial area effect. Image and Vision Computing. 2013;31(1):72-90.
387. Taylor GI. The viscosity of a fluid containing small drops of another fluid. Proceedings of the Royal Society of London Series A, Containing Papers of a Mathematical and Physical Character. 1932;138(834):41-8.
388. Taylor GI. The formation of emulsions in definable fields of flow. Proceedings of the Royal Society of London Series A, Containing Papers of a Mathematical and Physical Character. 1934;146(858):501-23.
389. Rallison JM. The Deformation of Small Viscous Drops and Bubbles in Shear Flows. Annual Review of Fluid Mechanics. 1984;16(1):45-66.
390. Rumscheidt FD, Mason SG. Particle motions in sheared suspensions XII. Deformation and burst of fluid drops in shear and hyperbolic flow. Journal of Colloid Science. 1961;16(3):238-61.
391. Li Z, Mak SY, Sauret A, Shum HC. Syringe-pump-induced fluctuation in all-aqueous microfluidic system implications for flow rate accuracy. Lab Chip. 2014;14(4):744-9.
392. Bong KW, Chapin SC, Pregibon DC, Baah D, Floyd-Smith TM, Doyle PS. Compressed-air flow control system. Lab on a Chip. 2011;11(4):743-7.
393. Lee L-T. Polymer–surfactant interactions: neutron scattering and reflectivity. Current Opinion in Colloid & Interface Science. 1999;4(3):205-13.

394. Penfold J, Thomas RK. Neutron reflectivity and small angle neutron scattering: An introduction and perspective on recent progress. Current Opinion in Colloid & Interface Science. 2014;19(3):198-206.
395. Pan F, Lu Z, Tucker I, Hosking S, Petkov J, Lu JR. Surface active complexes formed between keratin polypeptides and ionic surfactants. Journal of Colloid and Interface Science. 2016;484:125-34.
396. Besnard L, Protat M, Malloggi F, Daillant J, Cousin F, Pantoustier N, et al. Breaking of the Bancroft rule for multiple emulsions stabilized by a single stimulable polymer. Soft Matter. 2014;10(36):7073-87.
397. Campana M, Webster JRP, Lawrence MJ, Zarbakhsh A. Structural conformation of lipids at the oil–water interface. Soft Matter. 2012;8(34):8904-10.
398. Campana M, Webster JRP, Zarbakhsh A. Structural Studies of Nonionic Dodecanol Ethoxylates at the Oil–Water Interface: Effect of Increasing Head Group Size. Langmuir. 2014;30(34):10241-7.
399. Protat M, Bodin-Thomazo N, Malloggi F, Daillant J, Campbell RA, Fragneto G, et al. Neutron reflectivity measurements at the oil/water interface for the study of stimuli-responsive emulsions. The European Physical Journal E. 2018;41(7):85.
400. Zarbakhsh A, Webster JRP, Eames J. Structural Studies of Surfactants at the Oil–Water Interface by Neutron Reflectometery. Langmuir. 2009;25(7):3953-6.
401. Staples E, Penfold J, Tucker I. Adsorption of Mixed Surfactants at the Oil–Water Interface. The Journal of Physical Chemistry B. 2000;104(3):606-14.
402. Penfold J, Thomas RK, Li PX, Petkov JT, Tucker I, Webster JRP, et al. Adsorption at Air–Water and Oil–Water Interfaces and Self-Assembly in Aqueous Solution of Ethoxylated Polysorbate Nonionic Surfactants. Langmuir. 2015;31(10):3003-11.
403. Bumajdad A, Eastoe J, Nave S, Steytler DC, Heenan RK, Grillo I. Compositions of Mixed Surfactant Layers in Microemulsions Determined by Small-Angle Neutron Scattering. Langmuir. 2003;19(7):2560-7.
404. Tucker IM, Petkov JT, Jones C, Penfold J, Thomas RK, Rogers SE, et al. Adsorption of Polymer–Surfactant Mixtures at the Oil–Water Interface. Langmuir. 2012;28(42):14974-82.
405. Sokolova A, Christoforidis J, Eltobaji A, Barnes J, Darmann F, Whitten AE, et al. BILBY: Time-of-Flight Small Angle Scattering Instrument. Neutron News. 2016;27(2):9-13.
406. Sokolova A, Whitten AE, de Campo L, Christoforidis J, Eltobaji A, Barnes J, et al. Performance and characteristics of the BILBY time-of-flight small-angle neutron scattering instrument. Journal of Applied Crystallography. 2019;52(1):1-12.
407. Arnold O, Bilheux JC, Borreguero JM, Buts A, Campbell SI, Chapon L, et al. Mantid−Data analysis and visualization package for neutron scattering and μ SR experiments. Nuclear Instruments and Methods in Physics Research Section A: Accelerators, Spectrometers, Detectors and Associated Equipment. 2014;764:156-66.
408. Feigin LA, Svergun DI. Structure Analysis by Small-Angle X-Ray and Neutron Scattering: Springer US; 2013.
409. Hansen J-P, Hayter JB. A rescaled MSA structure factor for dilute charged colloidal dispersions. Molecular Physics. 1982;46(3):651-6.
410. Hayter JB, Penfold J. An analytic structure factor for macroion solutions. Molecular Physics. 1981;42(1):109-18.
411. Hammouda B. A new Guinier-Porod model. Journal of Applied Crystallography. 2010;43(4):716-9.
412. Hammouda B. Probing Nanoscale Structures: The SANS Toolbox http://www.ncnr.nist.gov/staff/hammouda/the_SANS_toolbox.pdf2008 [
413. Sapir L, Stanley CB, Harries D. Properties of Polyvinylpyrrolidone in a Deep Eutectic Solvent. The Journal of Physical Chemistry A. 2016;120(19):3253-9.
414. Yurekli K, Mitchell CA, Krishnamoorti R. Small-Angle Neutron Scattering from Surfactant-Assisted Aqueous Dispersions of Carbon Nanotubes. Journal of the American Chemical Society. 2004;126(32):9902-3.

415. Hayter JB, Penfold J. Self-consistent structural and dynamic study of concentrated micelle solutions. Journal of the Chemical Society, Faraday Transactions 1: Physical Chemistry in Condensed Phases. 1981;77(8):1851-63.
416. Hayter JB, Penfold J. Determination of micelle structure and charge by neutron small-angle scattering. Colloid and Polymer Science. 1983;261(12):1022-30.
417. Gawali SL, Zhang M, Kumar S, Ray D, Basu M, Aswal VK, et al. Discerning the Structure Factor of Charged Micelles in Water and Supercooled Solvent by Contrast Variation X-ray Scattering. Langmuir. 2019;35(30):9867-77.
418. Hassan PA, Fritz G, Kaler EW. Small angle neutron scattering study of sodium dodecyl sulfate micellar growth driven by addition of a hydrotropic salt. Journal of Colloid and Interface Science. 2003;257(1):154-62.
419. Bucci S, Fagotti C, Degiorgio V, Piazza R. Small-angle neutron-scattering study of ionic-nonionic mixed micelles. Langmuir. 1991;7(5):824-6.
420. Seguin C, Eastoe J, Heenan RK, Grillo I. SANS studies of the effects of surfactant head group on aggregation properties in water/glycol and pure glycol systems. Journal of Colloid and Interface Science. 2007;315(2):714-20.
421. Hammouda B. Temperature Effect on the Nanostructure of SDS Micelles in Water. Journal of Research of the National Institute of Standards and Technology. 2013;118:151-67.
422. Bergström M, Skov Pedersen J. Structure of pure SDS and DTAB micelles in brine determined by small-angle neutron scattering (SANS). Physical Chemistry Chemical Physics. 1999;1(18):4437-46.
423. Almgren M, Gimel JC, Wang K, Karlsson G, Edwards K, Brown W, et al. SDS Micelles at High Ionic Strength. A Light Scattering, Neutron Scattering, Fluorescence Quenching, and CryoTEM Investigation. Journal of Colloid and Interface Science. 1998;202(2):222-31.
424. Tianyi B, Tabor RF, Tardy BL, Jamieson EJ, Ainger NJ, Dagastine RR. Micellization of sodium lauryl sulfate surfactants with polydisperse headgroup. Submitted. 2020:1-18.
425. Tanford C. Micelle shape and size. The Journal of Physical Chemistry. 1972;76(21):3020-4.
426. Pedersen JS. Analysis of small-angle scattering data from colloids and polymer solutions: modeling and least-squares fitting. Advances in Colloid and Interface Science. 1997;70:171-210.
427. Hansen J-P, McDonald IR. Theory of simple liquids. [electronic resource] with applications to soft matter. 4th ed. ed: Academic Press; 2013.
428. Klapp SHL, Qu D, v. Klitzing R. Long-Range Interactions between Soft Colloidal Particles in Slit−Pore Geometries. The Journal of Physical Chemistry B. 2007;111(6):1296-303.
429. Arenas-Gómez B, Garza C, Liu Y, Castillo R. Alignment of worm-like micelles at intermediate and high shear rates. Journal of Colloid and Interface Science. 2019.
430. Moore JE, McCoy TM, de Campo L, Sokolova AV, Garvey CJ, Pearson G, et al. Wormlike micelle formation of novel alkyl-tri(ethylene glycol)-glucoside carbohydrate surfactants: Structure–function relationships and rheology. Journal of Colloid and Interface Science. 2018;529:464-75.
431. Jindal VK, Kalus J, Pilsl H, Hoffmann H, Lindner P. Dynamic small-angle neutron scattering study of rodlike micelles in a surfactant solution. The Journal of Physical Chemistry. 1990;94(7):3129-38.
432. Kalus J, Hoffmann H, Chen SH, Lindner P. Correlations in micellar solutions under shear: a small-angle neutron scattering study of the chain surfactant N-hexadecyloctyldimethylammonium bromide. The Journal of Physical Chemistry. 1989;93(10):4267-76.
433. Muench C, Hoffmann H, Ibel K, Kalus J, Neubauer G, Schmelzer U, et al. Transient small-angle neutron scattering experiments on micellar solutions with a shear-induced structural transition. The Journal of Physical Chemistry. 1993;97(17):4514-22.
434. Stellbrink J, Lonetti B, Rother G, Willner L, Richter D. Shear induced structures of soft colloids: Rheo-SANS experiments on kinetically frozen PEP–PEO diblock copolymer micelles. Journal of Physics: Condensed Matter. 2008;20(40):404206.

435. LaFollette TA, Walker LM. Structural and Mechanical Hysteresis at the Order-Order Transition of Block Copolymer Micellar Crystals. Polymers. 2011;3(1):281-98.
436. King SM, Heenan RK, Cloke VM, Washington C. Neutron Scattering from a Poly(oxyethylene)−Poly(oxypropylene)−Poly(oxyethylene) Copolymer in Dilute Aqueous Solution under Shear Flow. Macromolecules. 1997;30(20):6215-22.
437. Penfold J, Staples E, Tucker I, Carroll P, Clayton I, Cowan JS, et al. Elongational Flow Induced Ordering in Surfactant Micelles and Mesophases. The Journal of Physical Chemistry B. 2006;110(2):1073-82.
438. Cummins PG, Penfold J, Staples E. A study of the structure of mixed cationic/nonionic micelles by small-angle neutron scattering spectrometry. Langmuir. 1992;8(1):31-5.
439. Staples EJ, Cummins PG, Leng F, Penfold J. Neutron scattering of mixed micelles under shear. Chemical Physics Letters. 1988;149(2):191-5.
440. Penfold J, Staples E, Cummins PG. Small angle neutron scattering investigation of rodlike micelles aligned by shear flow. Advances in Colloid and Interface Science. 1991;34:451-76.
441. Penfold J, Staples E, Lhodi AK, Tucker I. The study of anisotropically shaped micelles subjected to shear flow by small-angle neutron scattering. International Journal of Thermophysics. 1995;16(5):1109-17.
442. Hammouda B. SANS from Polymers—Review of the Recent Literature. Polymer Reviews. 2010;50(1):14-39.
443. Hammouda B. SANS from homogeneous polymer mixtures: A unified overview. Polymer Characteristics. Berlin, Heidelberg: Springer Berlin Heidelberg; 1993. p. 87-133.
444. Beaucage G. Approximations Leading to a Unified Exponential/Power-Law Approach to Small-Angle Scattering. Journal of Applied Crystallography. 1995;28(6):717-28.
445. Cattoz B, de Vos WM, Cosgrove T, Crossman M, Espidel Y, Prescott SW. Interpolymer Complexation: Comparisons of Bulk and Interfacial Structures. Langmuir. 2015;31(14):4151-9.
446. Hammouda B. Analysis of the Beaucage model. Journal of Applied Crystallography. 2010;43(6):1474-8.
447. Knappe P, Bienert R, Weidner S, Thünemann AF. Characterization of poly(N-vinyl-2-pyrrolidone)s with broad size distributions. Polymer. 2010;51(8):1723-7.
448. Anitas EM. Small-Angle Scattering from Mass and Surface Fractals: IntechOpen; 2017 December 20th 2017.
449. Cabane B, Duplessix R. Decoration of semidilute polymer solutions with surfactant micelles. J Phys France. 1987;48(4):651-62.
450. Lee L-T, Cabane B. Effects of Surfactants on Thermally Collapsed Poly(N-isopropylacrylamide) Macromolecules. Macromolecules. 1997;30(21):6559-66.
451. Cabane B. Structure of some polymer-detergent aggregates in water. The Journal of Physical Chemistry. 1977;81(17):1639-45.
452. Cabane B, Duplessix R. Organization of surfactant micelles adsorbed on a polymer molecule in water : a neutron scattering study. J Phys France. 1982;43(10):1529-42.
453. Cabane B, Duplessix R. Neutron scattering study of water-soluble polymers adsorbed on surfactant micelles. Colloids and Surfaces. 1985;13:19-33.
454. Bergström LM, Kjellin URM, Claesson PM, Grillo I. Small-Angle Neutron Scattering Study of Mixtures of Cationic Polyelectrolyte and Anionic Surfactant: Effect of Polyelectrolyte Charge Density. The Journal of Physical Chemistry B. 2004;108(6):1874-81.
455. Claesson PM, Bergström M, Dedinaite A, Kjellin M, Legrand J-F, Grillo I. Mixtures of Cationic Polyelectrolyte and Anionic Surfactant Studied with Small-Angle Neutron Scattering. The Journal of Physical Chemistry B. 2000;104(49):11689-94.
456. Borsali R, Nguyen H, Pecora R. Small-Angle Neutron Scattering and Dynamic Light Scattering from a Polyelectrolyte Solution: DNA. Macromolecules. 1998;31(5):1548-55.
457. Borsali R, Rinaudo M, Noirez L. Light Scattering and Small-Angle Neutron Scattering from Polyelectrolyte Solutions: The Succinoglycan. Macromolecules. 1995;28(4):1085-8.
458. Milas M, Rinaudo M, Duplessix R, Borsali R, Lindner P. Small Angle Neutron Scattering from Polyelectrolyte Solutions: From Disordered to Ordered Xanthan Chain Conformation. Macromolecules. 1995;28(9):3119-24.

459. Hammouda B, Ho DL. Insight into chain dimensions in PEO/water solutions. Journal of Polymer Science Part B: Polymer Physics. 2007;45(16):2196-200.
460. Hammouda B, Ho DL, Kline S. Insight into Clustering in Poly(ethylene oxide) Solutions. Macromolecules. 2004;37(18):6932-7.
461. Teraoka I. Models of Polymer Chains. Polymer Solutions: John Wiley & Sons; 2002. p. 1-67.
462. Norwood DP, Minatti E, Reed WF. Surfactant/polymer assemblies. 1. Surfactant binding properties. Macromolecules. 1998;31(9):2957-65.
463. Mohr A, Nylander T, Piculell L, Lindman B, Boyko V, Bartels FW, et al. Mixtures of Cationic Copolymers and Oppositely Charged Surfactants: Effect of Polymer Charge Density and Ionic Strength on the Adsorption Behavior at the Silica–Aqueous Interface. ACS Applied Materials & Interfaces. 2012;4(3):1500-11.
464. Terada E, Samoshina Y, Nylander T, Lindman B. Adsorption of cationic cellulose derivatives/anionic surfactant complexes onto solid surfaces. I. Silica surfaces. Langmuir. 2004;20(5):1753-62.
465. de Gennes PG. Polymers at an interface; a simplified view. Adv Colloid Interface Sci. 1987;27(3-4):189-209.
466. Alexander S. Adsorption of chain molecules with a polar head a scaling description. J Phys (Paris) FIELD Full Journal Title:Journal de Physique (Paris). 1977;38(8):983-7.

Chapter 9: Appendices

Chapter 3: Experimental Methods

A9.1 Drop Cantilever Fabrication

To perform drop-drop direct force measurements in the AFM custom-made cantilevers with a gold disk at the end were fabricated by myself and fellow PhD candidates Mathew Biviano and Alisa Bai. The method was adapted from a process initially developed by Douglas Mair with the help of Daniel Smith at the Melbourne Centre for Nanofabrication (MCN). It can be broken down into four stages, namely; gold patterning onto the top silicone layer, cantilever definition, backside etch and cantilever release. An overview of the process is covered in Figure A9.1 through a series of side view schematics of the wafer development at each stage of the fabrication.

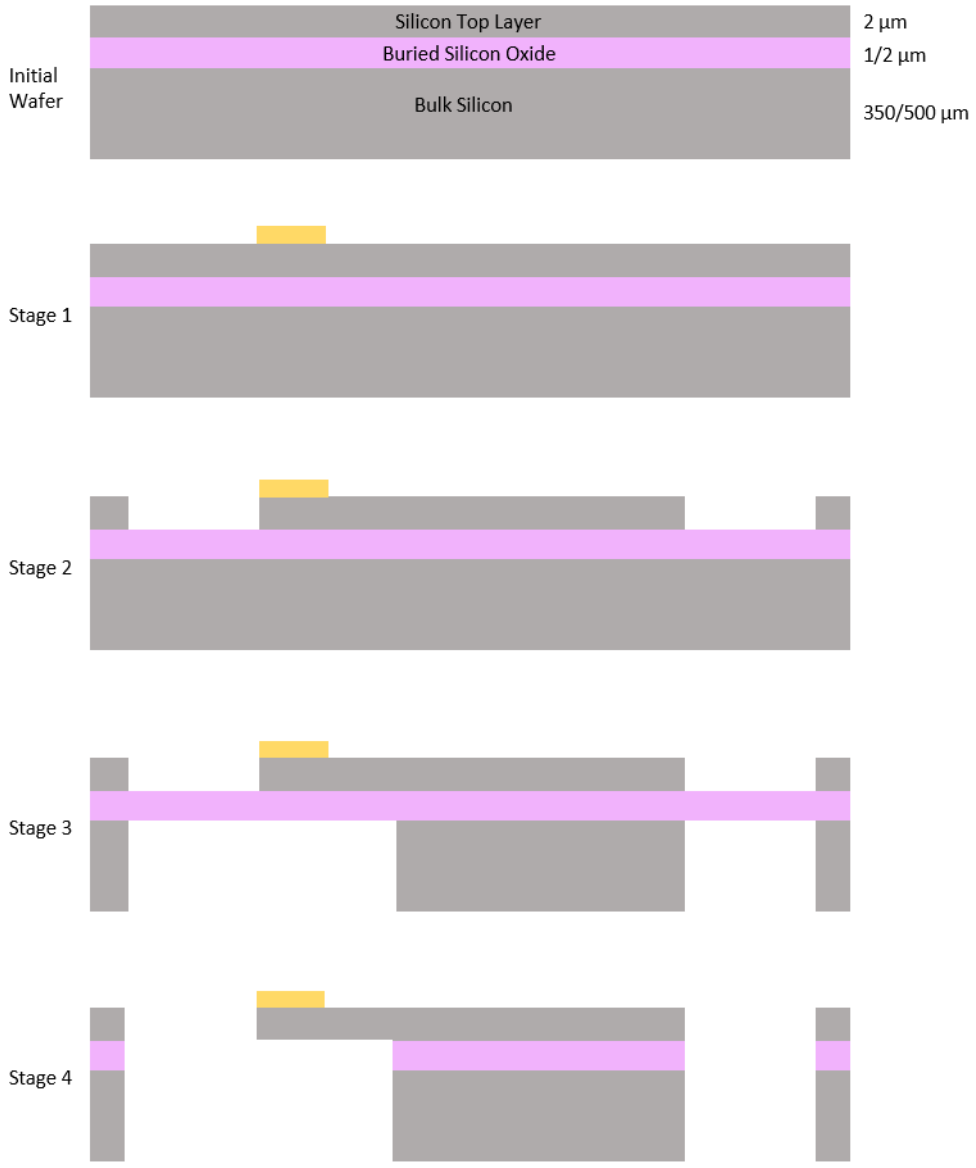

Figure A9.1 Side schematic of a wafer's development at each stage of the fabrication process

The cantilevers were made from custom silicon on insulator (SOI) 4-inch wafers (Ultrasil LLC, California, USA) composed of either a 350 or 500 µm silicon base coated with a 1 or 2 µm layer of silicon oxide respectively and a final 2 µm silicon layer of which the cantilever is formed out of. The two different wafer configurations were explored for variances in processing flexibility and final product use. However, ultimately no differences were identified as a result of these parameters. Photolithographic techniques were used during stages 1 to 3 of the process, each requiring a different chrome mask for patterning of the relevant features. The masks were designed using L-Edit and manufactured at the Bandwidth Foundry, ANFF.

A9.1.1 Gold Patterning (Stage 1)

Stage 1 covers the steps required to precisely evaporate the gold discs at the tip of the future cantilevers. Negative AZ 2035nLOF photoresist was spun onto the top silicon layer at 2000 rpm for 30 seconds using a SUSS Delta 80RC spin coater (SUSS MicroTec, Germany). The resist was partially set with a soft bake (SB) for 90 seconds at 110 °C prior to the wafer being aligned with the gold metallisation mask and exposed to 85 mJ/cm^2 of UV light with an EVG 6200 mask Aligner (EV Group, Austria). The wafer then underwent a post exposure bake (PEB) for 90 seconds at 110 °C and was allowed to cool for 10 minutes. The photoresist was developed for 40 – 60 seconds in undiluted AZ 726 metal ion free (MIF) developer. Prior to evaporation, the layer was inspected for defects using a microscope as it is still possible to entirely strip the resist and start over if there are any large unusable flaws at this point. A Nanochrome II electron beam and thermal evaporation system (Intlvac, New York, USA) was used to evaporate 7 nm of chrome flowed by 40 nm of gold onto the surface. The resist layer thickness should be set to around 10 times the combined thickness of the metal coatings. To remove the photoresist and excess gold the wafer was first soaked in an acetone bath prior to a thorough clean in fresh acetone and an ultrasonic bath for 60 seconds or until all features looked clear. Finally, the wafer was rinsed with acetone, isopropanol and deionised water, then dried with nitrogen gas.

A9.1.2 Cantilever Definition (Stage 2)

The shape of the cantilever is etched out of the top silicon layer during the second stage of the process. Positive AZ 4562 photoresist was spun onto the top surface at 3000 rpm for 30 seconds and put through a SB for 180 seconds at 110 °C. The cantilever definition mask was aligned over the wafer, utilising alignment markers at the sides of the cantilever designs (transferred on to the wafer with the gold patterning) to carefully position the cantilever pattern over the gold discs already set on the wafer and exposed to 150 mJ/cm^2 of UV light. The photoresist was developed for 3 - 4 minutes, or until the pattern was clear, in undiluted AZ 726 MIF developer, rinsed with deionised water and dried with nitrogen gas. A Plasmalab100 ICP380 (Oxford Instruments, UK) was used to DRIE etch the unwanted sections of the top silicon layer (2 µm thickness) to define

the cantilevers form. The Bosch process implemented to perform the etch was run for 9 – 12 cycles to ensure all the silicon was removed and the buried silicon oxide layer was completely uncovered, where over rather than under etching was more important. As before the remaining photoresist was removed with acetone and an ultrasonic bath, and lastly the wafer was cleaned and dried.

A9.1.3 Backside Etch (Stage 3)

The cantilever bases are made in a similar fashion as stage 2, where instead the bulk silicon is etched to remove the wafer beneath the cantilevers. As shown in Figure A9.1, after this stage the final form of the entire cantilever has been shaped. To protect the frontside of the cantilevers during the backside etching process AZ 4562 photoresist was spun onto the top surface at 2000 rpm for 30 seconds. For additional strength after an initial SB of 5 minutes at 110 °C, a second SB of 10 minutes at 140 °C was also performed. The wafer was turned over and cleaned thoroughly to remove resist and contaminants built up as a result of exposure to equipment surfaces in earlier processing. The surface was first swapped with acetone to clean off bulk contamination, then etched for 5 minutes using only oxygen gas. Positive AZ 40XT photoresist was spun onto the bottom surface at 50 rpm for 10 seconds, 200 rpm for 20 seconds, 500 rpm for 10 seconds and finally 1000 rpm for 60 seconds, before a SB of 5 minutes at 126 °C. The backside etch mask was aligned with the previously mentioned alignment markers on the wafer to ensure consistent pattern positioning and exposed to 400 mJ/cm^2 of UV light. To prevent the wafer sticking to the etching instrument edge bead removal was performed using a flood exposure tool for 40 seconds at 10.4 MW/cm^2. This was followed with a PEB of 5 minutes at 105 °C and cooling down period of 10 minutes. The photoresist was developed for 3 - 4 minutes, or until the pattern was clear, in undiluted AZ 726 MIF developer, rinsed with deionised water and dried with nitrogen gas. The wafer was twice placed in a vacuum oven at 90 °C for 18 hours to drive solvent out of the photoresist to avoid it burning and bubbling during the deep etch step.

The bulk silicon was removed using a standard Bosch process without a descumming step and with a back pressure of 5 Torr to remove the requirement of a carrier wafer. The etching was performed gradually, with 90% of the silicon removed in one turn and the remaining amount etched in small quantities until the buried silicon oxide layer was exposed. Wafers with a 500 μm bulk silicon layer required around 1250 cycles in total, while the 350 μm wafers required around 830 cycles, however the number of cycles was primarily dependent on each wafer. At this stage the wafer is incredibly fragile, with cantilevers held in place via the remaining buried silicon oxide layer and tabs incorporated in the frontside cantilever layer. The remaining backside resist and all the frontside protect was stripped off the wafer using a Piranha solution of 3:1 concentrated sulphuric acid and 30% hydrogen peroxide for roughly 5 minutes.

A9.1.4 Cantilever Release (Stage 4)

Stage 4 removes the remaining buried silicon oxide layer such that the cantilevers in their holders are all that remain. This is achieved by submerging the wafers in 5% hydrofluoric acid (HF) for 40 minutes to remove 1 μm layers and 80 minutes to remove 2 μm layers. The etch rate of silicon oxide in HF at 5% is around 50 nm every 6 minutes. The wafer is rinsed in calcium carbonate to neutralise the HF and rinsed in deionised water before carefully drying it. The wafer was stored on UV saw tape to secure them for transportation and aide cantilever detachment into gel boxes for use.

Chapter 4: Forces between oil drops in polymer-surfactant systems: Linking direct force measurements to microfluidic observations

A9.2 Microfluidic Design Schematics and Dimensions

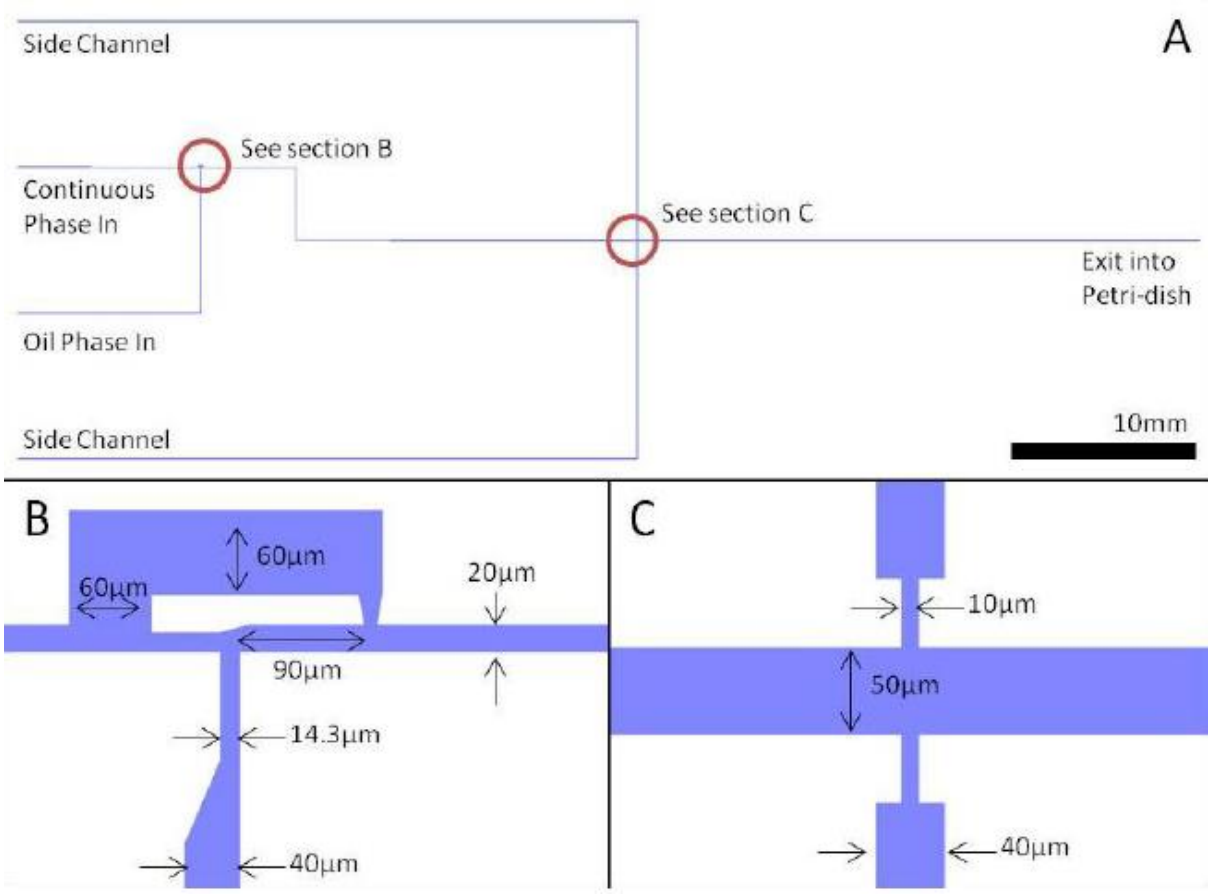

Figure A9.2 Schematic diagram of the microfluidic design used for drop chaining experiments showing (A) an overview of the device from entry to exit, (B) the dimensions and geometry of the block and break design, and (C) the dimensions and geometry of the exit channels for removal of excess aqueous solution.

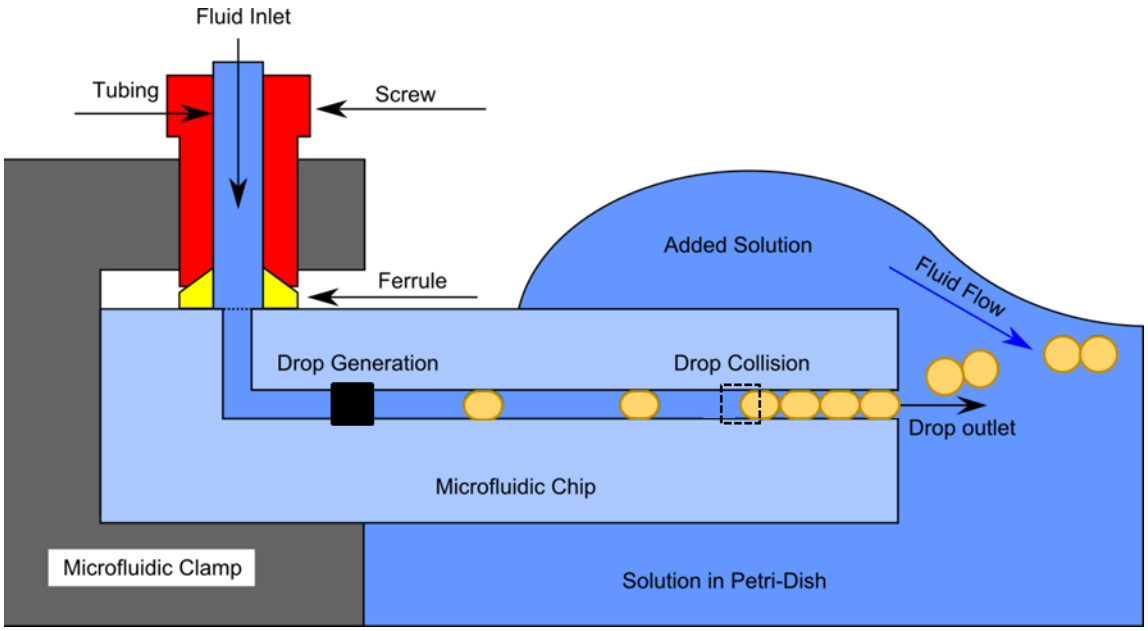

Figure A9.3 : Side on schematic diagram of the microfluidic apparatus and surrounding fluid designed to generate drop chains. After the drops are generated and collided within the microfluidic device the droplet chains flow into solution. Additional solution is added on the top of the microfluidic device and flows over the exit port, mitigating against drop aggregation at the exit of the microfluidic device.

A9.3 AFM force curves between two hydrophilic silica surfaces in PVP/SDS solutions

The force between silica surfaces has been well studied in the literature as a model hydrophilic system, which is predominant in many colloidal probe measurements. Figure A9.4(A) shows direct force measurements between a 2.5 μm radii silica particle and glass slide in solutions of 0.5% PVP and 2mM, 10mM and 30 mM SDS. These curves show behaviours consistent with the presence of a steric brush, with increasing repulsion at close separation. Despite the potential for polymer bridging, it is important to note that there is no evidence of an adhesive force or hysteresis on the retract curve that would indicate bridging over the three concentrations. With increasing concentration, the slope of the curve increases, signifying an increase in brush length.

PVP and SDS have been shown in the literature to absorb at the silica-water interface as a complex brush (129, 130). Prescott *et al.* provided evidence of a three-stage binding process with increasing surfactant concentration, essentially comprising of initial surfactant binding, chain elongation and finally desorption of the adsorbed complex. From SANS and NMR experiments they demonstrate that around the CAC (~2.5 mM) surfactants begin to aggregate to the adsorbed polymer, and at SDS concentrations above the CMC there is a barely discernible presence of a layer, concluding that desorption of the complex had occurred.

The steric forces were modelled using the potential energy between parallel plates of separation h with adsorbed polymer brushes of size L_o according to the de Gennes model (465, 466):

$$E_{Steric} = \begin{cases} \dfrac{8k_bTL_o}{35s^3}\left[7\left(\dfrac{2L_o}{h}\right)^{\frac{5}{4}} - 5\left(\dfrac{h}{2L_o}\right)^{\frac{7}{4}} - 12\right] & for\ h < 2L_o \\ 0 & for\ h \geq 2L_o \end{cases} \qquad \text{(A9.1)}$$

Using the Derjaguin approximation for a sphere and infinite surface, a model was fitted to the experimental data to extract the polymer brush length at each SDS concentration. Figure A9.4(B) shows the calculated polymer brush lengths at each SDS concentration. These results are in strong agreement with those obtained by Prescott et al. (130).

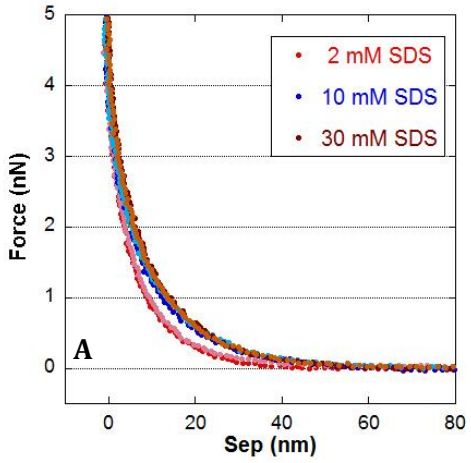

B

SDS Concentration (mM)	Brush Length (nm)
2	22.6 ± 0.3
5	24.6 ± 0.6
10	29.1 ± 0.3
15	29.5 ± 0.2
20	30.2 ± 0.4
30	28.84 ± 0.6

Figure A9.4 (A) The approach and retract AFM force curves between a silica particle and glass slide in an aqueous solutions of 0.5% PVP with 2mM SDS (red), 10mM SDS (blue) and 30mM SDS (brown) **(B)** Summary of the complex brush length determined by fitting a de Gennes model to the AFM curve data.

A9.4 Surfactant molecule mass balance – determining solution ionic strength

Zana et al. showed through florescence studies of a SDS and PVP system that polymer bound micelles increase in aggregation number from 18-50 as the SDS concentration increases from 10 to 30 mM (102). Surfactants in micelles have an 'effective degree of counterion disassociation' (α), with Bales et al. reporting a value of 0.272 for SDS over a range of salt concentrations (103). However, the degree of disassociation is also dependent on the aggregation number of the micelle. Therefore, Wan-Badhi et al. used electrochemical measurements and gel filtration to provide the counterion disassociation as a function of surfactant concentration for a PVP-SDS system, recording a decrease from 0.45 to 0.27 with increasing SDS concentration from 10 to 30 mM. They also predict that one polymer molecule is in contact with approximately 40 micelles at saturation of a 700 000 MW PVP polymer, giving approximately 158 PVP monomers per micelle (100).

Based on the above studies, setting the salt concentration of the solution is equal to the summation of the contribution of disassociated ions from polymer bound SDS micelles (subscript p), free SDS molecules in solution (subscript s) and free SDS micelles (subscript m), which can be represented by the following equation:

$$[Salt] = \alpha_p[SDS_p] + [SDS_s] + \alpha_m[SDS_m] \quad \text{(A9.2)}$$

The number of PVP monomers per SDS molecule can be calculated from the number of SDS molecules per micelle (obtained from Zana et al.) and the number of PVP monomers per micelle (obtained from Wan-Badhi et al.), assuming that the number of bound micelles remains constant and the aggregation number alone increases with increasing SDS concentration. Using the PVP

monomer amount of 4.5 mmol for a 0.5 wt% PVP solution, it is then possible to calculate the amount of SDS bound to the PVP as summarised in Table A9.1.

Table A9.1 Summary of variables for the calculation of polymer bound SDS molecules in different solutions of SDS and PVP

SDS concentration (mM)	10	15	20	30
SDS amount (mmol)	1	1.5	2	3
PVP monomer/ micelle	158	158	158	158
SDS molecule/ micelle	18	30	38	50
PVP monomer/ SDS molecule	8.76	5.26	4.15	3.15
SDS on PVP (mmol)	0.51	0.86	1.09	1.43
SDS on PVP (mM) $[\boldsymbol{SDS_p}]$	5.14	8.57	10.9	14.3

Deducting the concentration of polymer bound SDS from the total amount of SDS added to solution gives the total amount of SDS free in solution. As the CMC of SDS is ≈8 mM, free surfactant concentrations above this value are considered to be in the form of micelles, thus contributing to the free micelle concentration. Table A9.2 details these values, the disassociation factors (α) and final salt concentrations for each of the solutions.

Table A9.2 Summary of variables for the calculation of total electrolyte concentration in different solutions of SDS and PVP

SDS concentration (mM)	10	15	20	30
SDS free in solution (mM)	4.86	6.43	9.14	15.7
Free SDS molecules (mM) $[\boldsymbol{SDS_s}]$	4.86	6.43	8	8
Free SDS micelles (mM) $[\boldsymbol{SDS_m}]$	-	-	1.14	7.71
Polymer bound micelle disassociation factor $[\boldsymbol{\alpha_p}]$	0.45	0.27	0.27	0.27
Free SDS micelle disassociation factor $[\boldsymbol{\alpha_p}]$	0.27	0.27	0.27	0.27
Salt (mM)	7.17	8.74	11.24	13.94
Concentration of additional Electrolyte	4.86	6.43	8.31	10.1

To apply scaling theory analysis the concentration of additional electrolyte is also required. This is simply the sum of the ions contributed by the free SDS molecules and free SDS micelles, as shown in Table A9.2.

A9.5 AFM forces curve of 0.5 wt% PVP and no added SDS

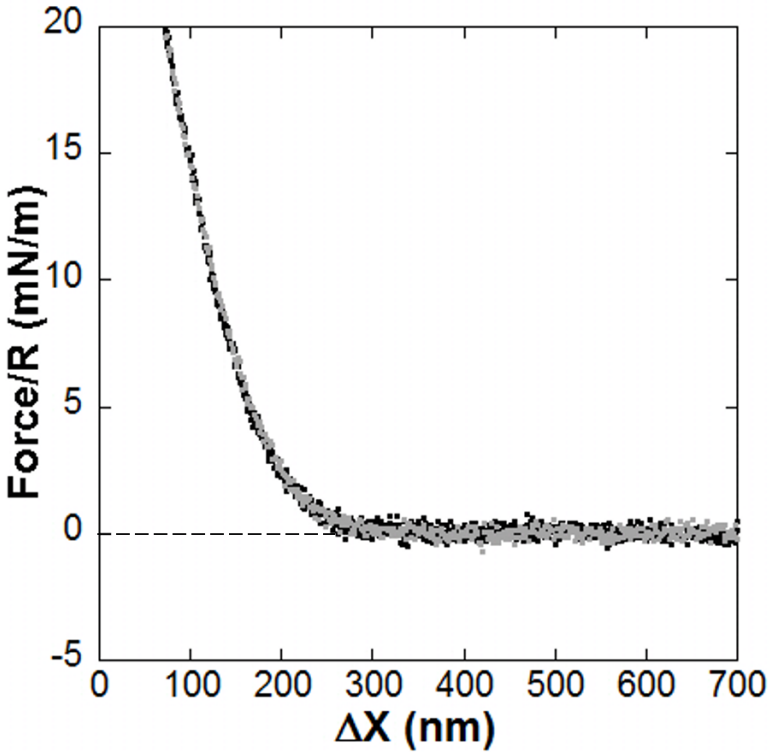

Figure A9.5 Force versus separation for the interaction between an 82µm and 75µm diameter TD drop in 0.5 wt% PVP solution, showing the approach (grey) and retract (black) from an AFM measurement.

A9.6 Fitting parameters for deformable force measurements

Table A9.3 Summary of fitting variables used in and obtained from fitting equilibrium force curves between two tetradecane drops while in the presence of 0.5wt% PVP and varying SDS concentrations

SDS concentration (mM)	10	15	20	30
Interfacial Tension (mN/m)	16.4 ± 3	13.4 ± 3	11.1 ± 3	8.5 ± 3
Drop-Substrate Radii (µm)	28.5 ± 2	28 ± 2	28 ± 2	27.2 ± 2
Drop-Cantilever Radii (µm)	37.2 ± 2	33.5 ± 2	33.5 ± 2	23.2 ± 2
Drop-Substrate Contact Angle (θ)	124.3 ± 5	130.8 ± 5	130.8 ± 5	130.9 ± 5
Drop-Cantilever Contact Angle (θ)	137.5 ± 5	131.7 ± 5	131.7 ± 5	139.7 ± 5
Spring Constant (N/m)	0.132	0.132	0.132	0.282
Ionic Strength (mM)	7.2 ± 0.3	9.1 ± 0.7	11.7 ± 0.5	13.94
Calculated Debye Length (nm)	3.6	3.2	2.8	2.6
Rigid Fit Surface Potential (mV)	15 ± 2	15 ± 2	15 ± 2	16 ± 2
Rigid Fit Depletion Length (nm)	12.8 ± 0.9	11.5 ± 0.8	11.4± 0.6	9.7± 1.0
Rigid Fit Osmotic Pressure (Pa)	667 ± 65	572 ± 51	738 ± 63	1117± 109
Fitted Surface Potential (mV)	-26 ± 2	-14 ± 2	-23 ± 2	-14 ± 2

Chapter 5: Microfluidic Interfacial Tension

A9.7 Taylors plot from inner contour data

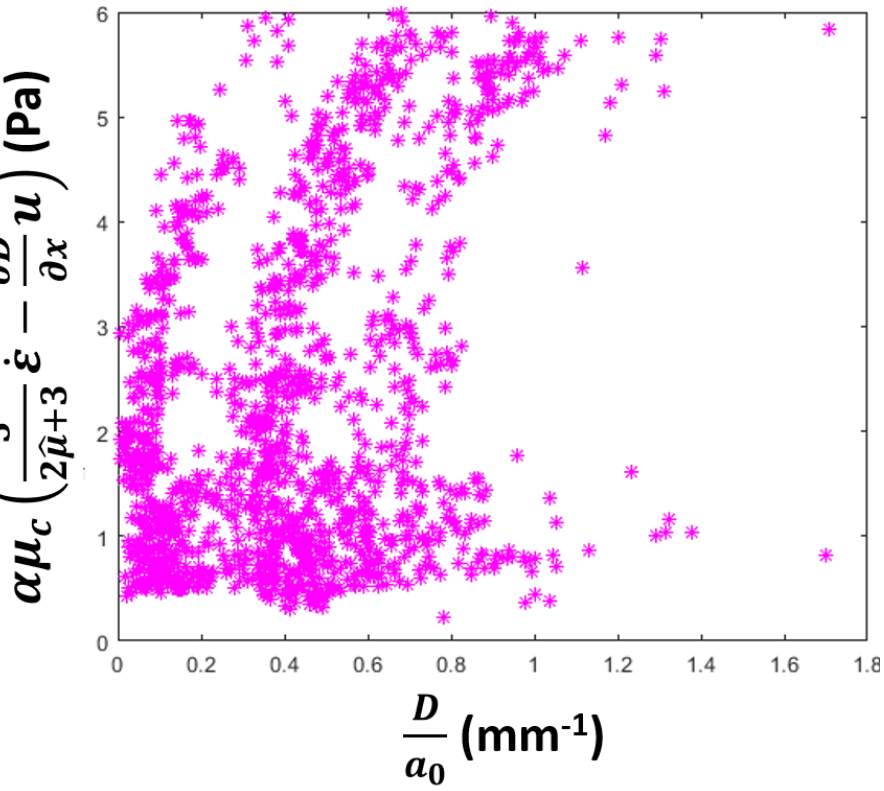

Figure A9.6 Example of a Taylors plot using the inner contour to measure the drops deformation.

A9.8 Drop generation from a block-and-break geometry

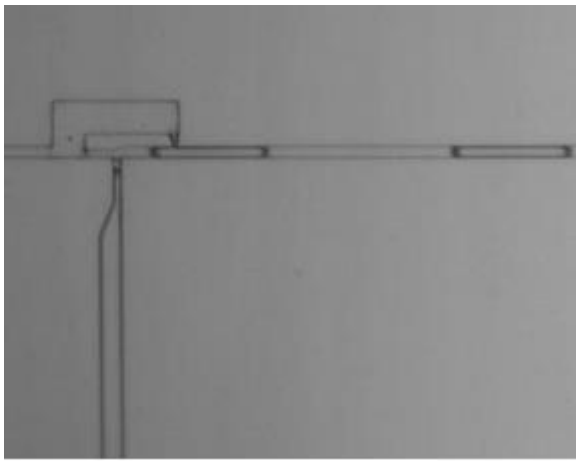

Figure **A9.**7 Image of the drops generated using a block-and-break geometry for solutions containing SDS and PVP. The size of the drop is larger than the space between the T-junction inlet and bypass exit (377).

Chapter 6: Droplet Microfluidic SANS

A9.9 Analysis of scattering potentials for design of the SANS microfluidic device.

Table A9.4 Scattering fraction of SDS micelles calculated using data obtained from the analysis of a standard static 20 mM SANS measurement as presented in Chapter 6

Molecular Weight of SDS (g/mol)	288.4
SDS Concentration (mol/L)	0.02
SDS Critical Micelle Concentration (mol/L)	0.008
Avogadro's Number	6.02×10^{23}
Number of Molecules in Micelles (molecules/L)	7.22×10^{21}
Aggregation Number (molecules/micelle) [a]	70
Number of Micelles (micelle/L)	1.03×10^{20}
Volume of a Micelle (nm^3) [a]	24.8
Scattering Volume (mm^3) [b]	157.1
Number of Surfactants in Scattering Volume	1.13×10^{18}
Number of Micelles in Scattering Volume	1.62×10^{16}
Volume of Micelles in Scattering Volume (mm^3)	0.4
Volume Fraction of Micelle Scattering	0.0026

[a] Value obtained from SANS fitting, presented in Chapter 6.
[b] Given a circular-beam footprint with a radius of 5 mm

Table A9.5 Predicted scattering fraction of adsorbed layers from a microfluidic design as detailed in the "Channel Dimensions" list.

Channel Dimensions	
Width (µm)	55
Spacing between channels (µm)	45
Height (µm)	50
Drop Diameter (µm)	45
Channel Length (µm)	10000
Drop Spacing (µm)	40
Shell Thickness (µm) [c]	0.025
Volume Analysis	
Number of Channels in Illumination Zone	100
Number of Drops per Channel	117
Number of Drops in Illumination Zone	11765
Volume of Drop (μm^3)	47713
Volume of Drop with Layer (μm^3)	47872
Layer Volume (μm^3)	159
Volume of Channel (μm^3)	2.57×10^7
Volume of Drop (μm^3)	5.61×10^6
Volume of Layers (μm^3)	1.87×10^4
Volume of Continuous Phase (μm^3)	2.19×10^7
Volume Fraction of Layer Scattering	0.00068

[c] Value taken as a conservative estimate from the brush length measured from direct force measurements between two hydrophilic silica particles presented in Chapter 4.

A9.10 SANS Fitting Parameters

A9.10.1 Fitting parameters for SDS micelles

The SLD of the solvent and micelle was calculated from the coherent scattering lengths (b) of each individual atom (i) within the compound with n atoms using the formula:

$$SLD = \frac{\sum_{i=1}^{n} b_i}{V_m} \quad \text{(A9.3)}$$

Where V_m is the molecular volume.

Table A9.6 Parameters used in fitting SDS micelles in Chapter 6

Model	Ellipse form factor with Hayter Penfold MSA structure factor				
System	20 mM SDS (Static)		50 mM SDS (Flow)		PFO Drops with 50 mM SDS (Flow)
	Fixed Radius	Variable Radius	Fixed Radius	Variable Radius	
Background (cm^{-1})	0.0509 ± 0.0002	0.0502 ± 0.0002	0.0084 ± 0.0005	0.0075 ± 0.0006	0.0003
Charge (e)	34.67 ± 1.36	33.65 ± 1.33	84.87 ± 5.68	82.88 ± 5.35	69.57 ± 11.82
Dielectric Constant	79.76	79.76	79.76	79.76	79.76
Salt Concentration (mM)	11.24	11.24	19.34	19.34	19.34
Equatorial Radius (R_e) (Å)	16.70	15.99 ± 0.16	16.70	16.08 ± 0.17	16.19 ± 10.30
Polar Radius (R_p) (Å)	21.20 ± 0.16	22.90 ± 0.42	22.51 ± 0.17	23.95 ± 0.46	16.45 ± 20.80
Axial Ratio	1.27	1.43	1.35	1.49	1.02
Micelle Volume ($Å^3$) [a]	24766	24520	26292	25943	18060
Aggregation Number (N_{agg})	71	70	75	74	51
Scale	1	1	1	1	1
SLD - Surfactant	-0.25 ± 0.10	-0.21 ± 0.11	0.55 ± 0.06	0.51 ± 0.06	0.51
SLD - Solvent	6.34	6.34	6.34	6.34	6.34
Temperature (K)	293	293	293	293	293
Volume Fraction	0.003	0.003	0.008	0.008	0.003
Reduced X^2	1.28	1.21	1.87	1.75	7.48

[a] Calculated with the relationship $V_{micelle} = \frac{4}{3}\pi R_p R_e^2$

A9.10.2 Fitting parameters for PVP

Table A9.7 Parameters used in fitting PVP in Chapter 6

Model	Guinier Porod Model	
System	0.5% w/w PVP	
	Static	Flow
Scale	1	1
Background (cm^{-1})	0.011	0.004
Radius of Gyration (R_g) (Å)	114 ± 0.701	159 ± 1.15
s	0.05 ± 0.002	0.95 ± 0.007
Porod Exponent (d)	1.58 ± 0.004	4.81 ± 0.030
Reduced X^2	2.97	4.88

A9.11 Results from Image Processing and Drop Analysis

Table A9.8 Parameter list of the primary observables taken from analysis of drop images taken before and after SANS measurements

System	50 mM SDS		20 mM SDS and PVP		30 mM SDS and PVP	
	Before	After	Before	After	Before	After
Drop Diameter (µm) [b]	49.6	52.6	51.6	50.4	51.9	50.2
Drop Volume (μm^3) [b]	63827	76081	71916	67109	73108	66382
Major Axis Length (µm) [b]	55.0	58.0	59.4	53.8	57.1	55.3
Minor Axis Length (µm) [b]	52.2	53.1	54.7	51.3	52.7	52.1
Eccentricity	0.29	0.39	0.33	0.29	0.36	0.31
Frequency (Hz)	151	228	111	150	54	166
Number of Drops Processed	3028	3056	1289	2574	548	1672
Scattering Volume	0.87	.077	0.87	0.84	0.93	0.79

[b] Converted from pixels with the relationship $\mu m = 1.93 \times pixel$. Conversion obtained from a calibration scale captured using equivalent camera settings

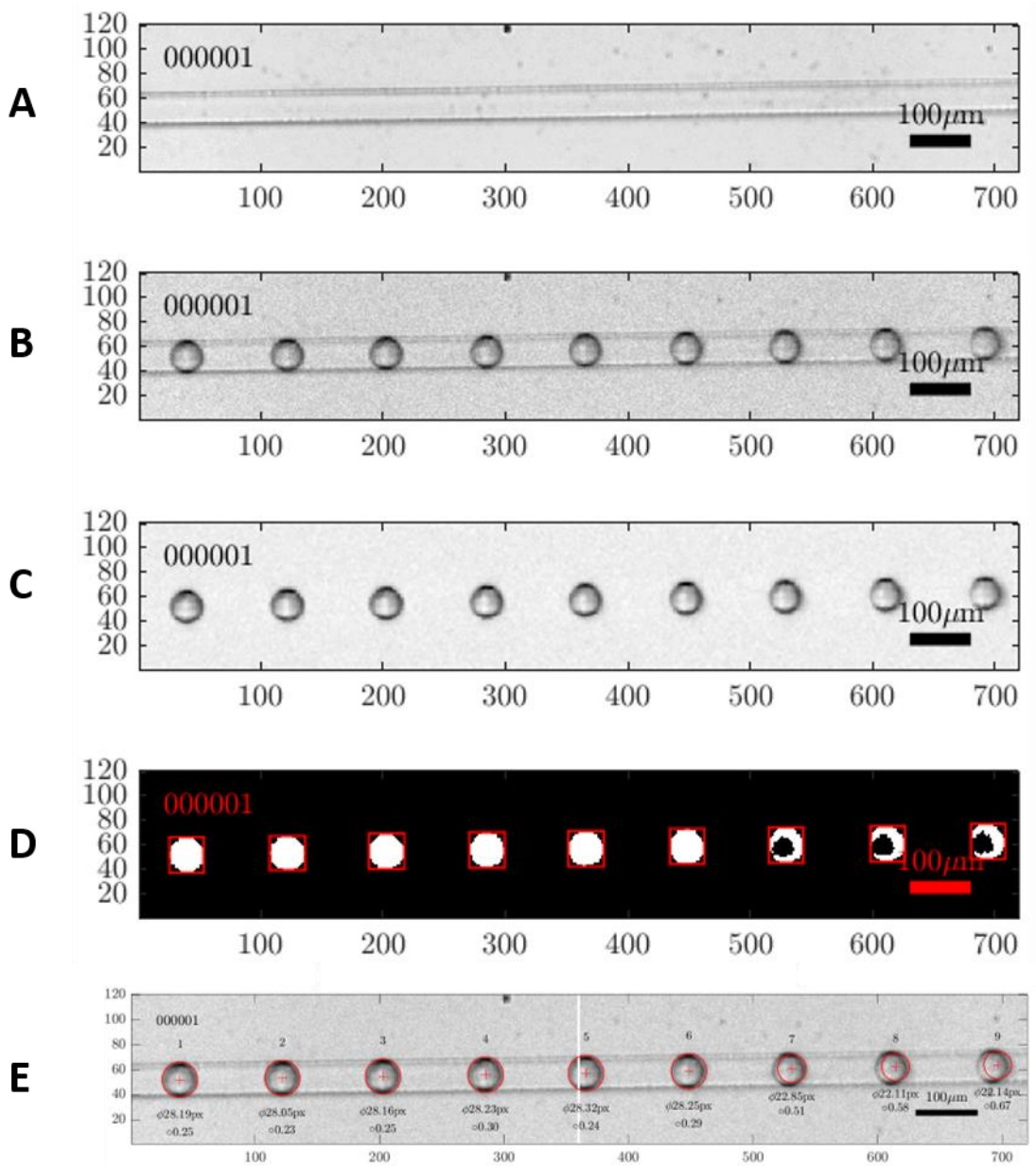

Figure A9.8 Example of the results from image processing with a threshold below the minimum limit. Image of the **A)** Background **B)** Raw data **C)** Raw data with background subtracted **D)** Black and white mask post thresholding **E)** Raw data with drop perimeters and centroids from the fit shown in red. The drops on the far right have nonsensible fits where their centroids are of centre and diameters a fraction of the expected values.